UNCLASSIFIED

FINAL REPORT

DEVELOPMENT OF CO_2 LASER DOPPLER INSTRUMENTATION DETECTION OF CLEAR AIR TURBULENCE

ER70-4203

5 June 1970

RAYTHEON COMPANY

EQUIPMENT DIVISION

Reproduced by
NATIONAL TECHNICAL
INFORMATION SERVICE
U S Department of Commerce
Springfield VA 22151

(NASA-CR-127058) DEVELOPMENT OF CARBON DIOXIDE LASER DOPPLER INSTRUMENTATION DETECTION OF CLEAR AIR TURBULENCE Final Report C. Sonnenschein, et al (Raytheon Co.) 5 Jun. 1970 270 p

N72-26420

CSCL 20E G3/16

Unclas
30926

RAYTHEON COMPANY
EQUIPMENT DIVISION

RAYTHEON

FINAL REPORT

DEVELOPMENT OF CO_2 LASER DOPPLER INSTRUMENTATION DETECTION OF CLEAR AIR TURBULENCE

ER70-4203

5 June 1970

CONTRACT NAS-8-24742

Prepared for

GEORGE C. MARSHALL SPACE FLIGHT CENTER
NASA
Huntsville, Alabama 35812

Prepared by

Dr. C. Sonnenschein
A. Jelalian
Dr. W. Keene

RAYTHEON COMPANY
EQUIPMENT DIVISION
EQUIPMENT DEVELOPMENT LABORATORY

Sudbury, Massachusetts 01776

PRECEDING PAGE BLANK NOT FILMED

CONTENTS

CONTENTS (Continued)

CONTENTS (Continued)

CONTENTS (Continued)

CONTENTS (Continued)

ILLUSTRATIONS

ILLUSTRATIONS (Continued)

ILLUSTRATIONS (Continued)

TABLES

ABSTRACT

This final report describes the analytical, experimental, and developmental work performed under NASA Contract NAS-8-24742 during the period 6 June 1969 through 5 June 1970. An airborne pulsed, CO_2, laser-optical radar system that detects clear air turbulence, and which performs Doppler measurements of this air-motion phenomenon, is discussed. Certain conclusions and specific recommendations emerging from this study are also given.

SECTION 1

INTRODUCTION AND SUMMARY

1.1 SCOPE OF THE PROGRAM

It is well known that radiation scattered from a moving target undergoes a frequency change, called the Doppler shift, that is proportional to the velocity component parallel to the direction of propagation of the radiation. This shift, therefore, gives a measurement of the velocity component, or, in the case of several targets, of the targets' velocity distribution.

Raytheon has already built a system under NASA Contract NAS-8-21293 that measures a velocity component of the atmospheric wind by heterodyning the radiation scattered by atmospheric aerosols. Since many such aerosol particles are simultaneously present in the beam, a frequency spectrum is obtained. Data about both the mean velocity and its spatial variation are contained in this spectrum. For the reason that clear air turbulence is characterized by velocity fluctuations, this heterodyning technique should be capable of remotely detecting such turbulent areas.

Since the last reporting period, activity was concentrated primarily in two areas: (1) developing a pulsed CO_2 laser transmitter for use in the optical, Doppler radar system, and (2) a continuance of system studies pertinent to the construction of a CAT detection arrangement suitable for flight use in an aircraft. As expressed in Section 6 of this report, the design objectives of the transmitter as a component of the overall radar system were all met and in some cases exceeded. System investigations that were continued during this final reporting interval utilized the optical heterodyne approach for determining velocity distribution of aerosols suspended in the atmosphere, and also the configuring

of various components within the transmitter. These configurations are detailed in Section 6 of this report.

Five bimonthly reports have been issued under the current contract. These reports have covered the work performed during each reporting period. This final report, therefore, discusses all significant work performed during the program commencing 6 June 1969, and ending 5 June 1970.

The remaining sections in this report are organized as follows:

Section 2 - A discussion of the characteristics of clear air turbulence and the way these properties affect its detection

Section 3 - A description of the analytical work performed to develop the information required for the transmitter and receiver design. This includes a sensitivity and an error analysis of the receiver

Section 4 - A receiver design

Section 5 - A detailed analysis of the gain characteristics of a pulsed laser amplifier

Section 6 - A complete discussion of the experimental effort that has resulted in a laser transmitter exceeding contract specifications

Section 7 - Conclusions

Section 8 - Recommendations

In the remainder of this section, paragraph 1.2 provides a separate introduction to the receiver design; paragraph 1.3 supplies an introduction solely to the transmitter efforts; and paragraph 1.4 gives a summary of the entire report.

1.2 LASER CAT DETECTOR RECEIVER DESIGN PRINCIPLES

1.2.1 INTRODUCTION

This section discusses the design principles for the laser CAT detector experiment. The objective of the study was to view the experiment as a united whole, and to achieve a compatible design of the instrument. A balanced design is desired in terms of a laser pulse length suitable for making doppler measurements of CAT in the 10.6 μ band. The laser must be sufficiently powered to allow measurement at a substantial distance from the aircraft. To do so requires the ability to interrelate atmospheric effects with radar observables.

Basically, the study program had two sets of problems; namely,

a. What are the radar parameters needed to discriminate a non-CAT atmosphere from a CAT situation? This is discussed in Section 2.

b. What are the radar parameters needed to assure aerosol detection at a suitable range? This is discussed in Section 3.

These two questions involved distinctly different solutions. The solution to the second problem, fundamentally, was addressed solely to the problem of determining the laser power requirements needed to sense the presence of the aerosols. In this case, the target signature was such that the radar could operate in its maximum sensitivity mode (that is, matched in all respects). For this purpose, it was assumed that the detection took place only in respect to the total energy of the echo (i.e., independent of the phase information contained in the echo) and that only incoherent integration could be done on an interval of time approximately equal to the time in which the vehicle carrying the CAT radar traverses a distance equal to the round trip pulse length. On this

basis, the signal-to-noise ratio required to reliably differentiate such an echo from the receiver noise may be calculated.

The first problem approached in the study was far more subtle, and concerned whether or not the laser parameters consisting of the laser frequency, the laser pulse width, the laser beam coverage and the receiver processing technique, were well matched to the difficulty of measuring the presence of CAT. To make this determination, a suitable model for predicting the behavior of the aerosols under various turbulence conditions had to be obtained. Then a determination of the interacting effects aerosols had on the radar observables was made. Following this, the degradation to the lidar observables inserted by the fluctuations of the echoes and the receiver noise were considered. Finally included were the non-optimum character of a practical receiver in further inserting measurement errors.

In brief, the aim of this study was to arrive at an error analysis of the laser CAT instrument in terms of the part attributable to the uncertainty of the atmosphere in the model, the part ascribed to the echo fluctuations, the part assigned to the choice of the laser parameters, and the part due to the noise.

1.2.2 TRADEOFF FACTORS

1.2.2.1 Turbulence Theory

The basic objective of the laser CAT experiment was to demonstrate that the CAT affecting an aircraft can be sensed remotely from a moving aircraft. It is important then that there be general agreement about the definition of CAT and that the criteria for judging the value of the radar instrument be well understood by both the designers and the users. There are thus three distinct points of view that must be reconciled; namely, (1) the definition of CAT commonly accepted by meteorologists, (2) the effects of CAT detrimental to aircraft as specified by the

aerodynamicists, and (3) the tracers of the CAT which are the only items which are measurable by the radar.

The present state of affairs may be summarized as follows. There is general agreement that the velocity distribution of the air motion in homogeneous CAT (in the inertial subrange) is well described by theory. There is somewhat less agreement on how this theory is to be interpreted. In particular, just what it implies in terms of the spatial distribution and the magnitude of the gust components likely to be encountered in CAT of a certain degree of severity is far less certain. There is growing evidence that the vertical component is essentially inhomogeneous with the CAT occurring only at the interface between two layers of air which are in primarily laminar relative motion. Likewise, when the condition occurs the CAT affected region is likely to have a large extent in the horizontal dimensions.

At this point, there are possibly large discrepancies among the different types of disciplines involved regarding the sets of parameters thought to be representative of certain levels of CAT activity. Data sets taken from aircraft derived data support the theory in the sense that the shape of the spectra inferred from the experiments are in general agreement with the theory. Nonetheless, the detailed values of the parameter describing CAT intensity; namely eddy dissipation rate, varies substantially between investigators, and similarly, the mean square air velocity associated with a certain level of CAT activity varies considerably between various data sources.

There is general agreement that the wind tracers; namely, the natural aerosols, introduce no distortion of the air motion and that their velocity distribution essentially mimics the air turbulence. Furthermore aerosols have been detectable by a 10.6 μ radar at ground level. There is sufficient evidence that aerosols

exist in sufficient profusion at the levels at which the CAT may be found.

There is also agreement that the eddy dissipation rate ϵ would be a valuable parameter to measure in sensing the presence of CAT. The radar, however, can measure this quantity indirectly from a velocity spectrum. The radar by its action permits the measure of both instantaneous and average velocity distributions. Thus it appears that it is capable of measuring both highly transient gusts and the slowly varying statistic; namely, the velocity variance. High velocity gusts, however, are a low probability transient phenomena. In this case the mass of data is concentrated in one part of the spectrum and the transient phenomena occurs infrequently, very weakly, but very near to the residual effects of the mass of data. (In conventional radar theory, this is known as the problem of detecting a weak signal in a clutter background.) There are difficulties in measuring and establishing the significance of a small spike in a spectrum at a low amplitude level compared to measuring the major elements of the spectrum. Likewise, the significance of detecting a highly localized transient of short duration, may be questionable from the point of view of taking effective action in the aircraft.

The conclusion reached, then, is that it is better for the radar to aim at measuring the statistically stable quantities in the CAT. In terms of radar capability, this amounts to measuring the variance of the velocity distribution. Turbulence theory, when properly modified by the radar interaction, allows this quantity to be translated into a measure of ϵ.

As stated in an earlier report, the range of values of ϵ characterizing CAT available from all data sources is from 35 to 1000 cm^2/sec^3. Turbulence theory allows the estimation of the velocity variance of the turbulence corresponding to this range,

assuming some knowledge of the scale size L_o (see Section 2 for additional details). This then represents the values of σ_v^2, the velocity variance, which must be measured, and which contains a parameter L_o (expressing again the uncertainty of the knowledge of the turbulence model).

1.2.2.2 Radar Interaction

It can be shown that the output of a properly matched system suitably designed to cover the full range of parameters introduced by the target can be described by the convolution shown below

$$|P(\tau,f)| = \int_{-\infty}^{\infty}\int_{-\infty}^{\infty} \psi^2(\tau' - \tau,\ f - f')\ \sigma(\tau',f')\ d\tau' df' \qquad (1\text{-}1)$$

where

$$\psi^2(\tau,f) = \left| \int_{-\infty}^{\infty} s^*(t)\ s(t+\tau)\ e^{i2\pi ft}\ dt \right|^2 \qquad (1\text{-}2)$$

$s(t)$ = analytic represention of the transmitted signal

$\sigma(\tau,f')$ = scattering function of the aerosols

τ = time delay (proportional to range)

f = frequency (proportional to doppler velocity)

In words, the mean square output of the radar at a certain range (τ) and doppler frequency (f), is the convolution of the ambiguity function of the lidar (ψ^2) centered on τ and f, with the aerosol characteristics at all ranges and frequencies.

The scattering model for the aerosol itself must be represented by a convolution relating the properties of the individual aerosol particles to the shape of the region in which the particles may be found. Thus, homogeneous turbulence may be characterized by a scattering model in which the frequency distribution is

essentially, say, the von Karman spectrum, and the range distribution is the auto-correlation function corresponding to the Von Karman spectrum. The non-homogeneity can then be represented by another convolution of a function representing the range extent and the mean velocity drift of the CAT.

In its simplest terms this theory predicts that even if the aerosols were stationary there would be a finite width to the measured spectrum of approximately the reciprocal of the laser pulse duration. As the turbulent motion of the aerosols increases, the spectrum of the echoes broadens; but, essentially, the broadened width is the RMS sum of the widths of the radar ambiguity function (the laser bandwidth) and the equivalent Doppler width of the scatterers. To measure Doppler width, therefore, the radar must measure deviations from the natural line width of the laser. The major consideration in the design of the laser, subsequently, is that its ambiguity function be chosen consistent with the minimum Doppler width of the observable scatterers.

To this, sufficient margin of safety must be added to account for the inaccuracies interjected by the lidar. These inaccuracies are basically related to the signal-to-noise ratio available for the measurement, and the deviation of a practical instrument from that of an ideal matched system.

1.2.2.3 Radar Inaccuracies

Assuming that the lidar is optimally matched to the measurement requirement, an assessment of the degradation to the nature of the signals and the measurement technique must be made. It is clear, that on any given pulse cycle, the echo which one observes is statistically fluctuating and reflects itself directly in the fluctuations observed at the output of a spectrum analyzer driven by the radar. These fluctuations contribute to the uncertainty with which the spectral width may be measured. Furthermore, the

addition of random noise to this input, further degrades the performance.

In order to obtain some quantitative appreciation of the extent of the problem, a brief study was conducted of the performance measures of an optimum width estimator. This work showed that, theoretically, the spectral width could be measured to an accuracy proportional to the geometric mean between the true scatterer Doppler width and the frequency resolution obtainable from coherent integration over the full observation time. This result, except for a numerical scaling factor, was virtually invariant with per pulse signal-to-noise ratio.

As a practical matter, currently available laser technology does not permit us to accomplish the coherent integration over periods comparable to the observation time. Indeed it is assumed that coherent integration can be obtained only within the pulse duration and that outputs due to successive pulses can only be added incoherently. This assumption is tantamount to placing a lower limit on the output spectral width and would amount to a significant deviation from the desired ideal system. As a consequence, the actual result will deviate from the theoretical accuracy predicted.

In order to simplify the work, it is assumed that in a practical system estimation, accuracy may be achieved due to statistical fluctuations comparable to the optimum measurements. But these measurements will be degraded by a bias error which will express the fact that there is a lower bound to the resolvable bandwidth. To get some quantitative bound on the magnitude of the effect, a model of the receiver was constructed. The receiver consisted of a filter bank, each member of which had a bandwidth properly matched to the pulse length, and which was spaced apart by an interval equal to exactly this pulse length. It is clear that regardless of the shape of the true input spectrum, the output of

each filter bank member must be regarded as a sample of the input spectrum at the center frequency of the filter. It is also clear that this mechanism introduces a bias error which is a function of the input width. All the factors involved were considered and a formula relating the bias errors to the laser and scatterer parameters has been derived.

1.2.2.4 Meteorological Considerations

Two factors affect the region of the atmosphere sampled by the radar system: transmitter pulse length, and receiver range gate. As the time for which the range gate is open approaches zero, a length of atmosphere equal to $c\tau/2$ is sampled, where τ equals the transmitter pulse length. As the length of the range gate increases, so does the length of the region from which atmospheric returns are obtained. If the range gate equals the pulse length, the length of the total sample equals $c\tau$. However, for a square pulse, three-quarters of the energy in the return comes from a length equal to $c\tau/2$. Therefore $c\tau/2$ will be assumed to equal the range resolution.

The velocity resolution is determined by a combination of factors including the pulse length, the range gate, and the atmospheric velocity distribution. Neglecting the effect of the atmosphere, the echo returned from any target, illuminated by a pulse of length τ and detected in a range gate of equal lengths, has a minimum bandwidth of $\sqrt{2}/\tau$. Since frequency and velocity are related by the Doppler equation, this implies a velocity resolution of

$$\Delta V = \frac{\sqrt{2}\,\lambda}{2\tau} \qquad (1\text{-}3)$$

Or, since the range resolution

$$\Delta R = \frac{c\tau}{2} \qquad (1\text{-}4)$$

Then

$$\Delta V = \frac{\sqrt{2}\,\lambda\, c}{4\Delta R} \qquad (1\text{-}5)$$

Thus as the range resolution increases (a larger length of atmosphere is sampled), the velocity resolution decreases (smaller velocity differences are detectable).

This is the first consideration in setting the width of the individual filters. Filters should be no narrower than the frequency resolution; i.e., $\sqrt{2}/\tau$. However, the width of a filter should also be equivalent to the velocity spread expected from non-turbulent conditions. Thus the return from conditions of no turbulence would slightly exceed this width (due to the effects of pulse and range gate) and would activate one or two filters. Turbulence, on the other hand, would cause signals to exist in more than two filters; the number of filters activated would depend upon the kinetic energy contained in the turbulent region.

Some information is available concerning the anticipated rms velocities for turbulent and non-turbulent conditions. (This is discussed in Section 2.) The rms velocities apparently must vary monotonically with range, although the details of the variation are unknown. In fact, there has been disagreement among meteorological experts about whether the rms velocity will continue to increase when the range resolution increases beyond 1000 feet.

To make an optimal selection of pulse length, range gate, and filter bandwidth, knowledge of these atmospheric parameters is essential. The alternative is to design a versatile experimental receiver (a construction which would be more complex, costly and difficult to operate) capable of operating under all possible conditions. With such a design, and after the necessary data has been obtained, operational systems could be built with fewer possible adjustments.

1.3 LASER CAT DETECTOR TRANSMITTER DESIGN CONSIDERATIONS

1.3.1 INTRODUCTION

Using the laser Doppler heterodyne approach, an airborne research-type instrument was designed in order to investigate the capabilities and limitations of this technique in the detection of clear air turbulence. The CO_2 laser transmitter design and development aspects of the overall instrument are discussed in Section 6. Conceptual definition and experimental apparatus discussions preview the successful transmitter feasibility demonstration which is described in detail. The transmitter feasibility demonstration showed that peak power and average power in excess of contractual requirements could be obtained, and that even higher powers and repetition rates may well be achieved in the near future.

The pulsed CO_2 laser amplifier designed and developed for the feasibility demonstration was of the multiple tube, folded type. The present length of 7 feet is considered appropriate for packaging in the system being designed for airborne research on CAT; however, the length can be reduced if necessary. The amplifier was capable of higher output power than the White cell amplifier which was designed, fabricated, and tested under this contract.

The section on experimental apparatus includes discussions of the laser oscillator, the modulator, the folded amplifier, and the electronics and power supplies. The performance of these laboratory equipments met or exceeded contractual requirements for CAT research applications. The results of studies on the electro-optical, opto-mechanical, electro-mechanical and thermal aspects of the overall system are presented in connection with the individual components to which they apply, and throughout the transmitter feasibility demonstration discussion.

1.3.2 TRANSMITTER DESIGN

The conceptual design of a research-type CAT detection instrument must involve a consideration of the CAT phenomenon and the interaction of CAT with an aircraft in flight. Since the localized velocity distributions in CAT lead directly to time dependent forcing functions applied to an aircraft as it flies through CAT areas, measurements of atmospheric velocity distribution ahead of an aircraft would be highly desirable.

A CO_2 laser Doppler radar is ideally suited to this task. The 10.6 μm wavelength of CO_2 lasers leads to a doppler shift at an aircraft velocity of Mach 1 equal to 60 MHz from the doppler equation $f_D = 2v/\lambda$. Velocity resolution of 2.5 m/sec corresponds to 500-kHz bandwidth and 2-μsec pulses. Spatial resolution corresponding to this pulse length is 1000 feet, which is equal to several aircraft lengths and to a minimum frequency of the CAT-induced forcing function acting on the aircraft of one cycle every several seconds at Mach 1. This is well below typical aircraft minimum fundamental resonances. System high-frequency response extends well above maximum aircraft fundamental resonant frequencies of several Hz. These frequencies would be driven by the higher spatial frequencies of CAT.

In considering the conceptual design of a CO_2 laser transmitter, a MOPA (master oscillator-power amplifier) configuration appeared to be ideally matched to the requirements of CAT detection through velocity measurement. A master oscillator requires frequency control of only 500 kHz over the round trip time, and provides a local oscillator beam for heterodyne purposes. Further, with a MOPA, pulse length can be controlled within the limits of amplifier saturation over a range of several microseconds, and a pulse shape can be adjusted by a modulator located between the oscillator and amplifier. Additionally, spatial resolution can also be increased by extending the duration of the range gate. MOPA

components and the feasibility demonstration of power and pulse width were described in the Fourth Bi-Monthly Report.

1.3.3 TRANSMITTER AMPLIFIERS

As explained in an earlier report, two types of pulsed CO_2 laser amplifiers were considered for application in the CAT transmitter; a multiple-tube folded configuration, and a two-mirror, multiple-pass single tube configuration called a "White cell", both features of which are discussed in Section 6. The similarities between the amplifiers included (1) pulsed electrical excitation, (2) injection of pulsed or modulated radiation at 10.6 μm from a stable oscillator, and (3) amplification by means of stimulated emission of radiation from an inverted population of CO_2 molecules. The multiple-tube folded amplifier has advantages of easier optical alignment and higher self-oscillation threshold than the White cell. However, the White cell offers a more convenient packaging geometry, lower voltage requirements, and less weight.

Power and pulse-width feasibility tests have been successfully carried out on the multiple-tube folded amplifier. Tests on the White cell, which had been modified and re-designed several times during the course of the contract, showed that self-oscillation still limited the output power at a level well below system requirements. The White cell configuration, however, still has appeal with its small volume, light weight, and low voltage. Self-oscillation in the White cell was further reduced, nevertheless, and the gain, by careful optical design, increased to a degree where the White cell was comparable to the multiple-tube folded amplifier in power output. However, these efforts did not appear justified in the light of the few advantages that could be gained with the incorporation of the White cell amplifier into the research instrument. Work on the White cell was therefore terminated, and the multiple-tube folded amplifier developed for use in the CAT transmitter.

1.4 SUMMARY OF ACCOMPLISHMENTS AND FUTURE PLANS

1.4.1 DESIGN STUDIES

The design of the receiver depends significantly upon the parameters of the atmosphere in both turbulent and non-turbulent conditions. A given spatial volume should exhibit a certain velocity variation that will increase as the degree of turbulence increases. The rms value of velocity depends upon the size of the resolution volume as well as on the amount of turbulent energy contained within the volume. Even for non-turbulent conditions, the rms value will not equal zero.

As described in paragraph 3.6, optimal detection sensitivity of an individual filter is dependent on its width which should approximately equal the anticipated width of the return signal spectrum for non-turbulent conditions. Therefore it is important to obtain definitive data relating the velocity spread (equivalent to a spectral width through the Doppler relationship) to the size of the resolution volume and to the amount of turbulent energy. Some data on this subject is already available; but there seem to be some areas of disagreement.

There is, however, a method for designing the receiver without answering all these questions. This entails making a versatile instrument capable of successful operation whatever range of rms velocities are encountered. This, therefore, has been the approach taken. More conclusive data, however, will enable the design of a less expensive, less complex receiver system. All meteorological inputs available up to the time of this report were reflected in the receiver design.

The analysis required for the receiver design has also been completed. Detection sensitivity and the false alarm ratio have been computed as a function of the signal-to-noise ratio at the output of the optical detector (see paragraph 3.5). To complete

the analysis, radar results were obtained that related system signal-to-noise ratio to the laser output power, range, altitude, and optics diameter (see paragraphs 3.2, 3.3 and 3.4).

Additionally, the error involved in measuring the mean and width of a spectrum generated by a stochastic process was calculated in terms of the width of the individual filters making up the filter band (see paragraph 3.6).

A detailed receiver design has been completed (see Section 4). This design has resulted in a block diagram of the elements of the receiver. Selections have been made of the optimal manner to set up a filter bank, integrate pulses, and display data. Also, a recommendation has been made for an RVI display.

In summary, all analysis tasks have been successfully completed.

1.4.2 TRANSMITTER

Power feasibility of the MOPA transmitter conceptual design has been successfully demonstrated, with a peak output pulse power of 5 kilowatts, a 200-pps repetition rate, and a 2-μsec pulse width (variable as noted below).

The transmitter electronics required for the laser Doppler CAT system have all been defined. The electro-optical modulator is currently capable of pulse widths variable from 0.5 to 10 μsec. The decision to use the multiple-tube folded amplifier, instead of the White cell in the MOPA chain, has been noted earlier in this section and is covered in detail in Section 6.

SECTION 2

CHARACTERISTICS AND MEASUREMENT OF CLEAR AIR TURBULENCE

2.1 INTRODUCTION

In order to design an instrument for the remote detection of Clear Air Turbulence (CAT), it is important to have a good understanding of its basic characteristics. Paragraph 2.2 describes some of the properties of CAT and attempts to point out the many areas of uncertainty requiring further knowledge.

Paragraph 2.3 discusses certain aspects of the measurement of CAT intensity by a pulse Doppler laser radar. The basic premise is that CAT should be detected and its intensity estimated by sensing the rms turbulent velocity in a remote spatial volume.

2.2 CAT CHARACTERISTICS

Clear Air Turbulence (CAT) has been defined by the National Committee for Clear Air Turbulence (1966) as "all turbulence in the free atmosphere, of interest in aerospace operations that is not in or adjacent to visible convective activity. This includes turbulence found in cirrus clouds not in or adjacent to visible convective activity." CAT thus considers all bumpy flight conditions away from convective clouds, as they affect airplanes, rockets, VSTOLs, etc.

While there has been considerable theoretical and experimental work in this area, a thorough understanding of CAT is still lacking. A detailed bibliography is contained in Appendix A. As a consequence the design of an instrument for the remote detection of CAT is subject to various uncertainties. To clarify some of these

problem areas, a brief description of the relevant characteristics of CAT follows:

Clear air turbulence is generally regarded as a stochastic process and thus is described statistically. It is characterized by all wavelengths of motion, although only a limited range is of importance for aircraft. For the Boeing 707 type aircraft, eddies of dimensions 60 m to 500 m can cause bumpy flight conditions, if the kinetic energy in this range of wavelengths is of sufficient magnitude[1]. Eddies smaller than this scale will be integrated by the surface of the aircraft whereas larger eddies will not cause accelerations large enough to be felt as (severe) bumps. For supersonic aircraft, this eddy range will have to be increased by about one order of magnitude[2].

While atmospheric turbulence is not statistically stationary, Gaussian, or isotropic over long distances, it is often considered to be so "locally" (over small distances). Unfortunately, quantitative data concerning the accuracy of these assumptions is not available.

A fairly large amount of data exists on the power spectrum of turbulence; i.e., the Fourier transform of the space correlation function of the turbulent velocity. Many of these spectra were determined from velocity time histories obtained by flying an aircraft through turbulent regions. Assuming the turbulence is "frozen" (unchanging) for the duration of the flight through the turbulent region, and assuming a constant aircraft airspeed, the velocity time histories are equivalent to velocity spatial histories. Correlation functions and spectra are then computed in a straightforward manner. It should be noted that these spectra are only valid for long wavelengths (> 30 m) due to the response times associated with the velocity measuring equipment. A detailed description of an analysis of some of this aircraft data is given in Appendix B.

Fichtl[1] and Lake[3] state that experimental data indicate the shape of the spectrum remains fairly constant over a wide range of altitude, yet Lake[3] goes on to present seemingly contradictory data. Vinnichenko[4] relates that after intensive investigations of CAT in the middle and upper troposphere, at least four types of turbulence spectra are measured:

"First one (about 50 percent of all cases) is the spectrum of decayed turbulence which is characterized by a very sharp slope of spectral curve (spectrum usually fits well with power law - k^{-n}, where k is a wave number and n ranging from 2.5 to 3) and by a very low intensity at microscale (rate of energy dissipation ε changes from 10^{-2} to 1 cm^2/sec^3).

The main feature of second type spectra (about 30 percent of all cases) is that low frequency part of the spectra has a sharp slope ($n \sim 3.0$), but high frequency one follows "5/3 Kolmogorov-Obukhov law". Change of spectral laws takes place at scales from 400 to 800 m. For that type of spectra ε is ranging from 10^{-1} to 200 cm^2/sec^3.

Spectra which fit well "-5/3 law" in the whole range of scales (about 20 percent) are usually measured in intensive turbulent zones where aircraft is affected by bumpiness (values from 1 to 400 cm^2/sec^3 and more).

And finally, the fourth type of spectra is measured when short gravity waves or cellular convection exists, which leads to the appearance of a "hump" on the spectral curve at scales corresponding to the wave lengths of these phenomena."

These results cited by Vinnichenko seriously question the conclusion of Fichtl and Lake, as well as other workers in the field, that CAT can be characterized by a single spectral form.

Obviously if there are different types of CAT, the design of a device for its detection is that much more difficult. However, Vinnichenko's results indicate that highly turbulent regions (which are the ones of importance here) generally obey the Kolmogorov spectral law. Furthermore, this type of spectra has been studied extensively whereas others have not. For these reasons the subsequent analysis will be based on the Kolmogorov law which in its one-dimensional form is[5]:

$$E(k) = A_1 \epsilon^{2/3} k^{-5/3} \qquad (2\text{-}1)$$

where $E(k)$ ($cm^2\ sec^{-2}$/rad cm^{-1}) is the one-dimensional energy spectrum of the velocity perturbations (i.e., the Fourier transform of the space correlation function of velocity perturbations), ϵ (cm^2/sec^3) is the rate of dissipation of turbulent energy per unit mass, k (cm^{-1}) is the wave number corresponding to the scale $L = 2\pi/k$, and A_1 is a constant whose value, based on both theory and experiment, is 0.5 for perturbations along the direction of flow and 0.64 for those transverse to the flow.

The Kolmogorov spectrum was derived for the inertial subrange; that is, those wavelengths where no production or dissipation of energy takes place, but in which only inertial transfer to smaller and smaller eddies occurs. Atlas[5] indicates that this range may extend from about 1 cm to about 600 m for CAT.

Assuming clear air turbulence is characterized by the Kolmogorov spectrum, it is evident from Equation (2-1) that the intensity of turbulence is proportional to the rate of energy dissipation (ϵ) to the two thirds power. Thus if ϵ can be estimated, the severity of CAT is determined. In non-turbulent regions ϵ decreases roughly linearly with altitude, typical values being 1000 cm^2/sec^3 at 1m and 0.1 cm^2/sec^3 at 1000 m[6]. Turbulent regions

appear to be characterized by large values of ϵ. For CAT the following classification has been proposed by Atlas[5]:

CAT Severity	ϵ (cm^2/sec^3)
Light	$35 < \epsilon < 110$
Moderate	$110 < \epsilon < 400$
Severe	$400 < \epsilon$

The width of the Doppler spectrum can be related to $E(k)$ in the following manner. $E(k)$ is defined as the Fourier transform of the space correlation function of velocity perturbations. Thus

$$R(\ell) \equiv \overline{V(x + \ell)\ V(x)} \tag{2-2}$$

where the bar above the symbols represents an ensemble average. Therefore

$$E(k) = \frac{2}{\pi} \int_0^\infty R(\ell) \cos k\ell d\ell \tag{2-3}$$

and

$$R(\ell) = \int_0^\infty E(k) \cos k\ell dk \tag{2-4}$$

From Equation (2-2) and (2-4)

$$\overline{V^2(x)} = R(0) = \int_0^\infty E(k)dk \tag{2-5}$$

In other words, the rms value of velocity is equal to the area under the curve of $E(k)$ versus k.

It is important to remember that $k = 0$ refers to wavelengths that are infinite, whereas $k = \infty$ corresponds to zero wavelength. A pulsed transmitter will therefore respond to values of k from

a lower limit equal to $4\pi/c\tau$ to an upper limit of infinity. Subsequently,

$$\overline{v^2(x)}_{pulse} = \int_{\frac{4\pi}{c\tau}}^{\infty} E(k)\, dk \qquad (2\text{-}6)$$

For regions where the Kolmogorov spectrum is valid

$$\overline{v^2(x)}_{pulse} = A_2\, \epsilon^{2/3}\, \tau^{2/3} \qquad (2\text{-}7)$$

where

$$A_2 = \frac{3A_1}{2}\left(\frac{c}{4\pi}\right)^{2/3} \qquad (2\text{-}8)$$

Thus the spectral width is direct measurement of the eddy dissipation rate, ϵ.

Even if some types of CAT do not follow the Kolmogorov law, their energy (velocity) spectra must somehow "scale" with the degree of turbulence; i.e., an increase in the amount of turbulence will correspond to an increase in ϵ. Likewise, the mean square turbulent velocity, which is given by the integral of the energy spectrum, must also reflect the degree of turbulence. Consequently, even if the functional dependence of the spectra on ϵ is unknown (i.e., non-Kolmogorov), the degree of turbulence could still be estimated.

Finally, it should be noted that aircraft are not substantially affected by turbulent velocities on the order of the rms turbulent velocity (which typically is no more than a few m/sec), but rather by gust velocities which are several times as large. However, due to the "approximately" Gaussian distribution of velocities, these high gust velocities are relatively improbable. In addition, they can be transitory in nature and of rather limited spatial extent. Therefore, it appears that a remote CAT detector should not try to sense them, but should rely on a measurement of the rms turbulent velocity.

2.3 MEASUREMENT APPROACH

The instrument designed for the detection and measurement of CAT is a pulsed laser doppler radar. The "targets" of the laser are natural aerosols distributed throughout the troposphere. These aerosols scatter energy back to the detector. This signal can be used to infer the presence of CAT. This is possible because the aerosols are small, light particles which relax to the atmospheric velocity in the order of milliseconds. Thus they serve as excellent tracers of the wind and enable an estimate of root mean square turbulent velocity to be made.

While the exact nature of scattering from a distributed target has not been completely analyzed, there appears to be agreement as to its general characteristics. From the doppler principle it is known that each scatterer will shift the frequency of the backscattered wave by an amount $2v/\lambda$, where v is the velocity component of the particle in the direction of the laser propagation vector and λ is the laser wavelength. When a volume in space that contains many aerosols is illuminated a "summation" of the individual responses is the result.

If an ideal CW laser (zero line width) illuminates a certain volume of space, the received doppler spectrum D(f) will be proportional to the probability density function p(v) of the radial velocities of the scatterers in the region, with v given by $\lambda f/2$

$$D(f) \sim p\ (v = \lambda f/2) \qquad (2\text{-}9)$$

Here p(v) refers to a velocity distribution at a particular time. As time changes, p(v) can change and so will the doppler spectrum.

When a doppler laser radar that is non-coherent from pulse to pulse is employed and the transmitted waveform is a rectangular pulse, the transmitted spectrum has the form

$$T(f) = \left[\frac{\sin \pi f\tau}{\pi f\tau}\right]^2 \qquad (2\text{-}10)$$

where τ is the transmitted pulse length and the frequency f refers to deviations from the laser frequency.

The transmitted pulse length τ, the receiver range gate τ_g, and the laser beam shape then determine a certain volume in space which is being examined. At an instant of time, t_o after the beginning of the pulse transmission, a region of space located between ranges $c\,t_o/2$ and $c(t_o - \tau)/2$ is observed. The region of observation propagates through space at one-half the speed of light. At the end of the range gate, the region between $c(t_o + \tau_g)/2$ and $c(t_o - \tau + \tau_g)/2$ is seen. Thus the total return signal is an integrated effect of the scatter from ranges between $c(t_o - \tau)/2$ to $c(t_o + \tau_g)/2$. (For the remainder of the discussion it is assumed that $\tau = \tau_g$.) To gain some insight as to the nature of the radar-scatterer interaction, it is useful to consider four specific cases:

(1) Single Scatterer

So long as the range gate is positioned so that the entire scattered wave is observed, the received spectrum will have the same form as the transmitted spectrum; but it will be shifted by the doppler frequency $f_d = 2v/\lambda$. Note that if the range gate is "improperly" positioned so that only part of the scattered wave is observed (duration τ_1), then the same doppler shift will occur causing the overall spectrum to broaden

$$D(f) = \left[\frac{\sin \pi\,(f - f_d)\,\tau_1}{\pi\,(f - f_d)\,\tau_1}\right]^2 \qquad (2\text{-}11)$$

(2) Many Scatterers at Same Range

Assume the scatterers all lie at the same range and are distributed in a radial velocity according to the probability density function p(v). Then if the range gate is positioned so that the entire scattered wave is observed, the doppler spectrum will be given by the convolution of p(v) with T(f)

$$D(f) = \int_0^\infty p\left(v = \frac{\lambda f_1}{2}\right) \left[\frac{\sin \pi (f - f_1) \tau}{\pi (f - f_1) \tau}\right]^2 df_1 \qquad (2\text{-}12)$$

If only a portion τ_1 of the scattered wave is observed, τ is replaced by τ_1 in equation (2-12).

(3) Many Scatterers at Same Radial Velocity

Assuming a large (infinite) number of scatterers with independent phases but the same radial velocity, it is hypothesized that the spectrum of the received range gated signal may be approximated by

$$D(f) = \int_0^1 \left[\frac{\sin \pi (f - f_d) \tau x}{\pi (f - f_d) \tau x}\right]^2 dx \qquad (2\text{-}13)$$

Essentially this integral represents a summation of the spectra of the range gated responses of the individual scattering particles in the resolution cell, assuming they are independent. Expanding the integrand in a Taylor series and carrying out the integration gives

$$D(\Omega) = 1 - \frac{1}{9}\Omega^2 + \frac{2}{225}\Omega^4 - \frac{1}{2205}\Omega^6 + \frac{2}{127575}\Omega^8 + \ldots \qquad (2\text{-}14)$$

where $\Omega = \pi (f - f_d) \tau$. From equation (2-14) it is estimated that the half-power points occur at about $\Omega \pm \pi$, giving a spectral width of roughly $2/\tau$. Since the transmitted waveform has a spectral width of about $1/\tau$, the spectral broadening characteristics of a spatially distributed target are obvious.*

(4) Many Scatterers at Varying Ranges and Radial Velocities

Green[7] has shown that the average power out of a receiver that is matched to the transmitted waveform (except that the filter is misaligned upward by f in frequency and the output is observed at $t = t_o + \tau$ instead of $t = t_o$) will be

$$P(\tau, f) = \int_{-\infty}^{\infty} \int_{-\infty}^{\infty} \psi^2(\tau' - \tau, f - f')\, \sigma(\tau' \sigma f')\, d\tau'\, df' \qquad (2\text{-}15)$$

where $\sigma(\tau, f)$ is the so-called scattering function of the distributed target and $\psi^2(\tau, f)$ is the ambiguity function of the complex envelope $u(t)$ of the transmitted pulse

$$\psi^2(\tau, f) = \left| \int_{-\infty}^{\infty} u^*(t)\, u(t + \tau)\, e^{i2\pi ft}\, dt \right|^2 \qquad (2\text{-}16)$$

At a given range (constant τ) the scattering function $\sigma(\tau, f)$ is the probability density function of the doppler frequency f (or equivalently the velocity $v = \lambda f/2$). As long as the ambiguity function is narrow relative to $\sigma(\tau, f)$, i.e., like a delta function, then $P(\tau, f) \simeq \sigma(\tau, f)$.

---

*Recall that the transmitter pulse length and range gate were assumed equal. By similar reasoning it follows that if the pulse length is held fixed but the range gate is increased, the amount of spectral broadening decreases. In that limit where the range gate becomes infinite, there is no spectral broadening due to the target.

Equation (2-15) was derived on the assumption that scattering from adjacent incremental range elements is uncorrelated. Even though turbulence possesses a velocity correlation in space, it is still felt that this equation is applicable, since each aerosol particle essentially adds a random phase angle to its scattered wave, and thus decorrelates the return from adjacent range elements.

In equation (2-15) it is important to note that the power $P(\tau,f)$ and the scattering function $\sigma(\tau,f)$ are ensemble averages. The "instantaneous" power at a particular range and doppler frequency will of course fluctuate in time because the scattering function is changing. The doppler spectrum will accordingly measure the "instantaneous" distribution of aerosol radial velocities within the single pulse resolution cell of the radar.

The results of paragraph 3.5 show that it will be necessary to do post-detection integration of the returns from at least 10 pulses, which at a pulse repetition frequency of 200 Hz is equivalent to averaging over 0.05 second. In other words, at least 10 estimates of the doppler spectrum made at 5-ms intervals will be added together to get the final spectral estimate. The standard deviation of this doppler spectrum ($\hat{\sigma}_f$) and the standard deviation of the turbulent velocity ($\hat{\sigma}_v = \lambda\ \hat{\sigma}_f/2$) can then be evaluated by any reasonable method.

In using this type of processing, it is important to realize just what is being estimated. If $\hat{\sigma}_v$ is intended to be an estimate of the "total" root mean square turbulent velocity of CAT, then an average must be taken over a time (spatial) scale that is large compared to the correlation time (distance) of turbulence. However, in determining the degree of turbulence, it is not essential that the "total" mean square turbulent velocity be estimated; i.e., the total area under the spatial velocity spectrum. For example, it is possible (and may be even desirable) to estimate the mean

square turbulent velocity in a limited spatial volume. In so doing, the velocity spectrum has been weighted by a factor which suppresses all spectral components having wavelengths longer than the dimensions of the volume[8]. So long as this region is examined in a time which is less than the correlation time of turbulence, this weighting factor should apply.

Proceeding on this basis, the estimate $\hat{\sigma}_v$ is equivalent to an estimate of σ in the Von Karman spectrum described by Fichtl[1]. Assuming it is the longitudinal component of turbulence that is being measured, the Von Karman spectrum is

$$E(k,L) = \sigma^2 \frac{2L}{\pi} \frac{1}{\left[1 + (1.339\ L\ k)^2\right]^{5/6}} \qquad (2\text{-}17)$$

where σ^2 is the variance of turbulence, L is the scale of turbulence, and k is the wave number. Asymptotically for large k L this has the form

$$E(k,L) \simeq \sigma^2 \frac{2L}{\pi} \frac{(L\ k)^{-5/3}}{(1.339)^{5/3}} \qquad (2\text{-}18)$$

which is precisely the form of the Kolmogorov spectrum given by equation (2-1). Equating the right hand sides of equations (2-18) and (2-1) and solving for the eddy dissipation rate ϵ gives

$$\epsilon = \left[\frac{2}{A_1 \pi}\right]^{3/2} (1.339)^{-5/2} \frac{\sigma^3}{L} \qquad (2\text{-}19)$$

In the cgs system of units, A_1 is .5, σ must be in cm/sec and L must be in cm. Putting in this value of A_1 equation (2-19) becomes

$$\epsilon = .67 \frac{\sigma^3}{L} \qquad (2\text{-}20)$$

Thus the eddy dissipation rate can be estimated by replacing σ by $\hat{\sigma}_v$ and L by $\hat{L}$. $\hat{\sigma}_v$ is obtained from the laser radar measurements

and $\hat{L}$ is obtained from meteorological data. For example, Fichtl[1] indicates that above the 2500-foot level typical values of L are in the order of 3000 to 6000 ft.

Expanding equation (2-20) to first order,

$$(\Delta\epsilon) \simeq \frac{2\sigma^2}{L} (\Delta\sigma) - .67 \frac{\sigma^3}{L^2} (\Delta L) \qquad (2\text{-}21)$$

where $\Delta\epsilon$ is the error in ϵ due to "small" errors in σ and L; i.e., $\Delta\sigma$ and ΔL. It then follows that the mean square error is

$$\overline{(\Delta\epsilon)^2} = \frac{4\sigma^4}{L^2} \overline{(\Delta\sigma)^2} + .44 \frac{\sigma^6}{L^4} \overline{(\Delta L)^2} \qquad (2\text{-}22)$$

providing $\Delta\sigma$ and ΔL are independent errors (which they should be) and either $\Delta\sigma$ or ΔL is zero mean.

It appears that errors in estimating L could be substantial, however additional information is needed in this regard. At least three sources of error in the estimate of σ can be identified:

(1) Because of the fact that non-coherent pulse-to-pulse processing is being employed, the basic doppler resolution is on the order of $1/\tau$ and thus the velocity resolution is approximately $\lambda/2\tau$. (λ is the laser wavelength 10.6 μ and τ is the transmitter pulse length.) In order to keep this error from becoming substantial, we should choose the transmitter pulse length so that

$$\frac{\lambda}{2\tau} << \sigma_{min}$$

where σ_{min} is minimum RMS turbulent velocity desired to be estimated. Using equation (2-20) with an ϵ of 35 cm^2/sec^3 (lower threshold of light CAT) and take L as 10^5 cm, then σ_{min} equals 1.62 m/sec. For $\lambda/2\tau = \sigma_{min}/2$, τ must be about 6.5 μs.

In non-turbulent conditions at high altitudes (10 km), ϵ is about three orders of magnitude less than the ϵ value corresponding

to light CAT. This implies σ for non-turbulent conditions is on the order of .16 m/s, an order of magnitude less than light CAT. On the other hand some preliminary measurements by Hardy et. al., at AFCRL indicate that σ for non-turbulent conditions is 4 to 5 times larger. If this is actually the case, distinguishing between CAT and no CAT will not be easy due to the small spread in RMS velocities. In addition it is noted that the range of σ values for CAT itself is quite small. Since ϵ varies by a factor of about 10 in changing from light to severe turbulence, σ only varies by $10^{1/3}$ (about 2).

(2) A second type of error is due to the nature of the receiver processing. A filter bank containing a finite number of filters will actually perform the spectral analysis of the received signal. This introduces a quantization type error since all the power in each filter must be assigned to the center frequency of that same filter.

(3) A third type of error in estimating σ can be classified as a statistical error. It is due to receiver noise added to the desired signal as well as to the statistical nature of desired signal itself. Since the total processing time is limited, these errors can only be reduced to a certain level.

These errors will be considered in greater detail in Section 3. However the discussion thus far indicates the need for meteorological data. There exists a serious disagreement between various sources of data concerning the values of ϵ corresponding to turbulent conditions. In addition, the appropriate values for σ_v are in dispute. Until definitive numbers are determined for these parameters, a CAT detector must contain sufficient versatility to be able to cope with whatever levels are actually encountered.

SECTION 2 REFERENCES

1. Fichtl, G., "Environmental Information for the Design of the NASA-LASER Clear Air Turbulence (CAT) Detection Device," Internal memo, George C. Marshall Space Flight Center, August 22, 1969
2. Reiter, E.R., "The Nature of Clear Air Turbulence: A Review," Symposium on Clear Air Turbulence and Its Detection, Seattle, Washington, August 14-16, 1968.
3. Lake, H., "Atmospheric Aspects Involved in the Development of an Airborne Clear Air Turbulence Detector," Raytheon Memo HL-093:69, 21 October 1969.
4. Vinnichenko, N.K., "Recent Investigation of Clear Air Turbulence in the USSR," Symposium on Clear Air Turbulence and Its Detection, Seattle, Washington, August 14-16, 1968.
5. Atlas, D., Hardy, K.R., and Naito, K., "Optimizing the Radar Detection of Clear Air Turbulence," Jour. of App. Meteor., V.5, No. 4, pp. 450-460, August 1966.
6. Lumley, J.L. and Panofsky, H.A., The Structure of Atmospheric Turbulence, p. 123, John Wiley and Sons, New York, 1964.
7. Green, P.E. Jr., "Radar Astronomy Measurement Techniques," Lincoln Laboratory Tech. Report No. 282, December 12, 1962.
8. Rogers, R.R., and Tripp, B.R., "Some Radar Measurements of Turbulence in Snow," J. of App. Meteor., Vol. 3, pp. 603-610, October 1964.

SECTION 3

RECEIVER ANALYTICAL CONSIDERATIONS

3.1 INTRODUCTION

In Section 2 a description was given concerning some of the basic characteristics of CAT, and some of the general principles governing the measurement of this turbulence with a laser doppler velocimeter. It is now necessary to investigate in more detail the requirements of the receiver for the laser doppler-detection system.

Relative to the receiver, there are two important questions that require answers. The first is concerned with detection probability at a given false-alarm rate. The second involves the accuracy with which the width of the return doppler spectrum can be measured.

To analyze the detection probability, calculations were made of the signal-to-noise ratio at the output of the optical detector. The variation of signal-to-noise as a function of range, altitude, and filter bandwidth were included. A derivation then related the input receiver signal-to-noise ratio to detection probability and false alarm rate. The result of this work was a prediction of the number of pulses required for integration to obtain large detection probabilities.

Finally a relationship was derived concerning the accuracy with which parameters of a spectrum generated by a stochastic process could be measured. The mean and RMS errors associated with the measurement of the spectrum mean and width were calculated in terms of the width of the individual filters.

The significant design parameters obtained from these studies include:

1. Laser output power
2. Laser pulse repetition rate
3. Transmitter/receiver optics diameters
4. Number of pulses required for integration
5. Width of individual filters
6. Spacing between filters

3.2 GENERAL SIGNAL-TO-NOISE DERIVATION

This section discusses the general derivation of the signal-to-noise ratio for a coaxial heterodyne system that collects scattered radiation from the atmosphere. The following assumptions will be made:

1. The beam is Gaussian and matched to the transmitter.
2. The target is at a range significantly greater than the transmitter size, but not necessarily in the far field.

The laser emits a plane wave with a Gaussian amplitude distribution. Laser radiation passes through a lens with focal length, f. The coordinate system will be located with its origin at the center of the lens and the z-axes parallel to the beam direction.

There are two possible approaches to calculate the heterodyne signal: (1) a wave function could be defined to represent the electric field, and (2) the electric field at the detector could be computed. From this the optical signal power could be derived, and, using the detector responsivity, the heterodyne current could be found. Alternatively, a similar calculation could be performed, using a wave function representing the number of propagating photons. Then the detector quantum efficiency is needed to determine the conversion of photons to electrons. The latter approach shall be used.

The wave function incident on the transmitter lens,

$$\psi_{Inc} \alpha \exp\left[- i\omega t - \left(\frac{\vec{r}''}{R}\right)^2\right] \tag{3-1}$$

where

$\vec{r}''$ = two dimensional vector in the x, y plane of the transmitter lens

R = radius of transmitter lens.

The lens introduces a phase change, so that

$$\psi_{TR} \alpha \exp\left[-i\omega t - i\frac{\pi \vec{r}''^2}{\lambda f} - \left(\frac{\vec{r}''}{R}\right)^2\right] \tag{3-2}$$

At a distance L from the lens

$$\psi(x,y,L) = \frac{\sqrt{2n_T}}{\sqrt{\pi L R \lambda}} \int_{-\infty}^{\infty}\int_{-\infty}^{\infty} \exp\left[i\frac{\pi}{\lambda L}(\vec{r} - \vec{r}'')^2 - \frac{i\pi \vec{r}''^2}{\lambda f} - \left(\frac{\vec{r}''}{R}\right)^2\right] dx'' dy'' \tag{3-3}$$

where

$\vec{r}$ = two dimensional vector in x, y plane a distance L from the transmitter lens

n_T = number of photons transmitted per second.

The wave function has been normalized so that

$$\int_{-\infty}^{\infty}\int_{-\infty}^{\infty} |\psi|^2 dx'' dy'' = n_T \tag{3-4}$$

Equation (3-3) can be integrated by completing the square to give

$$\psi(x,y,L) = \frac{\sqrt{2\pi n_T}\, R}{\lambda L\left[1 - i\frac{\pi R^2}{\lambda L}\left(1 - \frac{L}{f}\right)\right]} \exp\left[-\frac{\left(\frac{\pi \vec{r}}{\lambda L}\right)^2}{1 + \left(\frac{\pi R^2}{\lambda L}\right)\left(1 - \frac{L}{f}\right)^2}\right]$$

$$\exp\left[i(kL - \omega t + \phi)\right] \qquad (3\text{-}5)$$

where

$$\phi = \frac{\pi \vec{r}^2}{\lambda L}\left[\frac{1 - \frac{L}{f}\left(\frac{\pi R^2}{\lambda L}\right)^2\left(1 - \frac{L}{f}\right)}{1 + \left(\frac{\pi R^2}{\lambda L}\right)^2\left(1 - \frac{L}{f}\right)^2}\right] \qquad (3\text{-}6)$$

The scattering properties of the wave function, ψ, is similar to the scattering of the electric field. Therefore for a single scattering particle

$$\psi_{Scat} = \frac{\alpha_{Scat}}{r'} \exp(ikr') \qquad (3\text{-}7)$$

The term α_{Scat} can be related to the incident field by the scattering amplitudes

$$\alpha_{Scat_L} = S_2 \psi_L + S_3 \psi_R \qquad (3\text{-}8)$$

$$\alpha_{Scat_R} = S_4 \psi_L + S_1 \psi_R \qquad (3\text{-}9)$$

where the subscripts L and R refer to polarization, parallel and perpendicular to the scattering plane. It will be assumed that, in the average, atmospheric particles are spherical. For spherical particles

$$S_3 = S_4 = 0 \qquad (3\text{-}10)$$

Also for the case of backscatter, where $\theta' = \pi$,

$$S_1(\pi) = S_2(\pi) \equiv S(\pi) \tag{3-11}$$

The scattered wave function, after passing through the receiver lens (which is assumed to be identical to the transmitter lens)

$$\psi_{Sc} = \frac{S(\pi)\psi}{L} \exp\left\{-i\left[\frac{\pi}{\lambda f}(\vec{r}')^2 - \frac{\pi}{\lambda L}(\vec{r} - \vec{r}')^2 - (kL + \Delta\omega t)\right]\right\} \tag{3-12}$$

where

$\vec{r}'$ = two dimensional vector in x-y plane immediately after receiver lens

$\Delta\omega$ = the Doppler shift caused by the moving scatterer.

The detector current that results from heterodyning the scattered signal with a reference signal equals

$$i_s = 2\eta G \, \mathrm{Re} \int \psi_{Sc} \psi^*_{Ref} \, d\vec{r}' \tag{3-13}$$

where

η = detector quantum efficiency

G = detector gain

The reference signal will be assumed to be a plane wave with a Gaussian amplitude distribution identical to that of the transmitted beam

$$\psi_{Ref} = \frac{\sqrt{n_{ref}}}{\sqrt{\pi}\, R} \exp -\left[i\omega t + i\phi_R - \left(\frac{\vec{r}'}{R}\right)^2\right] \tag{3-14}$$

where

n_{Ref} = number of reference photons per second

ϕ_R = phase of reference signal relative to transmitted signal.

Substituting equation (3-5), equation (3-12), and equation (3-14) into equation (3-13) and integrating by completing the square

$$i_s = \frac{2\pi\sqrt{2\, n_T\, n_{Ref}}\; R^2\; S(\pi)\; \eta\; G}{\lambda\, L^2 \left[1 + \left(\frac{\pi R^2}{\lambda L}\right)^2 \left(1 - \frac{L}{f}\right)^2\right]} \exp\left\{-2\left|\frac{\pi\, R\, \vec{r}}{\lambda L}\right|^2 \left[1 + \left(\frac{\pi R^2}{\lambda L}\right)^2 \left(1 - \frac{L}{f}\right)^2\right]^{-1}\right\} \cos\left\{2kL + \Delta\omega t - \phi_R + 2\phi + \tan^{-1}\left[\frac{\pi R^2}{\lambda L}\left(1 - \frac{L}{f}\right)\right]\right\} \tag{3-15}$$

The quantity desired is the average signal power, proportional to i_s^2. So for averages over time periods that are long with respect to $\frac{1}{\Delta\omega}$,

$$i_s^2 = \frac{4\pi^2\, n_T n_{Ref}\; R^4\; S^2(\pi)\; \eta^2\; G^2}{\lambda^2 L^2 \left[1 + \left(\frac{\pi R^2}{\lambda L}\right)^2 \left(1 - \frac{L}{f}\right)^2\right]^2} \exp\left\{-4\left(\frac{\pi R\, \vec{r}}{\lambda L}\right)^2 \left[1 + \left(\frac{\pi R^2}{\lambda L}\right)^2 \left(1 - \frac{L}{f}\right)^2\right]^{-1}\right\} \tag{3-16}$$

This is the signal current produced by a single scatterer. For a collection of scatterers, equation (3-16) must be appropriately summed. It has already been demonstrated that the diffuse nature of the targets requires the summing of signal powers rather than currents.

Therefore, for a uniform density of particles, ρ, equation (3-16) must be integrated over $\vec{r}$ and L. Thus after integrating over $\vec{r}$

$$(i_s^2)_{Total} = \pi\, n_T\, n_{Ref}\, R^2 \rho\, S^2(\pi)\, \eta^2 G^2 \int_o^\infty \frac{dL}{L^2 \left[1 + \left(\frac{\pi R^2}{\lambda L}\right)^2 \left(1 - \frac{L}{f}\right)^2\right]} \tag{3-17}$$

where

ρ = number of particles per unit volume.

The term

$$\rho S^2(\pi) = \beta(\pi) \tag{3-18}$$

where

$\beta(\pi)$ is the term commonly used.

For shot noise limited operation, the only significant source of noise is the shot noise caused by the reference signal. Thus for a photoconductive semiconductor detector

$$i_N^2 = 2\eta\, G^2\, n_{Ref}\, B \tag{3-19}$$

where

B = system bandwidth

Combining equation (3-17), equation (3-18), and equation (3-19) the system signal-to-noise ratio can be calculated

$$\frac{S}{N} = \frac{(i_s^2)_{Total}}{(i_N)^2} = \frac{\eta\, n_T\, \beta(\pi)\, \pi R^2}{2B} \int_o^\infty \frac{dL}{L^2 \left[1 + \left(\frac{\pi R^2}{\lambda L}\right)^2 \left(1 - \frac{L}{f}\right)^2\right]} \tag{3-20}$$

Since

$$n_T = \frac{P_T}{h\nu} \tag{3-21}$$

where

P_T = transmitter power

then

$$\frac{S}{N} = \frac{\eta\ P_T\ \beta(\pi)\ \pi R^2}{2B\ h\nu} \int_0^\infty \frac{dL}{L^2\left[1 + \left(\frac{\pi R^2}{\lambda L}\right)^2 \left(1 - \frac{L}{f}\right)^2\right]} \tag{3-22}$$

Equation (3-22) represents signal-to-noise ratio for the general case described previously. The next section will investigate several special cases of interest.

3.3 SPECIFIC CASES

In Section 2 a general derivation was given for the signal-to-noise ratio of a coaxial heterodyne system collecting scattered radiation from the atmosphere. This section will use the results of that derivation and apply it to specific systems. From equation (3-22)

$$\frac{S}{N} = \frac{\eta\ P_T\ \beta(\pi)\ \pi R^2}{2Bh\nu} \int_0^\infty \frac{dL}{L^2\left[1 + \left(\frac{\pi R^2}{\lambda L}\right)^2 \left(1 - \frac{L}{f}\right)^2\right]} \tag{3-23}$$

In a pulsed system, the receiver can be range gated so that only a limited region of space contributes to the signal. If the length of the resolved scattering volume is ΔL and L_{AV} is the average range to the scattering volume, then if $L_{AV} >> \Delta L$, the integral in equation (3-23) can be approximately evaluated.

$$\frac{S}{N} = \frac{\eta\ P_T\ \beta(\pi)\ \pi R^2\ \Delta L}{2B\ h\nu\ L_{AV}^2\left[1 + \left(\frac{\pi R^2}{\lambda L_{AV}}\right)^2 \left(1 - \frac{L_{AV}}{f}\right)^2\right]} \tag{3-24}$$

If the focal length is set equal to L_{AV}, then

$$\frac{S}{N} = \frac{\eta P_T \beta(\pi) \pi R^2 \Delta L}{2B h\nu L_{AV}^2} \tag{3-25}$$

For an unfocused system

$$\frac{S}{N} = \frac{\eta P_T \beta(\pi) \pi R^2 \Delta L}{2B h\nu L_{AV}^2 \left[1 + \left(\frac{\pi R^2}{\lambda L_{AV}}\right)^2\right]} \tag{3-26}$$

For a focused CW system collecting scatter from an infinite path, equation (3-23) can be directly integrated. Since by completing the square

$$\int_0^\infty \frac{dL}{L^2\left[1 + \left(\frac{\pi R^2}{\lambda L}\right)^2 \left(1 - \frac{L}{f}\right)^2\right]} = \frac{\lambda}{\pi R^2} \int_{-\frac{\pi R^2}{\lambda f}}^\infty \frac{dx}{1 + x^2} \tag{3-27}$$

So

$$\frac{S}{N} = \frac{\eta P_T \beta(\pi) \lambda}{2B h\nu} \left[\frac{\pi}{2} + \tan^{-1}\left(\frac{\pi R^2}{\lambda f}\right)\right] \tag{3-28}$$

For an unfocused CW system, the signal-to-noise ratio can be found by letting $f \longrightarrow \infty$ and integrating equation (3-23) or by letting $f \longrightarrow \infty$ in equation (3-28)

$$\frac{S}{N} = \frac{\eta P_T \beta(\pi) \lambda \pi}{4Bh\nu} \tag{3-29}$$

For a CW system collecting scatter from a path beginning at L_1 and ending at L_2, equation (3-23) must be integrated between L_2 and L_1. For a focused system

$$\frac{S}{N} = \frac{\eta\, P_T\, \beta(\pi)\, \lambda}{2B\, h\nu} \left\{ \tan^{-1}\left[\frac{\lambda L_2}{\pi R^2} - \frac{\pi R^2}{\lambda f}\left(1 - \frac{L_2}{f}\right)\right] - \tan^{-1}\left[\frac{\lambda L_1}{\pi R^2} - \frac{\pi R^2}{\lambda f}\left(1 - \frac{L_1}{f}\right)\right]\right\} \tag{3-30}$$

For an unfocused system

$$\frac{S}{N} = \frac{\eta\, P_T\, \beta(\pi)\, \lambda}{2B\, h\nu} \left[\tan^{-1}\left(\frac{\lambda L_2}{\pi R^2}\right) - \tan^{-1}\left(\frac{\lambda L_1}{\pi R^2}\right)\right] \tag{3-31}$$

Certain conclusions can easily be made. For the pulsed case, the ratio of signal-to-noise ratios for the focused and unfocused system

$$\frac{\left(S/N\right)_F}{\left(S/N\right)_{Unf}} = 1 + \left(\frac{\pi R^2}{\lambda L_{Av}}\right)^2 \tag{3-32}$$

Since the far field distance, D_{FF}

$$D_{FF} \simeq \frac{\pi R^2}{\lambda} \tag{3-33}$$

$$\frac{\left(S/N\right)_F}{\left(S/N\right)_{Unf}} \simeq 1 + \left(\frac{D_{FF}}{L_{Av}}\right)^2 \tag{3-34}$$

Thus, for an operation in the near field, a focused system performs considerably better. For far-field operation, the difference between the systems is less than 3 dB.

For CW operation on an infinite path, the ratio

$$\frac{(S/N)_F}{(S/N)_{Unf}} = 1 + \frac{2}{\pi} \tan^{-1}\left(\frac{\pi R^2}{\lambda f}\right) \qquad (3\text{-}35)$$

Using equation (11)

$$\frac{(S/N)_F}{(S/N)_{Unf}} \simeq 1 + \frac{2}{\pi} \tan^{-1}\left(\frac{D_{FF}}{f}\right) \qquad (3\text{-}36)$$

So the ratio varies between 1 and 2 depending upon the transmitter/receiver parameters.

CW operation on a limited path is harder to interpret because of the complexity of the expressions and must be analyzed numerically. Again, however, there can be a significant improvement for operation in the near field of a focused system.

To summarize,

$$\frac{S}{N} = \frac{\eta\, P_T\, \beta(\pi)\, \lambda}{2\, B\, h\nu}\, F(R,\ \lambda,\ f) \qquad (3\text{-}37)$$

where $F(R, \lambda, f)$ is the function found from integrating equation (3-23). For the cases previously calculated, $F(R, \lambda, f)$ is given in Table 3-1.

TABLE 3-1

S/N VARIATION

System	F(R, λ, f)
Pulsed-Focused	$\frac{\pi R^2 \Delta L}{\lambda L_{Av}^2}$
Pulsed-Unfocused	$\frac{\pi R^2 \Delta L}{\lambda L_{Av}^2 \left[1 + \left(\frac{\pi R^2}{\lambda L_{Av}}\right)^2\right]}$
CW-Infinite Path-Focused	$\frac{\pi}{2} + \tan^{-1}\left(\frac{\pi R^2}{\lambda f}\right)$
CW-Infinite Path-Unfocused	$\frac{\pi}{2}$
CW-Finite Path-Focused	$\tan^{-1}\left[\frac{\lambda L_2}{\pi R^2} - \frac{\pi R^2}{\lambda f}\left(1 - \frac{L_2}{f}\right)\right] -$ $\tan^{-1}\left[\frac{\lambda L_1}{\pi R^2} - \frac{\pi R^2}{\lambda f}\left(1 - \frac{L_1}{f}\right)\right]$
CW-Finite Path-Unfocused	$\tan^{-1}\left(\frac{\lambda L_2}{\pi R^2}\right) - \tan^{-1}\left(\frac{\lambda L_1}{\pi R^2}\right)$

3.4 NUMERICAL EVALUATION

Substituting the following values into equation (3-37)

$\eta = 0.5$

$P_T = 10$ kW

$\beta(\pi) = 1.4 \times 10^{-5}$ km^{-1} at an altitude of 30,000 ft

$\lambda = 10.6 \times 10^{-4}$ cm

$B = 500$ kHz

then

$$\frac{S}{N} = 4.1 \times 10^4 \, F(R, \lambda, f) \qquad (3\text{-}38)$$

Equation (3-38) represents the lossless signal-to-noise ratio at the output of the optical detector. There are two principal losses in the system that must be considered. These losses are the absorption of the laser radiation in the atmosphere and the optical losses in the transmitter and receiver. The latter loss shall be assumed to equal 10 dB. The atmospheric transmission can be represented by

$$T = e^{-\kappa x} \qquad (3\text{-}39)$$

The spectral absorption coefficient, κ, was calculated from data in Reference 1. Equation (3-39) is plotted in Figure 3-1 as a function of range at several aircraft altitudes.

Introducing these losses, the actual signal-to-noise ratio can be written

$$\left(\frac{S}{N}\right)_{ACT} = 4.1 \times 10^3 \, T^2 \, F(R, \lambda, f) \qquad (3\text{-}40)$$

---

(1) Yin, P. and Long, R., Ohio State University Report 2384-2.

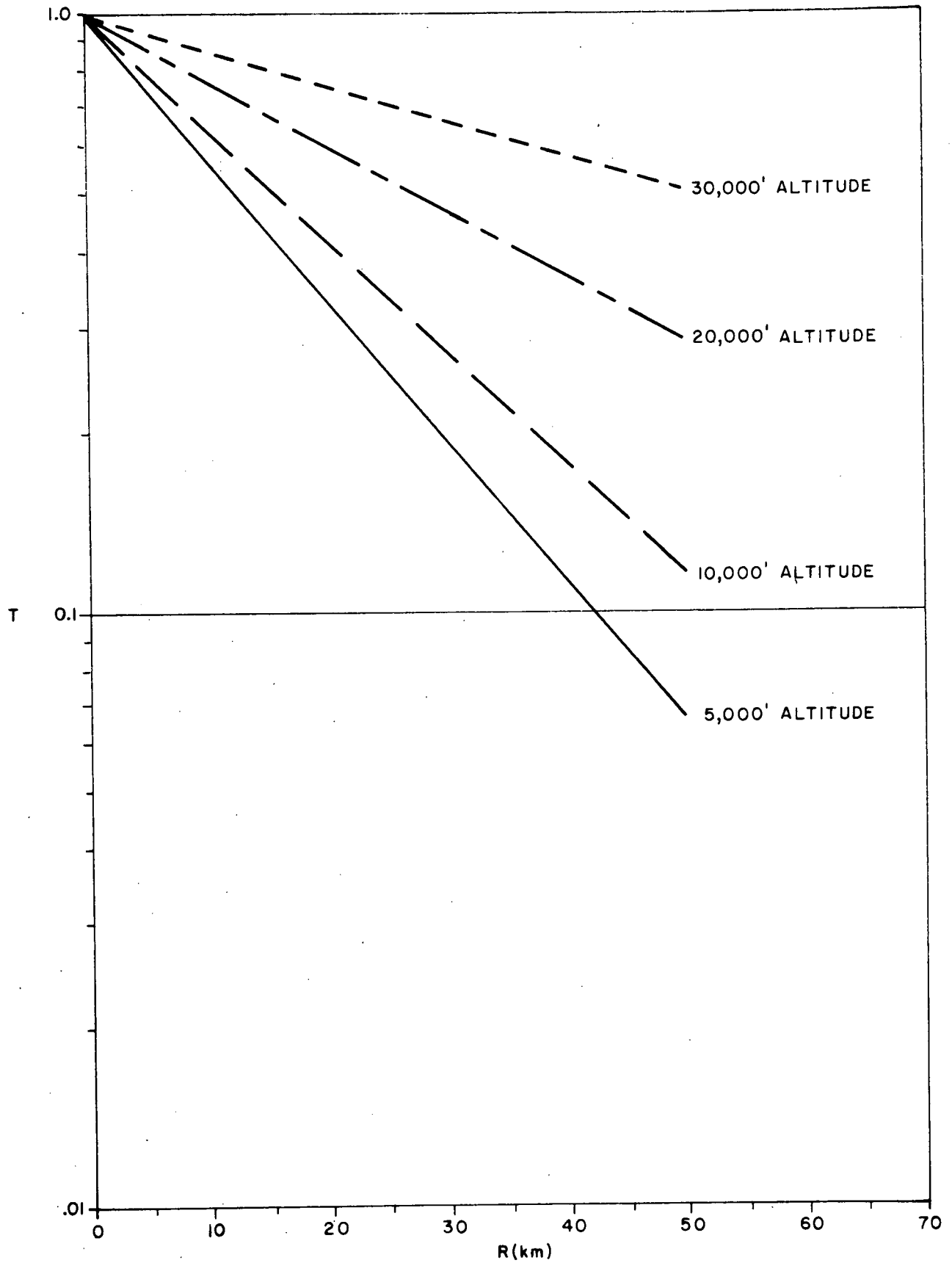

Figure 3-1 Atmospheric Transmission

Equation (3-40) is valid for an altitude of 30,000 feet. The variation of $\beta(\pi)$ with altitude can be found from data from AFCRL[2]. Since the size distribution of aerosol particles does not change with altitude, $\beta(\pi)$ varies linearly with aerosol particle density. The aerosol density is illustrated in Figure 3-2. From this figure, values for $\beta(\pi)$ were calculated and are illustrated in Table 3-2.

TABLE 3-2
ATMOSPHERIC BACKSCATTER COEFFICIENT

ALTITUDE (ft)	$\beta(\pi)$ (km^{-1})
5,000	1.3×10^{-2}
10,000	3.2×10^{-3}
20,000	2.4×10^{-4}
30,000	1.4×10^{-5}

Using these values, the actual signal-to-noise relationships can be given for different altitudes as shown in Table 3-3.

TABLE 3-3
SIGNAL-TO-NOISE RATIO

ALTITUDE (ft)	S/N
5,000	$3.8 \times 10^{6}\ T^2\ F(R, \lambda, f)$
10,000	$9.5 \times 10^{5}\ T^2\ F(R, \lambda, f)$
20,000	$7.1 \times 10^{4}\ T^2\ F(R, \lambda, f)$
30,000	$4.1 \times 10^{3}\ T^2\ F(R, \lambda, f)$

The expression $F(R, \lambda, f)$ was calculated for a variety of optics diameters and is plotted in Figure 3-3. Using the data

[2] Handbook of Geophysics and Space Environments.

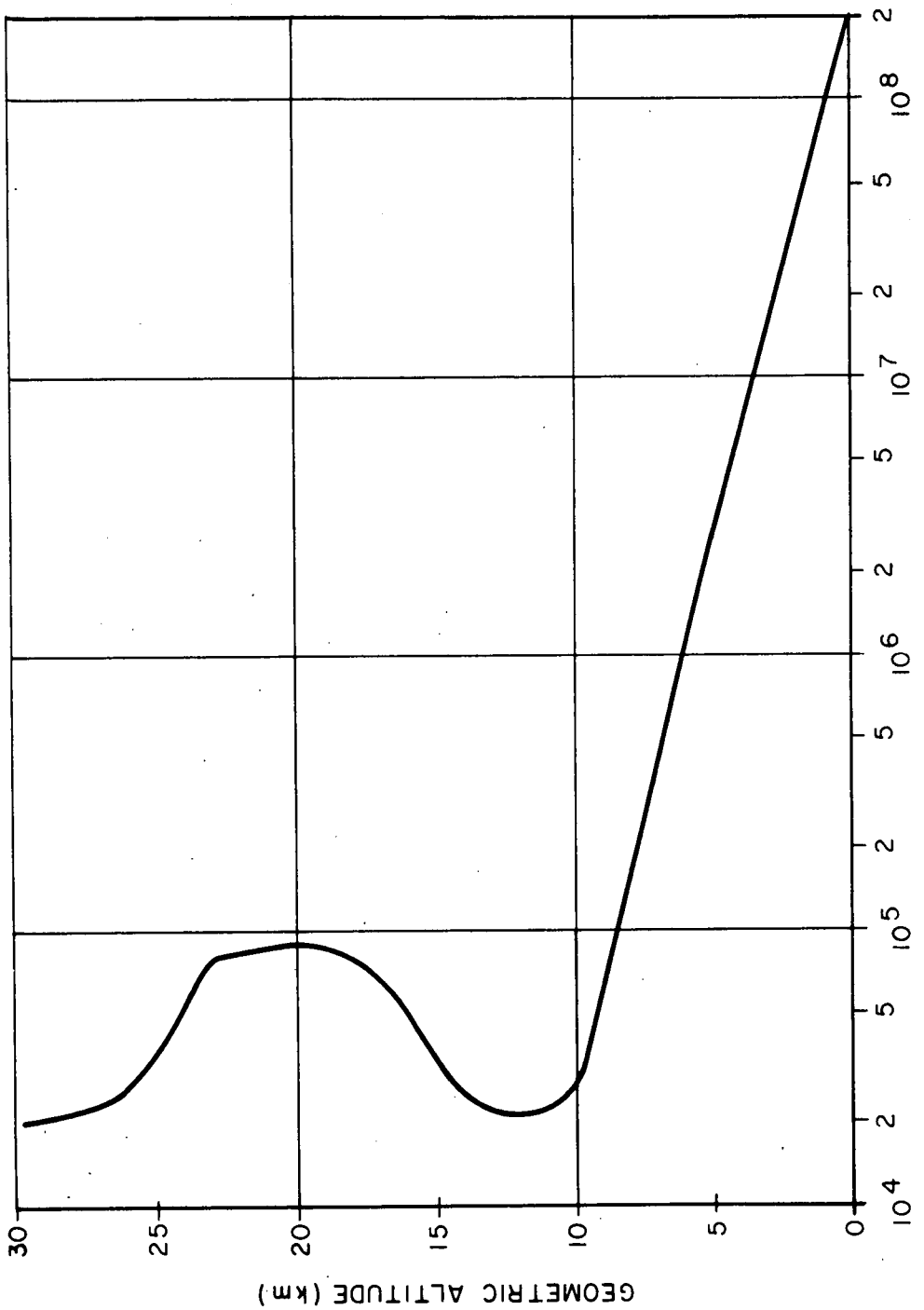

Figure 3-2 Aerosol Number Density

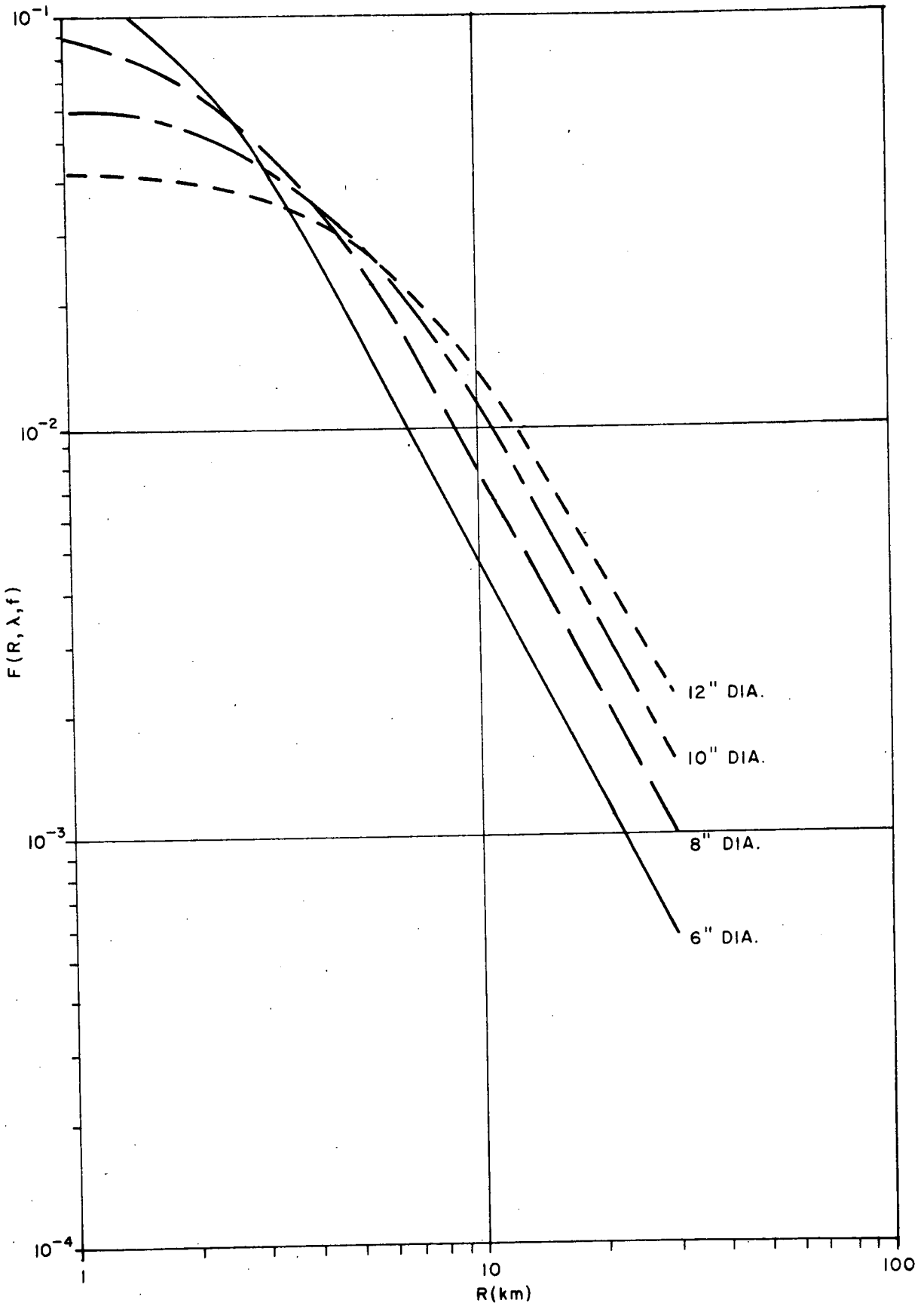

Figure 3-3 S/N Variation

C.2

from Figure 3-1 and Figure 3-3, signal-to-noise ratio was plotted versus range for several optics diameters and altitudes. These graphs appear in Figure 3-4 through Figure 3-7. They do not include the effect of the varying defracting index of the atmosphere.

The previous results were obtained for a filter bandwidth of 500 kHz. Discussions in Section 2 lead to the conclusion that a bandwidth of 150 kHz may be required. This leads to an increased signal-to-noise ratio, tabulated in Table 3-4 and illustrated in Figure 3-8 through Figure 3-11.

TABLE 3-4

SIGNAL-TO-NOISE RATIO

ALTITUDE (ft)	S/N
5,000	$1.3 \times 10^7 \, T^2 \, F(R, \lambda, f)$
10,000	$3.1 \times 10^6 \, T^2 \, F(R, \lambda, f)$
20,000	$2.3 \times 10^5 \, T^2 \, F(R, \lambda, f)$
30,000	$1.4 \times 10^4 \, T^2 \, F(R, \lambda, f)$

Having calculated the system signal-to-noise ratio, it is now required to translate these figures into a detection probability and a false alarm rate. This is accomplished in Section 4.

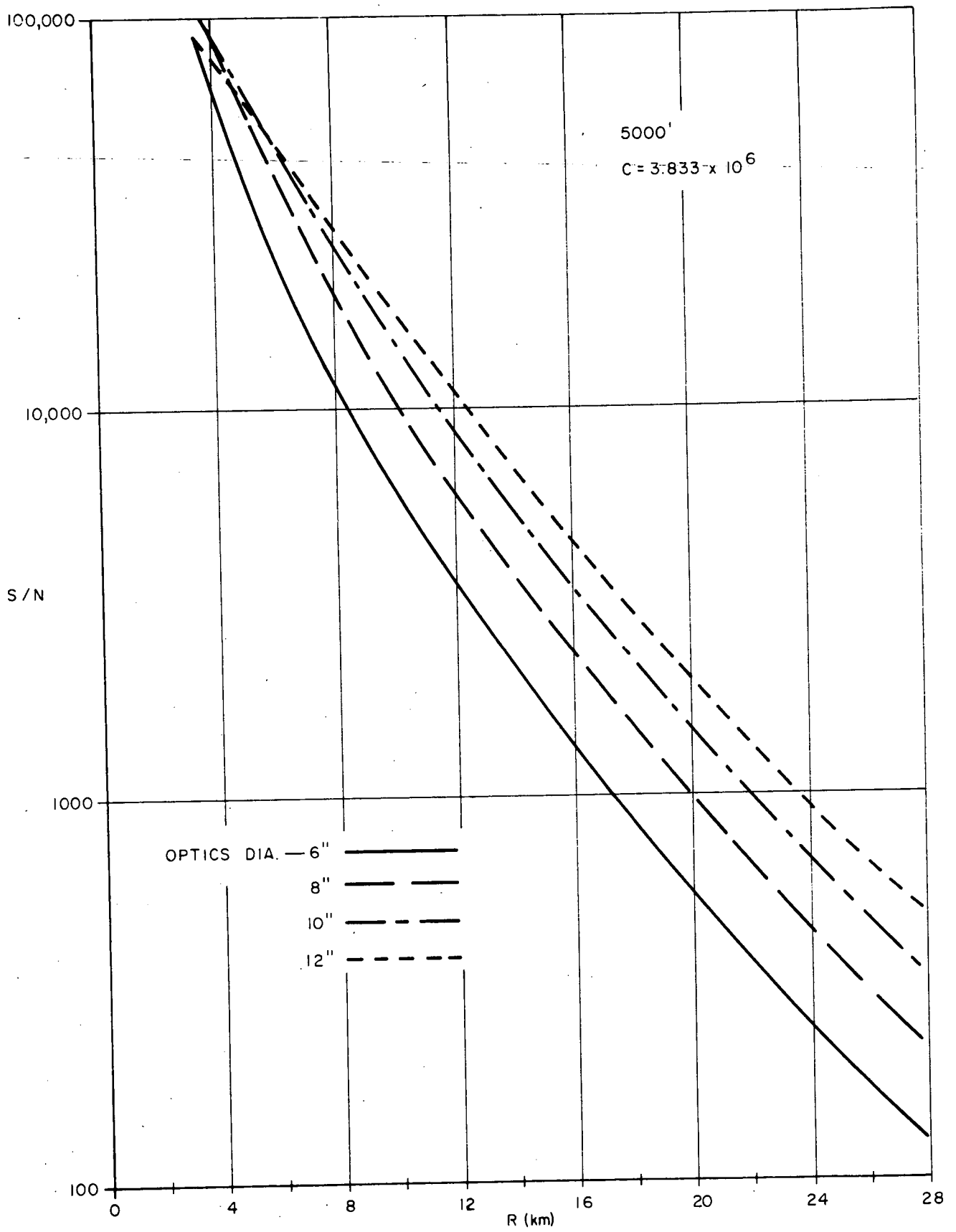

Figure 3-4 S/N at 5,000 Ft with 500-kHz Bandwidth

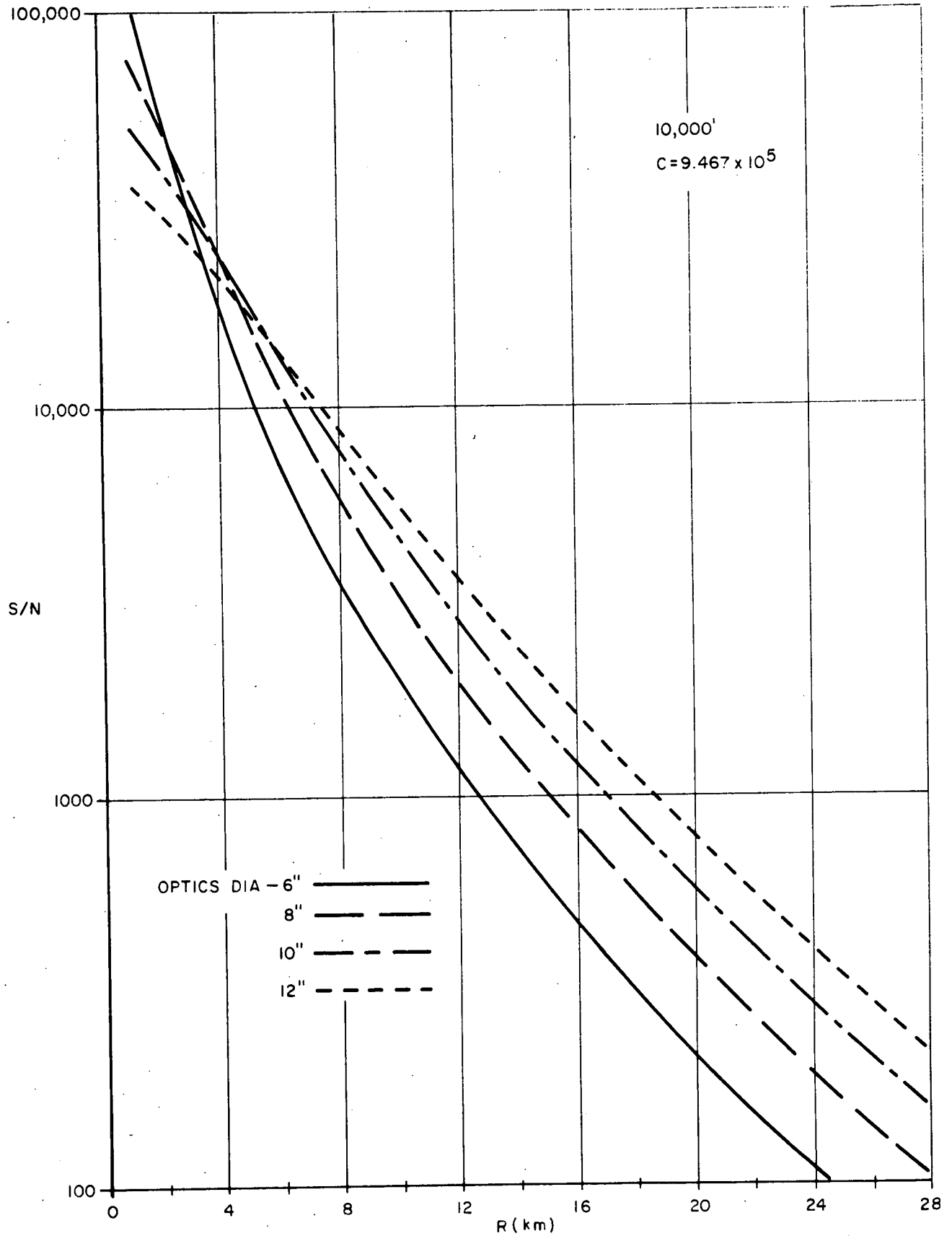

Figure 3-5 S/N at 10,000 Ft with 500-kHz Bandwidth

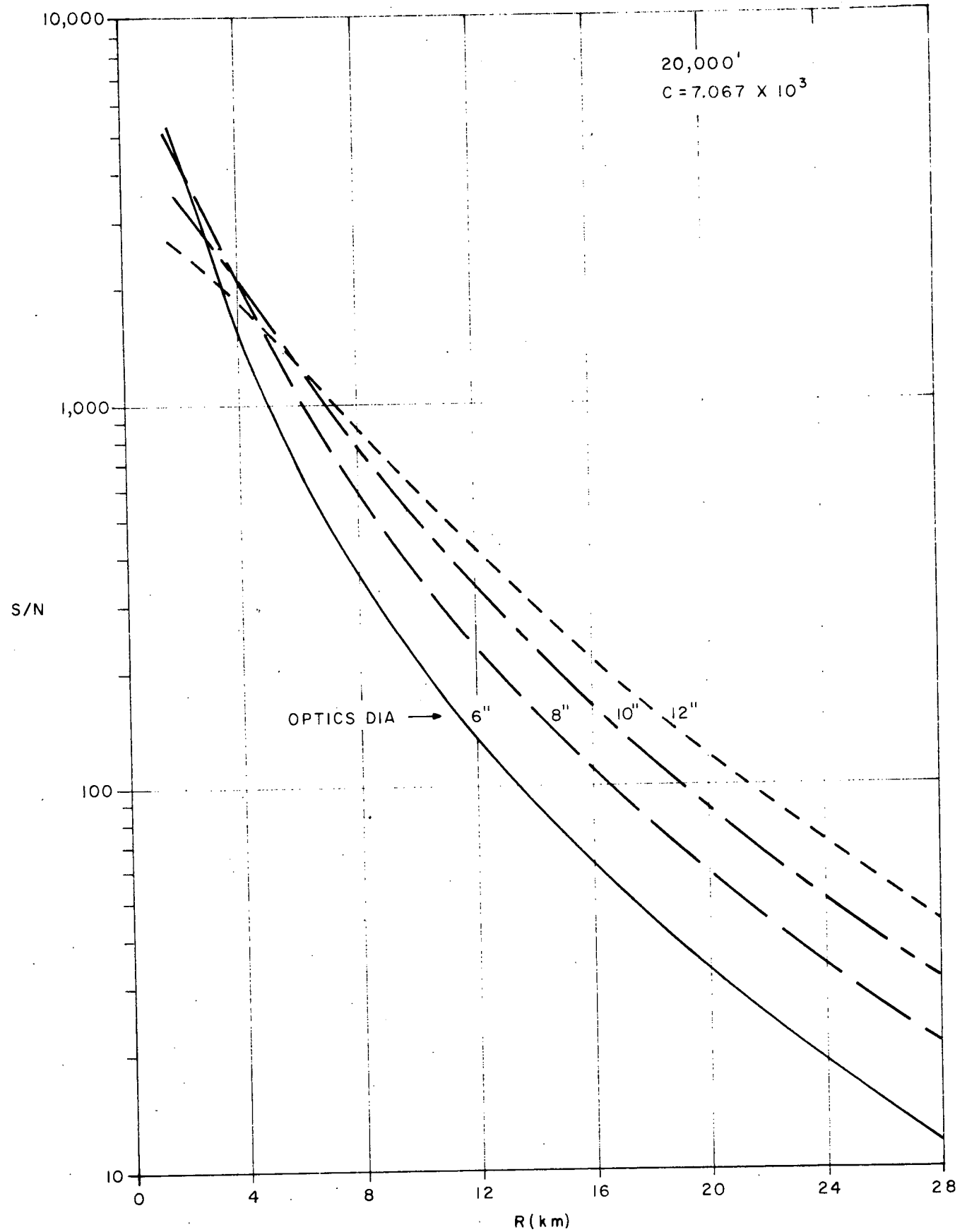

Figure 3-6 S/N at 20,000 Ft with 500-kHz Bandwidth

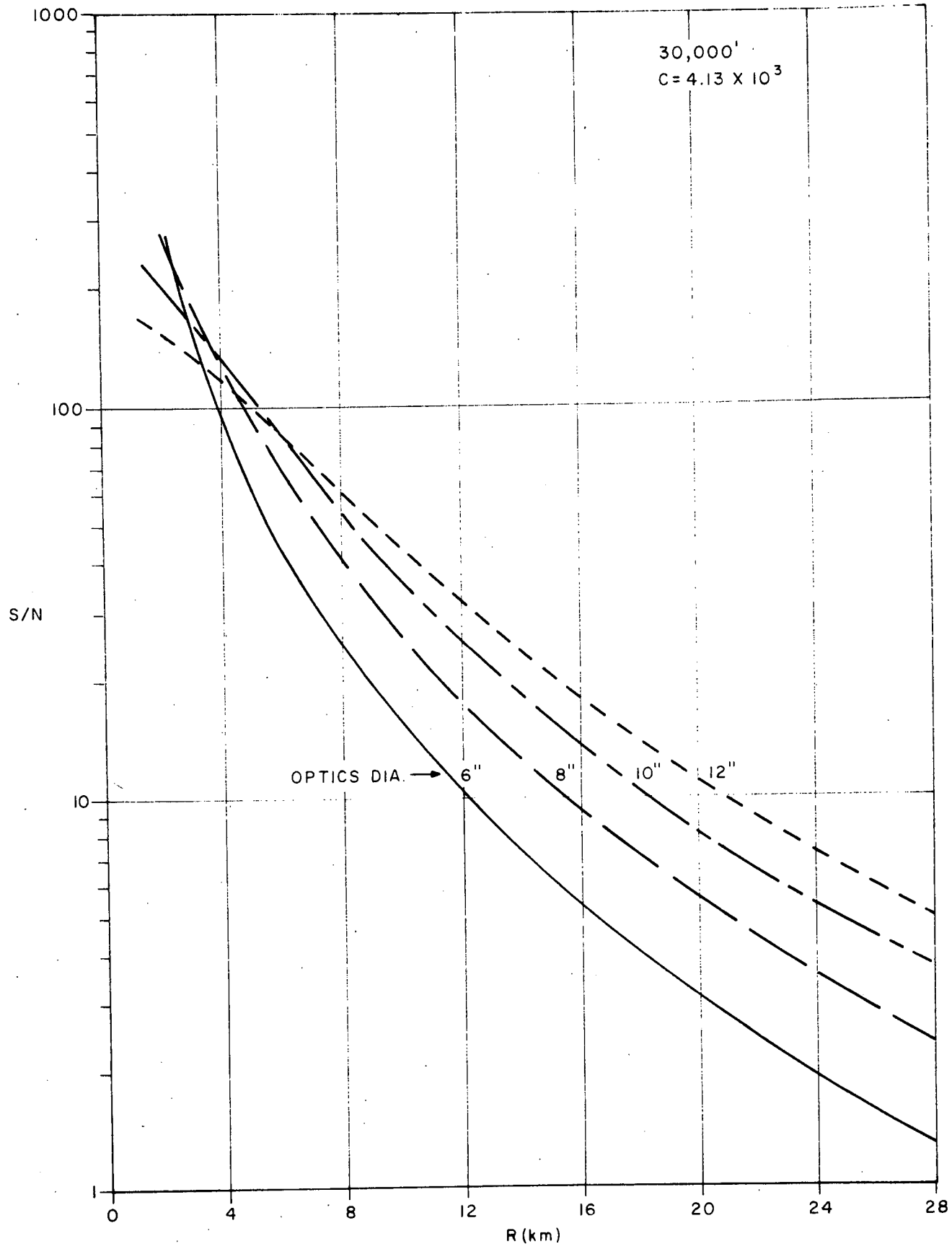

Figure 3-7 S/N at 30,000 Ft with 500-kHz Bandwidth

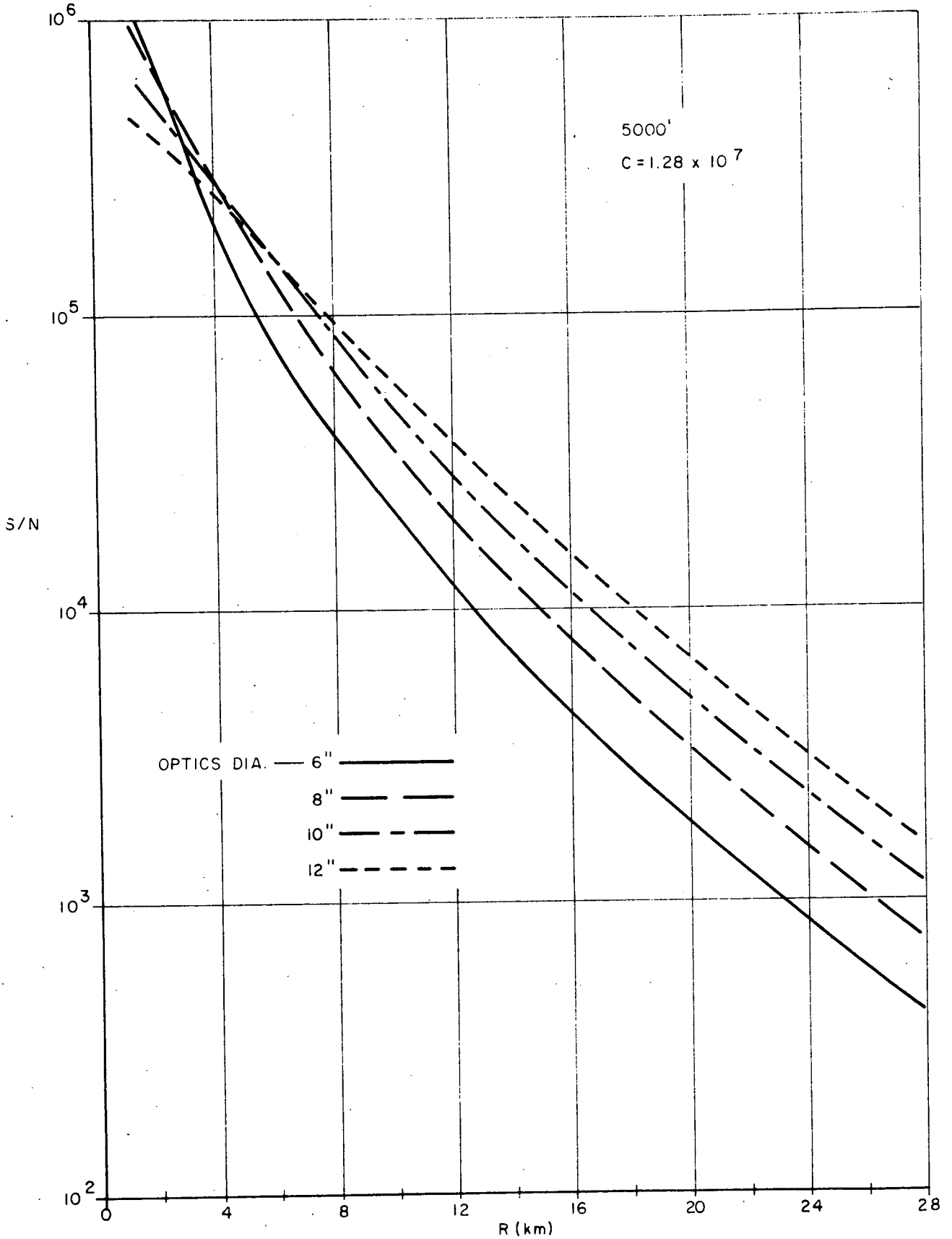

Figure 3-8 S/N at 5,000 Ft with 150-kHz Bandwidth

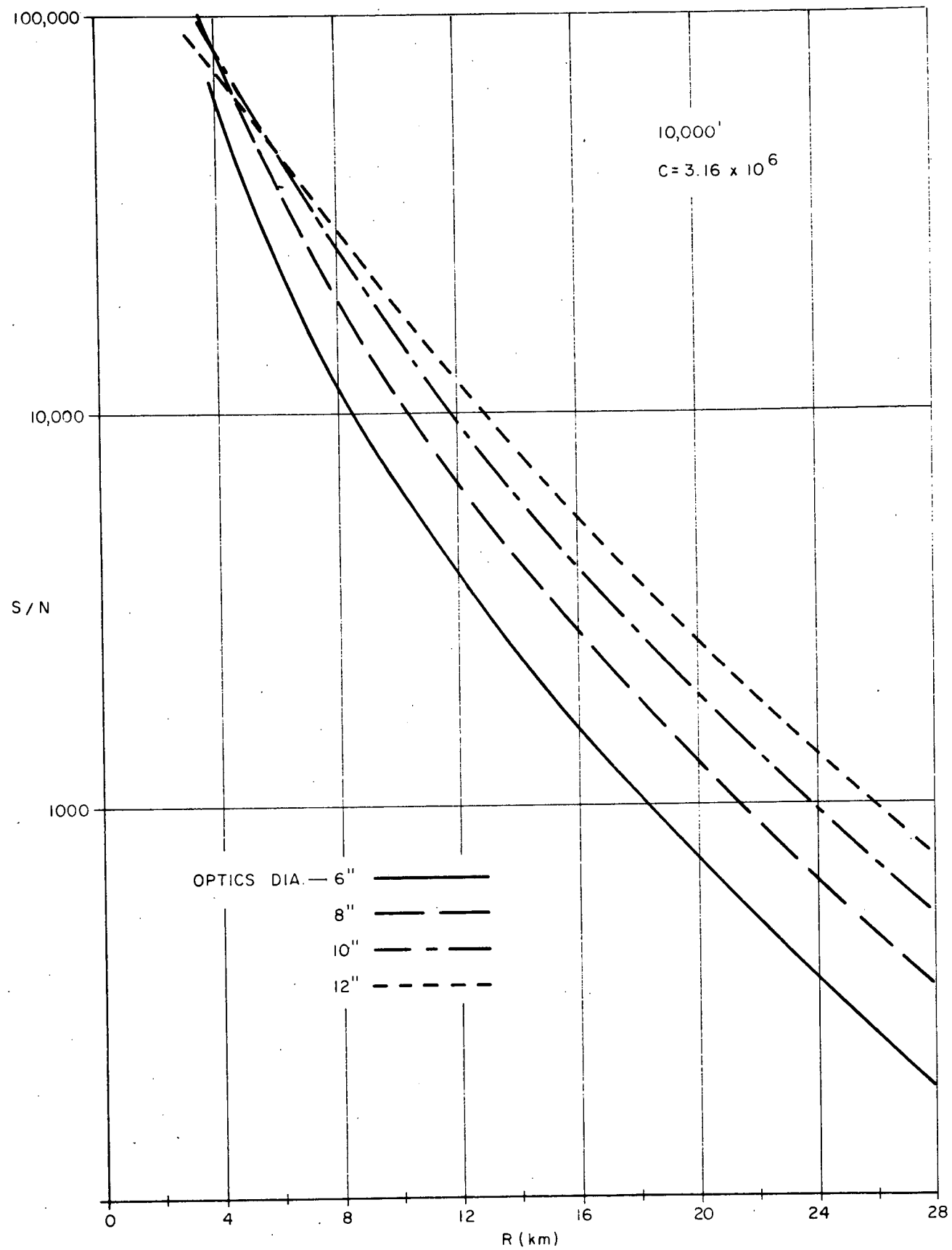

Figure 3-9 S/N at 10,000 Ft with 150-kHz Bandwidth

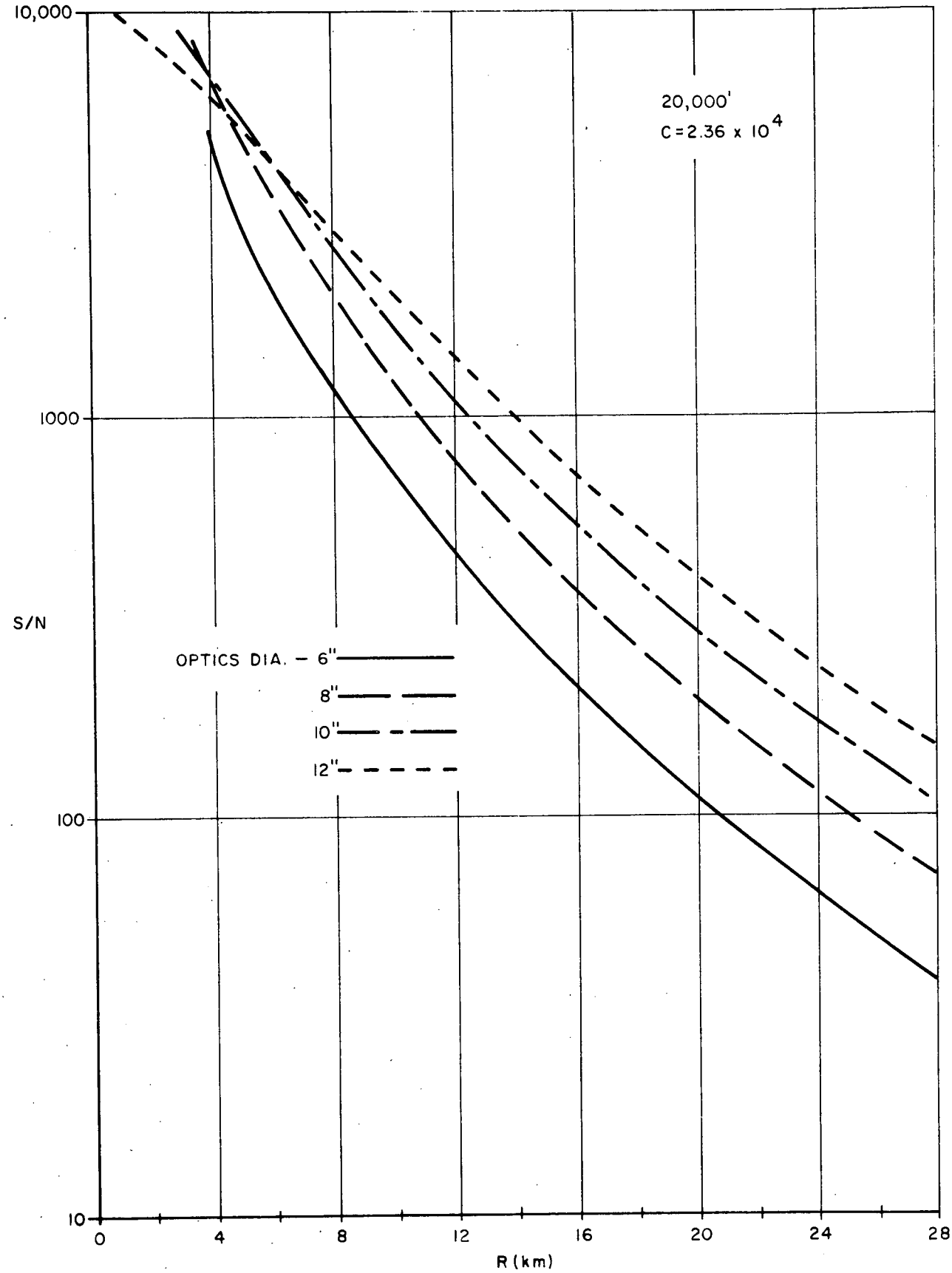

Figure 3-10 S/N at 20,000 Ft with 150-kHz Bandwidth

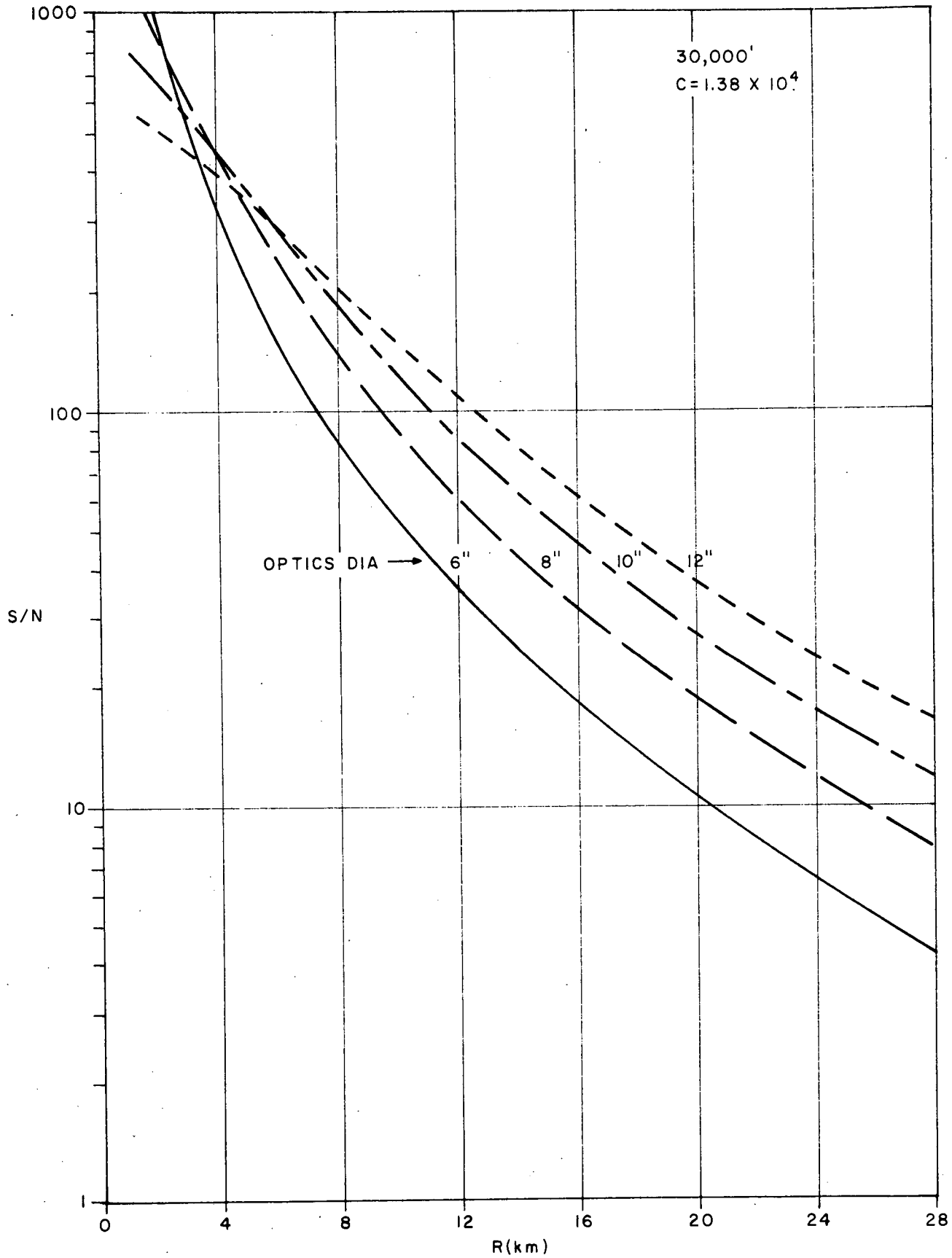

Figure 3-11 S/N at 30,000 Ft with 150-kHz Bandwidth

3.5 SENSITIVITY ANALYSIS

3.5.1 INTRODUCTION

In this section the performance of the proposed CAT aerosol detector is analyzed. A block diagram of the receiver and signal processor is shown in Figure 3-12. The IF portion of the receiver is a bank of fairly narrow tuned filters each of which is followed by an envelope detector. The detector outputs are sampled, box-carred and smoothed by a long-time-constant RC. (The overall device is essentially a coarse-grained spectrum analyzer.)

If a signal is present, it will appear in one or more of the tuned filters, and the level of the corresponding channel outputs will be expected to rise. Thus, all of the channel outputs are compared to a preassigned threshold level, and if one or more of them exceeds the threshold, a signal is declared to be present.

This section is not concerned directly with distinguishing spectral characteristics of the signal, such as bandwidth and doppler shift, but principally with the per-pulse S/N required for an echo of any type to be detectable. The detection performance is affected by the bandwidth, however, since the total signal energy in the return is fixed, whatever the shape of its spectrum. These effects are taken into account in the analysis below.

The effects of pulse integration are also discussed, and it is shown that the integration gain obeys the familiar "$M^{\frac{1}{2}}$" law, where M is the number of pulses integrated. The particular cases M = 1, 10, 100 are analyzed in detail.

3.5.2 ANALYSIS

3.5.2.1 Signal and Noise Models

Both the signal and noise processes are assumed to be zero mean, stationary and Gaussian over the frequency band of the receiver.

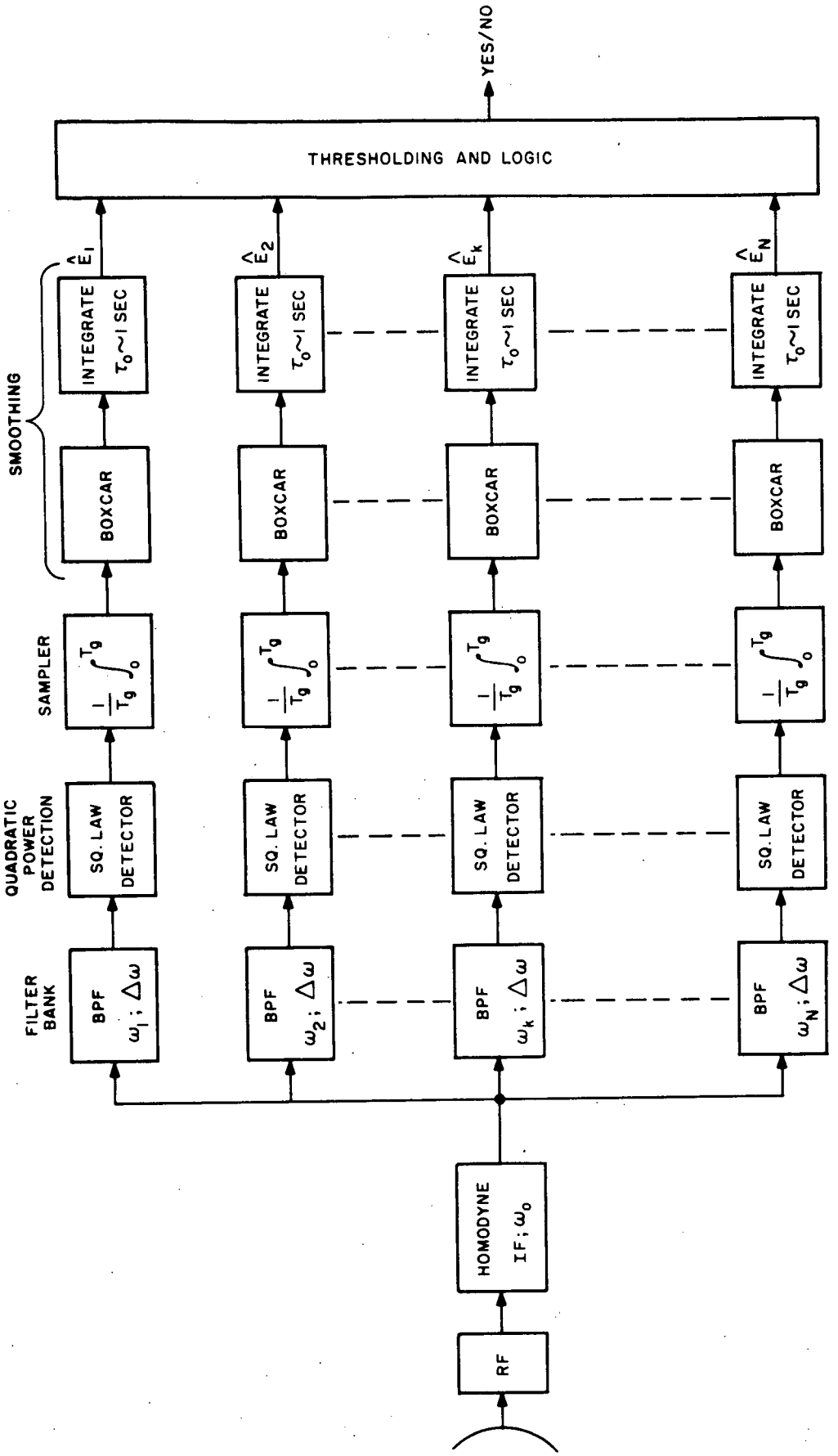

Figure 3-12 Block Diagram of Filter-Bank Spectrum Analyzer for Single Range Gate

Spectrally, receiver noise is uniformly distributed, with power density N_o. Thus, the average noise contribution to the output of each of the channels of the tuned-filter bank is the same for all channels, and is proportional to N_o.

The spectral model for the signal process is as follows:

(a) the <u>total</u> received signal power is S_o, independent of the strength of the turbulence (as measured by average kinetic energy density);

(b) the signal spectrum will be assumed to be <u>rectangular</u>, in the sense that the total received signal energy is uniformly distributed over a finite number, k, of doppler bins. In other words, out of N doppler bins, exactly k contain signal contributions, each of strength S_o/k. The quantity k measures, in a rough sense, the turbulence strength, since it is proportional to the doppler dispersion of the return.

Furthermore, it is assumed that the crossover between adjacent filters in the filter bank is negligible (say, less than -10 dB of overlap) in order that the separate channel outputs may be regarded to be statistically independent.

This model is admittedly somewhat crude; but it preserves the essential features of the original problem and yields simple and useful analytical results. As knowledge of CAT doppler spectra improves in the future, the model will be updated accordingly.

3.5.2.2 <u>Analysis of the Combinatorial Problem</u>

For present purposes,

Prob [output of a channel containing noise alone exceeds threshold] $\triangleq p_o$,

and

Prob [output of a channel containing signal plus noise exceeds threshold] $\triangleq p_1$.

(In the sequel, expressions will be obtained for p_o and p_1 in terms of N_o, S_o, k, N, the preassigned p_{FA}, and M, the number of pulses integrated.)

The probability that no thresholds are exceeded is given by

$$\text{Prob}\left[\text{no hits}\right] = (1 - p_o)^{N-k}(1 - p_1)^k \qquad (3\text{-}41)$$

The first parenthesis is the probability that all of the N-k noise-alone channel outputs are below threshold, and the second that all of the k signals plus noise channel outputs are below threshold.

Clearly then, the probability that one or more channel outputs (of either type) are above threshold is

$$\begin{aligned}\text{Prob}\left[\text{one or more hits}\right] &= 1 - \text{Prob}\left[\text{no hits}\right] \\ &= 1 - (1 - p_o)^{N-k}(1 - p_1)^k\end{aligned} \qquad (3\text{-}42)$$

The false alarm probability can be defined as the probability that one or more hits are observed when no signal is present, i.e., k = 0:

$$p(FA) = 1 - (1 - p_o)^N \qquad (3\text{-}43)$$

Similarly, the detection probability is the probability that one or more hits are observed when signal is present in 1, 2, 3 ... k bins:

$$p(D) = 1 - (1 - p_o)^{N-k}(1 - p_1)^k \qquad (3\text{-}44)$$

In the following section, the detection characteristics are derived for the per-pulse case. Subsequently, the effects of pulse-to-pulse integration are described.

3.5.2.3 Detection Characteristics for the Single Pulse Case

Mathematically it is more convenient to assume that a signal is always present in k of the doppler bins, and thus consider only p(D); p(FA) is obtained, then, by setting $S_o = 0$, or $k = 0$.

If p_o is small, (as it will turn out to be) the approximation $(1 - x)^{\nu} \sim 1 - \nu x$ can be used

$$p(D) \sim 1 - (1 - p_1)^k + (N - k)\, p_o (1 - p_1)^k \tag{3-45}$$

The probability density function of the channel outputs is easily shown to be exponential; for the noise channels

$$p_o(x) = \lambda_o e^{-\lambda_o x}, \quad x \geq 0 \tag{3-46}$$

and for the signal channels

$$p_1(x) = \lambda_1 e^{-\lambda_1 x}, \quad x \geq 0 \tag{3-47}$$

where

$$\left.\begin{aligned} \lambda_o &= N_o^{-1} \\ \lambda_1 &= (N_o + S_o/k)^{-1} \end{aligned}\right\} \tag{3-48}$$

Without loss of generality, $N_o = 1$, whence $S_o \triangleq \rho$ = per pulse input S/N. Hence, for threshold set at T,

$$p_o = e^{-T}, \text{ and } p_1 = e^{-\frac{T}{1 + \rho/k}} \tag{3-49}$$

Suppose that the desired false alarm probability is α; then

$$p(FA) = 1 - (1 - p_o)^N \sim N p_o = \alpha \tag{3-50}$$

Substituting in equation (3-49) for p_o

$$T = \log_e (N/\alpha) \tag{3-51}$$

p_1 can be found from equation (3-51) and equation (3-49):

$$p_1 = (\alpha/N)^{\frac{k}{k+\rho}} \tag{3-52}$$

The detection probability is

$$p(D;k) = 1 - \left[1 - \left(\frac{\alpha}{N}\right)^{\frac{k}{k+\rho}}\right]^k \left[1 - \alpha \cdot \frac{N-k}{N}\right] \tag{3-53}$$

For a false alarm time of one hour, at a prf of 600 Hz, the per-pulse false-alarm probability, α, turns out to be of the order of 5×10^{-7}. Also let N = 20 in the above equation, which is the number of doppler bins presently being considered.

A plot of p(D;k) vs ρ for various values of k is shown in Figure 3-13. Notice that the curves for the different values of k cross over in the vicinity of $p(D) \cong .5$. A heuristic reason for this is that for large k (many bins containing signal) and large ρ, the probability of getting <u>one or more</u> hits tends to increase with k, since there is a high per-bin hit probability in spite of the fact that the per-bin S/N decreases as ρ/k. The reverse is true for small ρ and large k, since the per-bin hit probability is very nearly unaffected by the presence of signal, and dispersing whatever weak signal is available over a broader range only degrades the performance.

Also, for reasons not well understood, this plot appears to approach linearity as k increases.

3.5.2.4 <u>Effects of Integration</u>

Suppose now that the channel outputs are integrated in an unweighted fashion* for a total of M pulses. The pdf of the

*The actual integration will be performed by a long-time-constant RC circuit. If the time constant of the latter is of the order of Mx pulse-rep-time, there is no significant difference in the results.

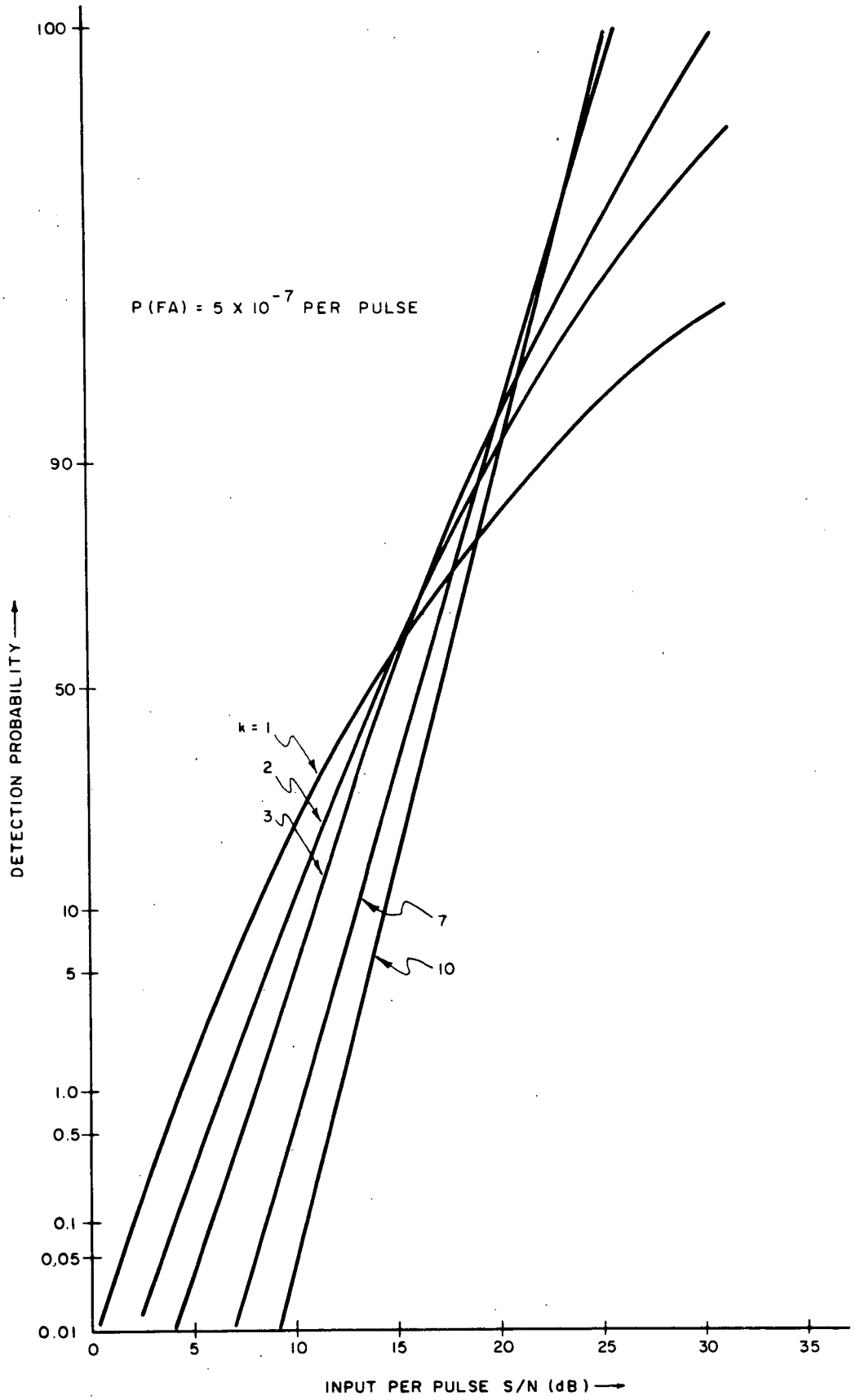

Figure 3-13 Detection Probability vs $(S/N)_m$ for Various k

channel outputs are no longer exponential; however, it will assume that M is sufficiently large that they may regard these as Gaussian (central limit theorem).

For the noise-alone channels, the output mean and variance are easily shown to be

$$\left.\begin{aligned} \mu_o &= M \\ \sigma_o^2 &= M \end{aligned}\right\} \qquad (3\text{-}54)$$

(where, $N_o = 1$).

Similarly, for the signal channels these are given by

$$\begin{aligned} \mu_1 &= M(1 + \rho) \\ \sigma_1^2 &= M(1 + \rho) \end{aligned} \qquad (3\text{-}55)$$

If a threshold at T is set, then the hit probability in the noise channel is

$$\begin{aligned} p_o &= 1 - \Phi\left(\frac{T - \mu_o}{\sigma_o}\right) \\ &= 1 - \Phi\left(\frac{T - M}{M^{\frac{1}{2}}}\right) \end{aligned} \qquad (3\text{-}56)$$

where

$$\Phi(x) = \frac{1}{\sqrt{2\pi}} \int_{-\infty}^{x} e^{-t^2/2}\, dt$$

To determine the proper value of T, given the desired false alarm rate, the following procedure is used: the false alarm probability per block of M integrated pulses can be permitted to be M times the per-pulse false alarm probability since it is the

false-alarm time which is held fixed. From the previous section, if the latter is taken to be 1 hour, then the per-pulse p(FA) is 5×10^{-7}; the per-blocks p(FA) is then

$$p_M(FA) = 5M \times 10^{-7} \tag{3-57}$$

Thus, from equation (3-50), T is determined by solving the relation

$$N\left[1 - \Phi\left(\frac{T - M}{M^{\frac{1}{2}}}\right)\right] = 5M \times 10^{-7} \tag{3-58}$$

Once T is known, then the detection probability can be found, as a function of ρ, from equation (3-45) where

$$p_1 = 1 - \Phi\left(\frac{T - \mu_1}{\sigma_1}\right)$$

$$= 1 = \Phi\left(\frac{T - (1 + \rho)\, M}{(1 + \rho)^{\frac{1}{2}}\, M^{\frac{1}{2}}}\right) \tag{3-59}$$

Equation (3-59) has been plotted for the cases k = 1 and 2 (one and two doppler bins containing signal) for M = 10 and M = 100. The curve for M = 1 has also been included.

These graphs (Figures 3-14, 3-15, and 3-16) require little comment, except perhaps to remark that the peculiar shapes are due possibly to the error of the Gaussian approximation. In the region of interest; however, $.1 < p(D) < .9$, they can be assumed to be quite accurate.

The effects of integration are most easily seen from Figure 3-16. This is a plot of the per-pulse input S/N required to yield a p(D) of 1/2 vs. the number of pulses integrated. It was assumed that k = 1.

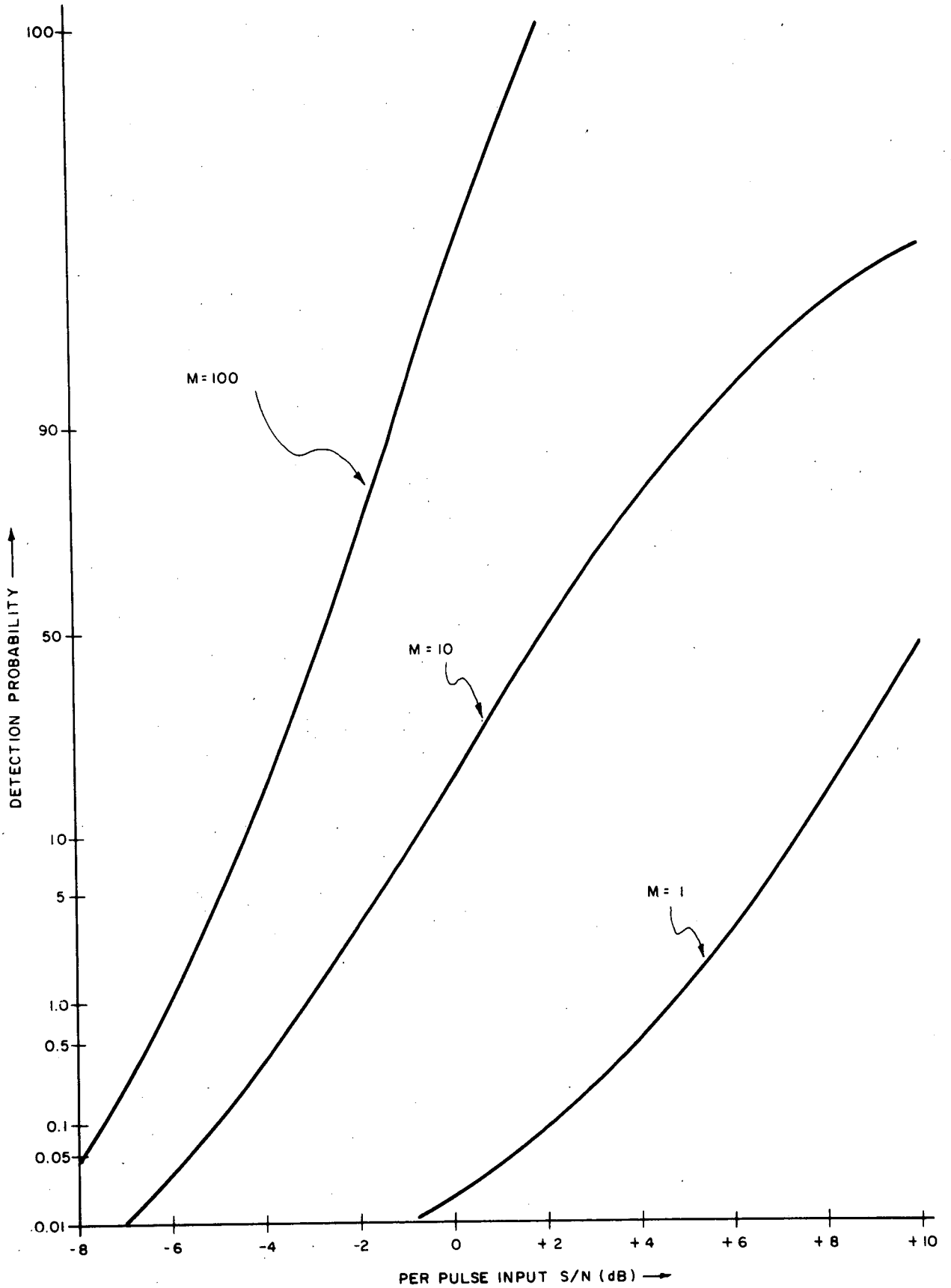

Figure 3-14 p(D) vs ρ for k = 1

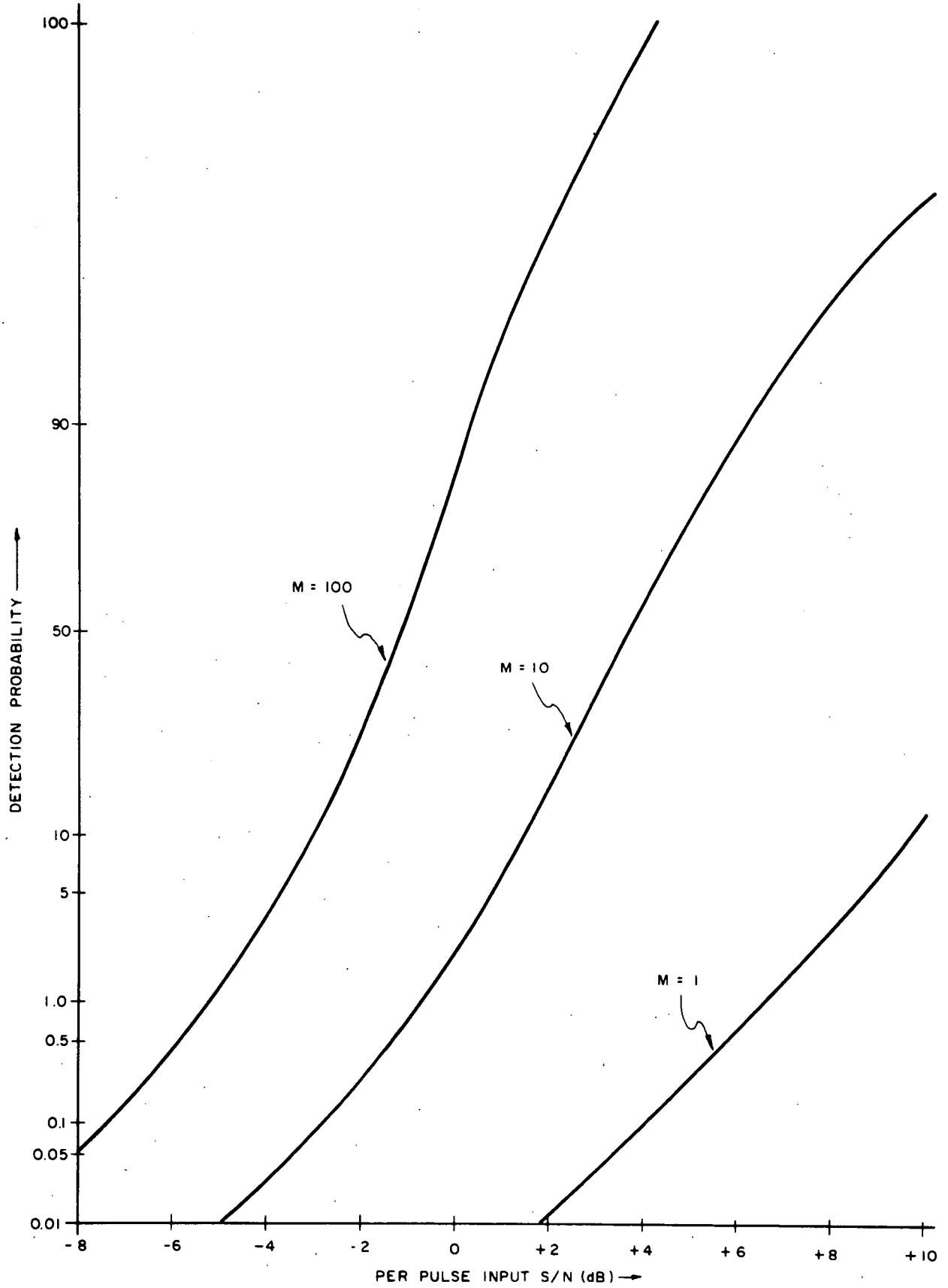

Figure 3-15 p(D) vs ρ for k = 2

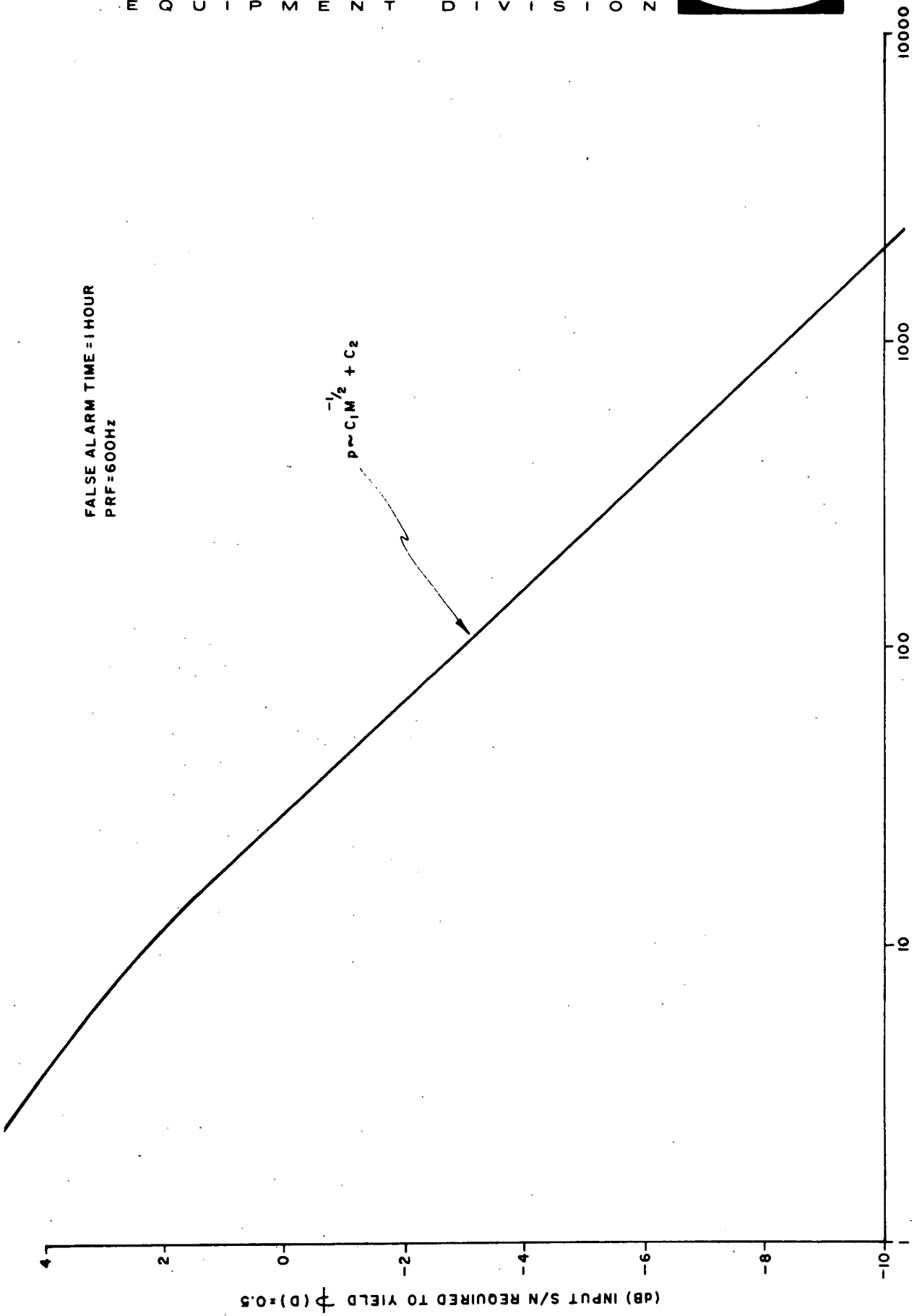

Figure 3-16 ρ vs M for p(D) = 1/2

For large M, the slope of the curve on the log-log coordinates is -1/2, indicating that the asymptotic dependence is as $M^{-\frac{1}{2}}$. This result is not at all unexpected.

3.5.2.5 Conclusions

The performance of the CAT aerosol detector has been analyzed, and the effects of spectral spreading and pulse integration have been discussed.

It has been shown that for low per-pulse input S/N the detection probability is degraded by spectral spreading; for sufficient high input S/N the increased bandwidth actually enhances the performance.

It has also been shown that the integration gain varies as the square root of the numbers of pulses integrated for long integration times.

The actual performance of the CAT detector can be determined by applying the results of Section 3.4 to the conclusions of this system. Figure 3-12 shows that the signal-to-noise ratio at an altitude of 30,000 ft, a range of 24 km, an optics diameter of 12 in, and a bandwidth of 500 kHz is 8.5 dB. Using Figure 3-14, integration of 10 pulses yields a 98.5% detection probability at a false alarm time of one hour. All other conditions yield a higher signal-to-noise ratio and therefore a higher detection probability for integration of the same numbers of pulses. Therefore sufficient detection probabilities can be achieved in times of the order of 0.1 second or less at the pulse repetition rate currently being obtained by the laser transmitter (see paragraph 6.4.3).

3.6 FREQUENCY MEASUREMENT ACCURACY

3.6.1 INTRODUCTION

The last section demonstrated that there was a sufficient signal-to-noise ratio to be able to detect a signal with a high detection probability and a low false alarm rate. It is now essential to determine the accuracy with which one can measure the center frequency and spectral width of the signal. A filter bank is used to make this measurement.

3.6.2 POWER AT FILTER BANK OUTPUTS

The spectrum at the filter bank input is assumed to have a Gaussian power density S(f).

$$S(f) = \frac{\rho}{\sqrt{2\pi\ \sigma_f^2}} \exp\left\{-\frac{1}{2}\left(\frac{f}{\sigma_f}\right)^2\right\} \qquad (3\text{-}60)$$

Since the integral of S(f) over all frequencies is ρ, this is the total power in the spectrum S(f). For convenience, S(f) is centered at zero frequency. The parameter σ_f is the root-mean-square frequency deviation of the spectrum.

The magnitude squared of the filter response is also assumed to have a Gaussian shape.

$$|H_i(f)|^2 = \frac{1}{\sqrt{2\pi\ \Delta_f^2}} \exp\left\{-\frac{1}{2}\left(\frac{f - f_i}{\Delta_f}\right)^2\right\} \qquad (3\text{-}61)$$

The i-th filter has center frequency f_i. The power gain of each filter is normalized to one, and the -3 dB points are at $f = f_i \pm 1.177\ \Delta_f$. The equivalent noise power bandwidth of each filter is $\sqrt{2\pi}\ \Delta_f$.

To compute the power P_i at the output of filter i, the product of equation (3-60) and equation (3-61) is integrated over all frequencies.

$$P_i = \int_{-\infty}^{\infty} S(f) \left| H_i(f) \right|^2 df \tag{3-62}$$

$$= \frac{\rho}{2\pi \sigma_f \Delta_f} \int_{-\infty}^{\infty} \exp \left\{ - \frac{1}{2} \left(\frac{f}{\sigma_f} \right)^2 + \left(\frac{f - f_i}{\Delta_f} \right)^2 \right\} df \tag{3-63}$$

The integral is evaluated by completing the square.

$$\frac{f^2}{\sigma_f^2} + \frac{f^2 - 2ff_i + f_i^2}{\Delta_f^2} = \frac{1}{k^2} \left\{ f^2 - \frac{2k^2 \, ff_i}{\Delta_f^2} \right\} + \frac{f_i^2}{\Delta_f^2} \tag{3-64}$$

$$= \frac{1}{k^2} \left\{ f - \frac{k^2 f_i}{\Delta_f^2} \right\}^2 - \frac{k^2 f_i^2}{\Delta_f^4} + \frac{f_i^2}{\Delta_f^2} \tag{3-65}$$

where $\frac{1}{k^2} = \frac{1}{\sigma_f^2} + \frac{1}{\Delta_f^2}$ (3-66)

$$P_i = \frac{\rho}{2\pi \sigma_f \Delta_f} \exp \left\{ - \frac{1}{2} \frac{f_i^2}{\sigma_f^2 + \Delta_f^2} \right\} \int_{-\infty}^{\infty}$$

$$\exp \left\{ - \frac{1}{2} \frac{1}{k^2} \left(f - \frac{k^2 f_i}{\Delta_f^2} \right)^2 \right\} df \tag{3-67}$$

The value of the integral is $\sqrt{2\pi}\, k$. Hence

$$P_i = \frac{\rho}{\sqrt{2\pi}\sqrt{\sigma_f^2 + \Delta_f^2}} \exp\left\{-\frac{1}{2}\left(\frac{f_i^2}{\sigma_f^2 + \Delta_f^2}\right)\right\} \qquad (3\text{-}68)$$

3.6.3 ESTIMATE OF CENTER FREQUENCY

Properly normalized, P_i can be visualized as the weight associated with frequency f_i. The average value of the f_i is therefore

$$\bar{f} = \frac{\sum_{i=-\infty}^{\infty} P_i f_i}{\sum_{i=-\infty}^{\infty} P_i} \qquad (3\text{-}69)$$

The indices on the summations are extended to ∞ only for convenience. In practice, only those filter outputs for which P_i is significant, i.e., for which a signal can be detected in the noise background, will be included in the summation. The summation of equation (3-69) is affected only slightly by extending the indices to $\pm\infty$ because P_i decreases very rapidly outside the set of filters in which detections can be made.

The true center frequency of the input spectrum is zero; hence equation (3-69) actually gives the error in the estimate of center frequency.

For a bank of uniformly spaced filters, f_i can be written as the i-th multiple of the spacing plus an offset frequency.

$$f_i = \delta + 2ia\,\Delta_f \qquad (3\text{-}70)$$

The offset is δ. All possible cases concerning the position of the input spectrum with respect to the filter bank are obtained by varying δ from 0 to $a\Delta_f$. With $\delta = 0$, the input spectrum center frequency is aligned with the center frequency of the zeroth filter; with $\delta = a\Delta_f$, the input spectrum is centered half-way between filter number -1 and filter number 0. The product $2a\Delta_f$ is the filter spacing. For an equal to one, the filters in the bank are separated by $2\Delta_f$.

Incorporating equation (3-70) into equation (3-68) gives

$$P_i = \frac{\rho}{\sqrt{2\pi\,(\sigma_f^2 + \Delta_f^2)}} \exp\left\{-\frac{1}{2}\,\frac{(\delta/\Delta_f + 2ia)^2}{(\sigma_f/\Delta_f)^2 + 1}\right\} \qquad (3\text{-}71)$$

Define the ratio of the RMS input spectral width σ_f to the filter width Δ_f to be σ', and the ratio of the offset $\delta/2a$ to Δ_f to be the normalized offset δ'. The exponential factor in equation (3-71) then takes the simple form

$$\exp\left\{-\frac{1}{2}\,\frac{(2a)^2\,(\delta' + i)^2}{\sigma'^2 + 1}\right\} \qquad (3\text{-}72)$$

Thus P_i can be evaluated as a function of a, δ', and σ'.

$$\delta' = \frac{\delta}{2a\Delta_f} \qquad (3\text{-}73)$$

$$\sigma' = \frac{\sigma_f}{\Delta_f} \qquad (3\text{-}74)$$

Unfortunately, the sums in equation (3-69) cannot be evaluated in closed form. As an alternative, they have been evaluated on a computer and plotted for typical values of a and σ'. The normalized form is

$$\frac{\bar{f}}{\Delta_f} = \frac{2a \sum_{i=-\infty}^{\infty} (\delta' + i) \exp\left\{-\frac{2a^2(\delta' + i)^2}{\sigma'^2 + 1}\right\}}{\sum_{i=-\infty}^{\infty} \exp\left\{\frac{-2a^2(\delta' + i)^2}{\sigma'^2 + 1}\right\}} \qquad (3\text{-}75)$$

The results have been averaged over the normalized offset δ' by assuming that δ' is uniformly distributed between -1/2 and +1/2; that is, doppler frequencies are uniformly distributed between the cross-over points of adjacent filters.

The estimate $\bar{f}$ of center frequency given by equation (3-69) is an unbiased estimate. The mean of $\bar{f}$, averaging over delta, equals zero, which is the center frequency of the input spectrum.

Figure 3-17 plots the mean value of the magnitude of the error in the estimate of center frequency, whereas Figure 3-18 plots the standard deviation of this error. For an example concerning the use of these figures, consider the case in which the filter width Δ_f is 125 kHz and the input spectrum width σ_f is also 125 kHz. (Observe that the equivalent noise bandwidth of the filter is $\sqrt{2\pi}(125) = 313.3$ kHz.) The value of $\sigma' = \sigma_f/\Delta_f$ is one. Assume that the value of a is 1.414, so that the filter spacing is $2a\Delta_f = 353.5$ kHz. This implies that the filters cross over at the -4.3 dB point.

Since the expected error in mean frequency is equally likely to be positive or negative, the mean frequency error is zero. From Figure 3-17, the mean of the magnitude of the error is $0.0387\ \Delta_f = 4.83$ kHz. The standard deviation of the error is $0.0414\ \Delta_f = 5.175$ kHz.

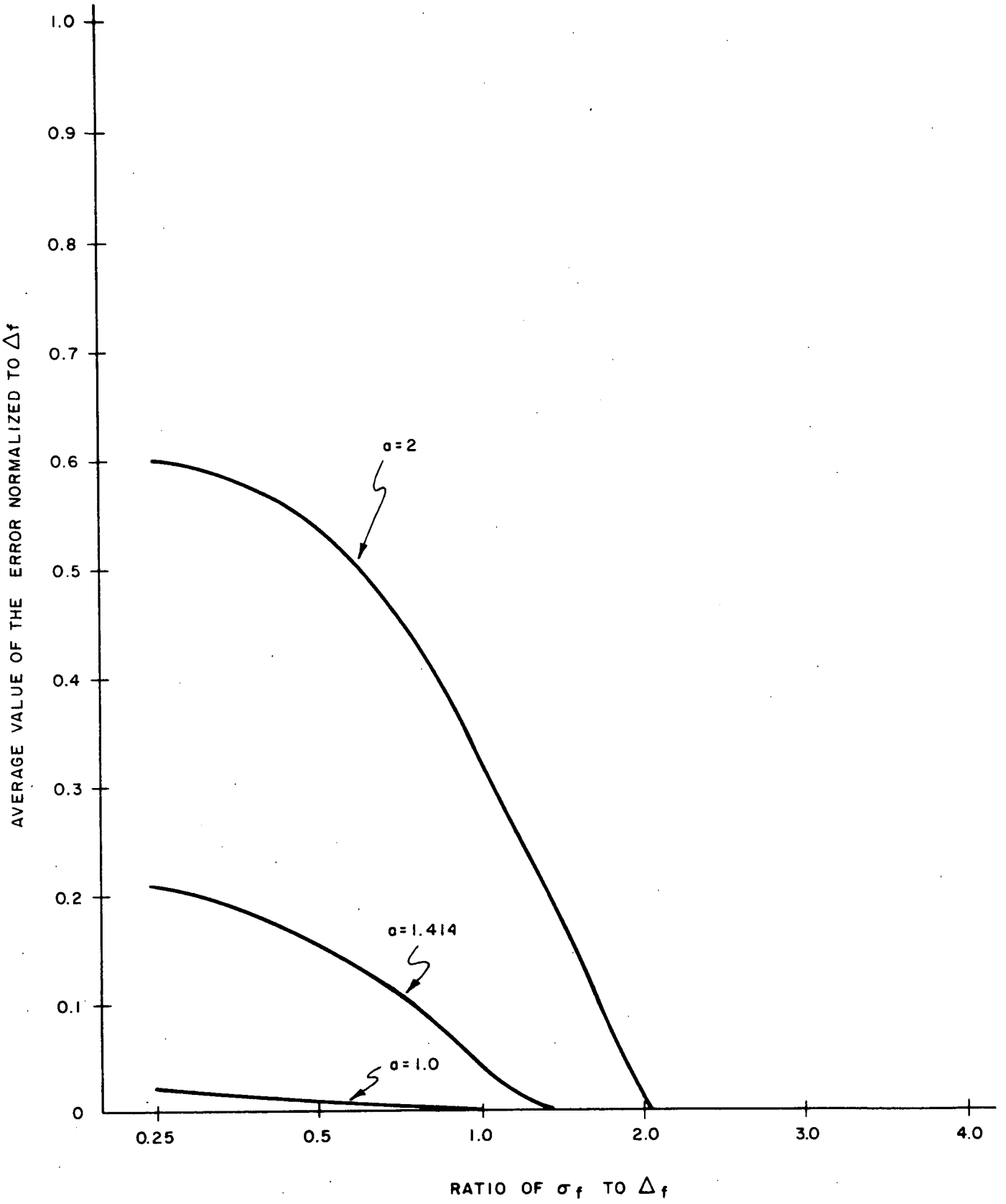

Figure 3-17 Magnitude of Error in Estimate of Center Frequency

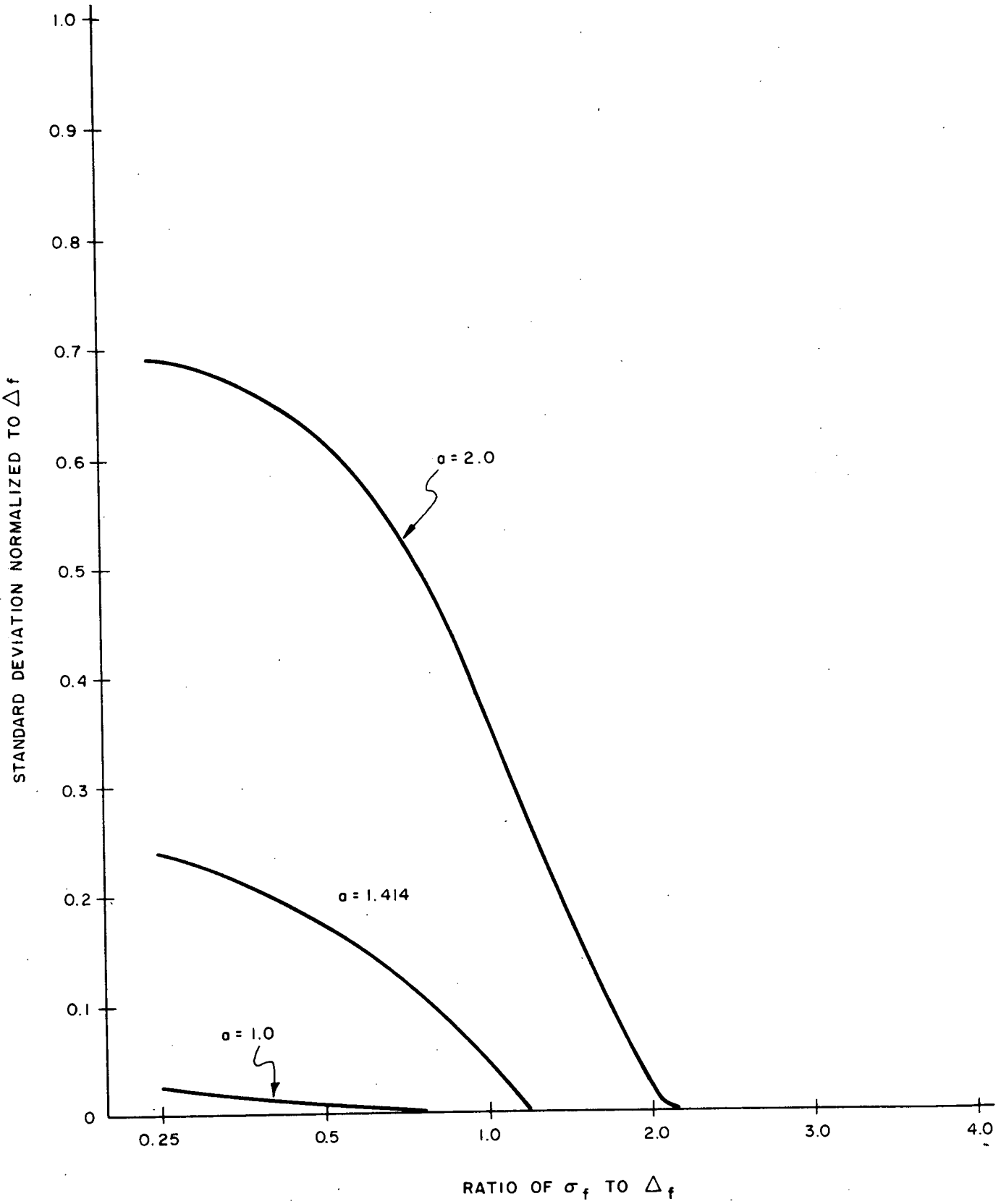

Figure 3-18 Standard Deviation of Error in Estimate of Center Frequency

Figures 3-17 and 3-18 demonstrate that the quality of the estimate of center frequency improves drastically as the filter spacing is reduced and/or as the ratio of spectral width to filter width is increased. To minimize signal-to-noise ratio loss, it is well that filters not be spaced so that the cross over is less than about -3 or -4 dB. Accordingly, once the minimum value of σ_f is established and once the tolerable estimation errors are specified, the value of Δ_f can be ascertained from the figures using the curves for a = 1.414.

3.6.4 ESTIMATE OF SPECTRAL WIDTH

One estimate of spectral width is to compute the square root of the variance of f_i about the mean value of f_i. It shall be shown that this estimate is poor for $\sigma' = \sigma_f/\Delta_f$ less than one and for a greater than 1.414, but that it rapidly improves as σ' increases and as a decreases.

$$\sigma_f^2 = \frac{\sum_{i=-\infty}^{\infty} f_i^2 P_i}{\sum_{i=-\infty}^{\infty} P_i} \tag{3-76}$$

$$= \frac{(2a)^2 (\Delta_f)^2 \sum_{i=-\infty}^{\infty} (\delta' + i)^2 \exp\left\{-\frac{2a^2(\delta' + i)^2}{\sigma'^2 + 1}\right\}}{\sum_{i=-\infty}^{\infty} \exp\left\{-\frac{2a^2(\delta' + i)^2}{\sigma'^2 + 1}\right\}} \tag{3-77}$$

As above, this equation cannot be evaluated in closed form. Computer techniques were used to evaluate the mean and variance of SQRT $(\sigma_f^2/(\Delta_f)^2)$, averaging over the random variable δ'. The normalized mean is plotted in Figure 3-19 and the normalized standard deviation is plotted in Figure 3-20.

Figure 3-19 demonstrates that the bias error is quite large, and although it decreases rapidly as σ' increases, the curves for the bias error do not decrease in slope as σ' increases. It is interesting that the bias error tends to be greater for narrower filter spacing than for broader spacing. This does not imply that the mean square error, the sum of the squares of the errors shown in Figure 3-19 and Figure 3-20, increases as a decreases; it in fact, decreases.

The standard deviation of the error in the estimate of spectral width is plotted in Figure 3-20. The curve for a = 0.707 cannot be distinguished from the x-axis. The standard deviation decreases rapidly as σ' increases; in fact, the slope of the curve decreases as σ' increases.

For an example, consider the case given above with $\sigma' = 1$ and a = 1.414. The bias error is 0.412 Δ_f = 51.5 kHz, and the standard deviation of the error is 0.0728 Δ_f = 9.1 kHz. Hence, for Δ_f = 125 kHz, the mean of the estimate is 125 + 51.5 = 176.5 kHz with a standard deviation of 9.1 kHz about this value. The root-mean-square error is $\sqrt{(51.5)^2 + (9.1)^2}$ = 52.3 kHz. It is clear that the predominant contributor to the root-mean-square error is the bias error. In cases like this, for which the bias error is much greater than the standard deviation of the error, including, now, noise errors in the standard deviation, much of the bias error can be removed by use of Figure 3-19. To estimate the bias error precisely requires that the standard deviation about the mean be zero; since it is not zero due to the inherent variance

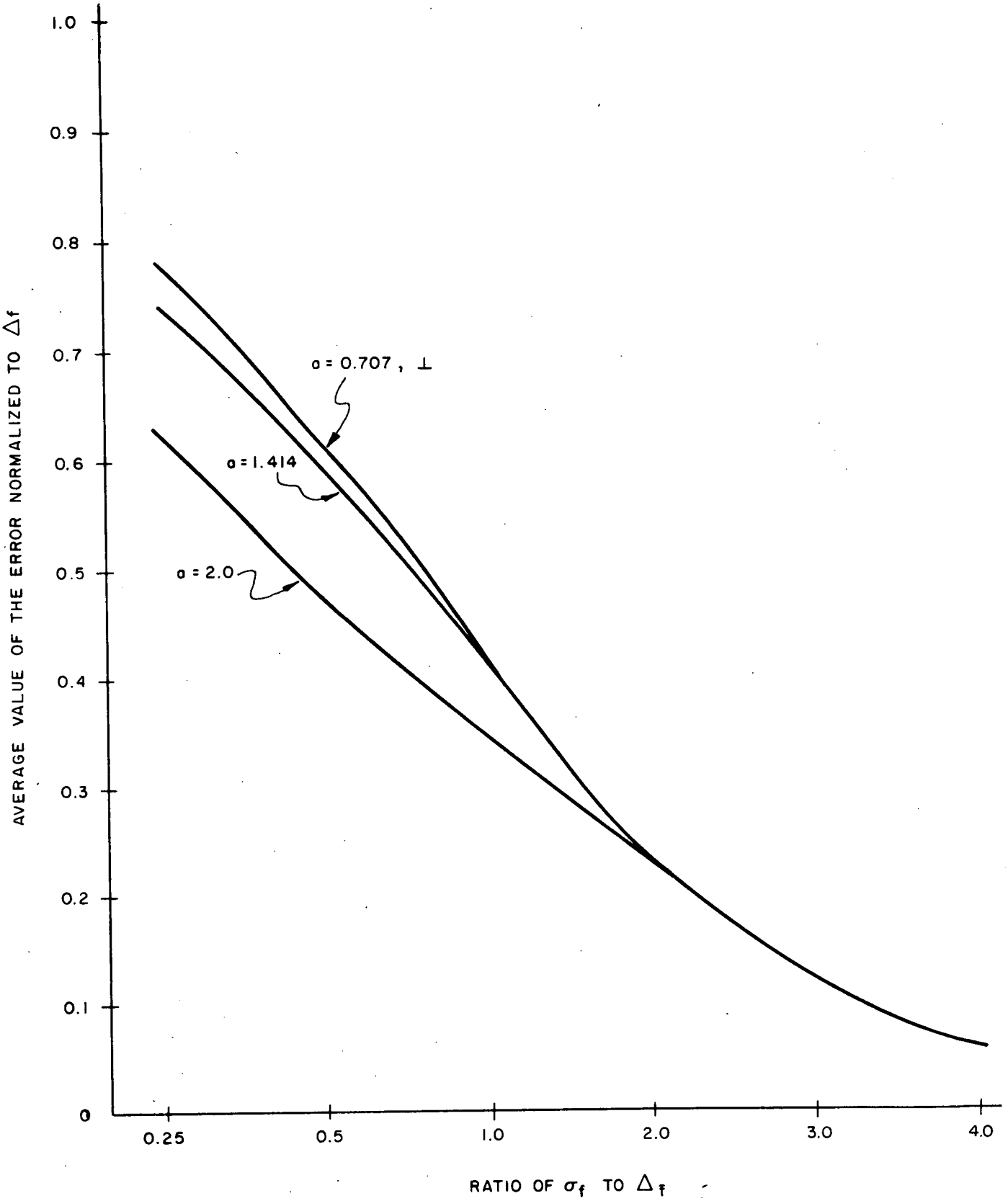

Figure 3-19 Average Value of Error in the Estimate of Spectral Width

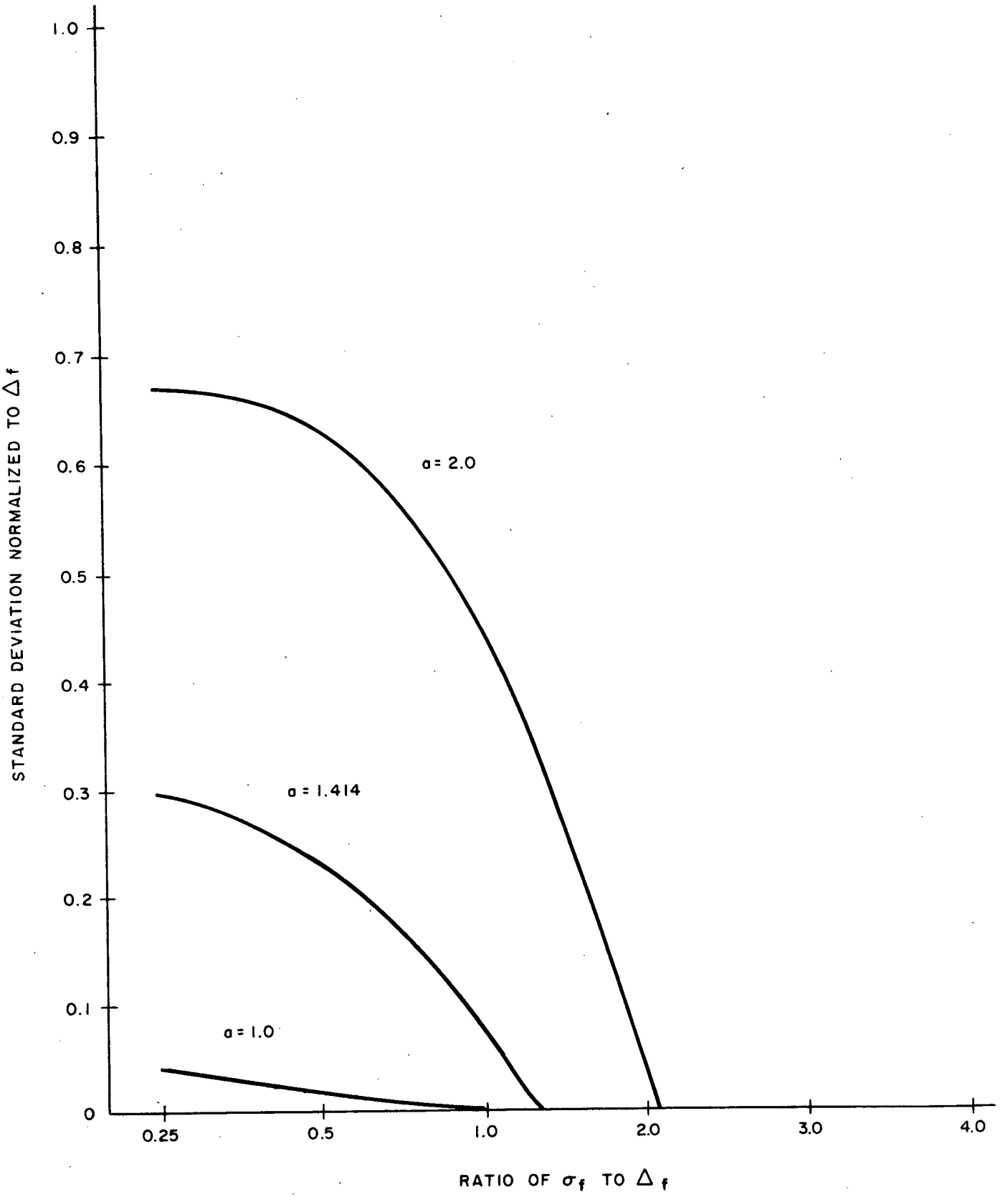

Figure 3-20 Standard Deviation of Error in the Estimate of Spectral Width

of the estimation procedure, of the receiver noise, and of the estimation of a statistical quantity, only a portion of the mean (bias) can be removed.

The mean value of the normalized estimate equals σ' plus the bias term.

$$E\left\{\text{SQRT}\left(\frac{\sigma_f^2}{(\Delta_f)^2}\right)\right\} = \sigma' + b(\sigma') \tag{3-78}$$

The function $b'(\sigma)$ is plotted in Figure 3-19. Over a small range of values of σ', the function $b(\sigma')$ can be approximated linearly*.

$$b(\sigma') = k_1 - k_2\,\sigma' \tag{3-79}$$

The ideal procedure would be to solve equation (3-78) for σ' and then to evaluate $b(\sigma')$. This is impossible, because $E\left[\text{SQRT}\ (\sigma_f^2/\Delta_f^2)\right]$ is not available. This value has an associated standard deviation. For convenience, define

$$\bar{u} = E\left\{\text{SQRT}\left(\frac{\sigma_f^2}{\Delta_f^2}\right)\right\} \tag{3-80}$$

and let δu represent the standard deviation about this mean value. The root-mean-square value of δu will differ in general from the value plotted in Figure 3-20. This is because δu must include the effects of receiver noise and of the averaging of a statistical quantity. Moreover, the root-mean-square value of δu can be reduced by post-detection integration.

Thus, approximately, we have

$$\sigma' + k_1 - k_2\,\sigma' = (\bar{u} + \delta u) \tag{3-81}$$

*A better approximation might be $b(\sigma') = k_1 - k_2 \log_2 \sigma'$.

Equation (3-81) is solved for σ'.

$$\sigma' = \frac{(\bar{u} + \delta u) - k_1}{1 - k_2} \qquad (3\text{-}82)$$

The quantity σ' is the corrected estimate of spectral width, and the quantity $(\bar{u} + \delta u)$ is the uncorrected estimate. The effect of δu is magnified by the division by $1 - k_2$, which is less than one.

In the above example, at σ' equals one, the value of k_1 is .662 and of k_2 is .25. The effect of δu is therefore magnified by a factor of 1.33. Whether or not this is acceptable depends on whether or not the total error is reduced. Without removal of the bias error, the mean square error in the example was 52.3 kHz. If the bias error is removed, the mean square error is $\sqrt{0^2 + (1.33)^2\ (9.1)^2} = 12.1$ kHz for a substantial reduction. In this case in general, it is desirable to remove the mean as long as $E(\delta u^2) < 51.5/1.33 = 38.7$ kHz.

Another source of error is the value of k_1 and of k_2. A linear approximation may not suffice over the expected range of values of σ' and either higher order expansions or evaluation of k_1 and k_2 based on a predicted value of σ' are required. A quadratic expansion would fit better over a wider range of values of σ'.

The spectral width that is estimated by this technique is the composite spectral width of the transmitted waveform and the doppler spectrum that exists within the range resolution of the transmitted pulse. For instance, if the transmitted pulse has a Gaussian power density spectrum and if the turbulence spectrum is Gaussian also, then the frequency variance of the received spectrum is the sum of the variances of the transmitted spectrum σ_t^2 and the turbulence spectrum σ_u^2.

$$\sigma_f^2 = \sigma_t^2 + \sigma_u^2 \qquad (3\text{-}83)$$

We estimate the composite width σ_f^2 from the outputs of the filter bank. The quantity σ_t^2 can be calculated from the parameters of the transmitted waveform; therefore it appears to be an easy matter to compute σ_u^2 by subtracting σ_t^2 from σ_f^2. Unfortunately, the matter is not quite so easy. First of all, equation (3-83) does not hold in general. Although a similar type of relation could be derived for a known transmitted spectrum and a known turbulence spectrum, the spectral shape of turbulence is not a precisely defined function, hence a relation of type (3-83) can be only approximate.

For good accuracy, σ_t^2 should be substantially smaller than σ_u^2. For example, if σ_t = 250 kHz and σ_u = 75 kHz, σ_f = 261 kHz is only 11 Hz greater than σ_t. With these parameters, variations in σ_u have little effect upon σ_f. The sensitivity coefficient of σ_u with respect to σ_f is

$$\frac{\partial \sigma_u}{\partial \sigma_f} = \frac{1}{\sqrt{1 - \sigma_t^2/\sigma_f^2}} \qquad (3\text{-}84)$$

If σ_t^2/σ_f^2 is near one, the sensitivity coefficient will be large and errors in the estimate σ_f will be greatly magnified. Let $\sigma^2(f)$ be the variance due to all causes of the estimate concerning the received spectral width; then the variance $\sigma^2(u)$ of the estimate of the turbulence spectral width is

$$\sigma^2(u) = \left(\frac{\partial \sigma_u}{\partial \sigma_f}\right)^2 \sigma^2(f) \qquad (3\text{-}85)$$

Let a^2 be an acceptable value of $(\partial\sigma_u/\partial\sigma_f)^2$. Then σ_t^2 must be less than $(a^2 - 1)$ times σ_u^2.

$$\sigma_t^2 \leq (a^2 - 1)\, \sigma_u^2 \qquad (3\text{-}86)$$

For instance, if σ_u is 125 kHz and an allowable value of a^2 is 2, equation (3-86) requires that σ_t = 125 kHz.

This again emphasizes the importance of obtaining accurate estimates of σ_u^2 since this value determines the selection of the filter bandwidth.

3.6.5 FREQUENCY ANALYSIS OF TRANSMITTER PULSE

The electric field of the transmitter pulse consists of two portions: the major pulse, which can be approximately written,

$$f(t) = A\, e^{-Bt} \qquad 0 < t < T_1 \qquad (3\text{-}87)$$

and the ringing portion, in the form

$$g(t) = C \sin Dt\, e^{-Gt} \qquad T_1 < t < T_2 \qquad (3\text{-}88)$$

The Fourier Transform of each of these functions will be determined.

$$F(\omega) = \frac{1}{\sqrt{2\pi}} \int_{-\infty}^{\infty} f(t)\, e^{-i\omega t}\, dt \qquad (3\text{-}89)$$

Substituting equation (3-87) into equation (3-89),

$$F(\omega) = \frac{A}{\sqrt{2\pi}} \int_{0}^{T_1} e^{-(B + i\omega)t}\, dt \qquad (3\text{-}90)$$

Integrating equation (3-90),

$$F(\omega) = \frac{A}{\sqrt{2\pi}} \left[\frac{1 - e^{-(i\omega + B)T}}{i\omega + B} \right] \qquad (3\text{-}91)$$

The signal intensity is proportional to $|F(\omega)|^2$, so

$$I(\omega) \propto \frac{A^2}{2\pi}\left[\frac{1 - 2e^{-BT}\cos \omega T + e^{-2BT}}{\omega^2 + B^2}\right] \tag{3-92}$$

After the main pulse is transmitted, a ringing in the modulator causes an additional transmission of the waveform indicated in equation (3-88). Transforming that wave function to

$$G(\omega) = \frac{C}{\sqrt{2\pi}} \int_{T_1}^{T_2} \sin Dt\, e^{-Gt}\, e^{-i\omega t}\, dt \tag{3-93}$$

Using the translation theorem, equation (3-93) is equivalent to

$$G(\omega) = \frac{C}{\sqrt{2\pi}} e^{-i\omega T_1} \int_{o}^{T'} \sin Dt\, e^{-Gt}\, e^{-i\omega t}\, dt \tag{3-94}$$

where

$$T' = T_2 - T_1 \tag{3-95}$$

Integrating equation (3-94)

$$G(\omega) = \frac{C}{2\sqrt{2\pi}\, i} e^{-i\omega T_1}\left\{\frac{\mathrm{EXP}\left[(-G - i\omega + iD)T'\right] - 1}{-G - i\omega + iA} - \frac{\mathrm{EXP}\left[(-G - i\omega - iD)\,T'\right] - 1}{-G - i\omega - iD}\right\} \tag{3-96}$$

Using a common denominator

$$G(\omega) = \frac{C}{2\sqrt{2\pi}\, i} e^{-i\omega T_1}\left\{\frac{2iD - (G + i\omega + iD)\,\mathrm{EXP}\left[(-G - i\omega + iD)T'\right]}{D^2 + (G + i\omega)^2} + \frac{(G + i\omega - iD)\,\mathrm{EXP}\left[(-G - i\omega + iD)T'\right]}{D^2 + (G + i\omega)^2}\right\} \tag{3-97}$$

The intensity is again proportional to $|G(\omega)|^2$, so

$$I'(\omega) \propto \frac{C^2}{4\pi} \left\{ \frac{2D^2 + e^{-GT'}\left[G^2 + D^2 + \omega^2 - (G^2 + \omega^2 - D^2)\cos 2DT' + DG \sin 2DT'\right]}{D^4 + G^4 + \omega^4 + 2D^2 G^2 + 2\omega^2 (G^2 - D^2)} \right\} \tag{3-98}$$

In the limit as $T' \rightarrow \infty$, equation (3-98) reduces to

$$I'(\omega) \propto \frac{C^2 D^2}{2\pi \left[D^4 + G^4 + \omega^4 + 2D^2 G^2 + 2\omega^2 (G^2 - D^2) \right]} \tag{3-99}$$

For a particular set of transmitter measurements

$$D = 1.4 \times 10^6 \text{ Hz}$$

$$G = 5.2 \times 10^4 \text{ sec}^{-1}$$

The ratio of the signal intensity at 10^6 Hz and 6×10^7 Hz can then be found to be equal

$$\frac{\left(I'(\omega)\right)_{60 \text{ MHz}}}{\left(I'(\omega)\right)_{1 \text{ MHz}}} = 7 \times 10^{-8}$$

Thus, the power from the ringing at 60 MHz is more than 70 dB below the power from the ringing at 1 MHz.

SECTION 4

RECEIVER

4.1 INTRODUCTION

This section presents the design of the CAT receiver. It is the result of a systems analysis to determine the optimum receiver design.

A block diagram of the signal processing is shown in Figure 4-1. An IF Post-Amplifier brings the signal levels up into the 100-millivolt region. This amplifier has two types of gain control. One control is manual, of ±10-dB range, so that the IF gain can be adjusted by the operator. The second control is a sensitivity time control or STC. The receiver sensitivity will be varied in accordance with a range-squared law from 1 to 20 miles. This is a 26-dB variation. From zero to 1 mile, the IF gain is at a minimum to minimize transients caused by the firing of the laser. The STC generator is triggered when the laser is fired and generates the appropriate waveform to control the amplifier.

The filter bank which follows the IF post-amplifier will span a 10-MHz bandwidth. This filter bandwidth will be variable in three steps to match a 2.0, 4.0 or 8.0-μs pulse. The matched bandwidths are approximately 500, 250, and 125 kHz, so that the number of filters in a 10-MHz band are 20, 40, and 80, respectively. One filter bank of eighty, 125-kHz filters will be constructed. It will be possible to double the bandwidth of 40 of these filters to 250 kHz, and to quadruple the bandwidth of 20 of these filters to 500 kHz.

The filter bank has 80 outputs. These are mutiplexed onto one line by a gating network controlled by a shift register. The

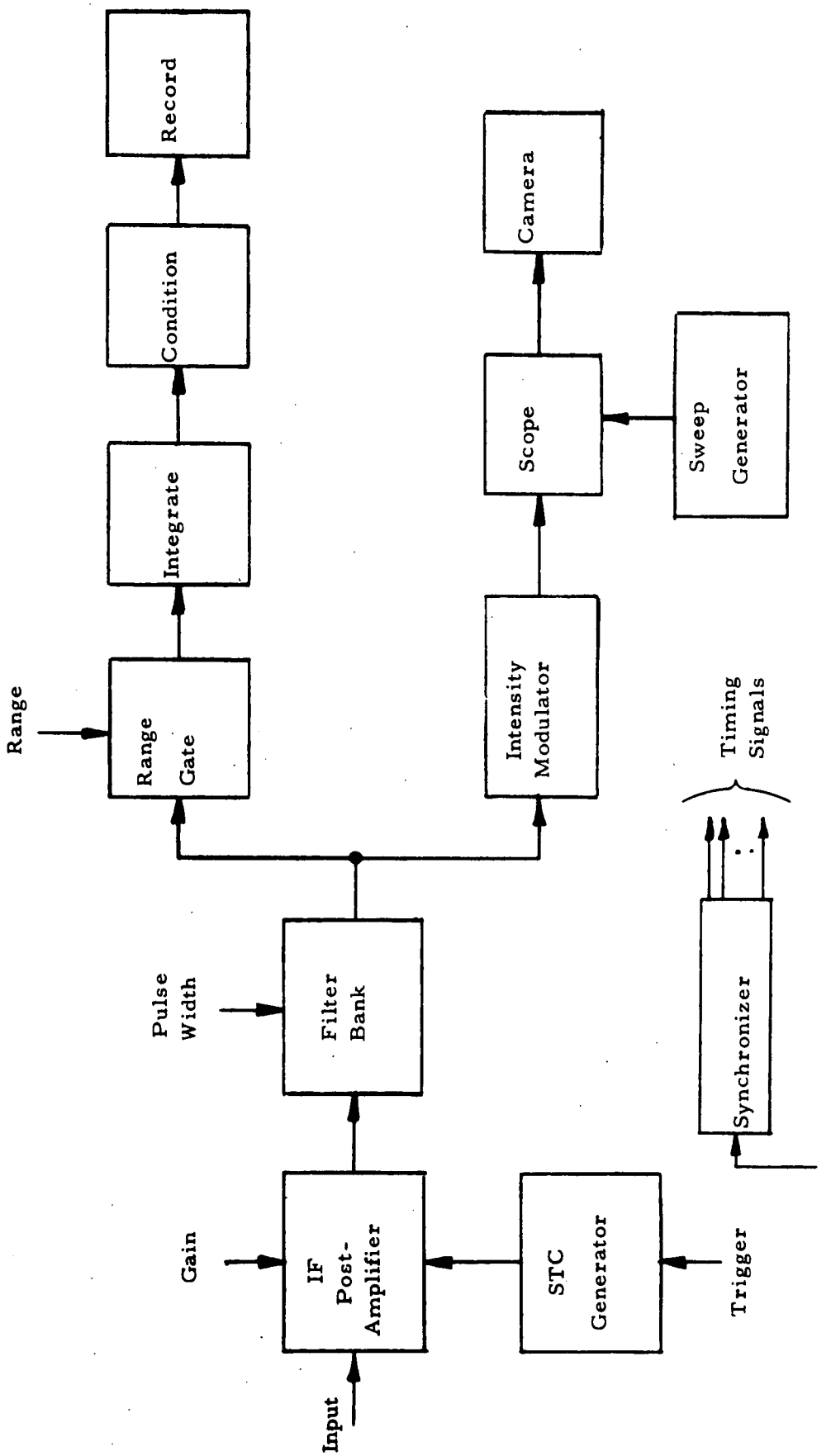

Figure 4-1 System Block Diagram

multiplexed signals intensity modulate an oscilloscope which presents a range-velocity display. The oscilloscope phosphor will be chosen for optimal integration (averaging) of the turbulence signals.

The vertical and horizontal axes of the scope are driven by a sweep generator. The period of the vertical sweep (velocity) will be approximately equal to the range resolution of the transmitted laser pulse, which is in turn approximately equal to the pulse width. The fly-back time must be a small portion of the sweep period.

Thus for a 2-μs pulse width, 20 filter outputs will be read out in 2 μs and displayed in a column on the oscilloscope. For a 8-μs pulse width, 80 filter outputs will be read out in 8 μs. In any case, the maximum rate of intensity modulation is 10 MHz.

The horizontal sweep has a duration of about 20 miles x 10 μs/miles ≈ 200 μs to extend out to 20 miles. At the conclusion of the sweep, the beam flies back until transmission of the next laser pulse when the sweep is reinitiated.

The table below gives the vertical (velocity) and horizontal (range) resolution on the display as a function of the transmitted pulse width. In any case, the resolution is about 2000 points, with resolution along one axis becoming lower as resolution along the other axis is improved.

TABLE 4-1

RESOLUTION OF RANGE-VELOCITY DISPLAY

Pulse Width	No. of Filters (Vertical)	No. of Range Cells (Horizontal)	Product
2 μs	20	100	2000
4 μs	40	50	2000
8 μs	80	25	2000

A camera is available to photograph the oscilloscope. It should be noted that the photographic film, as well as the phosphor, can be employed for integration.

To facilitate post-mission data analysis, a range-gated channel is included in the processor, as an option. The filter outputs are gated into the integrator at the desired range. The integrator will integrate a number of sweeps to reduce the rate of the recorder. A signal conditioner precedes the recorder to get the data into the proper format.

Included also in the receiver is a synchronizer to generate timing and control signals.

4.2 IF POST-AMPLIFIER AND STC GENERATOR

The purpose of the IF Amplifier is to bring signal levels up to the several hundred millivolt region. The amplifier will be capable of an output some 10 dB greater than this amount to avoid saturation on noise peaks.

The amplifier flat bandwidth must extend from 5 MHz to 15 MHz. (Small variations can be compensated in the subsequent filter bank.) It would be difficult to realize a bandwidth of this extent with a tuned circuit; therefore, a video amplifier will be employed. A number of manufacturers make amplifiers which will meet these specifications.

The amplifier will be gain controlled in two ways. One method will be a manual control of $\pm$10 dB available on the front panel. The second method is the STC to normalize the displayed signals as a function of range. As discussed above, the STC decreases the attenuation by 26 dB as the range increases from 1 to 20 miles. A block diagram of the circuit and of the pertinent waveforms are shown in Figure 4-2.

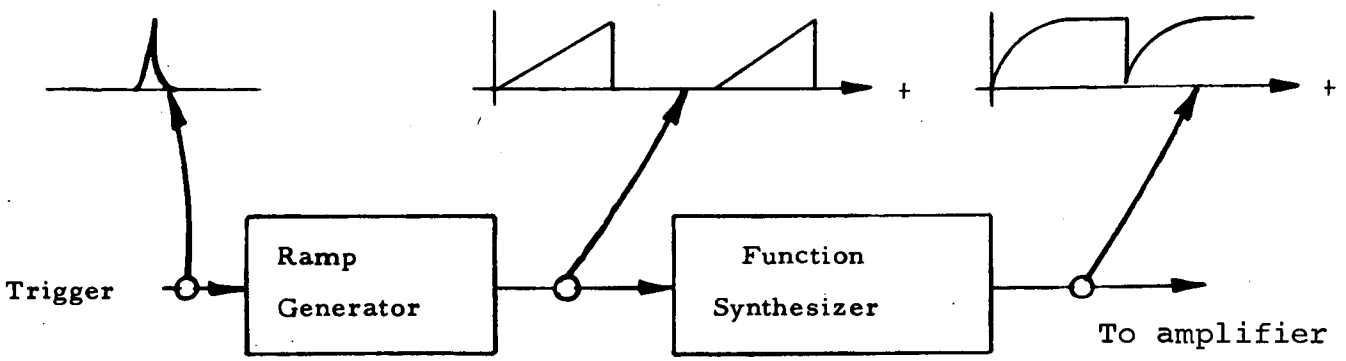

(a)

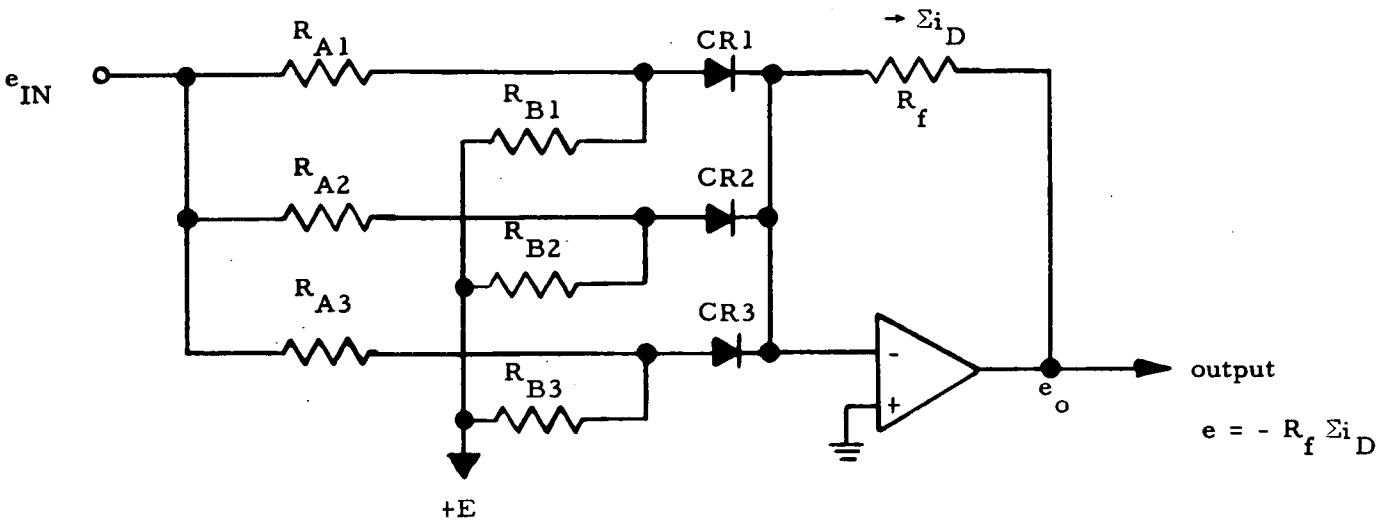

(b)

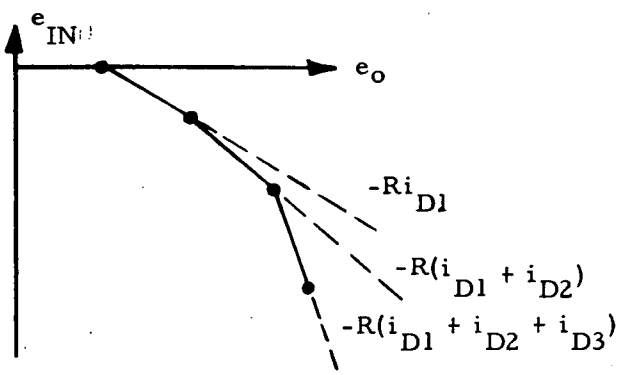

(c)

Figure 4-2 STC Circuit. (a) Block Diagram, (b) Non-Linear Function Generator, and (c) Non-Linear Function Synthesis

A ramp generator generates a ramp of about 200 μs duration upon receipt of a trigger. This ramp is shaped by a nonlinear shaping network shown in Figure 4-2(b). The input signal is connected to n networks, each forming a divider between e_{IN} and the negative reference voltage E. Above some value of e_1, the diode will conduct, driving a current into the summing point. The condition for the conduction is that

$$e_{IN} > \frac{R_A}{R_B} E \qquad (4\text{-}1)$$

When the diode conducts, the current that flows to the summing point (neglecting diode voltage drop) is e_{IN}/R_A. By properly setting up the diode break-points and resistor values, a nonlinear function may be synthesized as in Figure 4-2(c).

4.3 FILTER BANK

The filter bank covers the 10 MHz range from 5 to 15 MHz. The narrowest bandwidth filter that is employed is 125 kHz, so that the maximum $Q = \frac{15}{.125} = 120$. A Q of this magnitude is quite difficult to obtain in the megahertz region since even good inductors have Q's of this magnitude; therefore, it seems better to divide the band from 5 to 15 MHz into four 2.5-MHz sub-bands and to heterodyne these smaller bandwidths to a center frequency of 2.5 MHz. In this case the maximum Q is $\frac{2.5 + 1/2(2.5)}{.125} = 30$, giving a maximum Q that is only one-fourth of the Q without heterodyning. Moreoever, the four filter banks that perform the velocity resolution of the sub-bands are identical, so that some commonality is achieved.

Figure 4-3 illustrates the technique. Four pre-filters divide the 10-MHz band into four 2.5 MHz bands. The bandwidths of these filters are indicated in the figure; these are the bandwidths over which the filter response must be essentially constant, not the -3 dB bandwidth which is slightly larger.

The highest Q pre-filter is number 1. The Q is approximately $\frac{13.75}{2.5} = 5.5$, which is very moderate. The number of sections can be estimated from the steepness of the response characteristic. The filter must pass 15.0 MHz, but must have high attenuation at 17.5 MHz, which would mix with 16.25 MHz and fall into the band. The important parameter is the number of half-bandwidths between 13.75 MHz, the center frequency of the filter, and 17.5 MHz.

$$\bar{\omega} = \frac{17.5 - 13.75}{1.25} = \frac{3.75}{1.25} = 3 \qquad (4\text{-}2)$$

Reference to filter design tables indicates that a four section filter with low ripple can meet this requirement.

The output of the four one-filters is mixed down to a center frequency of 2.5 MHz. A high-side crystal oscillator is used to generate the proper frequency. A two transistor oscillator is used. One stage is a low-level oscillator stage, and the second stage is a buffer stage to drive the mixer.

The mixer outputs go to the filter banks. The mixer output must be amplified to make up for conversion losses and to get the power necessary to drive the bank of filters.

A filter channel is shown in Figure 4-4. The output from the driver is split up into 20 parallel channels. These are filtered by a single-tuned LC circuit, and then detected. The video is assumed by a gate-controlled amplifier and an operational amplifier.

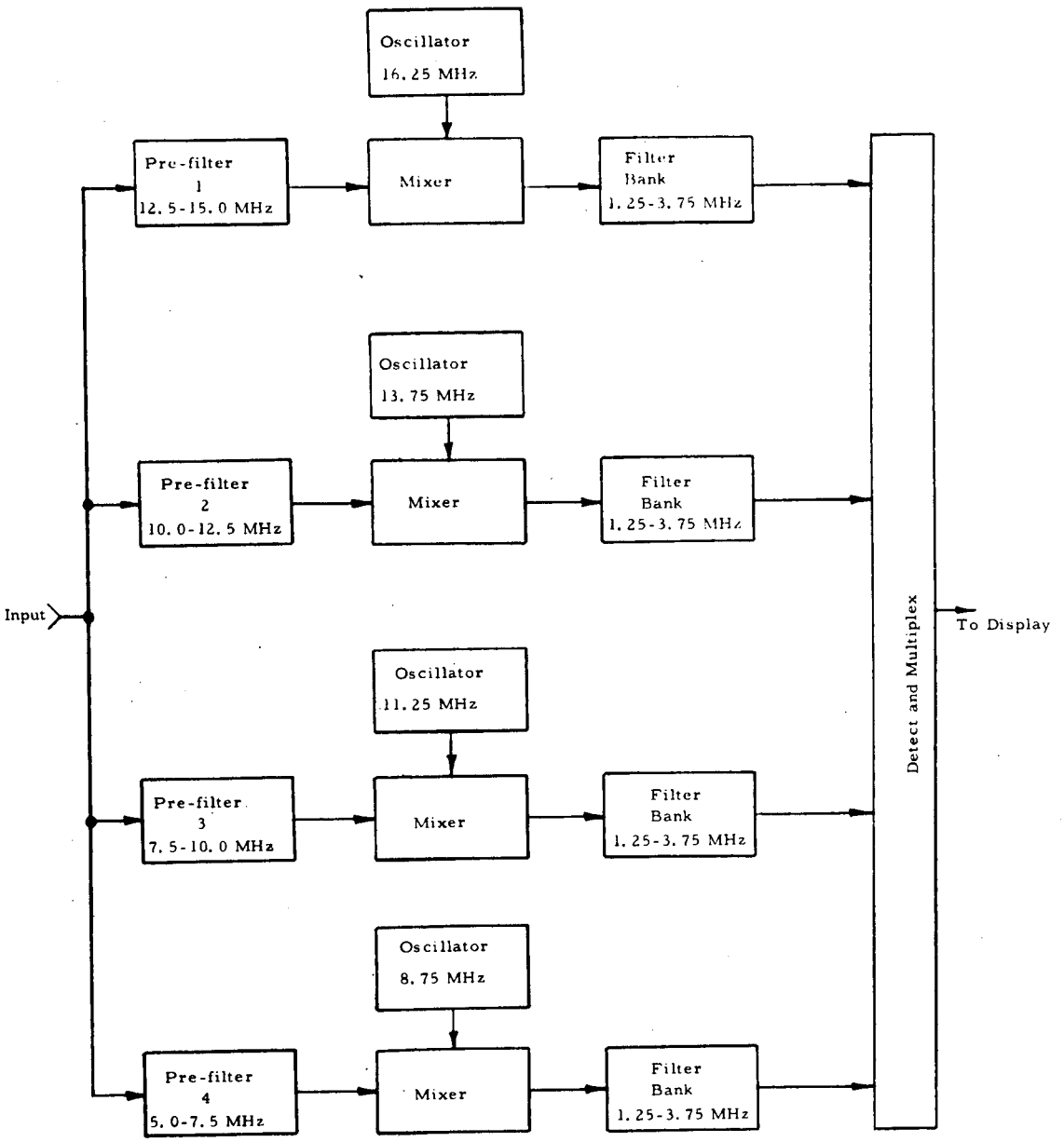

Figure 4-3 Filter Bank Implementation

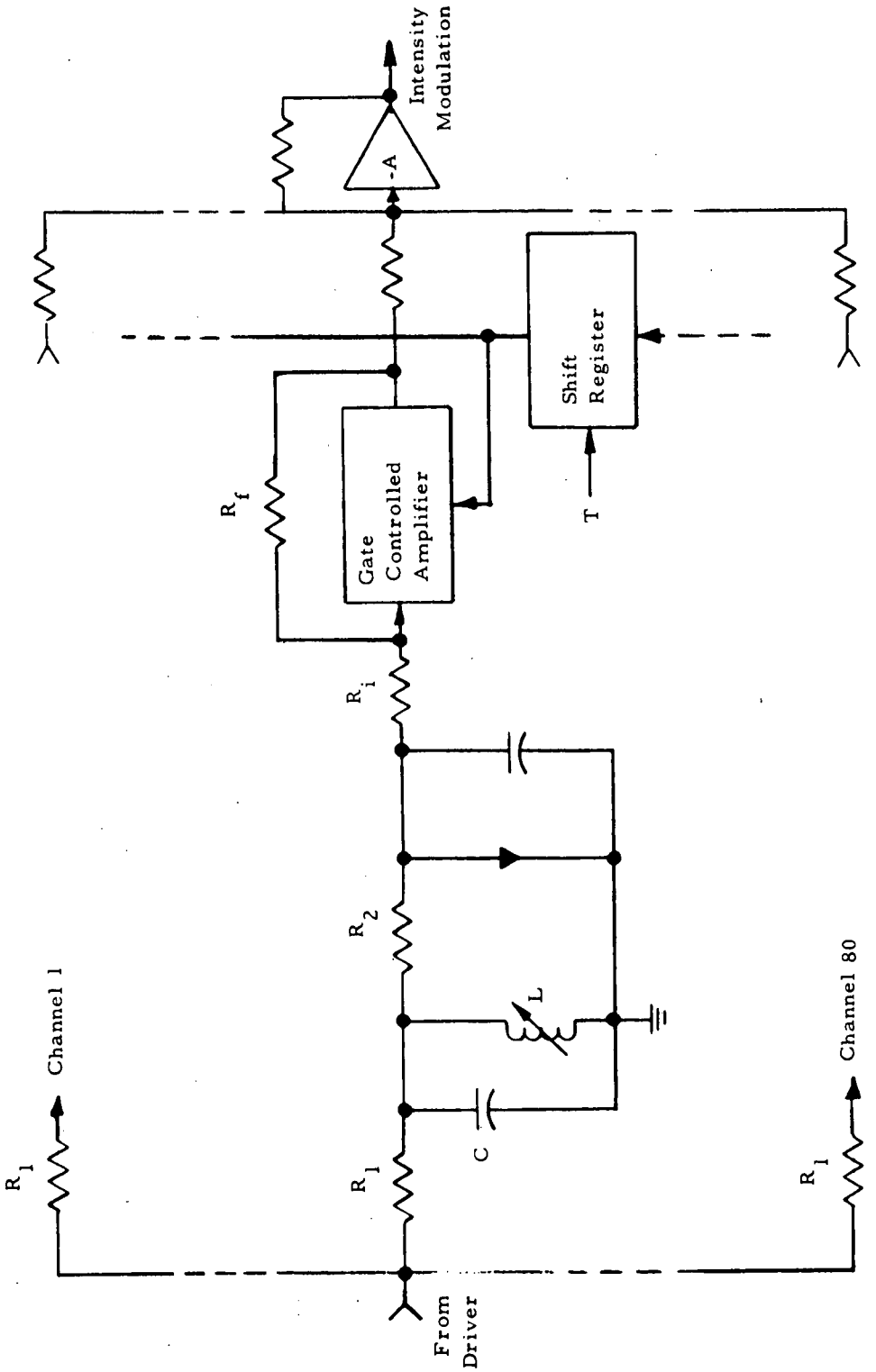

Figure 4-4 One Channel of Filter Bank (Filter Switching Not Shown)

The gate-controlled amplifier will have a select time under 20 ns, which is less than one-fifth of the time each channel is enabled. The amplifier will provide gain to bring signal magnitudes up near the volt region. The outputs of the 80 gate-controlled amplifiers are summed by an operational amplifier. In practice a two-level summing structure would be employed, with the first level summing eight lines per stage and with the second level summing the ten lines from the first stage.

The gates are controlled by an 80-stage shift register. A "one" is inserted into the end of the shift register and shifted upward at about 10-MHz rate: in this manner 80 channels are read out in 8 μs, 40 channels in 4 μs, and 20 channels in 2 μs. The "one" at a shift register output enables the gated amplifier to which it is connected; all other channels are disabled. The next clock pulse after the "one" reaches shift register number 80, a "one" is inserted at the beginning of the shift register and the process is repeated. This control circuitry is considerably simpler than other methods.

To match a 4-μs pulse width the bandwidth of 40 of the filters should be doubled. This could be done, for instance, by switching a resistor across each filter whose bandwidth is to be widened. If the bandwidth of every second filter is to be widened, however, then the combining network must be capable of selecting every second filter. A simpler method is to widen the bandwidth and simultaneously shift the center frequency of forty adjacent filters. In so doing, the bandwidth of forty filters can be changed, but the gain will remain constant. Moreover, the control logic remains very simple. It is merely necessary to sense when the "one" reaches the fortieth stage, inhibit it from proceeding further,

and cycle a "one" into the first stage of the counter. Similarly the bandwidth of twenty filters can be quadrupled to 500 kHz and their center frequency changed to match an 8 μs pulse. In this case the shift register must be 20 stages long.

The technique is illustrated in figures 4-5 and 4-6. Diodes are used to switch one of two filters into the channel. The cathode end of the diode is grounded through an RF choke. A diode is energized by being connected to the +v supply through the filter inductor. The value of +v should be low so that diode dynamic impedance can be made low without excessive dissipation. A diode is turned off by returning its anode to a negative voltage. A two-pole, two-position switch is shown. In the actual system this would be a three-pole, three-position switch to switch between the three bandwidths.

Figure 4-5 shows the control for the entire filter bank. In the 125-kHz mode, all 80 filters are employed, and the shift register is 80 stages long. In the 250-kHz mode, the 40 filters numbered 1 through 40 are used. An AND gate at the output of shift register number 40 prevents information from being transferred into the upper 40 shift registers. In the 500-kHz mode, the 20 filters numbered 41 through 60 are employed. This is accomplished by putting a one into shift register 41 every 2 μs and shifting it up to register number 60.

4.4 DISPLAY AND ASSOCIATED CIRCUITS

This display will use a general purpose 15-MHz oscilloscope with a special phosphor, P7, that has a long decay so that averaging can be performed on the oscilloscope screen. The averaging time of the eye is about one-tenth second; use of a P7 phosphor will extend the averaging time toward 1 second which is much better matched to the system parameters since it will take about 1 second for a 600 knot aircraft to fly the distance represented by a 2-μs pulse.

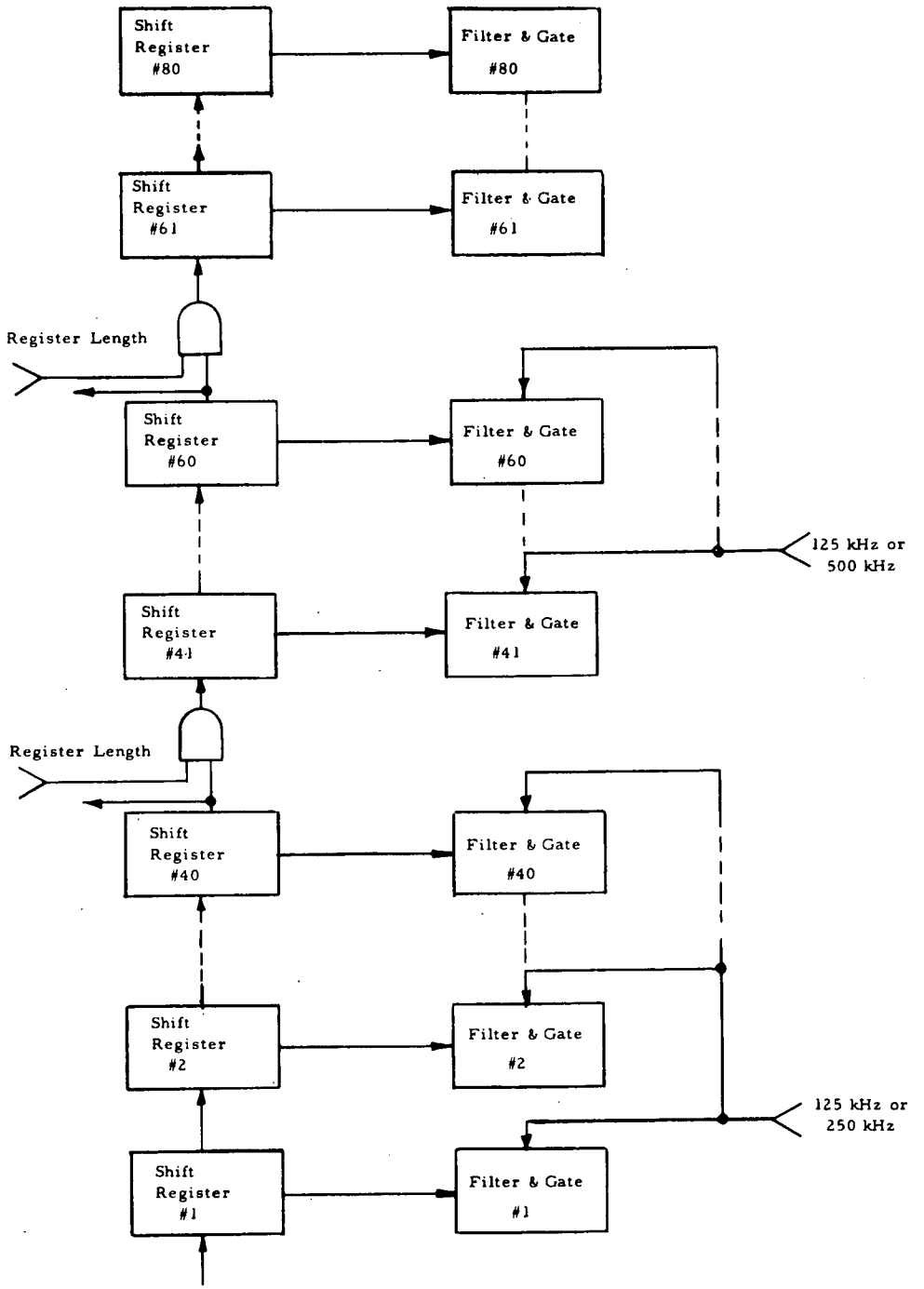

Figure 4-5 Filter Bank Control

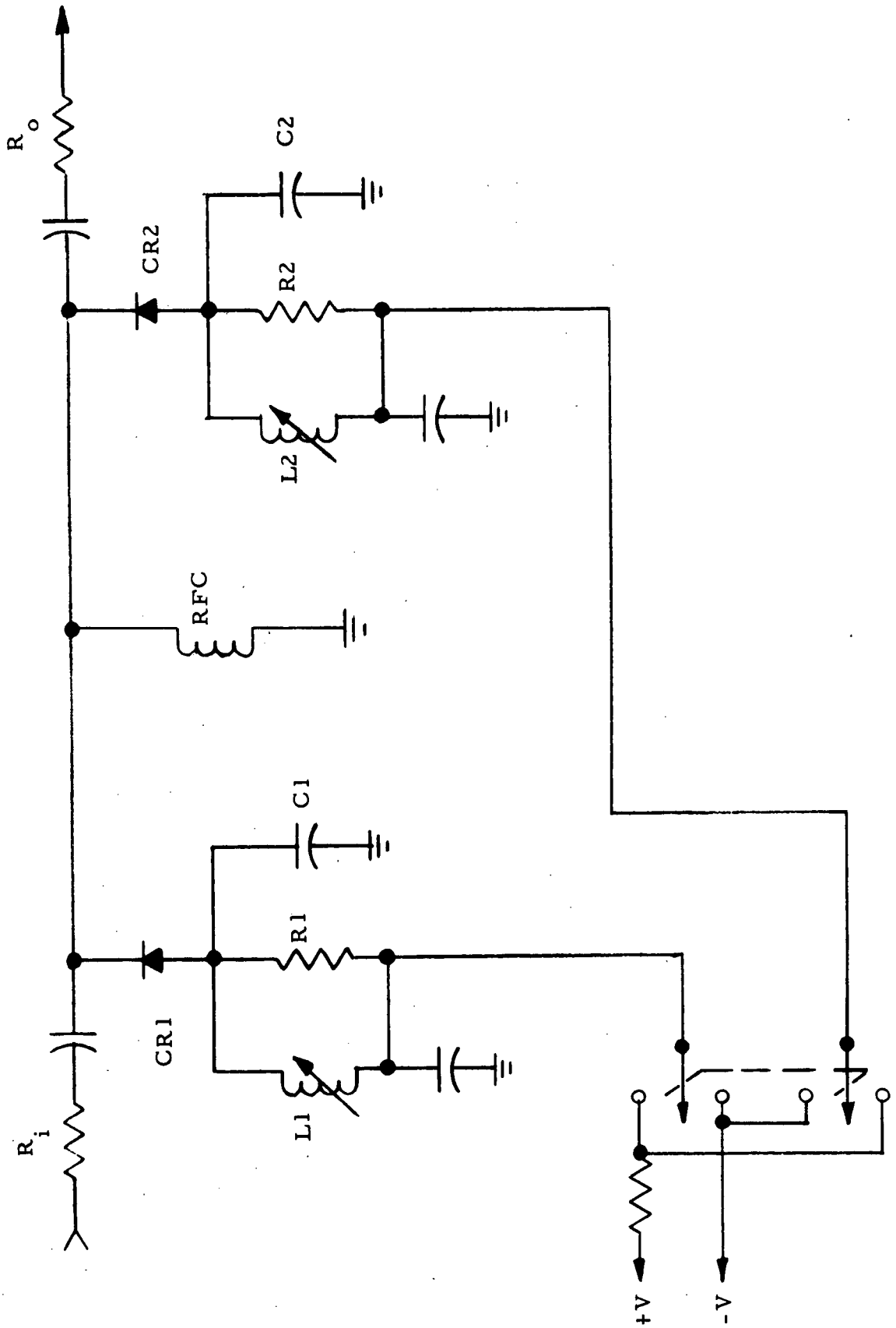

Figure 4-6 Change of Filter Center Frequency and Bandwidth

A Tektronix Type R422 oscilloscope will meet these requirements. This scope has environmental capabilities of 15,000 feet and -15°C operating temperature, which is more than sufficient to meet system requirements. The display is nearly square, 8 x 10 division (0.8 cm/div).

The vertical bandwidth of the scope is 15 MHz, giving a 24 ns rise time. To scan the beam, a sawtooth waveform is applied to the vertical input. The minimum period of this waveform is 2.0 μs, so that the fly-back time will be only 1 percent of the period. The sawtooth waveform will be generated by a sweep generator. There will be three periods of 2, 4, and 8 μs corresponding to the three pulse widths.

The horizontal sweep will be generated by the horizontal circuit within the scope. This sweep circuit is triggered at the start of each range sweep. By using the time/division controls, the range sweep can be expanded or compressed.

The intensity modulation is applied to the z-axis. The bandwidth requirements for the intensity modulation are quite moderate, they are only about 1/2 μs = 0.5 MHz.

A Tektronix C-30A camera will be supplied for photographing the display.

4.5 SYNCHRONIZER

Acting on receipt of the repetition frequency trigger, the synchronizer will generate the appropriate timing and control signals for the filter bank multiplier, the sweep generator, and the recording channel.

The heart of the synchronizer is a digital clock. The clock is enabled by the input trigger and generates a pulse train at 500 kHz, 250 kHz, or 125 kHz depending on the pulse width. The clock will be disabled beyond 20 miles and will remain in a quiescent state awaiting the next trigger.

The synchronizer will be implemented out of standard transistor-transistor logic elements. No difficulties are anticipated, because of the moderate speeds and simple design.

4.6 DATA RECORDING

The components of the data recording channel are shown in figure 4-7. The detected filter bank outputs are sampled and held. The rate of sampling is once per repetition period, or about 200 Hz. The position of the sampling pulse will be adjustable from 1 to 20 miles in range, and the width of the sampling pulse will be about .5 to 1 μs; that is, one-fourth to one-half of the minimum pulse width. The outputs of the sample and hold circuits are multiplexed onto a single line. Each channel is multiplexed onto a single line for 5 ms/80 = 62.5 μs. The multiplexer will be similar in design to the multiplexer used for the display. At this point, the analog signals will be converted to a digital format. The converter will have 36-dB dynamic range corresponding to six bits resolution. Conversion to six bits resolution in 62.5 μs can be accomplished quite readily with commercial converters that are packaged on a single printed circuit board.

The output of the converter is in bit serial form and the bit rate is just under 100 kHz. It would be possible to record this data on a digital tape recorder. At 120 inches-per-second, and 800 bits-per-inch, 96,000 bits-per-second can be recorded. This method of operation is not recommended for two reasons. A 1200 ft roll of tape lasts only 2 minutes under these conditions. Even more important is the fact that data reduction should be performed before recording.

A 600-knot velocity corresponds to about 1000 ft/s, and a 2.0-μs pulse corresponds to about 1000 ft. Hence, the returns over a 1 second or smaller period come from the same range resolution cell.

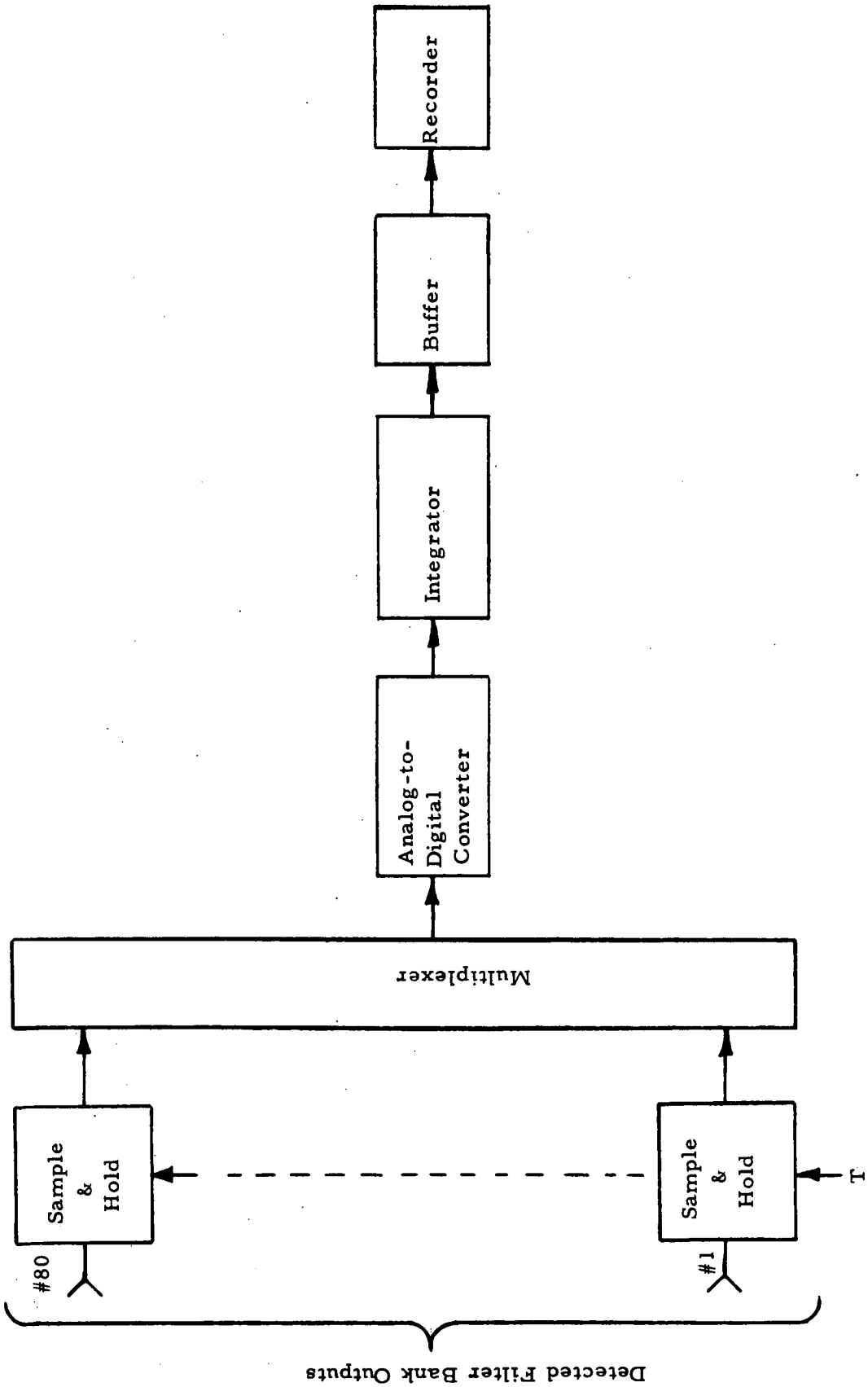

Figure 4-7 Recording of Single Range Gate Frequency Analysis

It is planned to integrate 32 returns in the integrator. The range gate is enabled at 5 ms intervals, hence returns will be integrated over 160 ms, or about 1/6 of a second. Fluctuations faster than 200 Hz/32 = 6 Hz will tend to be averaged out, but slower fluctuations will be evident. A 1200 ft reel of tape will last approximately an hour under these conditions.

The integrator must have the capability to integrate 32 pulses. This requires 5 bits above the 6 input bits or 11 bits in all. The integrator consists basically of a recirculating shift register and an adder. An integrand is recirculated to the integrator input at just the time that new input data appears. The length of the shift register is 80 x 11 = 880 bits. This can be realized by a small number of metal-oxide semiconductor (MOS) shift registers. The shift registers can be interfaced directly with transistor-transistor logic circuitry.

After 32 pulses have been integrated, the integrator is dumped into the buffer, and integration of another 32 pulses commences. During the period, 5 ms x 32 = 160 ms, the contents of the buffer are recorded. The serial output of the buffer must be converted to the proper format. A 11-bit binary word is equivalent to 3 binary-coded decimal characters.

4.7 PREAMPLIFIER

This paragraph presents an analysis of the coherent detection technique utilized in a CO_2 laser system, particularly with regard to specifying the noise figure (**F**) of the preamplifier immediately following the IR detector. The manner in which this preamplifier could affect the signal-to-noise ratio (S/N) of the system is of prime concern relative to the process of detection.

In coherent detection it is assumed that detector shot-noise generated by the local oscillator power (P_{LO}) predominates, overshadowing the thermal noise of the first subsequent amplifier

(preamplifier) in the receiver. However, there can be a considerable variance in (1) detector quantum efficiency (η), (2) responsivitry (ρ_i), (3) detector bias conditions (power dissipation as well as equivalent impedance), and (4) preamplifier input resistance (R_{IN}). Once the bias conditions of the detector are specified together with its electrical parameters, and once the required frequency response bandwidth is known, the preamplifier can be specified. In some cases, a suitable impedance matching network may be needed to preserve the preamplifier noise figure. In view of the above considerations it is important to study the coherent detection laser receiver in detail to ensure the optimum S/N condition.

In an ideal coherent detection situation the familiar S/N expression is

$$S/N = \frac{\eta P_{rx}}{2 h\nu \Delta f} \qquad (4\text{-}3)$$

where

P_{rx} = required power at the receiver input to obtain a specified S/N
η = detector quantum efficiency
h = 6.625×10^{-34} joules-sec
ν = 2.83×10^{13} Hz at 10.6 μ
Δf = system bandwidth after narrow banding

The basic starting point in specifying the receiver preamplifier is to determine the minimum η required to give a desired system S/N. Having specified η, one can then take various P_{LO} bias levels in conjunction with typical responsivities and, from them, calculate the required noise figure. As shown later, whenever the product of $P_{LO} \times (\rho_i)^2$ is sufficiently high the receiver preamplifier requirement will not become the limiting factor.

The expressions given as equations (4-4) through (4-9) are used in the noise figure analysis that follows.

$$i_n^2 = 4\ e\ G\ I_{DC}\ \Delta f \tag{4-4}$$

$$\rho_i = \frac{e}{h\nu}\ \eta\ G \tag{4-5}$$

$$Pwr_{(n)} = i_n^2\ R_{IN} \tag{4-6}$$

$$i_{na}^2 = 4\ KT\ \Delta f / R_{IN} \tag{4-7}$$

$$Pwr_{(na)} = i_{na}^2\ R_{IN}\ F$$

Substituting from equation (4-7),

$$Pwr_{(na)} = 4\ KT\ \Delta f\ F \tag{4-8}$$

$$F = \frac{Pwr_{(n)}}{Pwr_{(na)}}$$

Substituting from equations (4-6) and (4-8),

$$F = \frac{i_n^2\ R_{IN}}{4\ KT\ \Delta f} \tag{4-9}$$

where the parameters not defined earlier are

i_n^2	=	mean squared detector noise current
e	=	charge of an electron = 1.6×10^{-19} coulombs
G	=	detector current gain
I_{DC}	=	detector bias current = ($P_{LO} \times \rho_i$) amperes
ρ_i	=	detector responsivity (A/W)
$Pwr_{(n)}$	=	detector noise power at the preamplifier input
R_{IN}	=	preamplifier input resistance = 50 ohms or greater depending on the frequency response requirements
i_{na}^2	=	mean-squared thermal noise current
$4\ KT\ \Delta f$	=	thermal noise power for a given bandwidth, Δf

$4\ KT\ \Delta f$ = 16×10^{-15} W at room temperature and Δf = 1 MHz

$Pwr_{(na)}$ = preamplifier noise power which includes degradation due to its noise figure

The procedure used to determine F is as follows:

(1) Specify the desired η needed in equation (4-3) to obtain a particular system S/N ratio.

(2) Use this η in equation (4-5) with the detector ρ_i to obtain G.

(3) Knowing the bias current, calculate the noise current squared from equation (4-4).

(4) Use this i_n^2 with R_{IN} in equation (4-6) to calculate $Pwr_{(n)}$.

(5) Compare this to 4 KT Δf in equation (4-9) to solve for F.

Some typical bias conditions having a Ge:Cu detector were taken from the Wind Velocity Measurement Program[1] and are given in Table 4-2.

TABLE 4-2

TYPICAL BIAS CONDITIONS - Ge:Cu DETECTOR

P_{LO} LEVEL	DET. VOLTS	RESPONSIVITY	LO x RESPONSIVITY (I_{DC})
10 mW	20	0.55 A/W	5.5 ma
20 mW	20	0.50 A/W	10.0 ma
40 mW	12	0.25 A/W	10.0 ma
80 mW	8	0.15 A/W	12.0 ma
100 mW	10	0.18 A/W	18.0 ma

C.3

In accordance with the procedure outlined earlier, the required preamplifier noise figure has been computed in Table 4-2 using a low P_{LO} level (line 1), an intermediate P_{LO} level (line 2), and a high P_{LO} level (line 5), at R_{IN} equal to 50 ohms and 100 ohms. The results are tabulated in tables 4-3, 4-4, and 4-5. For convenience a Δf of 10^6 Hz (possible also on a per Hz basis) was used in the calculations.

TABLE 4-3

LOW P_{LO} LEVEL; ρ_i = 0.55 A/W

η	G	R_{IN}	DET. NOISE POWER	THERM. NOISE POWER	F
0.5	0.1375	50 Ω	2.42×10^{-14} W	$4 \times 4 \times 10^{-15}$ W	2 dB
0.5	0.1375	100 Ω	4.86×10^{-14} W	"	5 dB
0.25	0.275	50 Ω	4.86×10^{-14} W	"	5 dB
0.25	0.275	100 Ω	9.72×10^{-14} W	"	8 dB
0.125	0.55	50 Ω	9.72×10^{-14} W	"	8 dB
0.125	0.55	100 Ω	19.44×10^{-14} W	"	11 dB

TABLE 4-4

INTERMEDIATE P_{LO} LEVEL; ρ_i = 0.5 A/W

η	G	R_{IN}	DET. NOISE POWER	THERM. NOISE POWER	F
.5	.1250	50 Ω	4.0×10^{-14} W	$4 \times 4 \times 10^{-15}$ W	4 dB
.5	.1250	100 Ω	8.0×10^{-14} W	"	7 dB
.25	.25	50 Ω	8.0×10^{-14} W	"	7 dB
.25	.25	100 Ω	1.6×10^{-13} W	"	10 dB
.125	.50	50 Ω	1.6×10^{-13} W	"	10 dB
.125	.50	100 Ω	3.2×10^{-13} W	"	13 dB

TABLE 4-5

HIGH P_{LO} LEVEL; ρ_i = 0.18 A/W

η	G	R_{IN}	DET. NOISE POWER	THERM. NOISE POWER	F
0.5	.045	50 Ω	2.59×10^{-14} W	$4 \times 4 \times 10^{-15}$ W	2 dB
0.5	.045	100 Ω	5.18×10^{-14} W	"	5 dB
0.25	.09	50 Ω	5.18×10^{-14} W	"	5 dB
0.25	.09	100 Ω	1.036×10^{-13} W	"	8 dB
0.125	.18	50 Ω	1.036×10^{-13} W	"	8 dB
0.125	.18	100 Ω	2.07×10^{-13} W	"	11 dB

It can be seen that the noise figure requirements are about the same at a low P_{LO} level as they are at a high P_{LO} level. This is so because detector responsivity varies with bias, and decreases with higher P_{LO} levels. The important thing is that $I_{DC} \times \rho_i$ or, equivalently, $(\rho_i)^2 \times P_{LO}$, remained relatively constant.

From Table 4-4 it can be seen that noise figure requirements are less stringent at intermediate P_{LO} levels. This is so because $(\rho_i)^2 \times P_{LO}$ increased, indicative of a better detector bias situation. Consequently, the highest P_{LO} level on the detector may not be desirable, since the best operating point is at that level where the highest P_{LO} occurs in conjunction with the highest ρ_i.

4.7.1 PREAMPLIFIER NOISE FIGURE EXPRESSION

A convenient expression for the preamplifier noise figure (F) in terms of R_{IN}, I_{DC}, ρ_i, and η, is now derived. The mean squared noise current (i_n^2) caused by the local oscillator power (P_{LO}) is given by

$$(i_n)^2 = 4\, e\, G\, I_{DC}\, \Delta f \qquad (4\text{-}10)$$

but

$$\rho_i = \eta G \frac{e}{h\nu}$$

and

$$G = \frac{\rho_i \, h\nu}{\eta \, e} \tag{4-11}$$

Substituting equation (4-11) into equation (4-10) gives:

$$(i_n)^2 = \frac{4e \, \rho_i \, I_{DC} \, h\nu \, \Delta f}{\eta \, e} = \frac{4\rho_i \, I_{DC} \, h\nu \, \Delta f}{\eta} \tag{4-12}$$

The amplifier noise power ($i_{na}^2 \, R_{IN}$) is equal to F x 4 KT Δf whereas the mean-squared amplifier noise current follows from

$$(i_{na})^2 = \frac{(i_{na})^2 \, R_{IN}}{R_{IN}} = \frac{4 \, KT \, \Delta f \, F}{R_{IN}} \tag{4-13}$$

If the noise powers from equations (4-12) and (4-13) are equated an expression for F can be obtained as follows:

$$\frac{4 \, KT \, \Delta f \, F}{R_{IN}} = \frac{4\rho_i \, I_{DC} \, h\nu \, \Delta f}{\eta}$$

or

$$F = \frac{R_{IN} \, I_{DC}}{\eta} \left(\frac{h\nu}{KT} \right) \rho_i = \frac{5 \, R_{IN} \, I_{DC} \, \rho_i}{\eta} \tag{4-14}$$

where $(h\nu/KT) \cong 5$. In a typical detection situation such as given in line 3 of Table 4-3 F can be calculated from the parameters R_{IN} = 50 ohms, I_{DC} = 5.5 ma, η = .25, and ρ_i = 0.55 A/W. Substituting into equation (4-14) gives

$$F = \frac{5 \times 50 \times 5.5 \times 10^{-3} \times 0.55}{0.25} = 3.024 \cong 5 \text{ dB}$$

This is in accord with the noise figure given in Table 4-3 for these same conditions.

4.7.2 PREAMPLIFIER IMPEDANCE MATCHING

When the noise figure of a preamplifier is specified it is valid with the correct driving source impedance. If the preamplifier is connected to a different source impedance the noise figure will be degraded. Generally, this is not critical (a two-to-one mismatch increases the noise figure by about 0.5 dB), but should be considered in the receiver design.

Consider the circuit of Figure 4-8 below in which the preamplifier should be driven by 50 ohms to realize its best noise figure. Without the 100-ohm resistor to ground, the preamplifier would see a source impedance of 5 kilohms in parallel with 3 kilohms = 1.875 kilohms, a bad mismatch. With the 100-ohm resistor it sees 5 kilohms, 3 kilohms, and 100 ohms all in parallel $\cong$ 95 ohms which does not materially affect its noise figure.

With regard to the calculations made earlier for a R_{IN} = 50 ohms, i_n^2 would flow into a resistor of 95 ohms in parallel with 50 ohms $\cong$ 33 ohms instead of 50 ohms, causing the preamplifier noise figure requirement to increase slightly. This latter example is given for illustration. In a specific application the best matching network would be selected and could consist of an emitter follower transistor stage.

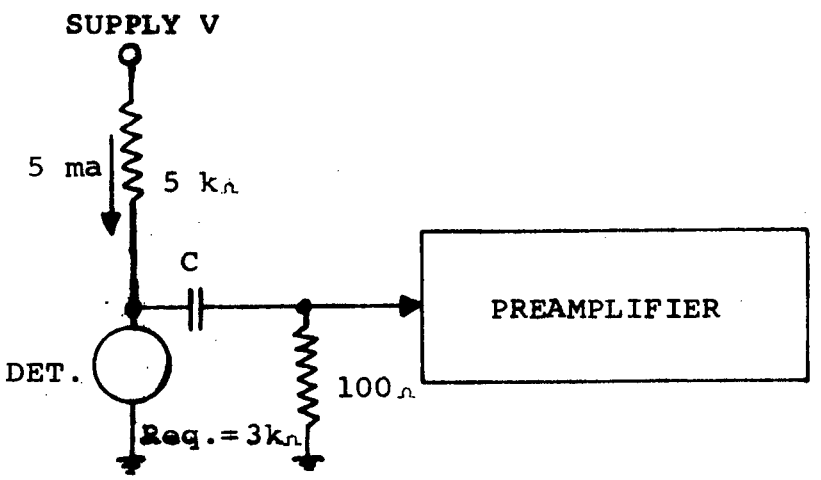

Figure 4-8 Typical IR Detector Bias Arrangement

4.7.3 CONCLUSIONS

The receiver preamplifier requirements for a coherent laser detection application have been discussed in detail. It was shown that the required noise figure (F) varies as a function of certain parameters (e.g., ρ_i, I_{DC}, η, and R_{IN}) and expressions were developed to analyze the problem. Some typical situations were evaluated and the results presented in Tables 4-3, 4-4, and 4-5.

Whenever conditions indicate that a particular noise figure is needed (Table 4-3, line 2, F = 5 dB), it should be emphasized that the system S/N would automatically be degraded by 3 dB if that particular F were used. This is so because preamplifier noise and shot noise were equated to calculate the values of F given in the tables. To preserve the S/N given by equation (4-3) would require preamplifier noise figures approximately 3 dB better than those given in the tables.

Basically, whenever $(\rho_i)^2 \times P_{LO}$ is sufficiently high, the receiver preamplifier should not be a limiting factor. However, a reasonable noise figure (5 dB) would probably be a minimum requirement. Preamplifier impedance matching, although not necessarily complicated, may be required in some designs.

SECTION 4 REFERENCE

1. Wind Velocity Measurements Report, No. R68-4197, 15 April 1968.

SECTION 5

AMPLIFIER GAIN ANALYSIS

5.1 INTRODUCTION

The analysis in this section attempts to determine what kind of gain, G(L,t), can be obtained from a CO_2 laser amplifier with a length L, a small signal gain coefficient g_o, a saturation parameter I_s, and a pulsed input intensity $I_{in}(t)$.

The analysis starts with the formulation of a set of N + 1 generalized rate equations which completely define the CO_2 laser amplifier system. These generalized equations are then reduced to a single gain-intensity time rate equation and the ramifications of the reduction are discussed. A gain-intensity length rate equation is then formulated and the two rate equations are solved to determine the gain, G(L,t), as a function of $I_{in}(t)$, g_o, I_s, L, and the inversion lifetime τ. Finally, the results of this analysis are applied to a CO_2 laser amplifier constructed at the Raytheon Research Division and compared to the experimentally obtained outputs from that amplifier.

5.2 THE CO_2 LASER RATE EQUATIONS

5.2.1 THE CO_2 LASER SYSTEM

CO_2 laser emission is the result of a population inversion established between the $(00^{\circ}1)$ and $(10^{\circ}0)$ vibrational energy levels. Each of these vibrational energy levels is made up of many rotational sublevels, each sublevel being characterized by a different value of the rotational quantum number J. The $(00^{\circ}1)$ vibrational level has rotational levels with odd values of J, whereas the $(10^{\circ}0)$ vibrational level has rotational levels with even (or zero) values of J.

Laser action between the $(00^{\circ}1)$ vibrational-rotational levels and the $(10^{\circ}0)$ vibrational-rotational levels occurs only on those transitions where the rotational quantum numbers of the $(00^{\circ}1)$ and $(10^{\circ}0)$ differ by ± 1. The laser transitions are labeled as being P branch transitions when $J_{001} - J_{100} = -1$, and as R branch transitions when $J_{001} - J_{100} = +1$. Individual transitions are generally specified by the J value of the lower laser level. Thus, P(20) corresponds to a P branch transition which terminates on a $(10^{\circ}0)$ rotational level with $J_{100} = 20$. Figure 5-1 shows a CO_2 energy level diagram and some P branch transitions.

The creation of an inversion between the $(00^{\circ}1)$ and $(10^{\circ}0)$ vibrational-rotational energy levels is a complex function of all the pumping and relaxation processes which take place in a CO_2 laser system. These processes include the subsequent:

1. Stimulated emission between the laser levels
2. Spontaneous emission on all possible transitions
3. Energy transfer induced by electrons colliding with molecules
4. Collision-induced energy transfer between vibrational energy levels of
   (a) The same vibrational mode and
   (b) Different vibrational modes
5. Collision-induced energy transfer between the vibrational modes and the translational mode
6. Collision-induced energy transfer between the rotational energy levels of the same vibrational level
7. Energy loss resulting from diffusion to the walls and the flowing gas exhaust

Some of the energy transfer dynamics of the CO_2 laser system are shown in Figure 5-2.

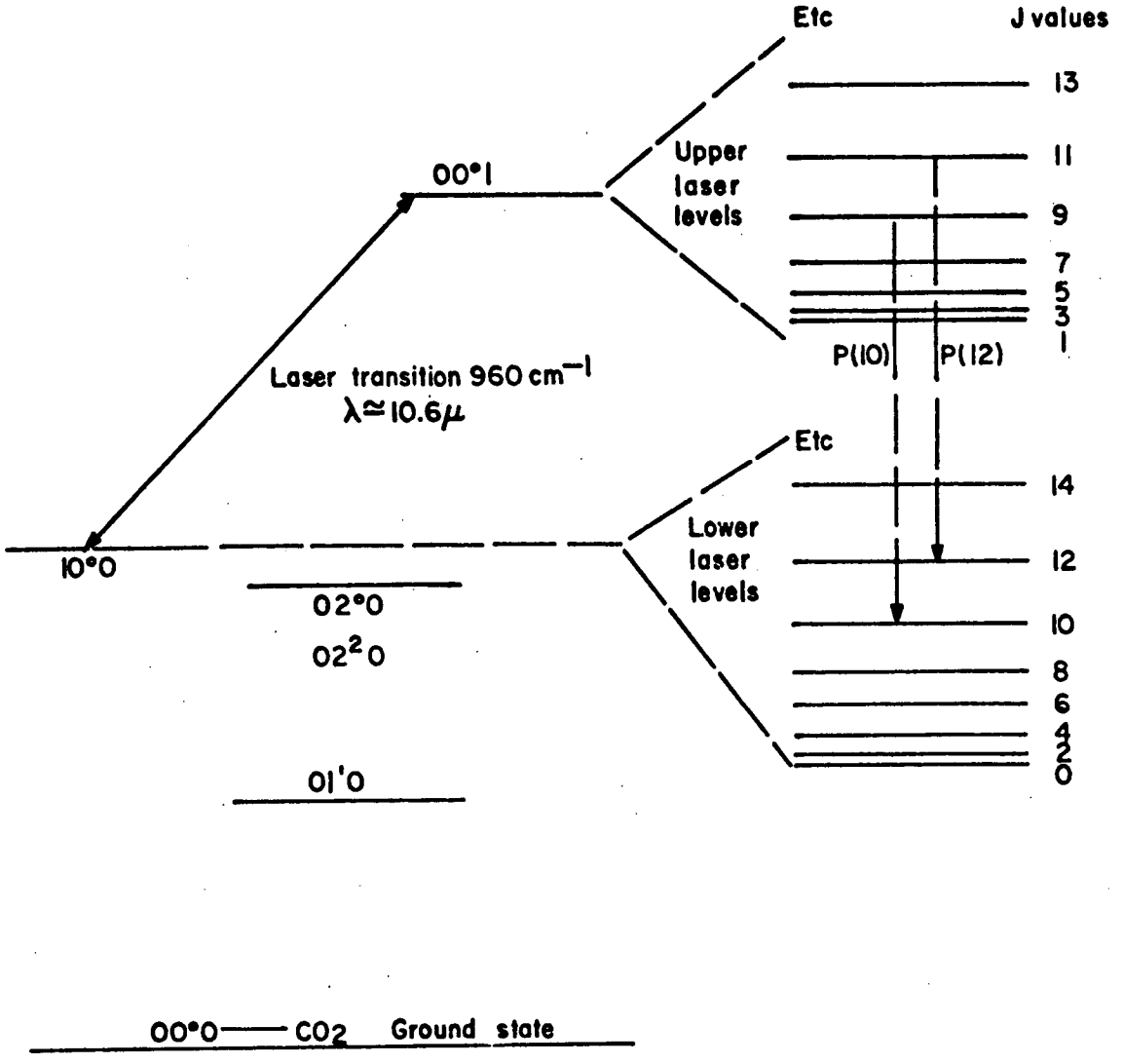

Figure 5-1 Vibrational-Rotational Energy Levels of CO_2 Involved in Laser Emission

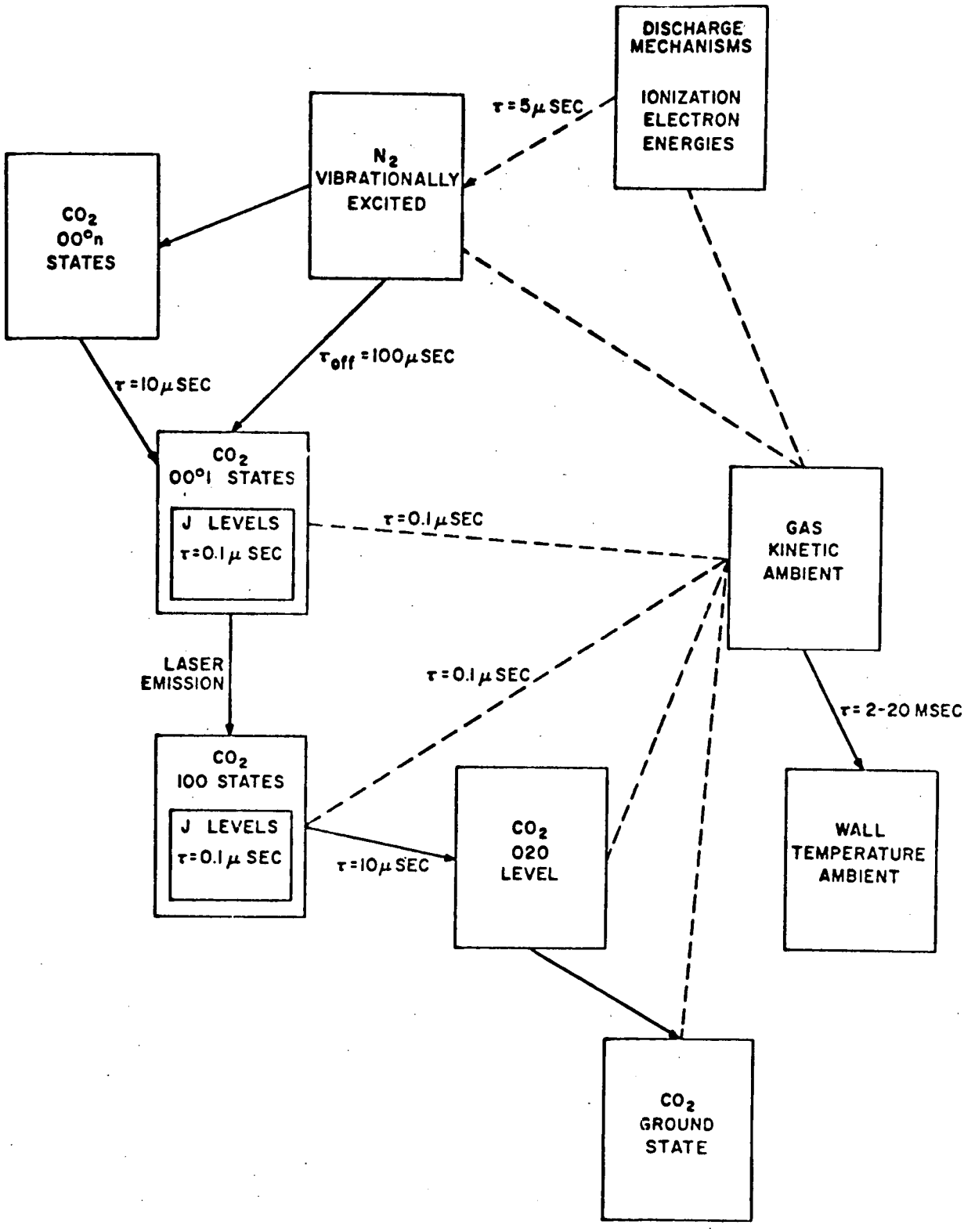

Figure 5-2 Molecular Level Dynamics in the CO_2 Laser (Schematic)

5.2.2 PROCESSES AFFECTING A PULSED AMPLIFIER

This analysis is directed at determining the gain of a laser amplifier for a pulsed input. The only energy transfer processes which could affect the gain of the amplifier are those which can occur in a time comparable to the length of the pulse. Thus, the singular processes which need to be considered are those which have time constants less than or comparable to the length of the pulse. Additionally, the processes must be able to affect the population density in the upper or lower laser levels.

For pulse lengths of less than 10-μsec duration, only four energy transfer processes need to be considered. They are:

1. Stimulated emission
2. Collision-induced energy transfer from the $(00^{\circ}n)$ vibrational energy levels to the $(00^{\circ}1)$ vibrational energy level
3. Collision-induced energy transfer from the $(00^{\circ}1)$ vibrational energy level to the $(02^{\circ}0)$ vibrational energy level
4. Collision-induced energy transfer between the rotational energy levels of the same vibrational level

5.2.2.1 Stimulated Emission

The rate at which stimulated emission occurs is a function of many parameters. Among the more important parameters are —

1. The population inversion density developed between the upper and lower laser levels,
2. The value of the Einstein B coefficient,
3. The frequency of the laser radiation,

4. The line shape of the transition defined by the upper and lower laser levels, and

5. The photon density of the laser radiation in the amplifier.

The stimulated emission process cannot be neglected as it is the mechanism which amplifies the input pulse. It directly affects, however, only two energy levels: those of the upper and lower laser levels.

5.2.2.2 Pumping of the $(00^{\circ}1)$ Vibrational Energy Level

It has been determined that intramode vibrational relaxation of the $(00^{\circ}n)$ vibrational levels takes place with a time constant of 10 μsec.[1] Relaxation from the upper $(00^{\circ}n)$ levels could provide a source for replenishing the depleted upper laser level in the $(00^{\circ}1)$ vibrational level.

Also, it has been estimated that there is 8.5 percent of the total CO_2 population in the $(00^{\circ}1)$ levels just prior to laser oscillation.[2] It can be estimated that there is only 1 percent of the total CO_2 population in the higher $(00^{\circ}n)$ vibrational levels. Therefore, relaxation of the $(00^{\circ}n)$ levels into the $(00^{\circ}1)$ could replenish less than 10 percent of the $(00^{\circ}1)$ population in 10 μsec. Hence this process will be neglected in the analysis.

5.2.2.3 Relaxation of the $(10^{\circ}0)$ Vibrational Level

The $(10^{\circ}0)$ and $(02^{\circ}0)$ vibrational energy levels are linked by a Fermi resonance, and hence, the relaxation time for energy flow between these two levels is quite fast (i.e. 10 μsec). Since the $(10^{\circ}0)$ vibrational level contains the lower laser level, this relaxational process could provide an effective method for removing population from the lower laser level. However, relaxation from the $(02^{\circ}0)$ to the ground state takes place through a slow vibra-

tional-translational energy exchange process, which negates the effect of the fast Fermi resonance relaxation. Thus, this process is not included in the analysis.

5.2.2.4 Rotational Relaxation

Rotational relaxation is a collision-induced energy transfer process which forces the population densities of the closely spaced rotational sublevels of a vibrational level into a Boltzmann distribution. The characteristic temperature of the distribution is the gas kinetic temperature of the discharge. This temperature is typically in the 350°K to 400°K range for a flowing, liquid-cooled system.

Rotational relaxation is a very fast process; the time constant is in the 10 nsec to 100 nsec range. Thus, during a 1.0- to 10-μsec pulse, ($00^{\circ}1$) rotational levels pour their population into the depleted upper laser level, and ($10^{\circ}0$) rotational levels take population from the overfilled lower laser level. Essentially, the total populations of the ($00^{\circ}1$) and ($10^{\circ}0$) vibrational levels are utilized. Since approximately 50 rotational lines are involved, the population available to the laser levels can increase by a factor of 10 to 100.

This process must be included in the analysis, and it affects every rotational level in the ($00^{\circ}1$) and ($10^{\circ}0$) vibrational levels. However, a preliminary theoretical analysis by Tang[3] indicates that rotational quantum number changes of $\Delta J = \pm 2$ are 10 to 100 times more probable than rotational quantum number changes of $\Delta J = \pm 4$ (or greater). Hence, rotational energy flows basically to adjacent rotational lines. This last fact is included as an assumption in this analysis.

5.2.3 THE TIME-RATE EQUATIONS

The mechanisms of energy transfer can be described in terms of the flow of population between energy levels in the CO_2 system. The population flow can be represented by a set of time-rate equations.

One rate equation must be formulated for every energy level which has a significant change in population during the time of the pulse. If stimulated emission and "adjacent line" rotational relaxation are assumed to the only energy transfer processes of consequence, then rate equations must be determined for every rotational level in the $(00^{\circ}1)$ and $(10^{\circ}0)$ vibrational levels.

If laser oscillation takes place on the P(20) transition, the rate equations for a CO_2 pulsed amplifier system are given in equation (5-1).

$$\frac{\partial N_0}{\partial t} = N_2 W_{2,0} - N_0 W_{0,2}$$

$$\frac{\partial N_1}{\partial t} = N_3 W_{3,1} - N_1 W_{1,3}$$

$$\frac{\partial N_J}{\partial t} = N_{J+2} W_{J+2,J} + N_{J-2} W_{J-2,J} - N_J (W_{J,J+2} + W_{J,J-2})$$

$$- \left[N_J - (g_J/g_{J+1}) N_{J+1} \right] B\, h\nu f(\nu-\nu_o) \Phi\, \delta(J-19)$$

$$- \left[N_J - (g_J/g_{J-1}) N_{J-1} \right] B\, h\nu f(\nu-\nu_o) \Phi\, \delta(J-20)$$

$$J = 2, 3, 4, \ldots, N-2$$

$$\frac{\partial N_{N-1}}{\partial t} = N_{N-3} W_{N-3,N-1} - N_{N-1} W_{N-1,N-3}$$

$$\frac{\partial N_N}{\partial t} = N_{N-2} W_{N-2,N} - N_N W_{N,N-2} \qquad (5\text{-}1)$$

where

N_J is the population density in the rotational level defined by the rotational quantum number J. [Note that rotational levels in the $(00^{\circ}1)$ vibrational level have odd values of J, and that rotational

levels in the ($10^{o}0$) vibrational level have even (or zero) values of J.]

$W_{i,j}$ is the rate of the transition from the rotational level i to the adjacent rotational level j.

B is the Einstein coefficient for stimulated emission from one energy level to a lower energy level.

$h\nu$ is the energy per photon of radiation with a frequency ν.

Φ is the density of photons with frequency ν in the amplifier.

$\delta(J-k)$ is the Kronecker delta function which has a value of zero when $J \neq k$ and a value of unity when $J = k$.

$f(\nu-\nu_o)$ is the lineshape factor for laser oscillation at a frequency ν on a transition with a center frequency ν_o.

N is the J value of the highest rotational energy level which contributes a significant population to the laser levels.

g_J is the number of degeneracies in the rotational level defined by rotational quantum number J. g_J has a value of $2J + 1$.

These N + 1 time-rate equations govern the flow of population between the rotational levels of the ($00^{o}1$) and ($10^{o}0$) vibrational levels.

5.2.4 REDUCTION OF THE TIME-RATE EQUATIONS

If the rotational transition rates, the stimulated emission terms, the time variation of the photon density, and the initial populations of the rotational levels are all known, the N + 1 time-rate equations can be solved to determine the rotational populations as a function of time. However, explicit values for the rotational transition rates, the initial rotational populations, and the time variation of the photon density are not known.

Nevertheless, the N + 1 time-rate equations can be reduced to a single time-rate equation. The reduction is justified by the extremely fast relaxation rate of the rotational levels. The fast relaxation rate links the rotational sublevels of a vibrational level so efficiently that the sublevels can be considered a single level.

This single level contains the population of the entire vibrational level and has a relaxation rate equal to that of the vibrational level. The population in this level is at least 15 times larger than the population in any individual rotational sublevel. Yet, the degeneracies and width of the single level remain the same as those in the original rotational level. Likewise, the spontaneous and stimulated emission rates from the single level must remain the same as from the original rotational level.

Considering the rotational sublevels to be a single level allows the N + 1 time-rate equation to be reduced to two time-rate equations. These two equations have the form shown below:

$$\frac{\partial N_{001}}{\partial t} = - \left[N_{001} - (g_{19}/g_{20})N_{100}\right]\frac{Bh\nu f(\nu-\nu_o)}{\Omega} \Phi \qquad (5\text{-}2)$$

$$\frac{\partial N_{100}}{\partial t} = - \left[N_{100} - (g_{20}/g_{19})\ N_{100}\right]\frac{Bh\nu f(\nu-\nu_o)}{\Omega} \Phi \qquad (5\text{-}3)$$

where

N_{001} is the population density in the $(00^{o}1)$ vibrational level

N_{100} is the population density in the $(10^{o}0)$ vibrational level

Ω is the ratio N_{001}/N_{19} and is approximately equal to the number of rotational levels with significant population in the $(00^{o}1)$ vibrational level. It is assumed that N_{001}/N_{19} is approximately equal to N_{100}/N_{20}.

The factor Ω is required to make the stimulated emission rate of the two level system the same as that of the N + 1 level system.

A further reduction can be made by multiplying equation (5-3) by a factor (g_{19}/g_{20}) and subtracting it from equation (5-2) to yield

$$\frac{\partial \Delta N}{\partial t} = - \frac{2 \Delta N B h\nu f(\nu-\nu_o) \Phi}{\Omega} \qquad (5\text{-}4)$$

where ΔN is the population inversion density between the $(00^{o}1)$ and $(10^{o}0)$ vibrational levels as defined by the equation

$$\Delta N = N_{001} - (g_{19}/g_{20}) N_{100} \qquad (5\text{-}5)$$

There are two important consequences of the reduction of the N + 1 time-rate equations into a single equation. First, the absolute magnitude of the population available to the laser levels is not as important as the difference in population between the two laser levels. Second, the inclusion of the factor Ω reduces the cross-section for stimulated emission by the ratio N_{001}/N_{19}.

5.3 FORMULATION OF THE GAIN-INTENSITY TIME-RATE EQUATION

5.3.1 INTRODUCTION

The formulation of the gain-intensity time-rate equation requires that an explicit form of gain be used in conjunction with equation (5-4). It will be shown that the formulation explicitly defines the inversion lifetime-saturation parameter product, τI_s.

5.3.2 GAIN IN LASER MEDIA

There are basically only two types of laser media: homogeneously broadened media and inhomogeneously broadened media. The gain coefficient, g, is approximately the same for both types of media (the form of lineshape factor being the only difference). However, the gain coefficient saturates differently in the two media.

5.3.2.1 Homogeneous Laser Media

In a homogeneously broadened laser medium all the molecules are affected in the same manner by laser radiation and are said to belong to the same class. The lineshape of homogeneously broadened transitions has the Lorentzian form

$$f_H(\nu-\nu_o) = \frac{(\Delta\nu/2\pi)}{(\nu-\nu_o)^2 + (\Delta\nu/2)^2} \tag{5-6}$$

where $\Delta\nu$ is the full width of the lineshape function at one-half its maximum value.

The gain coefficient for laser oscillation in a homogeneously broadened medium has the form

$$g = \frac{\Delta N\, c^2\, f_H(\nu-\nu_o)}{8\pi\, \nu^2\, t_s} \tag{5-7}$$

The laser gain in a homogeneously broadened medium is often expressed in terms of the small signal gain coefficient g_o, the laser intensity I, and a saturation parameter I_s. If these parameters are used the gain has the form

$$g = g_o / \left[1 + (I/I_s)\right] \tag{5-8}$$

where

$$g_o = \frac{\Delta N^o\, c^2\, f_H(\nu-\nu_o)}{8\pi\, \nu^2\, t_s} \tag{5-9}$$

$$I = \Phi\, h\nu c \tag{5-10}$$

$$I_s = \frac{8\pi\, h\nu^3\, t_s}{c^2(\tau_1+\tau_2)\, f_H(\nu-\nu_o)} \tag{5-11}$$

where

ΔN^o is the maximum population density obtainable in the absence of stimulated emission

c is the speed of light in the medium

t_s is the spontaneous emission lifetime of the laser transition

τ_1 is the relaxation lifetime of the upper laser level

τ_2 is the degeneracy adjusted relaxation lifetime of the lower laser level

and all other terms are as previously defined.

The saturation terms in the denominator of equation (5-8) are required by the law of conservation of energy. The net energy removed from an amplifier can never exceed the energy supplied to that amplifier. If the gain did not saturate, it would be possible to build an amplifier where the net output energy exceeded the energy supplied to the amplifier.

When the pressure (or collision) broadening determines the width of a transition, the transition is said to be homogeneously broadened.

5.3.2.2 Inhomogeneous Laser Media

In an inhomogeneously broadened laser medium the molecules are separated into different classes which are affected differently by laser radiation. The lineshape of inhomogeneously broadened transitions has the Gaussian form

$$f_I(\nu-\nu_o) = \frac{2}{\Delta\nu_D}\sqrt{\frac{Ln2}{\pi}} \exp\left[-\left(\frac{2(\nu-\nu_o)}{\Delta\nu_o}\right)^2 Ln2\right] \qquad (5\text{-}12)$$

where $\Delta\nu_D$ is the full width of the lineshape function at one-half its maximum value.

Each of the classes of molecules in the inhomogeneous media saturates as $\left[1 + (I/I_s)\right]^{-1}$; however, there are $\left[1 + (I/I_s)\right]^{\frac{1}{2}}$ classes affected by the laser radiation. Hence, the gain coefficient for CW laser oscillation in an inhomogeneously broadened medium is of the form

$$g = g_o \left[1 + (I/I_s)\right]^{-\frac{1}{2}} \tag{5-13}$$

where

$$g_o = \frac{\Delta N^o c^2 \, f_I(\nu-\nu_o)}{8\pi \, \nu^2 \, t_s} \tag{5-14}$$

$$I_s = \frac{8\pi \, h\nu^3 \, t_s}{c^2(\tau_1+\tau_2) \, f_H(0)} \tag{5-15}$$

$$I = \Phi \, h\nu c \tag{5-16}$$

When Doppler broadening determines the width of a transition, the transition is said to be inhomogeneously broadened.

5.3.2.3 Application to a CO_2 Laser Amplifier

The Doppler and pressure broadened widths of a 10.6μ CO_2 laser amplifier operating at a pressure of 10 torr and a gas kinetic temperature of 350°K are both about 55 MHz. Since these operating conditions are very close to the ones actually used, it is difficult to tell if the 10.6μ P(20) CO_2 transition is homogeneously or inhomogeneously broadened.

In this analysis it is assumed that the CO_2 10.6μ transition is homogeneously broadened. Since homogeneously broadened media saturate faster than inhomogeneously broadened media, the analysis should produce a conservative estimate of the gain through a pulsed CO_2 laser amplifier.

Another factor which must be taken into account is the highly efficient coupling of the rotational sublevels. It was previously

shown that the increased population requires a decrease in the stimulated emission cross-section by a factor Ω. Since the stimulated emission cross-section is related to the spontaneous emission lifetime through the Einstein B coefficient, the factor Ω must also be included in the gain equations for a CO_2 laser amplifier. Thus, equation (5-7) must be rewritten into the form

$$g = \frac{\Delta N \, c^2 \, f_H(\nu-\nu_o)}{8\pi \, \nu^2 \, t_s \, \Omega} \tag{5-17}$$

Since the spontaneous lifetime also appears in the saturation parameter, equation (5-11) must also be rewritten into the form

$$I_s = \frac{8\pi \, h\nu^3 \, t_s \, \Omega}{c^2(\tau_1+\tau_2) \, f_H(\nu-\nu_o)} \tag{5-18}$$

5.3.3 THE GAIN-INTENSITY TIME RATE EQUATION

If it is assumed that the rate of stimulated emission in the laser amplifier dominates over the rate of all other pumping and relaxation processes, the equations (5-4) and (5-17) can be used to determine the time rate of change in the gain of the amplifier. The partial derivative of the gain with respect to time can be written

$$\frac{\partial g}{\partial t} = \frac{\partial g}{\partial \Delta N} \cdot \frac{\partial \Delta N}{\partial t} \tag{5-19}$$

The derivative $(\partial \Delta N/\partial t)$ is given in equation (5-4), and the derivative $(\partial g/\partial_\Delta N)$ can be obtained from equation (5-17). Thus, the time rate of change in the gain evaluates to

$$\frac{\partial g}{\partial t} = -\, 2 \, Bh\nu \, f_H(\nu-\nu_o) \left[\frac{\Delta N \, c^2 \, f(\nu-\nu_o)}{8\pi \, h\nu^3 \, t_s \, \Omega}\right] \Phi \tag{5-20}$$

If equations (5-17) and(5-10) are used in equation (5-20), the derivative $(\partial g/\partial t)$ becomes

$$\frac{\partial g}{\partial t} = - \left[\frac{2B\ f_H(\nu-\nu_o)}{c}\right] gI \qquad (5\text{-}21)$$

The Einstein B coefficient for stimulated emission in CO_2 (reduced by a factor Ω) is related to the spontaneous emission lifetime t_s between the two laser levels by the well-known equation

$$B = (c^3/8\pi h\nu^3 t_s \Omega) \qquad (5\text{-}22)$$

Thus, equation (5-21) becomes

$$\frac{\partial g}{\partial t} = - \left[\frac{c^2\ f_H(\nu-\nu_o)}{4\pi\ h\nu^3 t_s \Omega}\right] gI \qquad (5\text{-}23)$$

A comparison of the bracketed part of equation (5-23) and equation (5-18) indicates that equation (5-23) can be reduced to

$$\frac{\partial g}{\partial t} = - \frac{gI}{\tau I_s} \qquad (5\text{-}24)$$

where I_s is given in equation (5-18) and τ is the inversion lifetime and has a value given by

$$\tau = \frac{\tau_1 + \tau_2}{2} \qquad (5\text{-}25)$$

Equation (5-24) is one of the gain-intensity equations which must be solved to determine the gain of a CO_2 pulsed laser amplifier.

5.4 FORMULATION OF THE GAIN-INTENSITY LENGTH RATE EQUATION

The formulation of the second gain-intensity equation is accomplished using the definition of the gain coefficient of a laser amplifier. By definition the gain coefficient is equal to the fractional increase in laser intensity per unit length of amplifier. Thus,

$$g \equiv \frac{1}{I} \cdot \frac{\partial I}{\partial z} \tag{5-26}$$

Equation (5-26) can be rearranged to give the gain-intensity length rate equation

$$\frac{\partial I}{\partial z} = gI \tag{5-27}$$

5.5 THE SOLUTION OF THE GAIN-INTENSITY EQUATIONS

5.5.1 THE SOLUTION

In order to solve the two gain-intensity equations shown below

$$\frac{\partial g}{\partial t} = - \frac{gI}{\tau I_s} \tag{5-28}$$

$$\frac{\partial I}{\partial z} = gI \tag{5-29}$$

a function ψ is defined such that

$$g = \frac{\partial \psi}{\partial z} \tag{5-30}$$

$$I = - \tau I_s \frac{\partial \psi}{\partial t} \tag{5-31}$$

Substituting equations (5-30) and (5-31) into equation (5-28) yields

$$\frac{\partial g}{\partial t} = \left(\frac{\partial \psi}{\partial t}\right)\left(\frac{\partial \psi}{\partial z}\right) \tag{5-32}$$

Differentiating equation (5-30) with respect to time gives

$$\frac{\partial g}{\partial t} = \frac{\partial^2 \psi}{\partial z \partial t} \tag{5-33}$$

Equating equations (5-32) and (5-33) produces the equation

$$\frac{\partial^2 \psi}{\partial z \partial t} = \left(\frac{\partial \psi}{\partial z}\right)\left(\frac{\partial \psi}{\partial t}\right) \tag{5-34}$$

It is easily shown that equation (5-34) has a solution of the form

$$\psi = - \text{Ln}\left[F(z) + K(t)\right] \tag{5-35}$$

where $F(z)$ is any function of z and $K(t)$ is any function of t.

Substituting equation (5-35) into equations (5-30) and (5-31) gives the gain and intensity in terms of $F(z)$ and $K(t)$. Thus,

$$g = - \frac{\partial F(z)/\partial z}{F(z) + K(t)} \tag{5-36}$$

$$I = \frac{\tau I_s \left[\partial K(t)/\partial t\right]}{F(z) + K(t)} \tag{5-37}$$

In order to evaluate the explicit form of the functions $F(z)$ and $K(t)$ two boundary conditions must be used. The most convenient boundary conditions to use are given below:

$$I(z = 0, t) = I_{in}(t) \tag{5-38}$$

$$g(z, t = 0) = g_o(z) \tag{5-39}$$

Equation (5-38) describes the intensity of the laser radiation entering the amplifier as a function of time, and equation (5-39) describes the gain in the laser amplifier in the absence of laser radiation as a function of length.

Applying the boundary conditions of equations (5-38) and (5-39) to equations (5-37) and (5-36) yields

$$g_o(z) = - \frac{\partial F(z)/\partial z}{F(z) + K(0)} \tag{5-40}$$

$$I_{in}(t) = \frac{\tau I_s \left[\partial K(t)/\partial t\right]}{F(0) + K(t)} \tag{5-41}$$

However, at $t = 0$

$$\frac{\partial F(z)}{\partial z} = \frac{\partial}{\partial z}\left[F(z) + K(0)\right] \tag{5-42}$$

and at $z = 0$

$$\frac{\partial K(t)}{\partial t} = \frac{\partial}{\partial t}\left[F(0) + K(t)\right] \tag{5-43}$$

Thus, equations (5-40) and (5-41) can be rewritten

$$\frac{\partial\left[F(z) + K(0)\right]}{F(z) + K(0)} = - g_o(z)\,\partial z \tag{5-44}$$

$$\frac{\partial\left[F(0) + K(t)\right]}{F(0) + K(t)} = \frac{I_{in}(t)\,\partial t}{\tau I_s} \tag{5-45}$$

Integrating both sides of equation (5-44) from a length $z = 0$ to a length $z = z$ yields

$$\mathrm{Ln}\left[\frac{F(z)+K(0)}{F(0)+K(0)}\right] = - \int_0^z g_o(z')\,dz' \tag{5-46}$$

Integrating both sides of equation (5-45) from a time t = 0 to a time t = t yields

$$\text{Ln}\left[\frac{F(0) + K(t)}{F(0)+K(0)}\right] = \frac{1}{\tau I_s} \int_0^t I_{in}(t')dt' \qquad (5\text{-}47)$$

Taking the exponential of both sides of equations (5-46) and (5-47) gives

$$\frac{F(z) + K(0)}{F(0) + K(0)} = \exp\left[-\int_0^z g_o(z')dz'\right] \qquad (5\text{-}48)$$

$$\frac{F(0) + K(t)}{F(0) + K(0)} = \exp\left[\frac{1}{\tau I_s} \int_0^t I_{in}(t')dt'\right] \qquad (5\text{-}49)$$

Adding equations (5-48) and (5-49) yields

$$\frac{F(z) + K(t)}{F(0) + K(0)} = \exp\left[-\int_0^z g_o(z')dz'\right] + \exp\left[\frac{1}{\tau I_s} \int_0^t I_{in}(t')dt'\right] - 1 \qquad (5\text{-}50)$$

According to Leibniz' formula the differentiation of an integral is given by the equation

$$\frac{\partial}{\partial\alpha} \int_{u_o(\alpha)}^{u_1(\alpha)} f(x, \alpha)dx = f(x, u_1)\frac{du_1}{d\alpha} - f(x, u_o)\frac{du_o}{d\alpha} + \int_{u_o(\alpha)}^{u_1(\alpha)} \frac{\partial f}{\partial\alpha}(x,\alpha)\,dx \qquad (5\text{-}51)$$

Applying Leibniz' formula to differentiate equation (5-49) gives

$$\frac{\partial K(t)/\partial t}{F(0) + K(0)} = \frac{I_{in}(t)}{\tau I_s} \exp\left[\frac{1}{\tau I_s}\int_0^t I_{in}(t')\,dt'\right] \qquad (5\text{-}52)$$

Dividing equation (5-52) by equation (5-50) and substituting the result into equation (5-37) yields the solution given below

$$I(z,t) = \frac{I_{in}(t)\exp\left[\int_0^t \frac{I_{in}(t')\,dt'}{\tau I_s}\right]}{\exp\left[\int_0^t \frac{I_{in}(t')dt'}{\tau I_s}\right] + \exp\left[-\int_0^z g_o(z')dz'\right] - 1} \qquad (5\text{-}53)$$

Since the gain of a laser amplifier is defined as the ratio of the power out to the power in, equation (5-53) can be used to determine the gain of a CO_2 pulsed laser amplifier. Provided that the input and output beams have the same cross-sectional area the gain of an amplifier of length L is given by the expression

$$G(L,t) = \frac{1}{1 + \exp\left[-\int_0^L g_o(z)dz - \int_0^t \frac{I_{in}(t')\,dt'}{\tau I_s}\right] - \exp\left[-\int_0^t \frac{I_{in}(t')dt'}{\tau I_s}\right]} \qquad (5\text{-}54)$$

The inversion lifetime-saturation parameter product τI_s can be seen from equations (5-23) and (5-24) to have a value

$$\tau I_s = \frac{4\pi h\nu^3\, t_s \Omega}{c^2\, f_H(\nu-\nu_o)} \qquad (5\text{-}55)$$

5.5.2 APPLICATION OF THE SOLUTION TO A CO_2 PULSED LASER AMPLIFIER

Equation (5-54) can be applied directly to determine the gain of a pulsed CO_2 laser amplifier as a function of the amplifier length and the input waveform.

The inversion lifetime-saturation parameter product is a constant whose value is determined by the frequency of oscillation and the linewidth of the transition. If the input pulse oscillates at the linecenter frequency ν_o on a transition with a linewidth $\Delta\nu$, the inversion lifetime-saturation parameter product has the form

$$\tau I_s = \frac{2\pi^2 h\nu_o^3 t_s \Omega \Delta\nu}{c^2} \qquad (5\text{-}56)$$

If the following values are used

$$\nu_o = 2.83 \times 10^{13} \text{ Hz}$$
$$h = 6.625 \times 10^{-34} \text{ joule-sec}$$
$$c = 3.00 \times 10^{10} \text{ cm/sec}$$
$$t_s = 6.15 \text{ sec}^{(4)}$$
$$\Omega = 100^{(5)}$$
$$\pi = 3.14$$
$$\Delta\nu = 6.00 \times 10^{7} \text{ Hz}$$

then τI_s has a value of

$$\tau I_s = 1.22 \times 10^{-2} \text{ joules/cm}^2 \qquad (5\text{-}57)$$

Generally, the small signal gain coefficient $g_o(z)$ is a constant over the length parameter z. This fact can be used to simplify equation (5-54).

Equation (5-54) can break down for extremely high gain systems by generating output pulses with rise-times in excess of the limit imposed by the bandwidth of the system. However, only the output intensity waveform as a function of time is affected. The energy content of the pulses should remain unchanged.

5.6 CORRELATION OF THEORETICAL AND EXPERIMENTAL RESULTS

5.6.1 EXPERIMENTAL RESULTS

An in-line CO_2 laser amplifier, 6 m in length, was constructed at the Raytheon Research Division. This amplifier, which is described in detail in Section 6, produced the pulses shown in Figure 5-3.

The modulation on (and following) the pulses in Figure 5-3 was caused by ringing on the input pulse from a Ga:As modulator. Since both the modulation and the pulse formed by modulator were amplified, there is some question about how much of the output energy is in the pulse and how much is in the modulation. However, if the pulses in Figure 5-3 represent typical output pulses, and if it is assumed that the modulation for both pulses falls exponentially with the same time constant, the peak power, the energy content, and the modulation time constant can be determined for each pulse. The results of such a calculation are shown in Table 5-1.

TABLE 5-1
DATA FOR PULSES SHOWN IN FIGURE 5-3

Pulse Duration	0.5 μsec	2.0 μsec
Energy in Pulse	3.9 mJ	15.1 mJ
Peak Pulse Power	10.2 kW	12.3 kW
Energy in Modulation	14.1 mJ	9.9 mJ
Modulation Time Constant	19.3 μsec	19.3 μsec

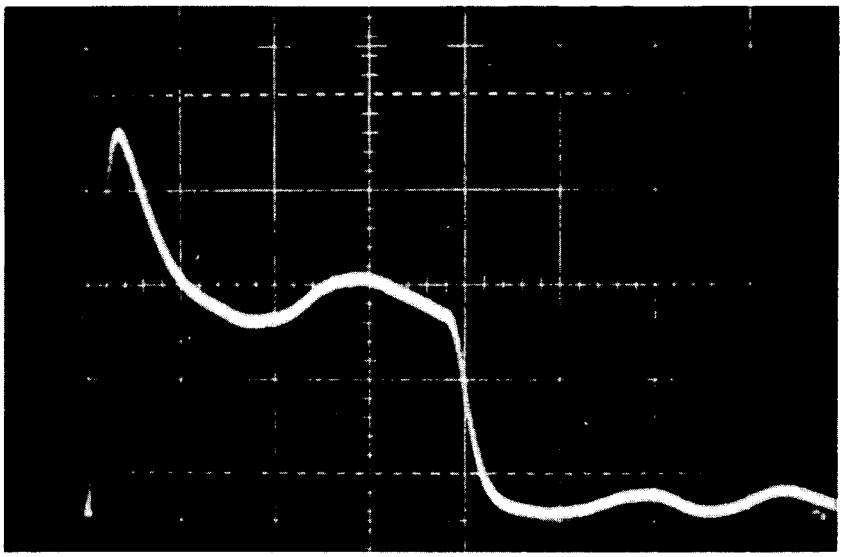

Amplifier Output

Average Output Power	2.5 w
Input Power	2.0 w
Pulse Rate	100 pps
Sweep Speed	0.5 μsec/Div.

Reproduced from best available copy.

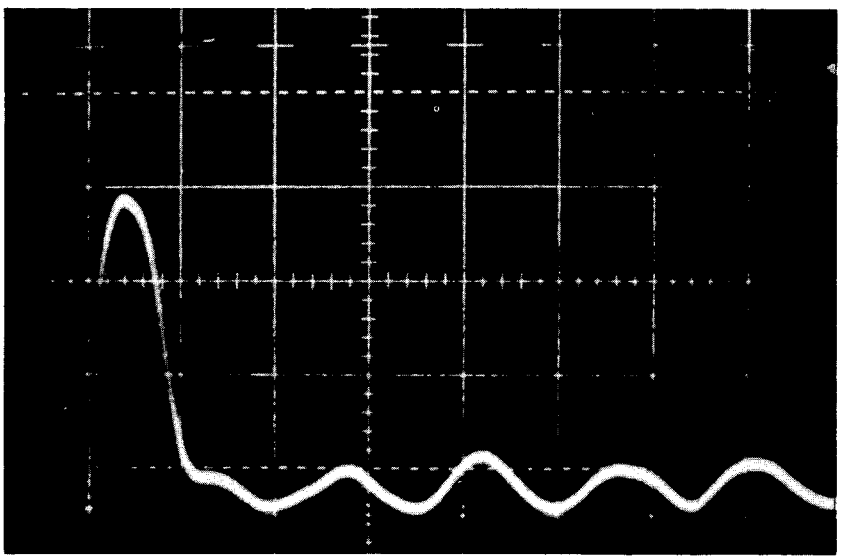

Amplifier Output

Average Output Power	1.8 w
Input Power	2.0 w
Pulse Rate	100 pps
Sweep Speed	0.5 μsec/Div.

Figure 5-3 Output Pulses from a 6-m In-Line CO_2 Laser Amplifier

Since the input and output pulse waveforms are known as a function of time, the gain of the experimental pulsed laser amplifier can be determined as a function of time.

5.6.2 CORRELATION OF RESULTS

If the gain of the experimental system and the total input energy density can be determined at two different times during the pulse, equation (5-54) can be used to determine experimental values for the small signal gain coefficient g_o and the inversion lifetime-saturation parameter product τI_s. Provided that the gain of the system is always greater than 100, it can be shown that τI_s, and g_o have the form

$$\tau I_s = \frac{G'(L,t_1)\ G'(L,t_2)\left[E_{in}(t_2) - E_{in}(t_1)\right]}{G'(L,t_1) - G'(L,t_2)} \tag{5-58}$$

$$g_o = \frac{1}{L} \mathrm{Ln}\left[\frac{\tau I_s \cdot G'(L,t_1)}{\tau I_s - E_{in}(t_1)G'(L,t_1)}\right] \tag{5-59}$$

where $G'(L,t)$ is the experimental gain from an amplifier of length L at a time t, and $E_{in}(t)$ is the input energy density at time t and is defined by the expression

$$E_{in}(t) = \int_o^t I_{in}(t')\ dt' \tag{5-60}$$

If the 2.0 μsec pulse in Figure 5-3 is used in such a calculation, g_o and τI_s have the experimental values

$$(g_o)_{ex} = 1.47\ m^{-1} \tag{5-61}$$

$$(\tau I_s)_{ex} = 2.34 \times 10^{-2}\ \text{joule/cm}^2 \tag{5-62}$$

The small signal gain coefficient is close to values appearing in the literature (see Reference 2 for instance). The experimental value for τI_s should be compared to the theoretical value calculated in equation (5-57). The experimental and theoretical values for τI_s differ by about a factor of two. This margin of error does not seem extreme since values for Ω and spontaneous emission lifetime, t_s, given in the literature can vary by a factor of two.

The final task in the correlation of experimental and theoretical results is to use equation (5-54) to generate an output pulse which can be compared to the 2.0 μsec pulse in Figure 5-3. The results are shown in Figure 5-4.

The two theoretical output waveforms in Figure 5-4 were obtained by substituting values for $g_o(z)$, $I_{in}(t)$, τI_s, and L into equation (5-53) and solving for the intensity $I(L,t)$ as a function of time. The length of the amplifier was 6 m, and the input waveform $I_{in}(t)$ is shown in Figure 5-5. Both theoretical waveforms were generated by using the small signal gain coefficient calculated in equation (5-61).

One theoretical waveform was generated using the theoretical value for τI_s given in equation (5-57). Another theoretical waveform was generated using the experimentally calculated value for τI_s given in equation (5-62).

The third waveform shown in Figure 5-4 is the experimentally obtained output from the amplifier, and is the same as the 2.0 μsec radiation pulse shown in Figure 5-3.

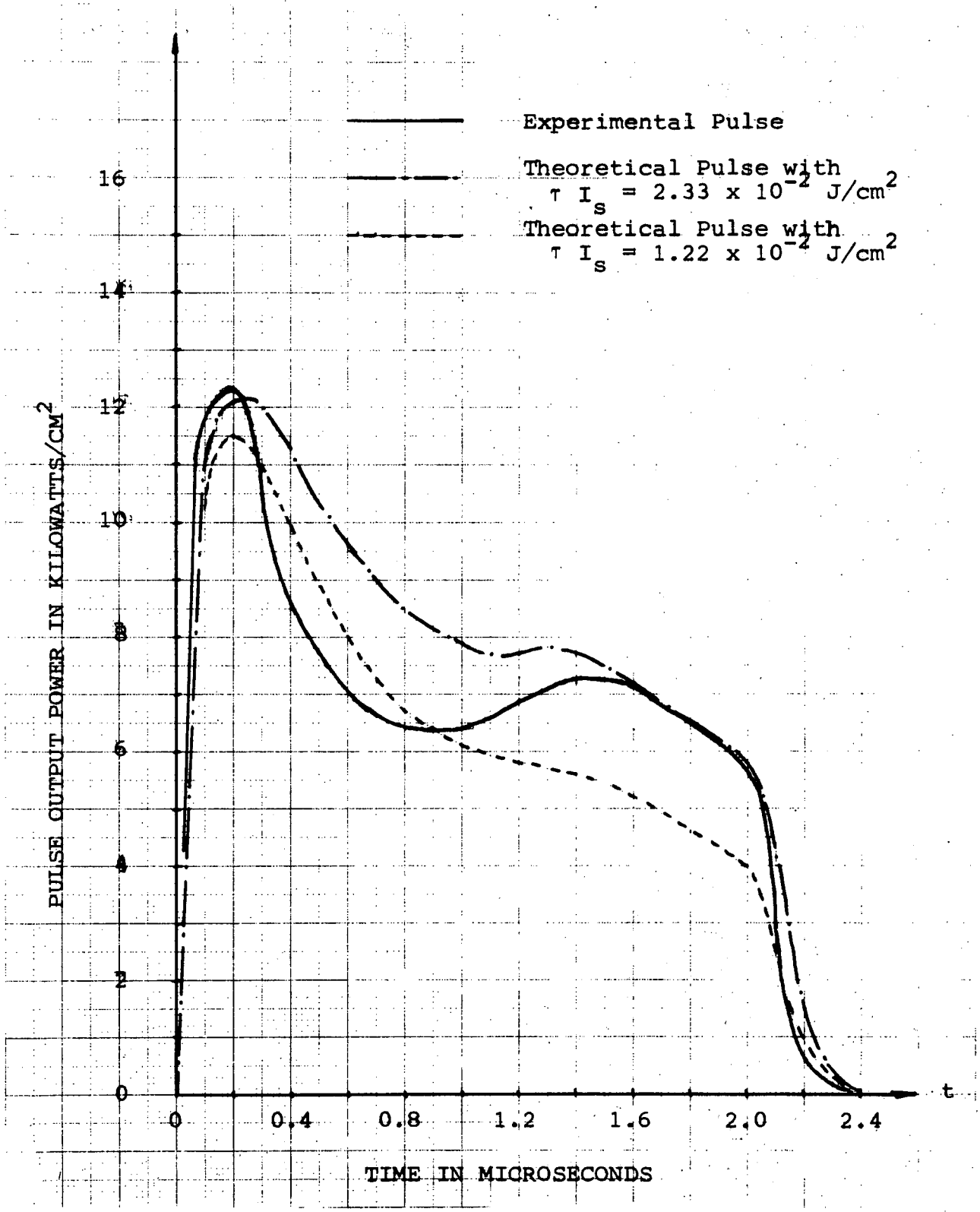

Figure 5-4 A Comparison of Experimentally and Theoretically Obtained Pulse Waveforms

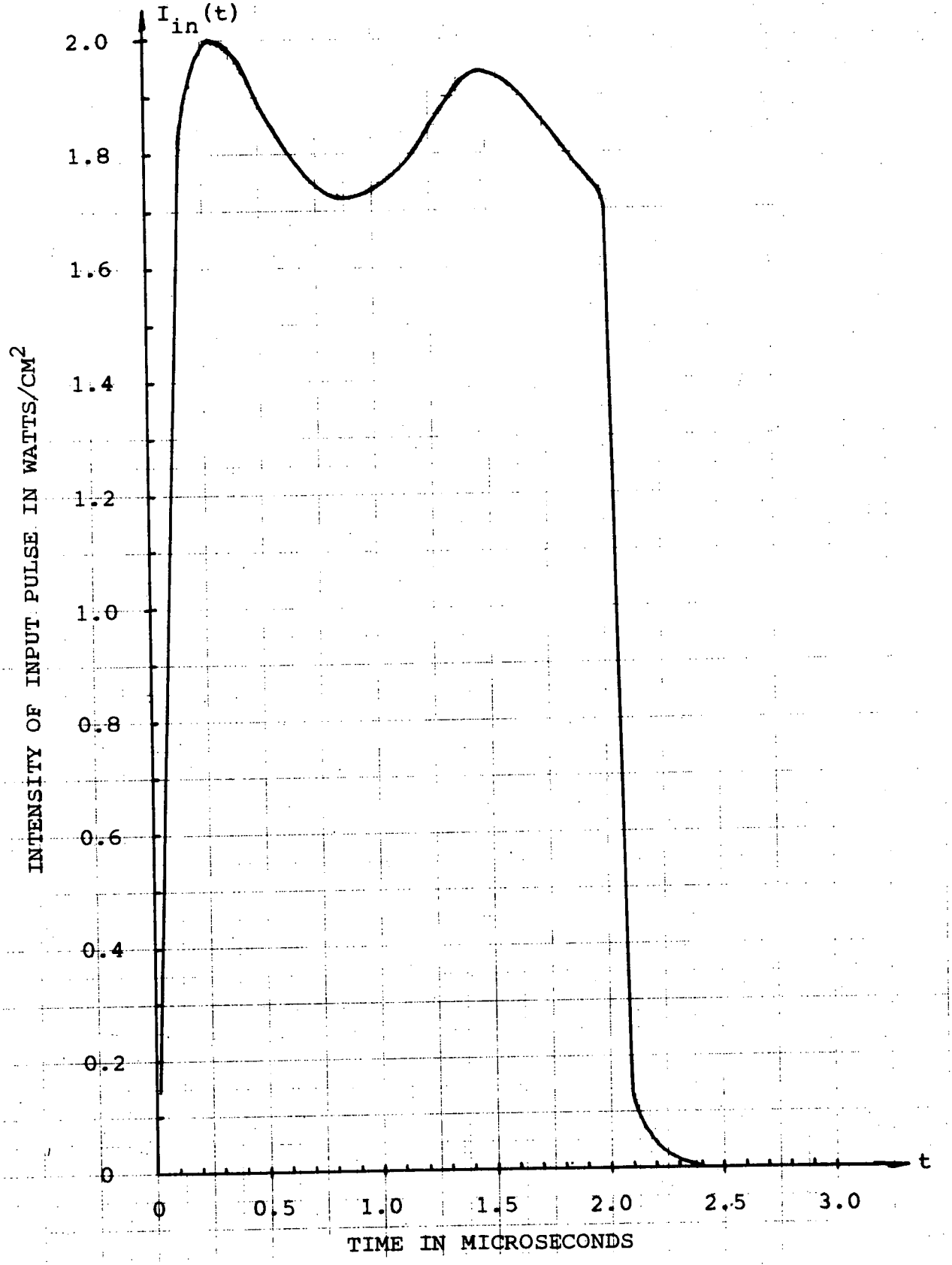

Figure 5-5 Amplifier Input Pulse Waveform

SECTION 5 REFERENCES

1. L. O. Hocker, M. A. Kovacs, C. K. Rhodes, G. W. Flynn, and A. Javan; "Vibrational Relaxation Measurements in CO_2 Using an Induced Fluorescence Technique," Physical Review Letters, Vol.17, No.5, 1 August 1966, pp.233-235.

2. N. Djeu, T. Kan, and G. J. Wolga, "Gain Distribution, Population Densities, and Rotational Temperature for the $(00^{\circ}1)$-$(10^{\circ}0)$ Rotation-Vibration Transitions in a Flowing CO_2-N_2-He Laser," IEEE Journal of Quantum Electronics, Vol. QE-4, No.5, May 1968; pp.256-263. There is a factor of two error in the population density results since the expressions for optical gain used in their analysis assume that every rotational line is present.

3. Private Communication from Dr. C. L. Tang.

4. This value for the spontaneous emission lifetime was calculated from the data presented by E. T. Gerry and D. A. Leonard, "Measurement of 10.6μ CO_2 Laser Transition Probability and Optical Broadening Cross Sections," Applied Physics Letters", Vol. 8, No. 9, 1 May 1966, pp.227-229. The difference in results is a consequence of the use of an erroneous expression for the collision broadened absorption coefficient by Gerry and Leonard.

5. This value for Ω was obtained by D. F. Hotz and J. N. Ferrer, "Intrinsic Flux Limits for Continuous and Q-Pulse Gain for the 10.6μ Line of CO_2," Journal of Applied Physics, Vol.39, No.3, 15 February 1968, pp.1797-1800

SECTION 6

TRANSMITTER

6.1 INTRODUCTION

This section presents the final results of a study to develop a pulsed, CO_2 laser transmitter. The transmitter will comprise part of an airborne, pulsed optical radar system capable of detecting clear air turbulence (CAT) from an airplane. A transmitter with a stable, single-frequency, single-mode output (rather than a multi-frequency or multi-mode output) was required for this study in order to avoid transmitting a beam which would otherwise contain a Doppler broadening effect. This effect would conflict with the detection of CAT by the optical radar system dependent on observing Doppler broadening caused by the motion of aerosols present in the turbulent air. Design goals of the transmitter were as follows:

Pulse width:	2-μsec
Peak pulse power:	5000-watts
Pulse repetition rate:	200-pps

The two-microsecond-wide pulses were produced by chopping the output of a stable, low-power, cw CO_2 laser with a GaAs electro-optic modulator. This pulsed output was then brought to the desired power level by an amplifier.

Initially two amplifier design concepts were explored in parallel. One was a conventional multitube amplifier, originally intended to be run in the sealed-off mode. The other was a multipass optical system contained in one flowing gas discharge tube — the White cell. The White cell concept was developed for use in spectroscopy in order to provide long absorption paths in a reasonable size absorption cell[1] and has been used to make dc-excited CO_2

oscillators and amplifiers.[2,3,4] This multipass, short, large-diameter configuration offered the potential advantages of small volume and high output power, with low-drive voltage and only two internal mirrors. Measurements of gain and power output were made on both systems. Because the White cell approach encountered difficulties that were not prevalent in the multitube technique, work on this approach was suspended about midway through the program.

The main body of this section summarizes the results obtained and the problems encountered. Paragraph 6.2 describes the experimental apparatus; paragraph 6.3 discusses the results obtained, paragraph 6.4 reports the problem areas remaining and makes recommendations for their solution, paragraph 6.5 comments on the use of heterodyne optics, and paragraph 6.6 provides a summary derived from the study.

6.2 EXPERIMENTAL

6.2.1 LINEAR TUBE AMPLIFIER

Figure 6-1 shows a simplified configuration of the CAT transmitter using the linear tube amplifier.

The transmitter is made up of the following components, each of which is described in detail below:

(a) Stable oscillator
(b) Gallium-arsenide electro-optic modulator
(c) Telescope
(d) Spatial filter
(e) Amplifier tubes
(f) Associated electronics

6.2.1.1 Stable Oscillator

The CO_2 laser oscillator used in this program was built under a Raytheon-sponsored program from a design by C. Freed of Lincoln Laboratories. The laser was designed to be highly stable in a laboratory environment.

Stability of the laser is achieved passively through mechanical and thermal design rather than actively through cavity modulation techniques. The length of the cavity is determined by four Super-Invar bars which are wrapped in foam to reduce short-term thermal excursions and wrapped in mu-metal to reduce magnetostrictive length changes. The granite end plates have their inner faces bearing against the ends of the Super-Invar rods. The mirrors in turn are attached so that they remain in the plane of the inner granite face. Mirror position is therefore dependent only upon the length of the Super-Invar rods. Additional stability can be obtained by regulating the temperature of the cooling water.

The time required for the laser to become thermally stable is on the order of one hour. The laser usually operates on one of three transitions, P-18, P-20, or P-22. During warm-up the laser operates on one line, then shifts to another after about one hour and stays there indefinitely. Output power is stable at 5-10 W in a beam diameter of slightly less than 3 mm.

The original oscillator design did not have any provision for fixing the polarization of the output. As a result, the direction of polarization was stable but not necessarily the same from day to day. To overcome this, one of the cavity reflectors was coated so that it had three nonreflective stripes on it. These caused greater loss for the polarization parallel to the stripes and determined the orientation of the output polarization. However, polarization did not remain when optical elements in front of the laser scattered power back into it. A polarizing element consisting of three parallel gold wires improved the stability, but still allowed the laser polarization to be pulled by the external optics. Finally, two plates of potassium chloride were mounted in the cavity at Brewster's angle. With this device, the laser has proven to be impervious to normal backscatter.

The amplitude of the laser output was monitored as the beginning of an examination concerning the effect of switching on the local oscillator. The beam was sampled with a NaCl flat placed between the laser and modulator. The greatest change in the L.O. power occurred at the time of actual switching of the modulator.

The prime source of the disturbance was the amplifier. When it was blocked at the input, the fluctuations were much smaller. Since the fluctuations were also much smaller when the amplifier was not excited, they were not caused simply by reflection from the amplifier windows.

6.2.1.2 Gallium-Arsenide Electro-Optic Modulator

In order to convert the cw output of the stable oscillator to the several microsecond-long pulses needed in the CAT system, a gallium-arsenide electro-optic modulator is used.

The modulator consists of a gallium-arsenide crystal placed between crossed polarizers. With no voltage on the crystal, the polarization of the beam is not altered and no radiation is transmitted. When the correct voltage is applied, the crystal becomes birefringent and, in effect, becomes a half-wave plate, causing the polarization of a linear polarized beam to be rotated 90^{o}. This beam, with its polarization rotated 90^{o}, will pass through the second polarizer. In this way, the voltage pulses applied to the electro-optic modulator produce optical pulses. The shape of the optical pulse is identical to that of the electrical pulse.

6.2.1.3 Telescope

In order to make optimum use of the 20-mm bore of the amplifier tubes, the 3-mm beam coming out of the modulator is put through an expanding telescope. Two anti-reflection coated KCl lenses having focal lengths of 3 inches and 15 inches are used for the telescope, giving an expansion of 5:1.

6.2.1.4 Spatial Filter

In order to provide a laser beam with a uniform phase front, the beam is spatially filtered by placing a pinhole filter at the focus of the telescope. This placement filters out all the stray radiation that fails to focus at the correct point, and also reduces the tendency of the amplifier to oscillate because of residual reflections.

6.2.1.5 Amplifier Tubes

The amplifier section consists of four 1.5-meter-long by 20-mm i.d., discharge tubes arranged side by side, with turnaround mirrors located at the ends. Each tube is fitted with Brewster's angle KCl windows, oriented to pass the horizontally polarized radiation which arrives from the modulator. The mirrors are gold-coated and located so that the plane of incidence is horizontal and the radiation remains linearly polarized. Angular adjustments of the mirrors are made by two screws arranged so that the axes of rotation are in the plane of the mirror.

The amplifier is mounted in a Plexiglas box. This box provides support for the amplifier tubes, the mirror mounting structures and the various electrical, gas, and cooling liquid lines. The Plexiglas has shown no indication of causing misalignment of the turnabout mirrors. Plexiglas has the advantage of being nonconductive, a matter of importance at the 30-kV discharge level.

The discharge tubes are cooled by flowing liquid through the cooling jackets surrounding them. The cooling liquids pass through a heat exchanger which, in turn, is cooled by water. Water is not a satisfactory tube coolant since the high dielectric constant prevents the initiation of the discharge. A nonflammable liquid with a low dielectric constant was sought and, as a result, trichlorethylene is being used at the present time.

Gases are fed into the amplifier tubes from a manifold at the high-voltage end. The gases - carbon dioxide, nitrogen, and helium - can be mixed in any desired ratio by adjusting flow valves and observing flow gauges. After flowing through the gauges, the gases enter a mixing manifold, pass through a length of tubing, and enter an input manifold near the discharge tubes. After passing through the discharge tubes, the gas flows into an exhaust manifold and to the pump. The input and exhaust manifolds are arranged so that the total path for each discharge tube is the same and hence the gas flows through the tubes are nearly the same.

6.2.1.6 Associated Electronics

The necessary electronic instrumentation and associated d-c power supplies required in the development of a pulsed CO_2 laser transmitter for use in an optical Doppler radar system is shown in the basic block diagram of Figure 6-1. A more detailed description concerning the operation of each electronic sub-system is discussed in this section. To implement the components of the electronics system for laboratory operation, standard, commercially available equipment was utilized wherever possible. Specialized electronics units were fabricated only when the commercial units for the intended application were unavailable or unsatisfactory. The results of the program have demonstrated that the electronic techniques selected were capable of achieving the desired overall system parameters with a high degree of reliability.

6.2.1.6.1 Stable Oscillator Power Supply

The initial or master oscillator of the CAT system consists of a stable CO_2 laser operating in a cw mode. The frequency stability of this laser is achieved passively through mechanical and thermal design, rather than actively by means of cavity modulation methods. As a result, the influence of ripple on the discharge current, arising from instabilities in the high-voltage positive and negative

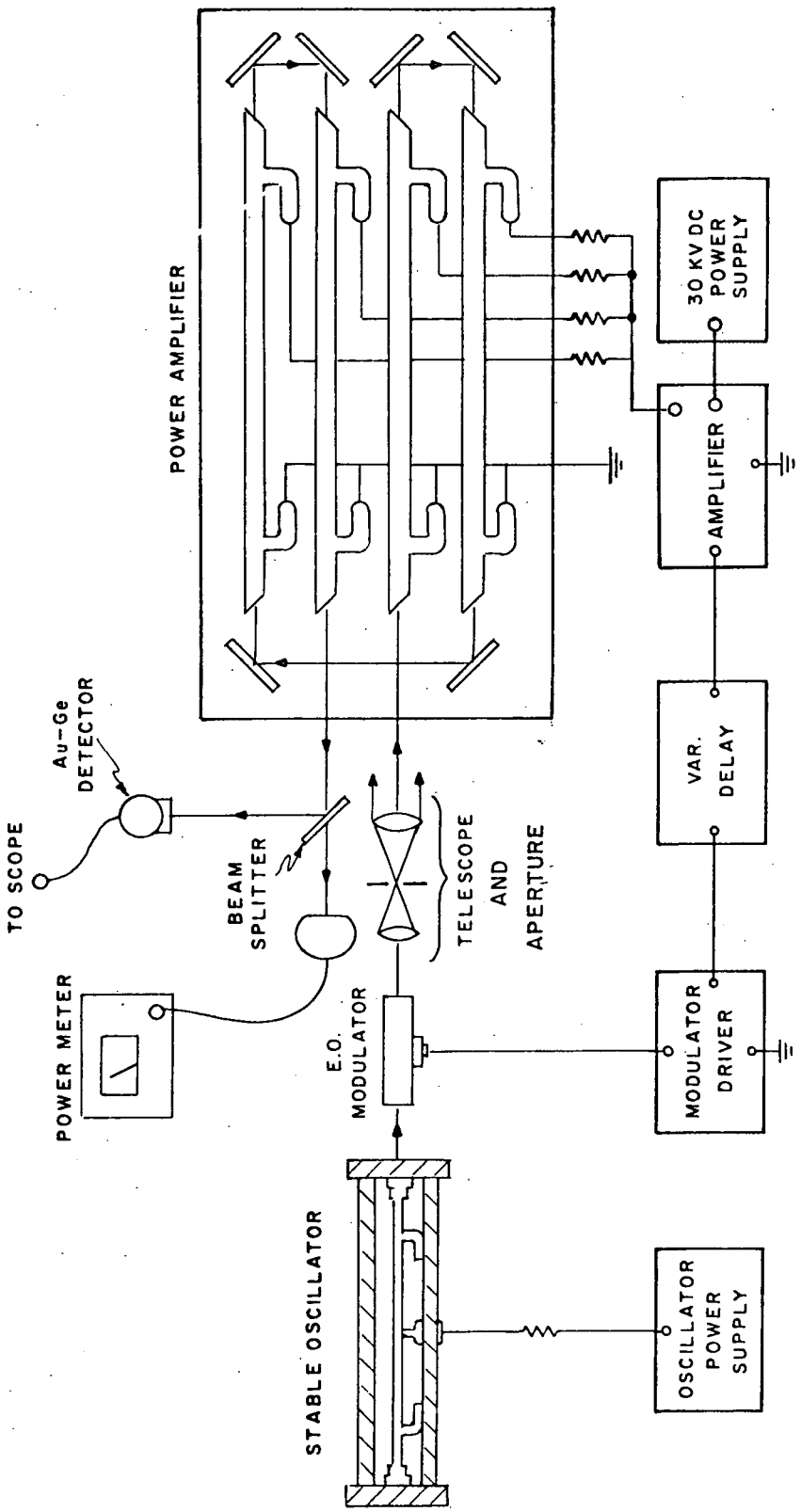

Figure 6-1 CAT Transmitter with Linear Tube Amplifier - Optical and Simplified Electrical Configuration

power supplies becomes a factor in obtaining stable operation of the laser. The primary requirement of the cw laser power supplies is to maintain a continuous, stable-voltage potential between the two anodes and the cathode of the discharge tube.

Figure 6-2 shows the electrical configuration for powering the cw laser oscillator. The laser tube is connected to the high voltage supplies through a passive resistor-type ballast network. The purpose of the ballast resistor is to compensate for the negative resistance of the CO_2 discharge tube while in normal operation. With the ballast as part of the load, current through the tube is limited and thus provides a source of constant current for the laser. Once the quiescent operating temperature of the laser system is attained, it becomes important for the d-c supplies to be stable in terms of voltage regulation and ripple superimposed on the d-c output voltage. These parameters directly affect the power output and operating frequency of the laser. For a CO_2 laser of this type, the sensitivity of output frequency to variation of discharge tube current is typically 0.5 to 1.0 MHz/milliamperes.

The d-c supplies chosen for use with the stable oscillator were selected on the basis of their rated specifications summarized below:

TABLE 6-1

Stable Oscillator Power Supply Characteristics

Characteristic	Parameter
Ripple:	2 millivolts peak-to-peak maximum
Regulation:	0.005% no-load to full-load
Stability:	0.01% for a line-voltage shift 105 VAC to 125 VAC at full output
Long Term Stability:	0.01% per hour; 0.1% per day

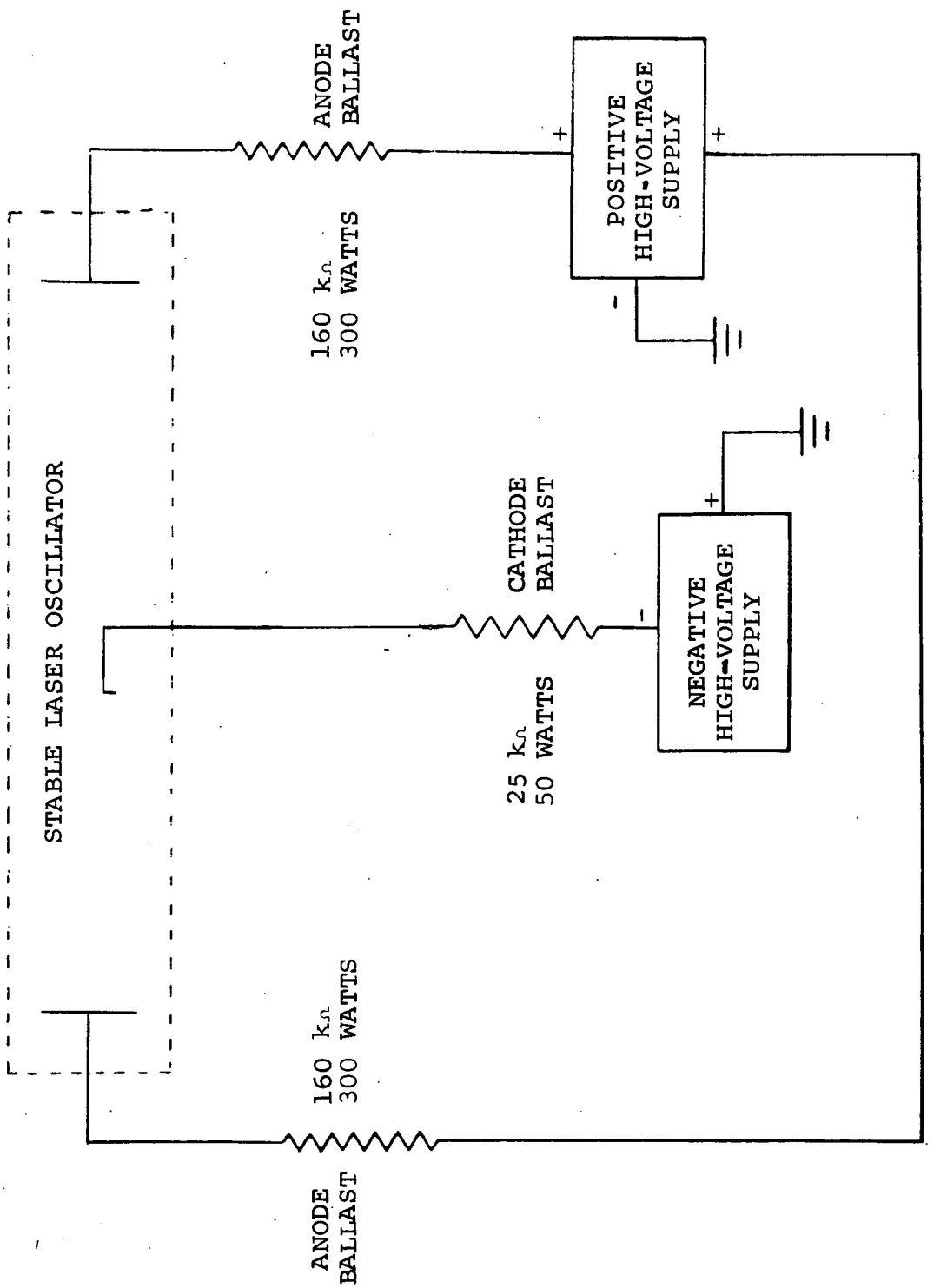

Figure 6-2 CW Laser Power Supply

These operating characteristics thus insure that the laser line will be stable to a point well below the allowable 1- to 3-megahertz shift within a given P-line. With minimum shift of the laser line, power output of the laser and ultimately the power produced at the output of the CO_2 laser power amplifier will not vary appreciably. High voltage supplies of this type have proven highly successful for operating a CO_2 laser in other programs, and should be equally accomplishable on the CAT program. For this reason, it could be expected that such d-c power supplies would be satisfactory for also powering an airborne CO_2 laser oscillator.

6.2.1.6.2 Optical Modulator Driver

The cw output of the stable laser oscillator is transformed into a pulse mode by means of pulsing an electro-optic switch. The gallium arsenide switch modulator is controlled by an electronic driver that provides voltage pulses sufficient in amplitude to cause the modulator to alternate between states of either maximum or minimum optical transmission. Most of the work on the CAT system was done with an electro-optic modulator containing a gallium arsenide crystal with dimensions of 3 mm x 3 mm x 7 cm in length. This particular device required about 4 kilovolts peak voltage for maximum transmission.

At the outset of the program it was originally planned to drive the CO_2 laser power amplifier with optical pulse triplets, arranged to provide a 200-μsec spacing between each set of three pulses. Time between each individual pulse within the triplets was expected to correspond to the N_2-CO_2 exchange time, thereby extracting more energy from the nitrogen system of the power amplifier.

In order to provide a flexible high-voltage pulser capable of supplying the required pulse repetition rate, pluse width, a number of pulses within a group, and spacing between pulse groups, a pulse generator was fabricated at Raytheon. Figure 6-3 is a block diagram

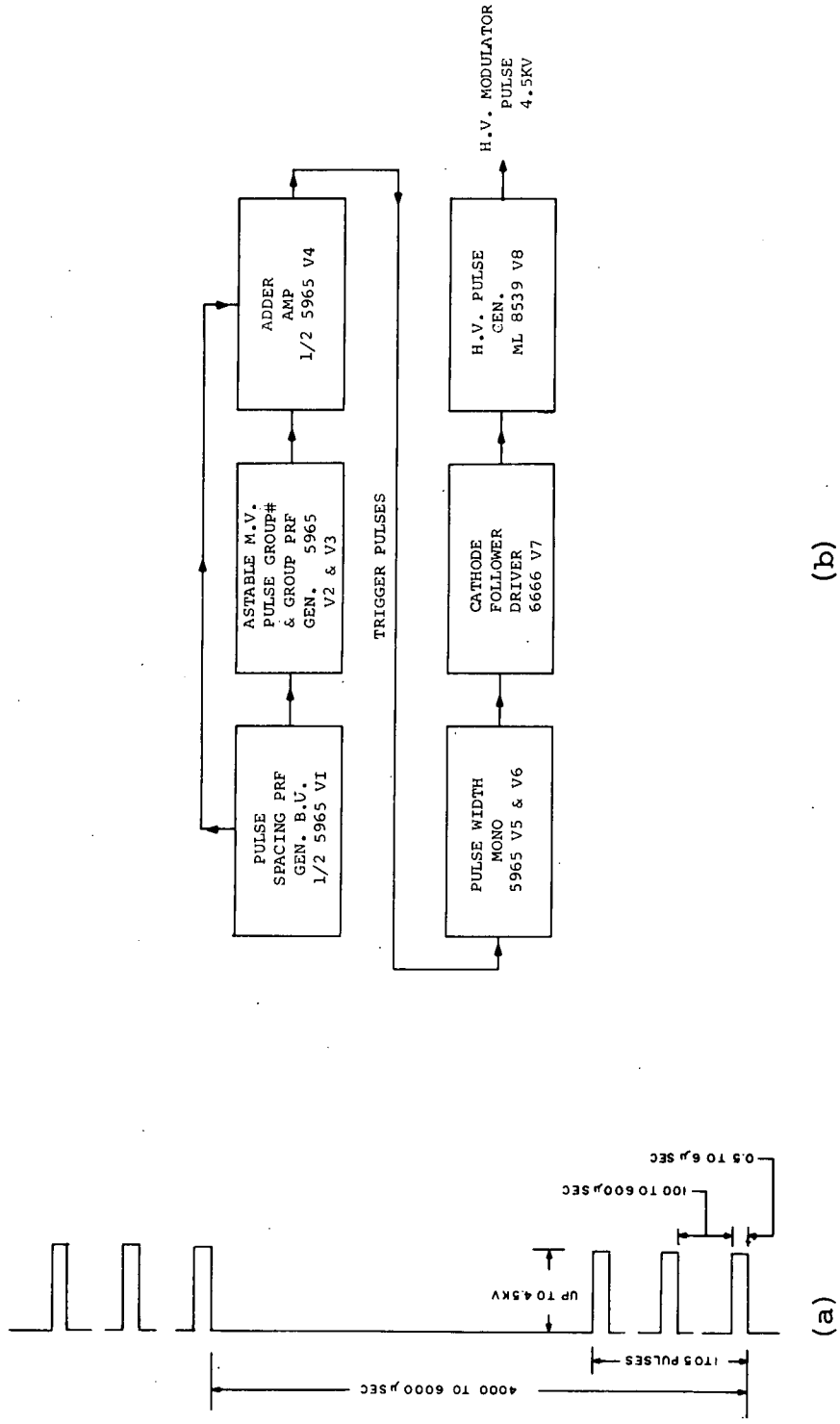

Figure 6-3 Initial Optical Modulator Driver. (a) Pulse Sequence of the Modulator, (b) Block Diagram of the Modulator

of the initial optical modulator driver utilized for the CAT system. The output format showing the obtainable flexibility in pulse parameters is also included in the same figure. A schematic diagram for the pulser is shown in Figure 6-4.

For this unit, tubes V1 through V6 are used to develop the timing sequence needed in generating the pulse triplets. The derived pulses are then amplified by tube V7 which act to drive the high-voltage switching tube V8. To switch the high-voltage on and off, the electro-optic modulator, a miniature planar type triode, was selected. The ML 8539 ceramic/metal pulse tube is designed for high-voltage, high-pulse current operation. Operation of this high-voltage switching circuit can be explained by first considering the tube V8 (ML 8538). This tube is non-conducting when no potential is applied to the optical modulator. The 0.02 microfarad energy storage capacitor is allowed to charge up to the potential of the high-voltage source. To maintain this cut-off condition, the grid of the triode is held at a negative potential close to -100 volts. Upon receiving an input pulse from the V7 driver, the switching tube is brought into a state of conduction and the switching circuit is completed to ground. Conduction of V8 discharges the storage capacitor in series with the GaAs optical modulator, thus permitting optical transmission for the duration of the pulse.

Originally it was this pulse generator that provided a pre-trigger pulse to drive the CO_2 linear power amplifier. Later, a modification was made to this pulse generator (Figure 6-5) to allow for external triggering of the optical modulator. In this way, a trigger pulse from a General Radio Model 1217B pulse generator could be used for driving the CO_2 power amplifier modulator. Additionally, the same trigger pulse, after passing through the variable delay network of the Tektronix Type 547 oscilloscope, could be used to drive the optical modulator. In this way, the pulse-repetition-rate and the group spacing could be more easily controlled by the General Radio pulser.

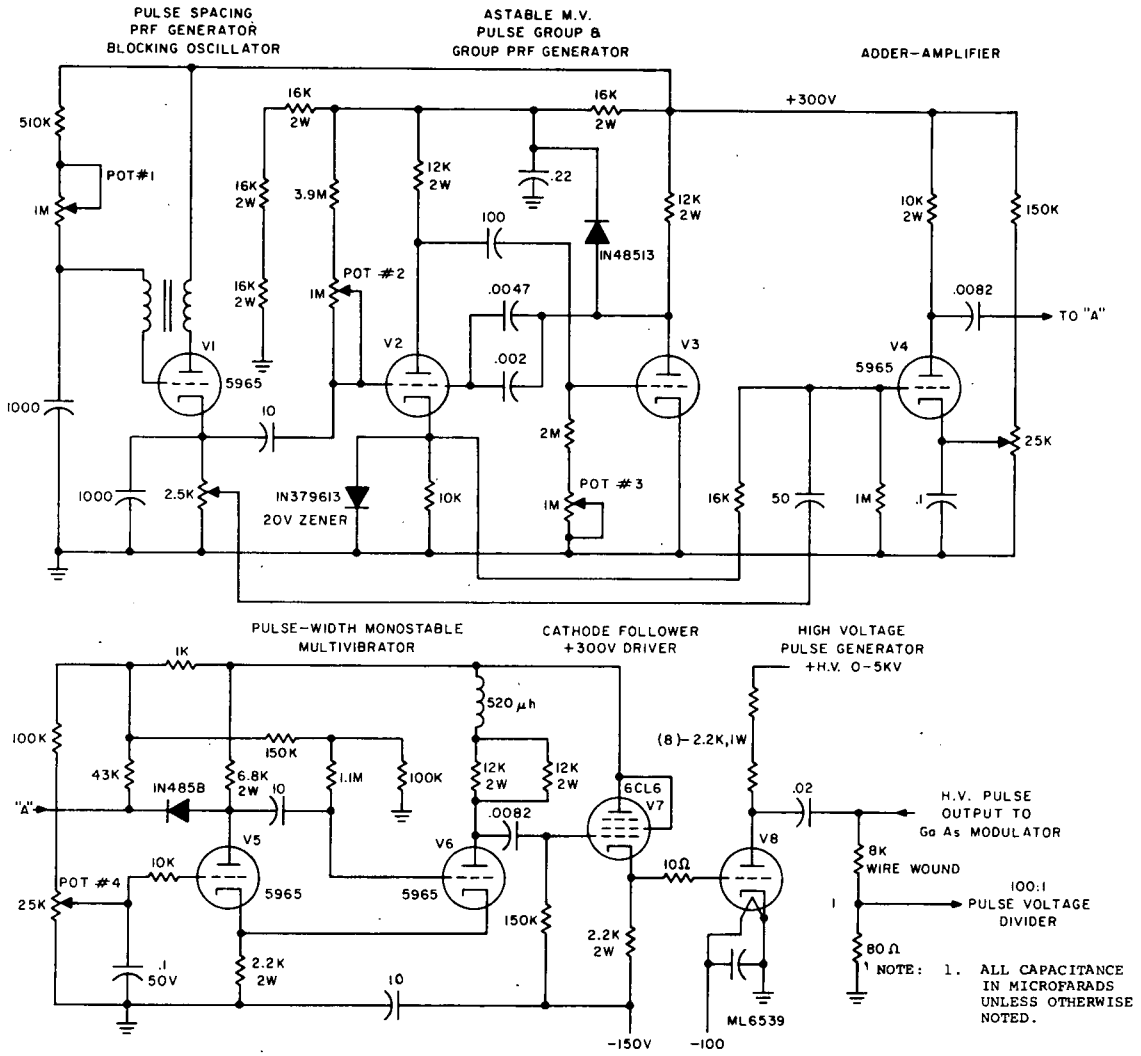

Figure 6-4 Initial Optical Modulator Driver Schematic Diagram

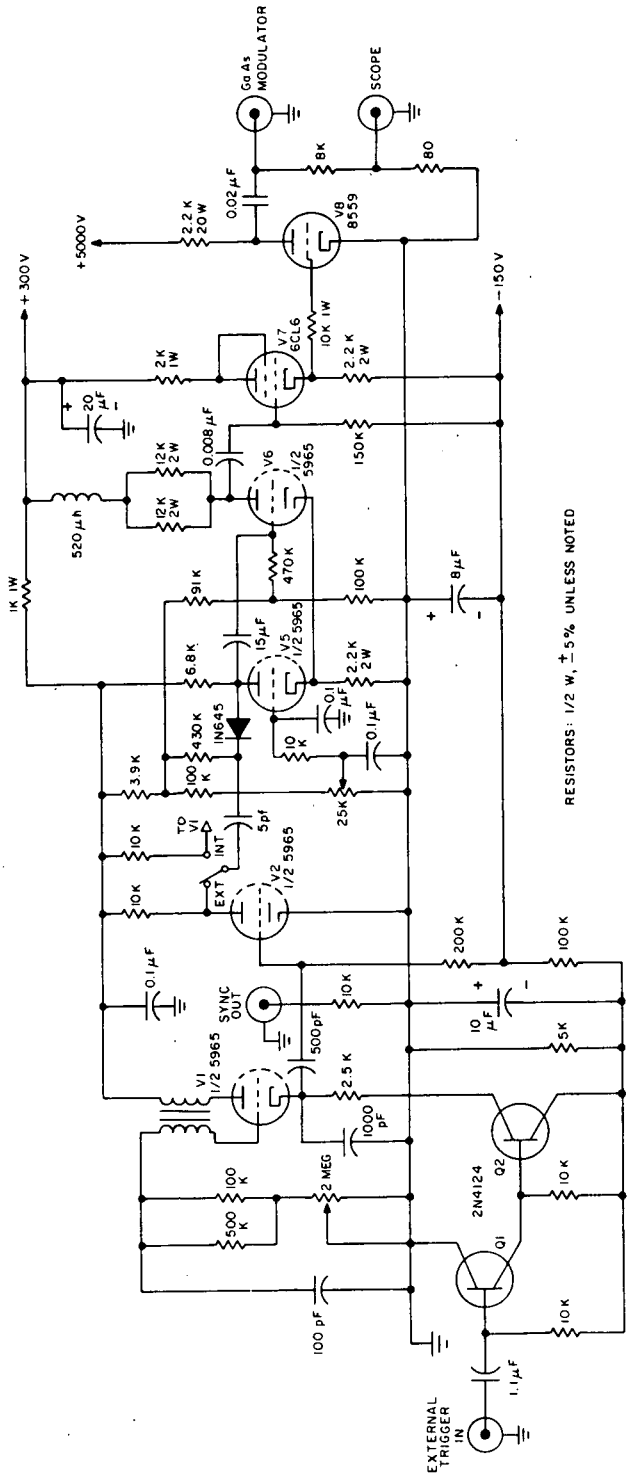

Figure 6-5 Modified Optical Modulator Driver Schematic Diagram

Towards the conclusion of the CAT program, a larger GaAs electro-optic modulator was obtained. The crystal in this device measured 5 mm x 5 mm x 5 cm in length. Peak pulse voltage required for maximum optical transmission was 9 kilovolts. To switch this modulator, the same basic electronic driver was used with two modifications. First, the high-voltage "keep alive" source was replaced with a supply capable of 12 kilovolts at 20 milliamperes. With the new supply, the same ML8538 switching tube could be employed to pulse the larger optical modulator.

The second modification consisted of a first attempt to use a solid-state driver for the ML8538 tube. Figure 6-6 shows that the grid of the switching tube is now controlled by a number of transistors. These transistors are connected in series in order to withstand the voltage pulse required by the grid to drive the switch tube. This transistor drive circuit worked very satisfactorily and proved to be quite reliable.

Recently the state-of-the-art in high-voltage, high-speed switching transistors has progressed to the point where new devices now available suggest immediate application in driving the ML8538 tube. Two such transistors, PT6905 from TRW, and 2N5660 from Solid State Products have the capability of switching 200 volts in less than 0.5 microsecond. An example of a schematic using a single drive transistor for controlling the ML8538 grid is shown in Figure 6-7.

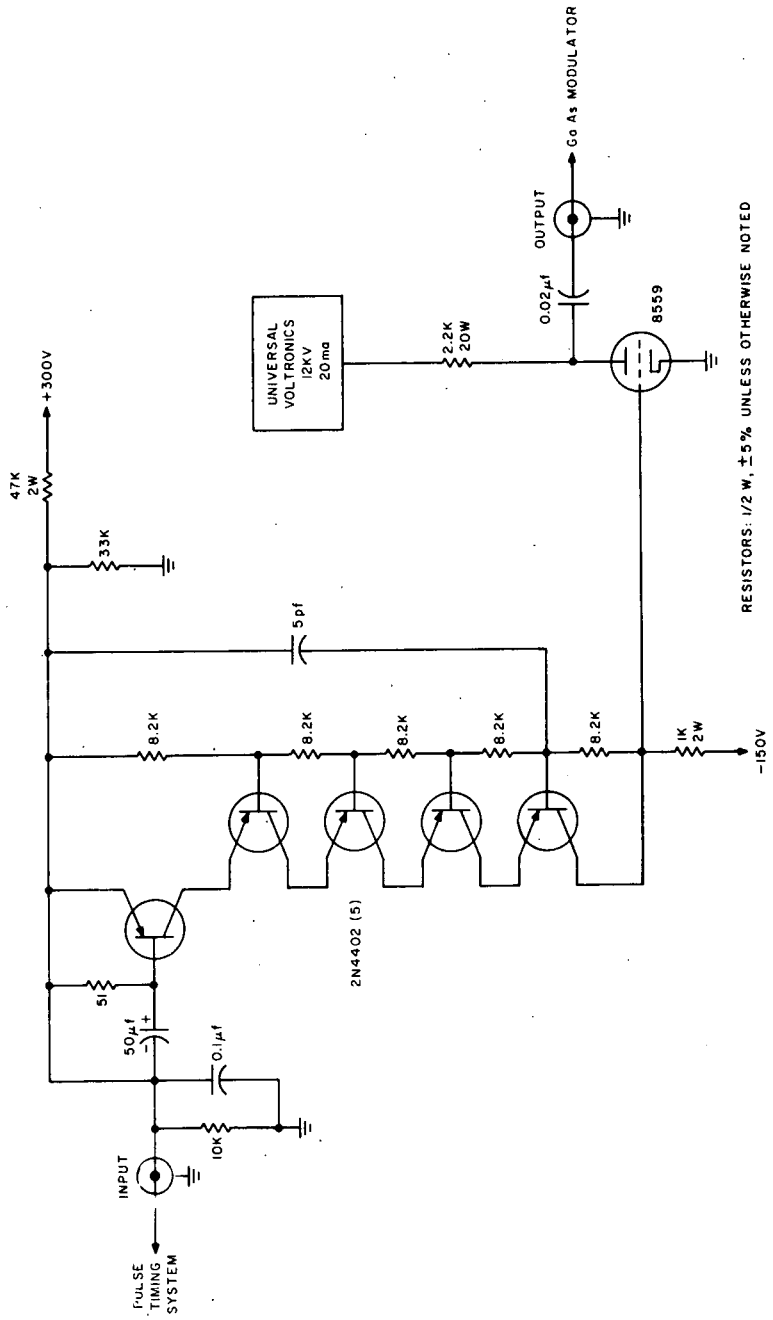

Figure 6-6 5-mm GaAs Modulator Driver Schematic Diagram

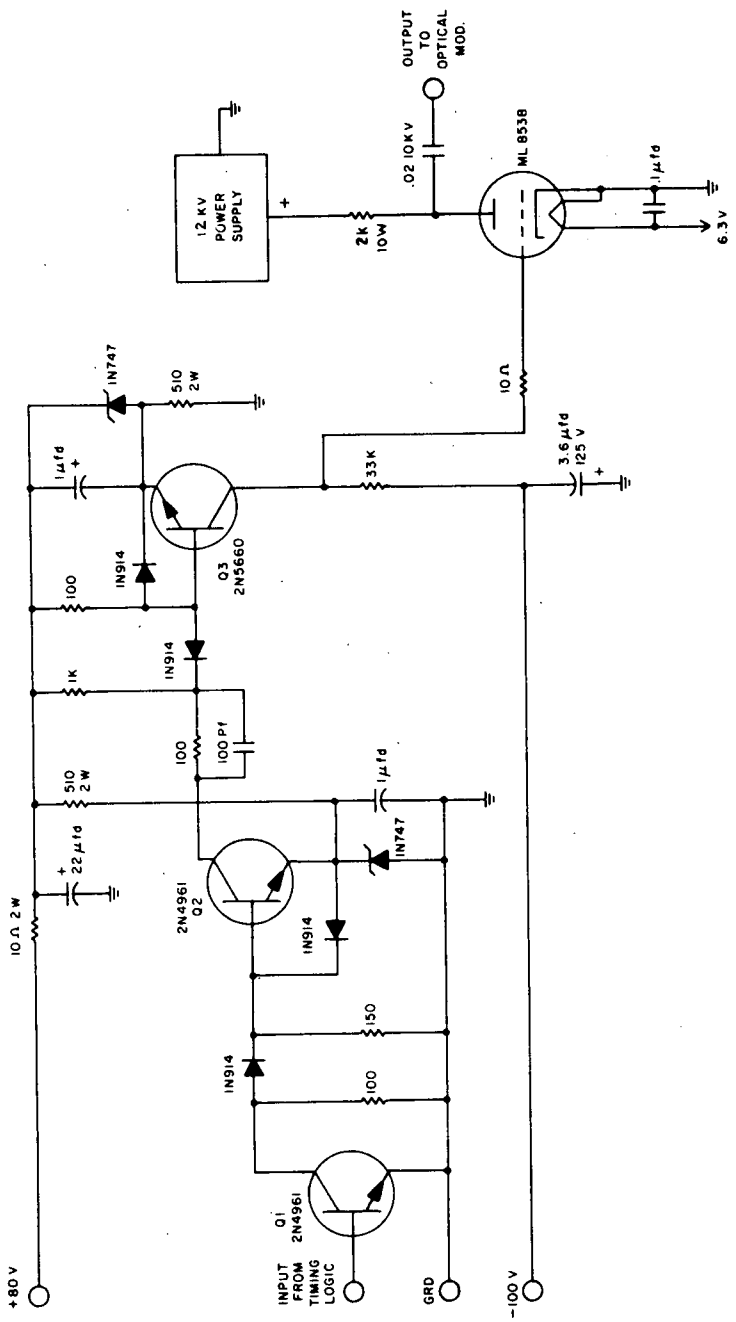

Figure 6-7 Recommended Optical Modulator Driver Schematic Diagram

6.2.1.6.3 Power Amplifier Modulator

The requirements of the high-voltage power supply for operating the CO_2 discharge tube of the linear power amplifier are quite different from those of the power supply described in paragraph 6.2.1.6.1. Voltage regulation is not as important a consideration here due to the fact that the laser device is used as an amplifier rather than as an oscillator. The primary requirement here is to have a sufficient potential difference across the tube so that the device will perform in a saturated gain mode. Since the power amplifier is to be operated under pulsed conditions, a reliable and efficient method has to be used for simultaneously switching the high-voltage to each of the discharge tubes. Therefore, it is necessary for the power amplifier modulator to provide consistent voltage pulses, in terms of amplitude and duration, to each of the amplifying tubes.

The initital electrical configuration used for operating the CAT system is shown in Figure 6-8. The General Radio Type 1217B pulse generator is used here as the system clock which triggers the pulse amplifier driving the 30-kilovolt switching tube. As explained in paragraph 6.2.1.6.2, the output of the GR pulser is delayed by the Tektronix 547 scope in order to trigger the optical triplet generator. Thus, the GR pulser begins the sweep and also starts the variable delay trigger system of the oscilloscope.

The arrival of the delayed trigger at the optical modulator generates a gate of variable width. Within this gate, pulses of adjustable duration and repetition rate are produced. The pulse sequence used to operate the optical modulator is displayed together with the pulse driving the power amplifier switch tube on the same oscilloscope. By comparing the two pulses on the same CRT while controlling the time delay, the relationship of the input optical pulse to the amplifier pumping time can be controlled.

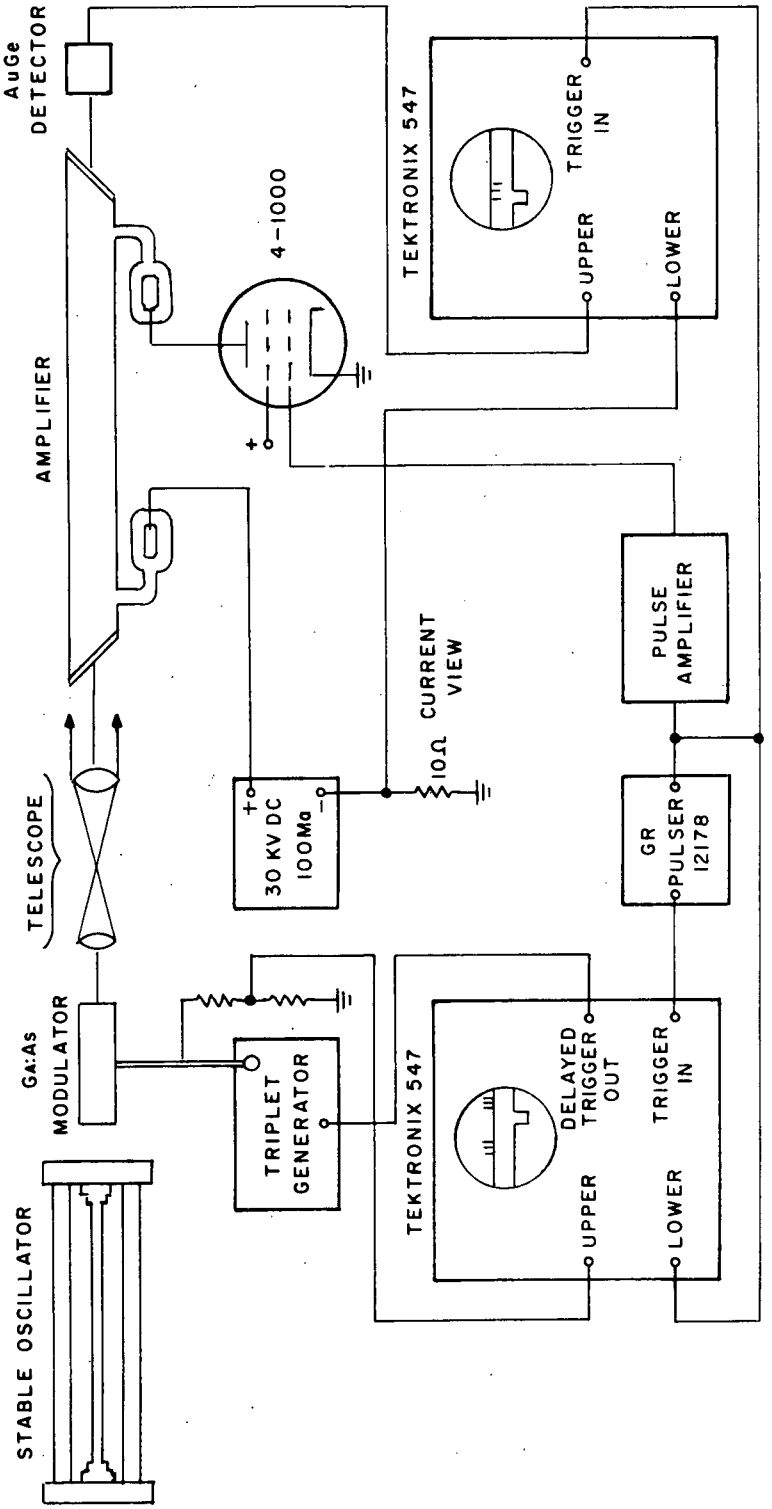

Figure 6-8 Initial CAT Transmitter Electrical Configuration

The switching element selected to apply the 30-kilovolt supply to the discharge tubes is a high-power radial-beam tetrode. This type of hard-tube pulse modulator is similar to those used in microwave radar systems. The high-voltage circuit is completed to ground and through the amplifier tubes when the grid of the 4-1000 tetrode is pulsed. The grid pulse is derived from the pulse amplifier which receives the initial pulse from the GR pulser and amplifies this pulse to the required level for driving the 4-1000 tube. Figure 6-9 is a schematic of the pulse amplifier.

This first electrical system proved to have some disadvantages especially in the high-voltage switching circuit. With this approach, both ends of the discharge tube are at a high potential at the same time during the firing. As a result, it was not possible to make adjustments to the amplifier mirrors without the danger of drawing an arc.

A significant improvement was made in the high-voltage switching circuitry by operating the discharge tubes with one end at ground potential. The ground end was chosen to be that side closest to the vacuum pump so that there would be no possibility of arcing through the vacuum tubing. With this arrangement, mirrors at the grounded end were capable of being adjusted without danger of arcing. The modified electrical configuration is shown in Figure 6-10. With careful adjustment of the ballast resistor associated with each tube for equalizing current, a high-voltage pulse discharged through the energy storage capacitor (0.25 μf) is applied simultaneously to all tubes.

As stated above, the high-voltage d-c supply need not be closely regulated since its only function is to charge the storage capacitor in series with the discharge tubes. This is a situation analogous to the optical modulator high-voltage switching circuit of paragraph 6.2.1.6.2. It is the discharge of this storage capacitor by the action of the control tube which actually supplies the

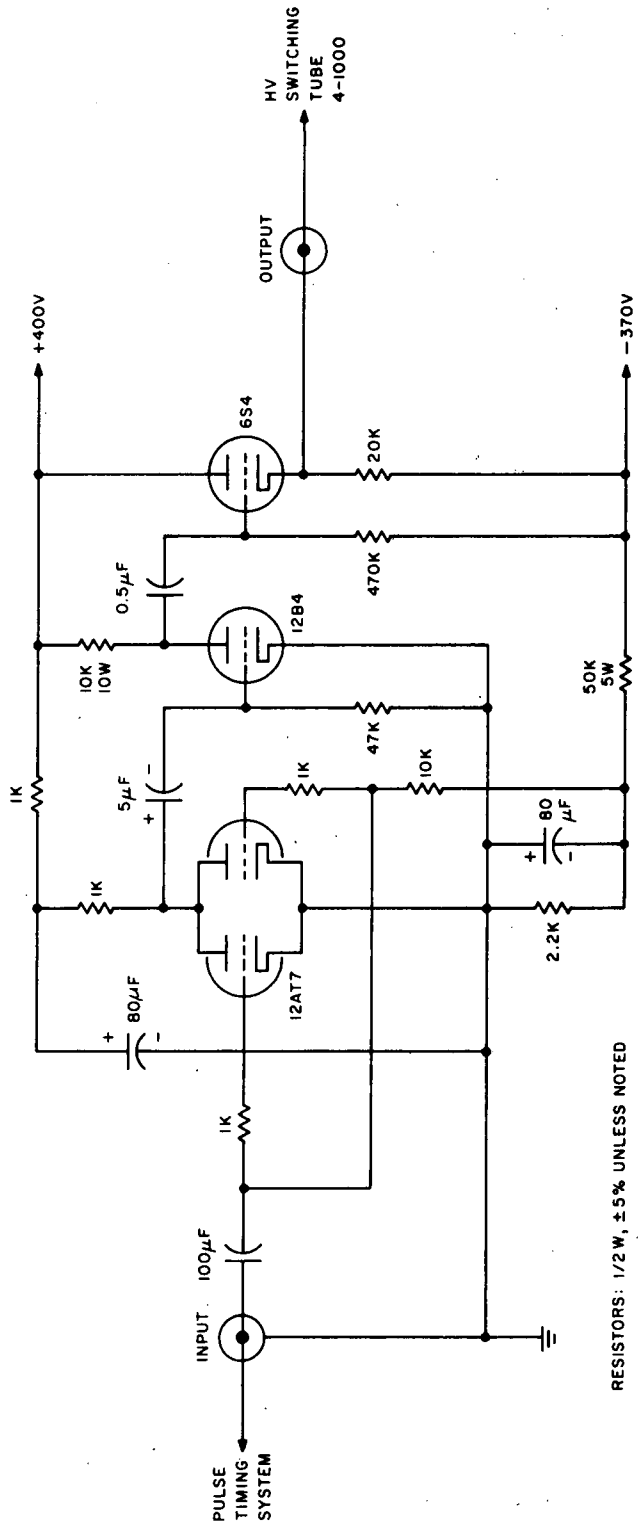

Figure 6-9 Linear Amplifier Pulser Schematic Diagram

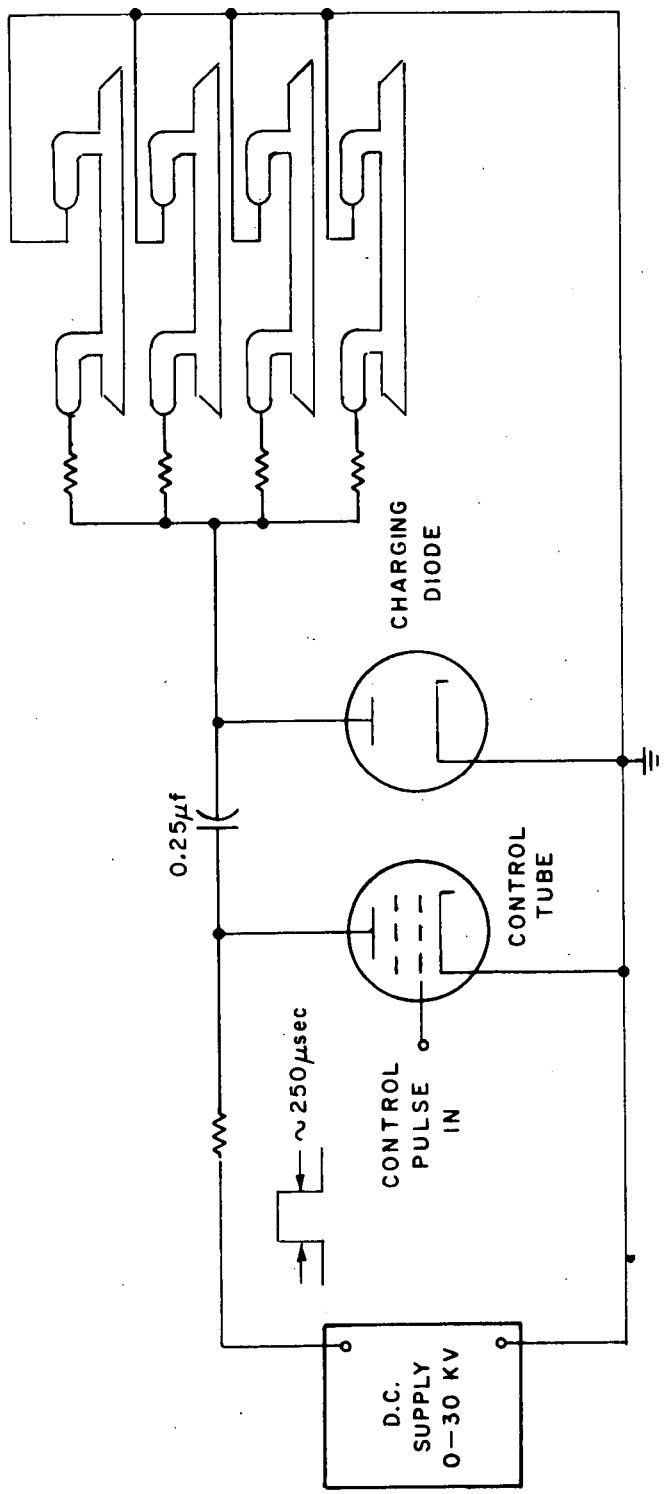

Figure 6-10 Modified Linear Amplifier Pulser Schematic

high-voltage pulses that ionize the CO_2 tubes. The purpose of the charging diode is to provide an electrical path back to ground for recharging the storage capacitor after the control tube has been turned off or is in a non-conducting state.

The use of a hard-tube pulser in the final electrical configuration has proven to be a reliable and efficient technique for operating the CAT linear amplifier. Figure 6-11 is a detailed diagram of the CAT transmitter developed during this program. It should be noted that this electrical system has not been optimized in terms of electrical efficiency or in mechanical design considerations with respect to an airborne environment; however, a definite electronics approach to the problem of operating a CO_2 laser transmitter have been established.

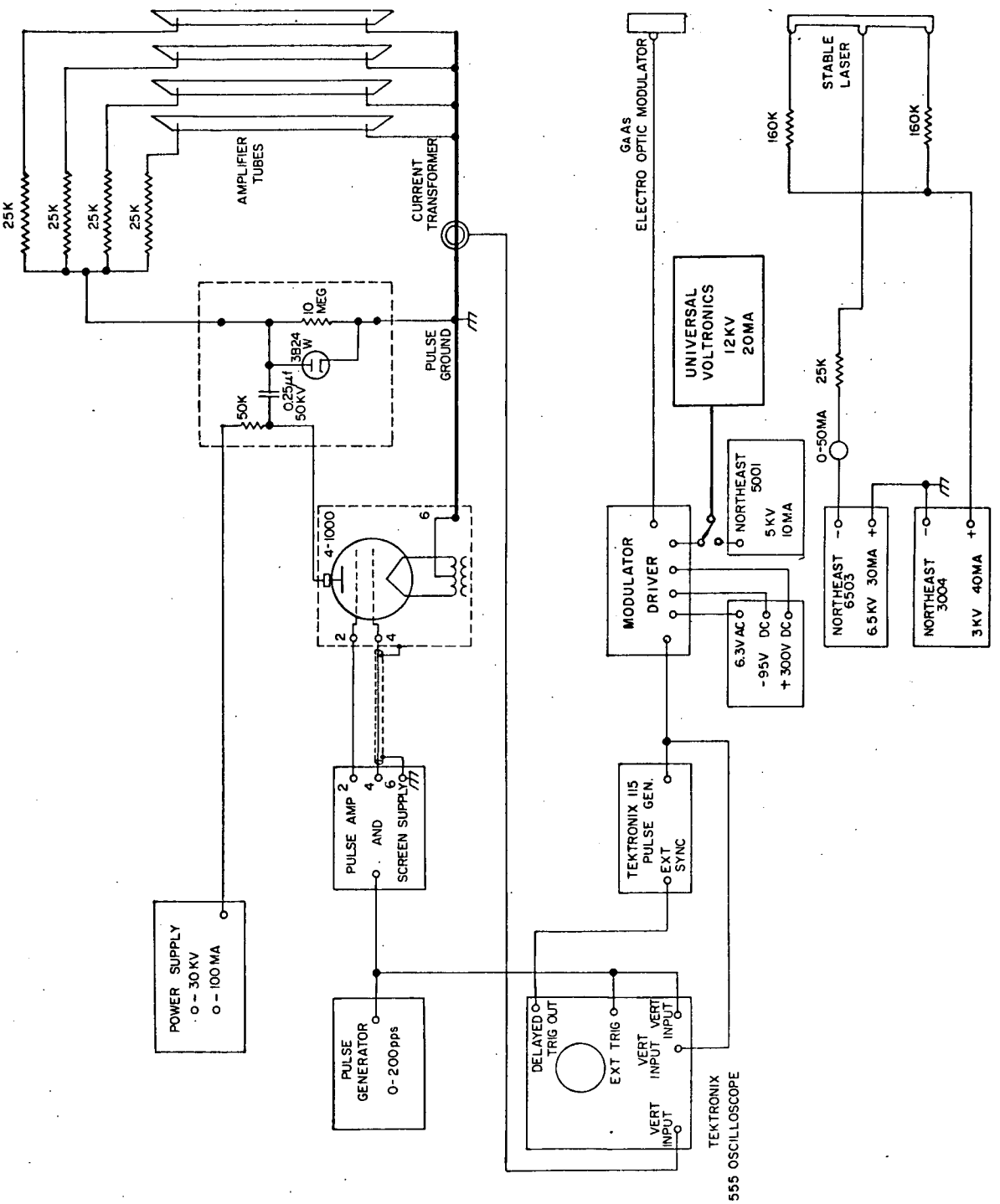

Figure 6-11 Final CAT Transmitter Electrical Configuration

C.9.

6.2.2 WHITE CELL AMPLIFIER

The optical configuration of the White cell is depicted in Figures 6-12 and 6-13. It is designed to allow a variable number of passes between the two mirrors. The number of passes within the amplifier is determined by the angle of the input beam, the mirror separation, and the radii of curvature. At successive reflections, the mirrors recollimate the beam and thus prevent excessive beam divergence over the long propagation path.

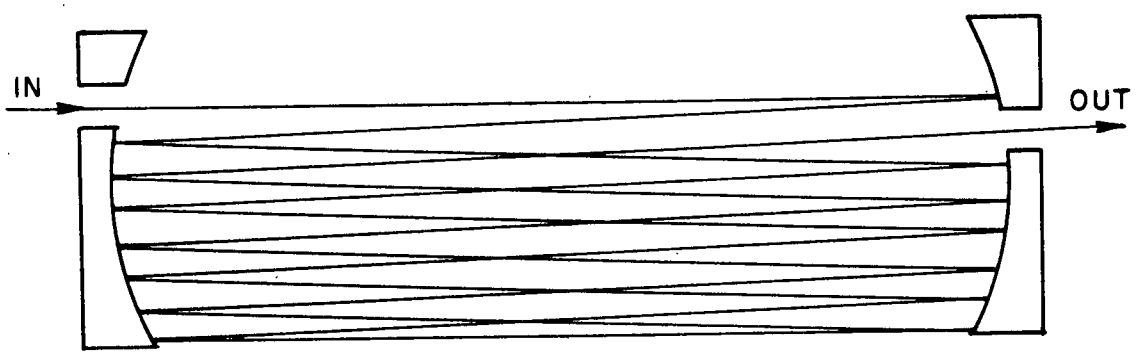

Figure 6-12 Cross Section of a White-Cell Configuration

The gold-coated mirrors, usually of 2.15-m radius, were separated by 95 cm. They were mounted within the vacuum envelope of the White cell, but could be adjusted by external micrometers which used "O" ring vacuum seals. The beam enters a Brewster-angle window, passes through a 3/8-inch diameter hole in the first mirror, reflects back and forth on the periphery of the mirrors, and exits through a hole in the second mirror. In practice the mirrors were adjusted with the glass discharge tube removed by using a He-Ne laser beam. When the desired number of passes was obtained, the discharge tube was inserted and the tube pumped out. The alignment changed slightly when the vacuum was applied. A small adjustment, however, would restore alignment.

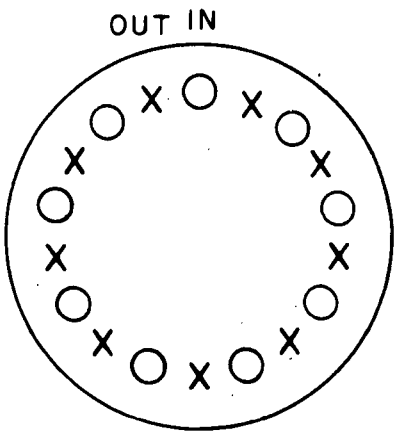

Figure 6-13 End View of White Cell with Circles Showing Spots on First Mirror and Crosses on Second

The water-cooled White cell discharge tube had an i.d. of 3 inches and a discharge length of 65 cm. The configuration was designed to allow high pumping speeds, should fast flow become desirable. The pumpout line was 2 inches in diameter. The gas input which consisted of only two ~ 1/8-inch diameter holes in the annular gas electrode was capable of being modified for higher flow rates.

The experimental configuration for the gain measurements is shown in Figure 6-14. Most of the apparatus used is similar to that described in the previous section on the linear tube amplifier. The hard tube pulser used was capable of providing current pulses of variable width, with amplitudes of up to 4A. Figure 6-15 shows typical current and voltage pulses. In contrast to the linear tube system, the optimum current pulse is higher (~ 4A peak) and shorter (~ 50 μsec), while the voltage pulse (~ 5 kV) is lower. The CO_2 oscillator used was a sealed unit with a wire grid polarizer; although it was single mode, the mode size, ~ 5-6 cm, was larger than that of the Freed laser.

6.3 RESULTS

6.3.1 LINEAR TUBE AMPLIFIER

6.3.1.1 Flowing Gas - Gain Measurements

To provide a basis for the design of the multitube amplifier, measurements were made of the gain for 2-μsec pulses of a single 1.5-m long, 20-mm i.d., tube with flowing N_2-CO_2-He gases. These measurements used both dc and pulsed excitation. With dc excitation, a maximum small-signal gain of ~ 2dB/meter was found, whereas, with pulsed excitation, a gain of 9.8 dB/meter at 100 pps and a current of 100 mA were observed. Subsequent measurements were made using pulsed excitation and are discussed in the paragraphs that follow.

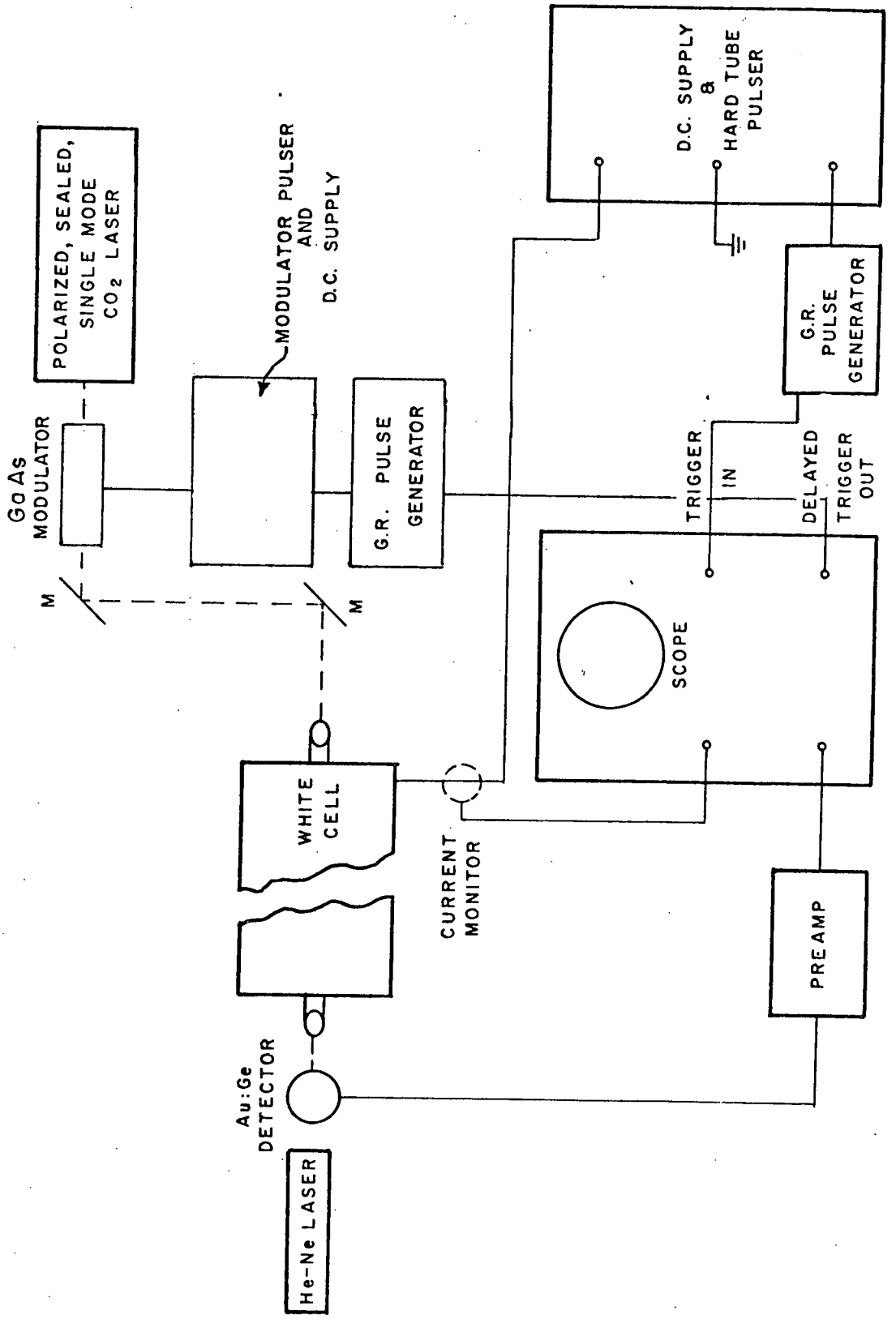

Figure 6-14 Test Configuration for White Cell Amplifier Gain Measurements

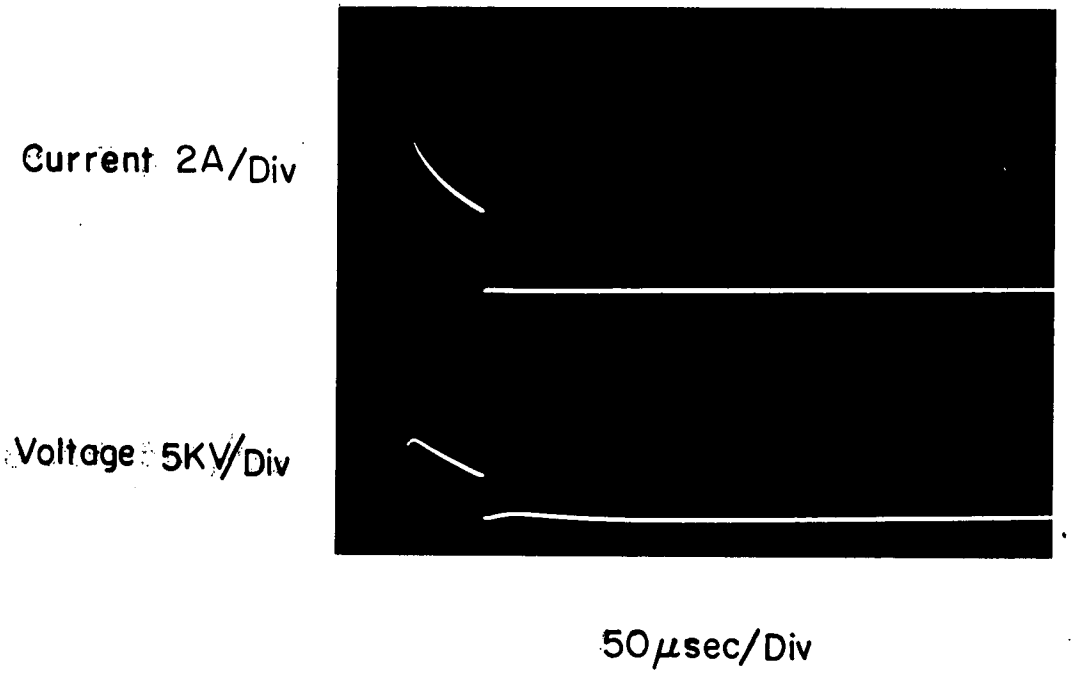

Figure 6-15 Typical Current and Voltage Pulses for 3-Inch i.d., 65-cm long White-Cell Amplifier

6.3.1.2 Sealed-Off Gain

Although all measurements on the multitube amplifier were made under flowing gas conditions, a single tube, with 6-inch long nickel electrodes designed to avoid having the discharge occur on the outside of the electrode, was studied as a sealed-off amplifier. This tube was run for almost four hours during which time the data in Figure 6-16 were taken. As indicated by these measurements, the input power level, approximating one watt, is such that saturation effects probably occurred. Thus the gain values obtained should be considered as a lower limit on the small-signal gains. No deterioration of gain was noticed during this time. The gas fill was based on previous sealed amplifier work by Carbone[5] and was not optimized.

6.3.1.3 Cooling Requirements

Cooling requirements for the heat exchanger were obtained by using a pair of Cr-Al thermocouples to measure the temperature rise of the water coolant flowing through the exchanger. These measurements were performed on the four-tube system. The measured power dissipation with 250-μsec wide, 200-mA peak current pulses was 95 W at 83 pps, and 210 W at 180 pps. These values are about 25 percent higher than those calculated using the measured peak current, peak voltage, pulse width, and duty cycle. The cooling requirements of the three tube amplifier should be about 150 W.

6.3.1.4 Modulator Characteristics

Two different electro-optic modulators were studied in this program. Although each came from a different manufacturer, the only difference between the two was the dimensions of the gallium arsenide crystal. The small crystal is 3-mm x 3-mm x 7-cm long and the larger crystal is 5-mm x 5-mm x 5-cm long.

Most of the work on the CAT system was done with the 3-mm aperture modulator, as the larger one was not purchased until near the end of the program. The size of the beam coming out of the oscillator

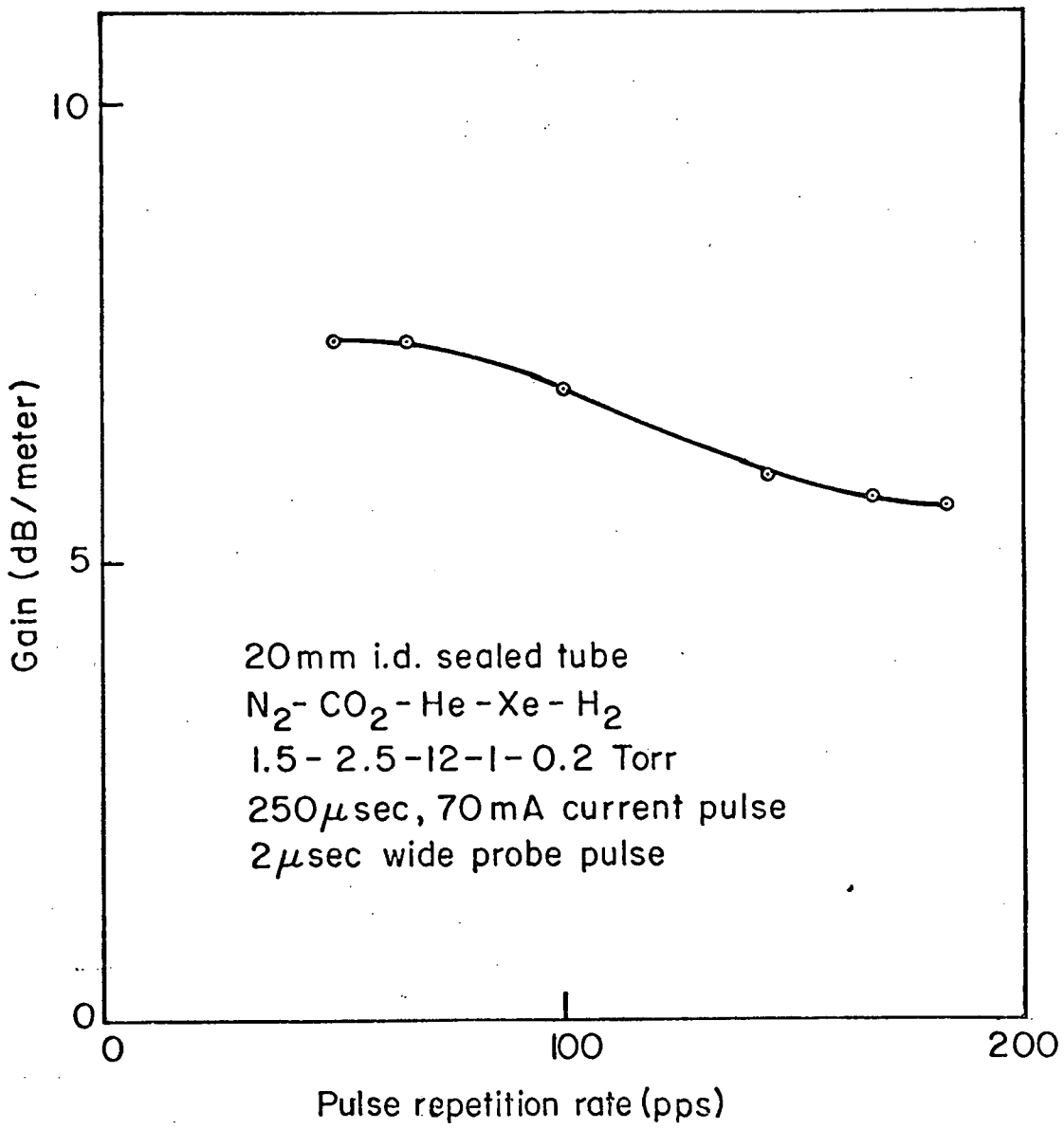

Figure 6-16 Gain vs Pulse Repetition Rate for a 20-mm Pulse-Excited Sealed-Off Tube

has approximately a 3-mm diameter, making the 3-mm modulator marginal for use in the system. Even with good antireflection coatings on the modulator, the transmission was only about 50 percent. Most of the loss is due to aperturing. Figure 6-17 shows this effect. Figure 6-17a shows the laser beam shape without the modulator in the circuit; Figure 6-17b shows the beam shape with the modulator in but without polarizer; Figure 6-17c shows the beam shape with the input polarizer in the modulator, and Figure 6-17d shows the beam shape with both polarizers in. From looking at these results it appeared that a larger aperture modulator would be desirable.

Similar tests were run on the 5-mm modulator. It showed almost no beam distortion. Its transmission varied from 79 percent to 92 percent because of thermal length tuning. Since the modulator crystal has plane parallel faces and since the antireflection coatings are not perfect, the crystal acts like a Fabry-Perot resonator whose transmission depends upon length. As the crystal heats up, its transmission changes until the crystal reaches an equilibrium temperature. This effect can be eliminated by having better multilayer antireflection coatings on the crystal.

The only disadvantage of the larger aperture modulator is that it takes considerably more voltage to operate it. The voltage needed to operate a modulator is proportional to its thickness and inversely proportional to its length. Since the 3-mm modulator is 7-cm long and the 5-mm modulator is 5-cm long it takes 2-1/3 times more voltage to operate the larger aperture modulator. The 3-mm crystal operates at about 4 kV and the 5-mm crystal operates at about 9 kV.

6.3.1.4.1 Modulator Leakage

It was found that the small amount of radiation leaking through the modulator was being amplified and contributing to the average power measured at the amplifier output as shown in Figure 6-18

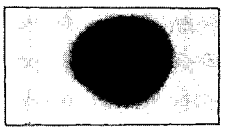

(a)
Beam Shape Without Modulator

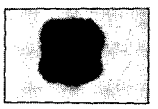

(b)
Beam Shape with Modulator

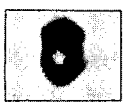

(c)
Beam Shape with Modulator and One Polarizer

(d)
Beam Shape with Modulator and Both Polarizers

Figure 6-17 Laser Beam Distortion Caused by GaAs Modulator

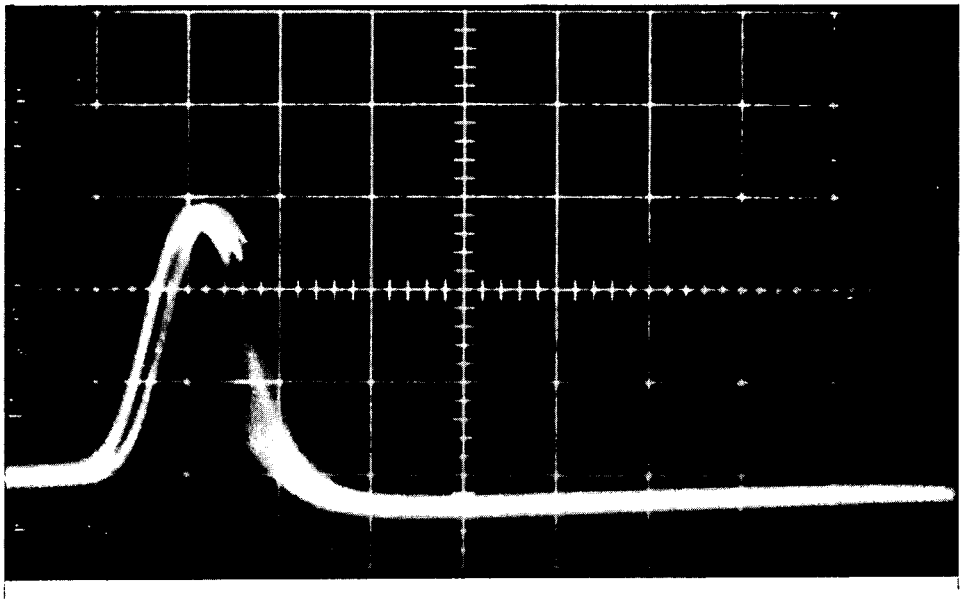

100 μsec/cm ⟶

Figure 6-18 Amplified Leakage

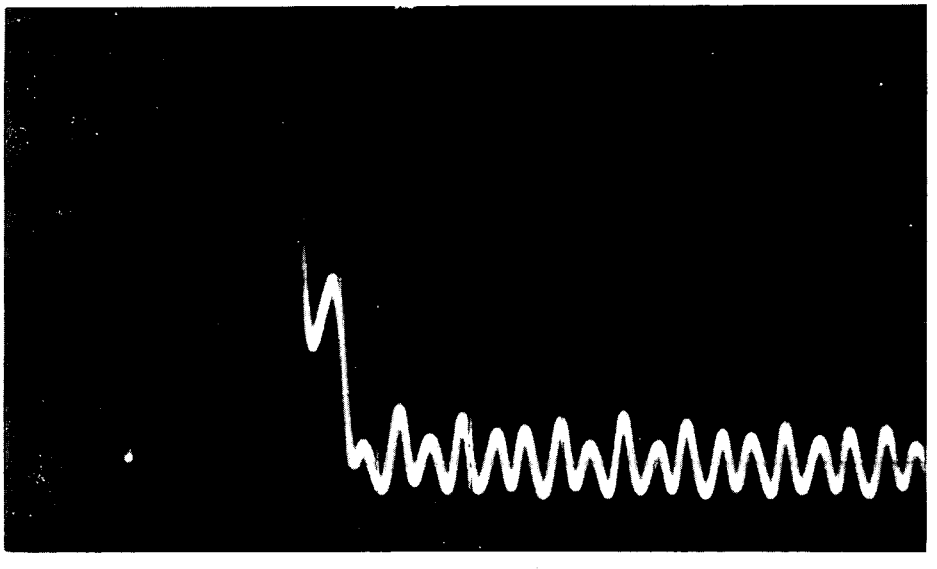

2 μsec/cm ⟶

Figure 6-19 Ringing Following Optical Pulse

Another "tent" of two germanium plates oriented at the Brewster angle was placed between the modulator and the beam expander to augment the two crossed polarizers already mounted on the modulator. The leakage power was reduced by a factor of more than one thousand, so that the average power measurements made at the amplifier output are no longer significantly influenced by modulator leakage. Under present operating conditions, the leakage energy is less than 1 percent of the pulse energy, and the leakage power is down by more than five orders of magnitude from the peak pulse power.

6.3.1.4.2 Modulator Ringing

Ringing has been observed in the gallium arsenide modulator for quite some time. Several experiments were performed to allow a better understanding of the phenomenon, and to reduce its amplitude.

The ringing may be observed either on the transmitted optical pulse (Figure 6-19) or on the 100:1 voltage divider which is a part of the drive circuit. Using the 3-mm crystal, the electrical ringing is at a very clean 700 kHz, whereas the optical ringing appears to be at 1.4 MHz. This increase in frequency would be expected if the voltage oscillations were around zero since these oscillations would lead to an apparent doubling through the sine squared response of the modulator.

If the 5-mm crystal is substituted for the 3-mm one, a change of frequency occurs. The change is from a period of 1.4 μsec for the 3-mm crystal to 2.35 μsec for the 5-mm crystal. The ratio is 1.7. The ratio of 5 mm to 3 mm is 1.7. These periods are also consistent with a two-mode oscillation of the modulator crystal. It is evident that the ringing is due to the piezoelectric and/or acoustic properties of the GaAs crystal.

6.3.1.5 Parameter Studies

It was originally planned to use pulse triplets, with a 200-μsec spacing between components of a triplet. Time between pulses was expected to correspond to the N_2-CO_2 exchange time, and thereby make possible the extraction of more energy from the nitrogen system. Although small-signal gain measurements on one tube did show almost equal energy by using two pulses, measurements made on the complete multitube amplifier showed that employing one pulse depleted the gain in the amplifier with the result that the pulses which followed had very low amplitudes. Subsequently all measurements were made using a single pulse.

A multitube amplifier, consisting of four 1.5-meter long 20-mm i.d. tubes together with a 3-mm aperture GaAs modulator, was used for most of the parameter studies on the system. Due to the high small-signal gain present in this system, self-oscillation occurred quite often. Several methods were tried in order to prevent this problem; most of these techniques are presented elsewhere in this report. However, in one major modification, the system was operated with only three tubes. This procedure cut down the small-signal gain by 25 percent, but hardly reduced the actual (saturated) gain.

Typical operating conditions with the three 1.5-meter long tubes and the 3-mm GaAs modulator are as follows:

Total average output	5-W
Peak output power	12.5-kW
Pulse repetition rate	180-pps
Optical pulse width	10-μsec
Amplifier gain (measured at peak of pulse)	5000
cw power from stable oscillator	5-W
Amplifier discharge pulse width	275-μsec
Total peak amplifier current	400-mA

Amplifier peak voltage	18-kV
Delay between start of discharge and optical pulse	260-μsec
dc power supply voltage	29-kV
dc power supply current	35-mA
Amplifier total gas pressure	10.35-torr
Helium pressure	6-torr
Nitrogen pressure	1.8-torr
CO_2 pressure	3.8-torr
Gas consumption	6-cubic-ft/hr
Amplifier coolant temperature	14°C

Parameter studies were also made using the three-tube system, which most closely resembles the final recommended transmitter. Except where noted, the system is set at approximately the typical operating condition given above, with the exclusion of the parameter being varied. The results are given below:

(1) Peak power vs optical pulse delay (Figure 6-20) - These curves show the behavior of the peak amplifier output power as a function of the delay time between the beginning of the excitation pulse and the beginning of the optical pulse. Measurements were made for four values of excitation pulse length. The best values are 250 - 300 μsec for both the excitation pulse duration and 250 - 300 μsec for the optical pulse delay.

(2) Energy per pulse and average power vs repetition rate (Figure 6-21) - The average output power of the system was measured as a function of repetition rate. This data was also converted to energy-per-pulse vs repetition rate. The energy-per-pulse peaks at about 100 pps, and falls off above that point because of gas-heating effects. The average power peaks at about 150 pps, and falls off slowly for higher rates.

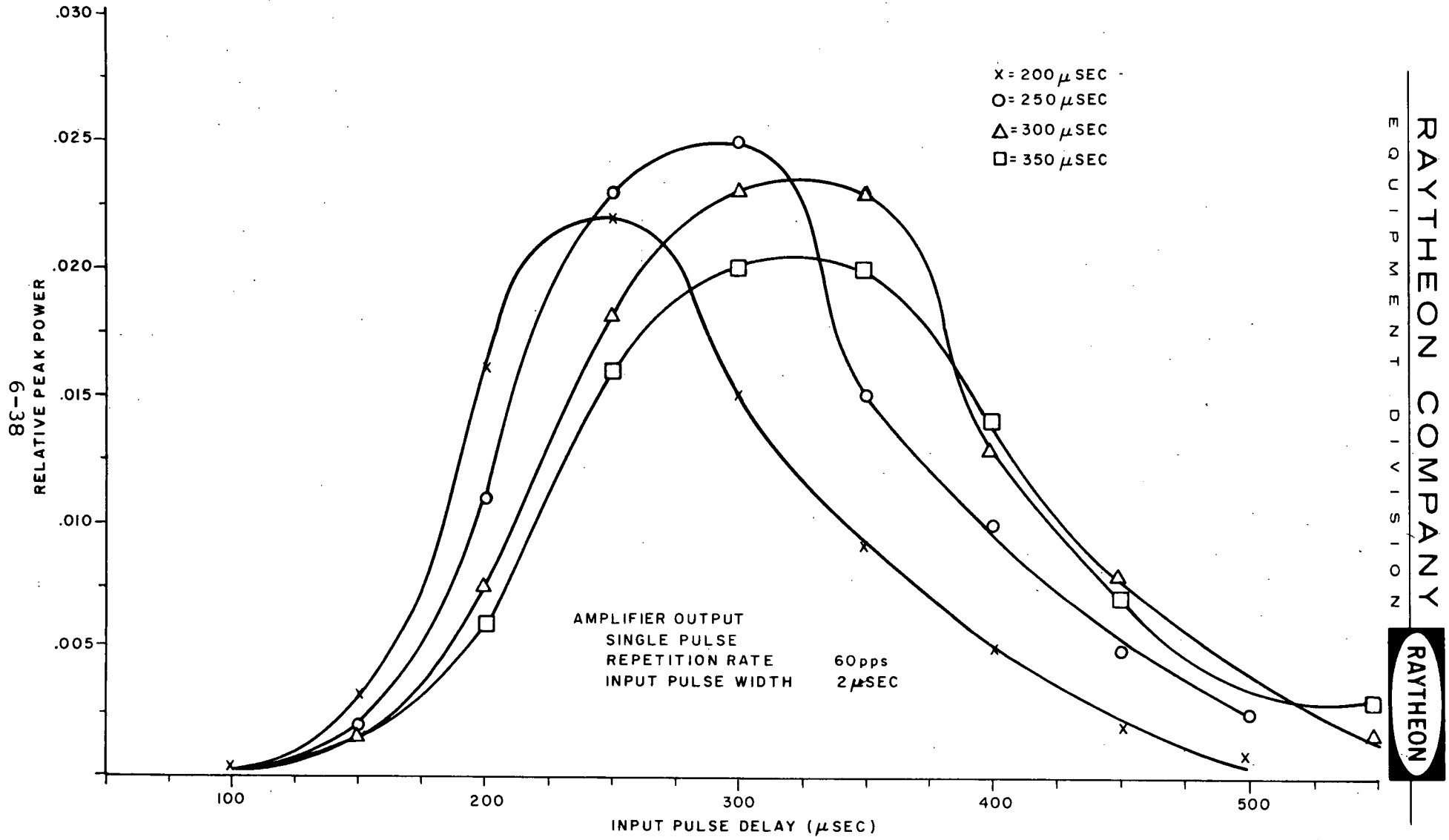

Figure 6-20 Peak Output Power of the Three-Tube CAT Transmitter vs Optical Pulse Delay Time

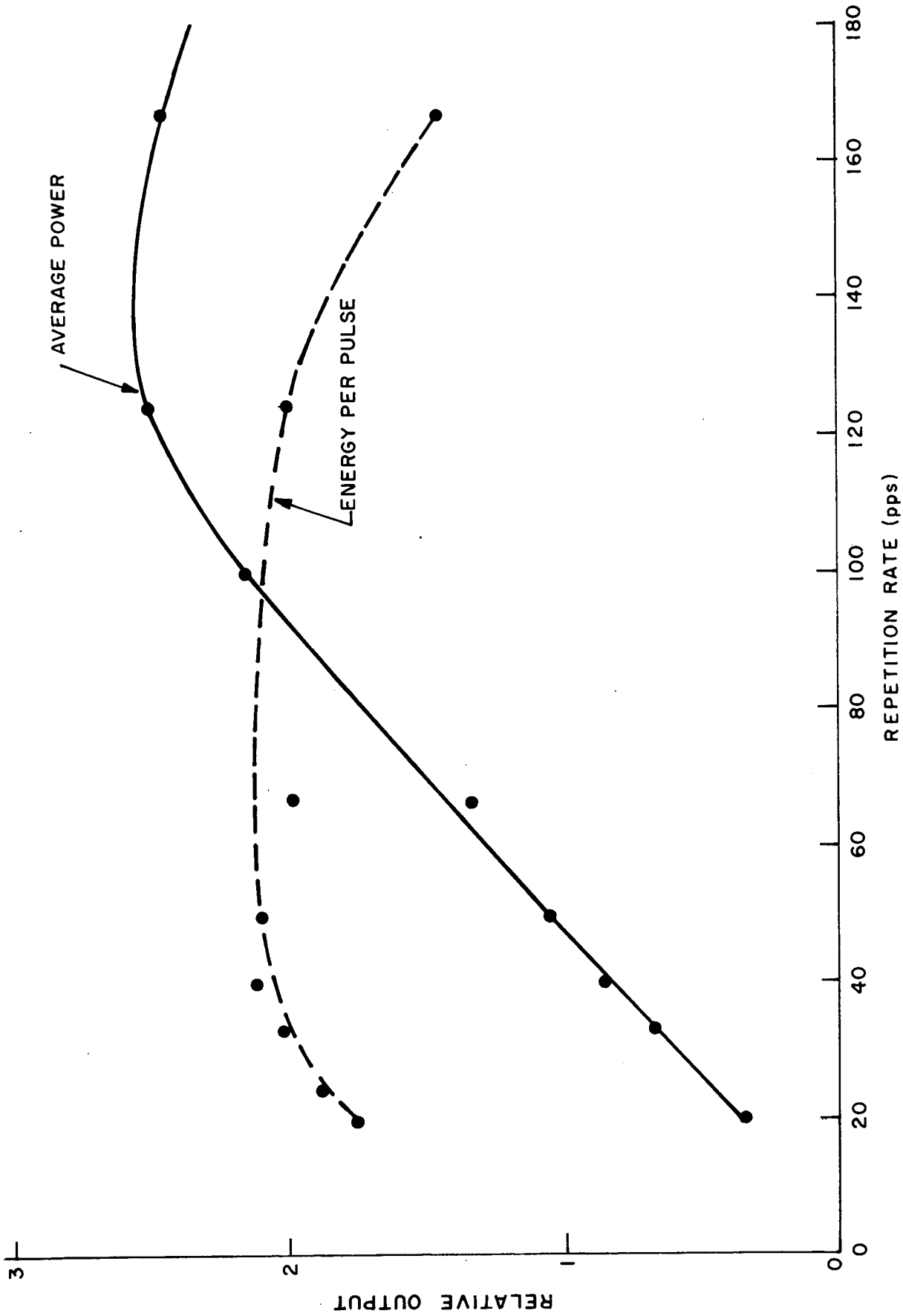

Figure 6-21 Energy Per Pulse and Average Power vs Pulse Repetition Rate for Three Tube CAT Amplifier

(3) Output power vs peak discharge current (Figure 6-22) - It appears that the output power reaches a maximum for a peak discharge current around 600 mA. Increasing the current above this point causes heating effects which lower the output power.

(4) Power output vs pulse length (Figure 6-23) - The output power of the system increases nonlinearly with increasing pulse length. This is due to saturation effects which allow the beginning of the pulse to see more gain than the end. Typical output pulses are shown in Figure 6-24.

6.3.2 WHITE CELL

6.3.2.1 Insertion Loss

A number of gain measurements, to be discussed in detail later, were made on the White cell. Despite the sizable gains measured, little power was extracted from the White cell. This led us to examine the losses of the entire system. The sealed-off source laser had a larger mode diameter than the Freed laser, resulting in a 40-percent power loss through the 3-mm aperture modulator alone. Early measurements of the insertion loss indicated a transmission through the White cell of 12 percent, using 20 passes and 2.15-m radius mirrors. Although this loss was initially attributed to reflective losses at the mirrors, a series of careful measurements in which power was traced through the system showed that only 1/3 of the power incident on the White cell passed through the first Brewster-angle window.

By opening the entrance port aperture to 1/2 inch and using a 4:1 reducing telescope at the White cell input, it was possible to increase the amount of incident power actually entering the cell to $\sim$ 70 percent. With the cell adjusted for 12 bounces, 46 percent of this internal power left the White cell. These measurements showed that a considerable portion of the insertion loss originally ascribed to the mirrors was due to aperturing of the beam from the

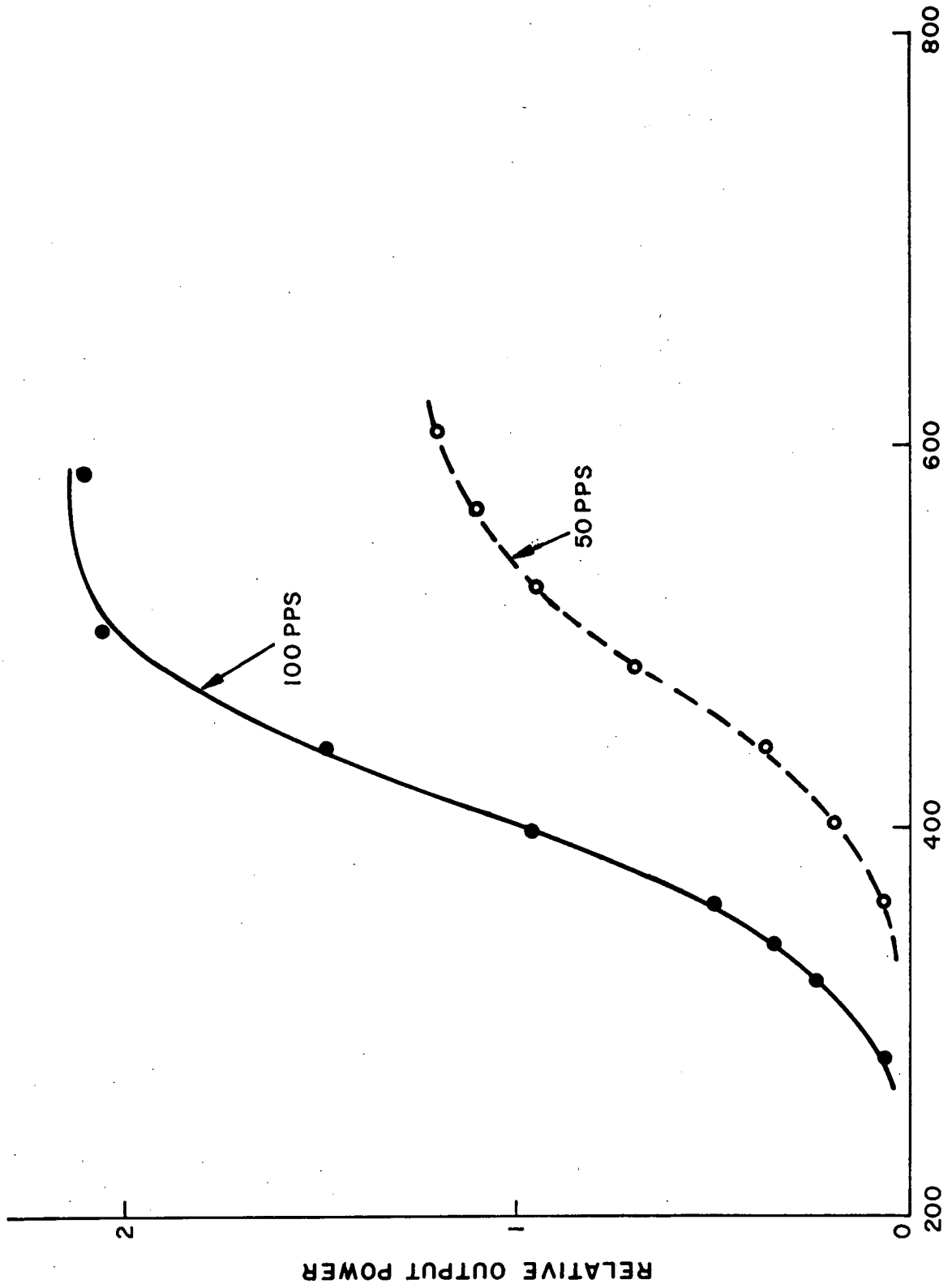

Figure 6-22 Relative Output Power vs Peak Discharge Current for Three Tube Transmitter

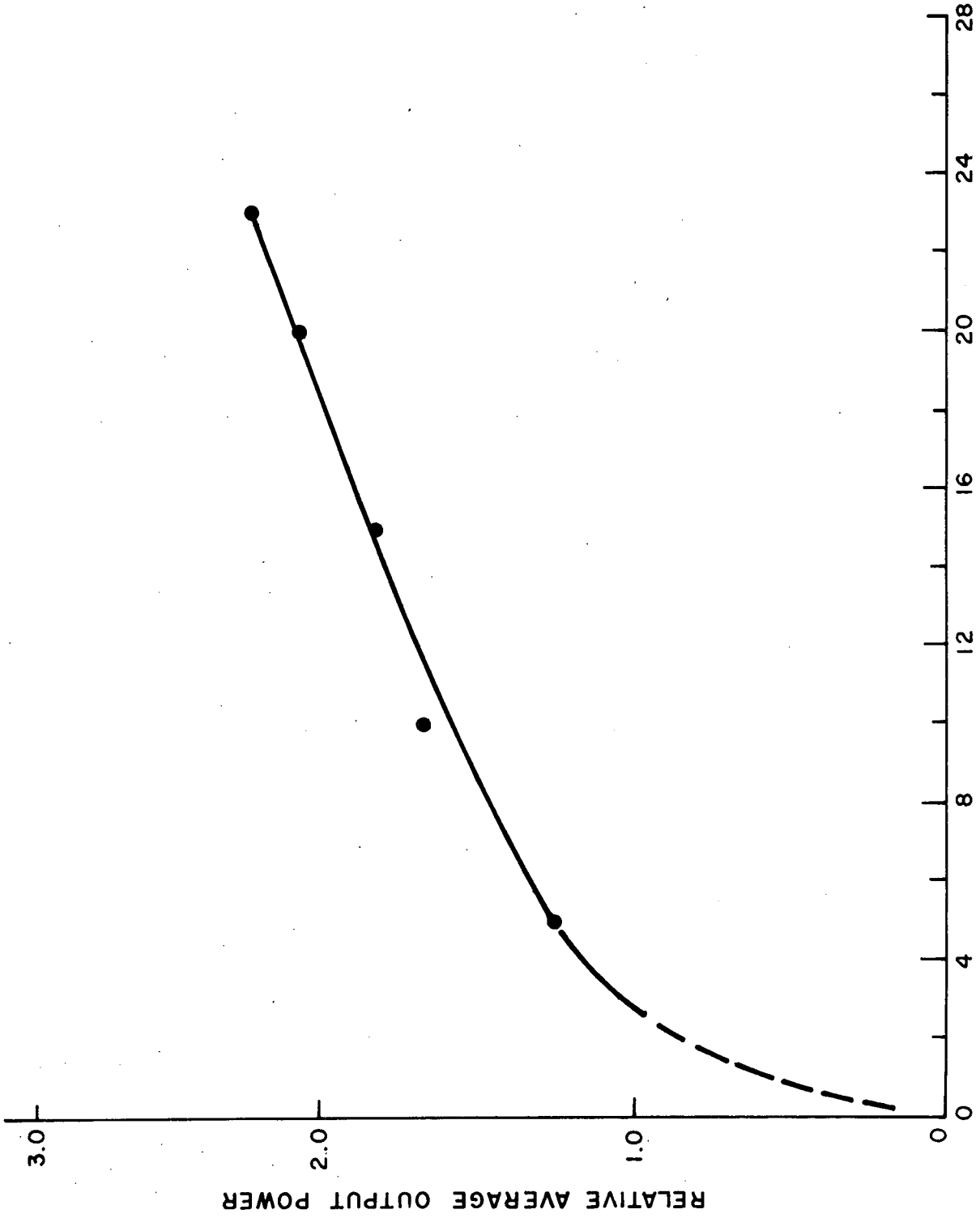

Figure 6-23 Average Output Power vs Optical Pulse Length for Three Tube CAT Transmitter

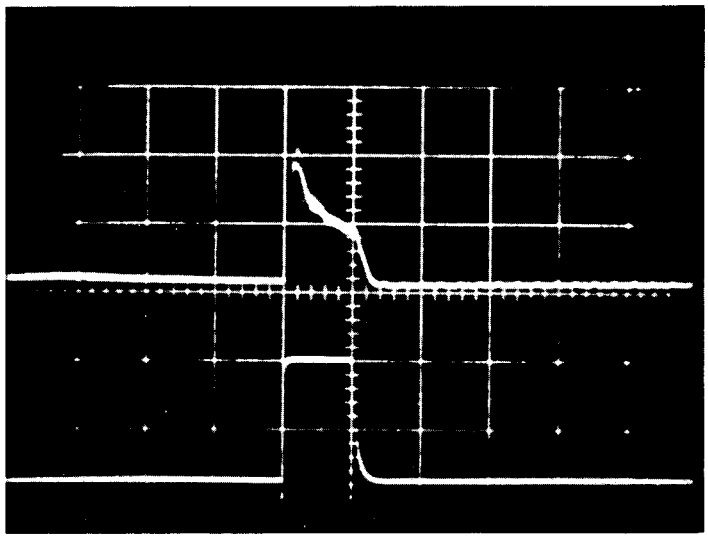

(a)

Amplifier Output and Modulator
Voltage Pulse - 5 μsec pulse

Reproduced from best available copy.

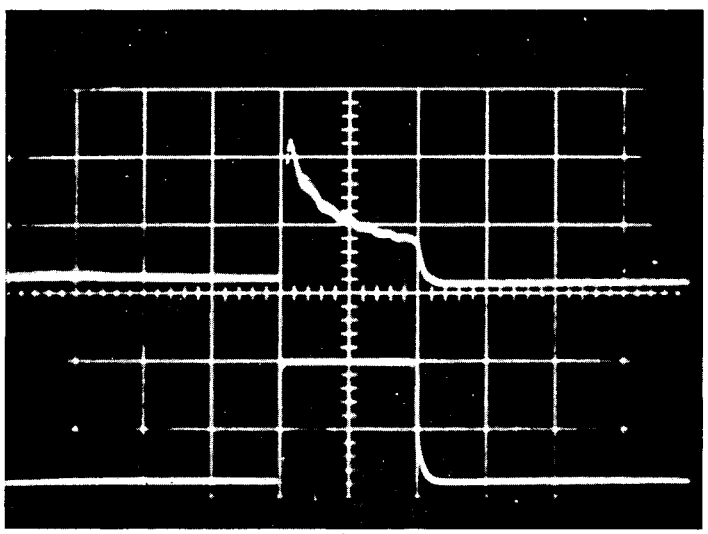

(b)

Amplifier Output and Modulator
Voltage Pulse - 10 μsec Pulse

Figure 6-24 Output of CAT Transmitter vs Time

source laser. Some of the difficulty in extracting power from the White cell was due to this high insertion loss.

6.3.2.2 Gain

Gain measurements were made on the White cell under a number of conditions. Typical gas pressures, as measured at the input, were 1 torr N_2, 1.4 torr CO_2 and 10.5 torr He. The excitation current pulses used were 50-μsec wide with peak amplitudes of 2 to 4 amperes. Utilizing 20 passes, gains obtained ranged from 500 to 16,000. The highest gains, without saturation, were obtained at repetition rates of ~ 50 pps. Figure 6-25 shows a typical amplifier output pulse with saturation.

6.3.2.3 Spurious Oscillations

Because of the high gain achieved in using the White cell system, spurious oscillations occurred which presented a problem. The use of black anodized aluminum masks to cover all but the needed annular region on the mirrors reduced these oscillations. In order to eliminate self-oscillation, however, it was necessary to reduce the number of passes within the cell to 15. Additionally, entrance to the cell was blocked at the highest excitation currents. Even with 15 passes, it was noted that reflections from the mirrors of the oscillator still caused oscillation. These can be minimized, however, by using crossed polarizers with the GaAs modulator. Despite considerable variations in the total amount of power extracted, the presence of the various spurious oscillations limited to ~ 0.25 watts the amount of power that was extracted by the 2-μsec pulse triplets. This result is similar to that found in the case of the linear amplifier where approximately the same amount of power was extracted by the 2-μsec pulses from three or four amplifier tubes. Total power output, however, was greater with four tubes.

The measurements suggest that it would be better to operate the White cell system with fewer passes. Fewer passes would reduce

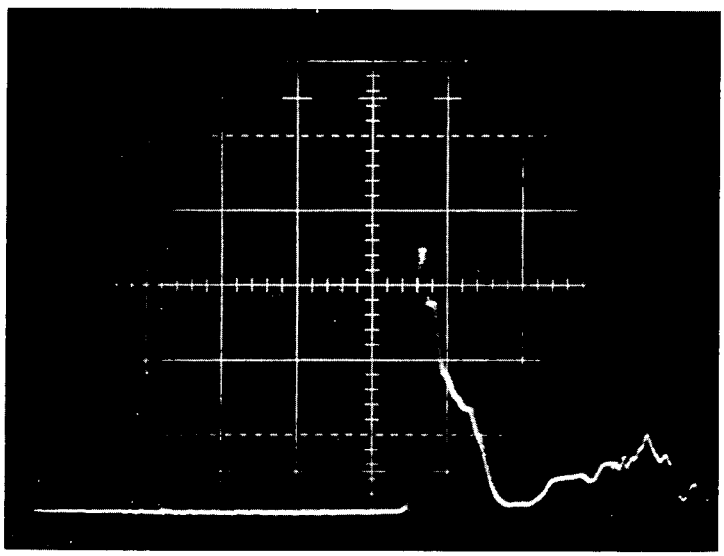

Reproduced from best available copy.

Figure 6-25 Output of White Cell Amplifier vs Time

mirror losses and allow the use of a larger entrance aperture, thereby reducing the insertion-loss problem. With fewer passes, a smaller tube bore could be used, increasing the gain per pass. A modified system, consisting of a 2-inch i.d. tube with an 18-mm aperture and adjusted to give 6 - 9 passes, would be considerably easier to align and use than the present system.

6.4 PROBLEM AREAS AND RECOMMENDATIONS

6.4.1 SPURIOUS OSCILLATIONS

A number of techniques to eliminate spurious oscillations were investigated. The introduction of a pinhole aperture at the focal point of the telescope was quite helpful in reducing spurious oscillations. The aperture consisted of a pinhole in a sheet of blackened Polaroid film. To further reduce reflections from the aperture, the use of apertures consisting of sandblasted, black anodized aluminum plates, with holes drilled at an angle away from the plate normal, should be investigated. Anti-reflection coatings should be applied to all components (such as a lens or a modulator) to prevent unwanted reflections. The use of single-layer antireflection coatings on the GaAs modulator crystals reduced the spurious-oscillation problem considerably. In spite of that, the coatings were not entirely satisfactory since a reflectance varying between 5 and 10 percent per face was still present. Even the multi-layer AR coatings investigated (provided by Spectrum Systems) left a reflectance of about 3 percent per surface. Multilayer coatings to reduce this reflection to less than 1 percent per surface will be needed and may require some work with vendors to develop. Alignment of components to prevent residual reflections from entering the amplifier, also reduces the tendency of the amplifier to oscillate. When the transmitter is incorporated into the final system with its output optics, care will be needed to eliminate reflections at the output end of the amplifier. It may be desirable to incorporate a gas bleaching cell filled with hot CO_2 at this position to provide some decoupling.

6.4.2 ELECTRO-OPTIC MODULATOR

There are a number of areas in which the performance of the electro-optic modulator should be improved. As mentioned above, the residual reflectivity from the single-layer anti-reflection coated surfaces of the modulator causes spurious oscillations. In addition to causing spurious oscillations in the amplifier, the residual reflections from the parallel surfaces of the GaAs modulator produce a Fabry-Perot resonator effect. This in turn produces some undesirable results, such as the occasional presence of interference fringes on the output of the modulator, and the variation of the transmission of the modulator with temperature caused by length tuning. The spatial distortion of the laser mode passing through the modulator crystal should be examined to determine its effect on the amplifier output.

The voltage required by the 0.5 x 0.5 x 5 cm modulator, in excess of 8 kV, should be reduced by using a crystal of 6- or 7-cm length.

Means of eliminating the acoustic ringing in the modulator crystal will have to be investigated. One possibility is to use a loaded resonant circuit in the drive line in order to reduce the circuit Q at the ringing frequency. Another possibility is to reduce the risetime of the driving pulse, thus reducing the drive at the ringing frequency. The use of a linear amplifier to drive the modulator would allow the pulse risetime to be varied and would, further, allow shaping the drive pulse so as to produce a more rectangular output pulse. The recent development of large-size high-resistivity crystals of CdTe, whose modulation figure of merit $n_o^3 r_{41}$ is approximately twice that of GaAs*, offers the possibility of making a modulator requiring a substantially lower drive voltage than for GaAs.[6] If the piezoelectric constant of DcTe,

*n_o is the refractive index and r_{41} the unclamped electro-optic efficient.

(whose room-temperature value is not known) is not larger than that of GaAs, the acoustic ringing should also be reduced.

6.4.3 OUTPUT INVESTIGATIONS

Properties of the amplifier output in both the spatial and the frequency domain must be better characterized. If the spatial mode of the oscillator is still satisfactory after passing through the modulator and the polarizers, the shape of the amplifier output mode should be investigated. The use of burn patterns on thermofax paper taken at a distance should reveal gross features of the beam profile. A more detailed study will require scanning a fast detector across the beam. This will also show the extent to which saturation effects flatten the beam profile at the center.

Frequency stability of the system will have to be investigated. The stability of the cw signal from the local oscillator during the pulsing of the amplifier should first be investigated by heterodyning it with a separate local oscillator. The output signal from the pulsed amplifier should then, in turn, be examined by heterodyning it with a separate stable CO_2 oscillator.

6.4.4 COOLING

The present system uses closed-cycle liquid cooling with a liquid-to-liquid heat exchanger. It should be possible to use a liquid-to-air heat exchanger, thus eliminating the need for external water lines. It may also be possible to construct amplifier tubes using metal cooling fins and forced-air cooling. However, so long as the stable oscillator still requires liquid cooling, the advantage in air cooling the amplifier seems marginal.

6.4.5 MECHANICAL AND ELECTRICAL STABILITY

The experiments on the transmitter described here involved components mounted on two separate tables with a total length of 18 ft. Although the tables were mounted on heavy concrete bases it became

evident that mechanical alignment was a problem and that the entire transmitter should be mounted on one rigid table. In addition, after the measurements showed that the entire usable gain of the system could be extracted from three tubes with 1-1/2 meters of discharge length each, it was clear that it would be desirable to design an amplifier using shorter tubes. This would reduce the operating voltage of the tubes, now close to 30 kV, and permit a more compact system. Figure 6-26 shows the optical design for a Mark II CAT transmitter incorporating these ideas. All the components are now on one table having an overall length of 8 ft. The tubes, which have a 1-meter long by 20-mm i.d. discharge section, are designed for use with flowing gas and employ simple in-line electrodes. Figure 6-27 shows the electrical diagram for the system, which is essentially the same as that used in this work. Figures 6-28 and 6-29 show the proposed gas handling and cooling systems respectively.

6.4.6 SEALED OPERATIONS

The gain measurements on the sealed-off tube indicated that a gain of at least 7.4 dB per meter could be obtained at 70 pulses-per-second. However, further testing is needed; first, to determine the optimum fill and pulse length for sealed conditions, and, second, to investigate tube life under these conditions. Although the 6-inch nickel re-entrant electrodes used in this tube appeared to be satisfactory in preliminary experiments, additional evaluation is needed.

6.5 HETERODYNE OPTICS

The airborne research type instrument for laser Doppler CAT detection utilizes the optical heterodyne approach for determining the velocity distribution of aerosols suspended in the atmosphere. The following paragraphs discuss methods of configuring the various components within the transmitter in order to heterodyne the return signal beam with a local oscillator beam.

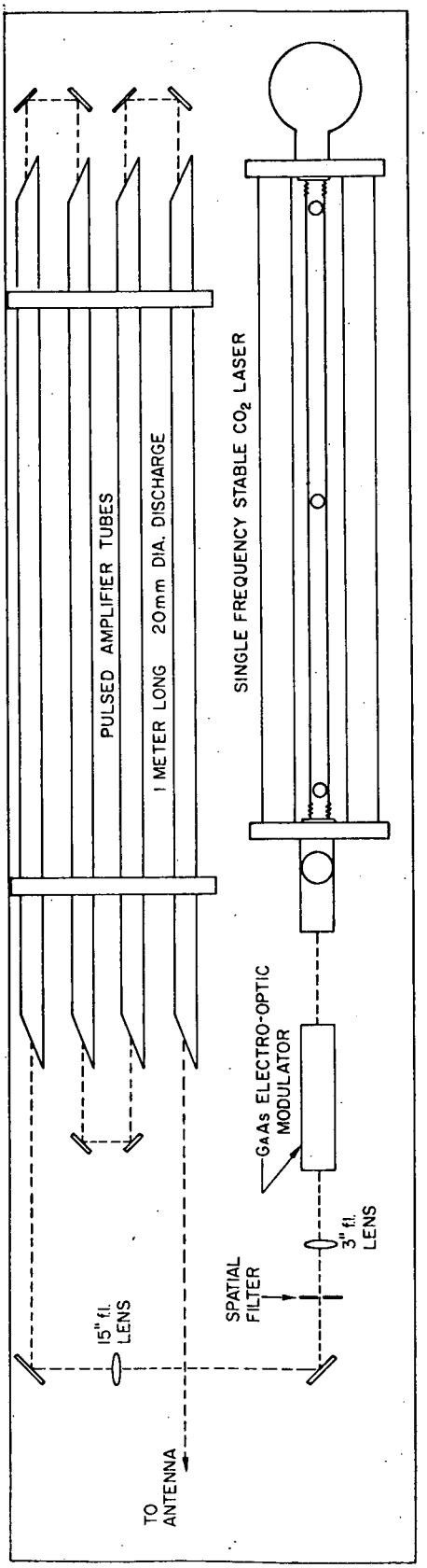

Figure 6-26 Optical Design of Mark II CAT Transmitter

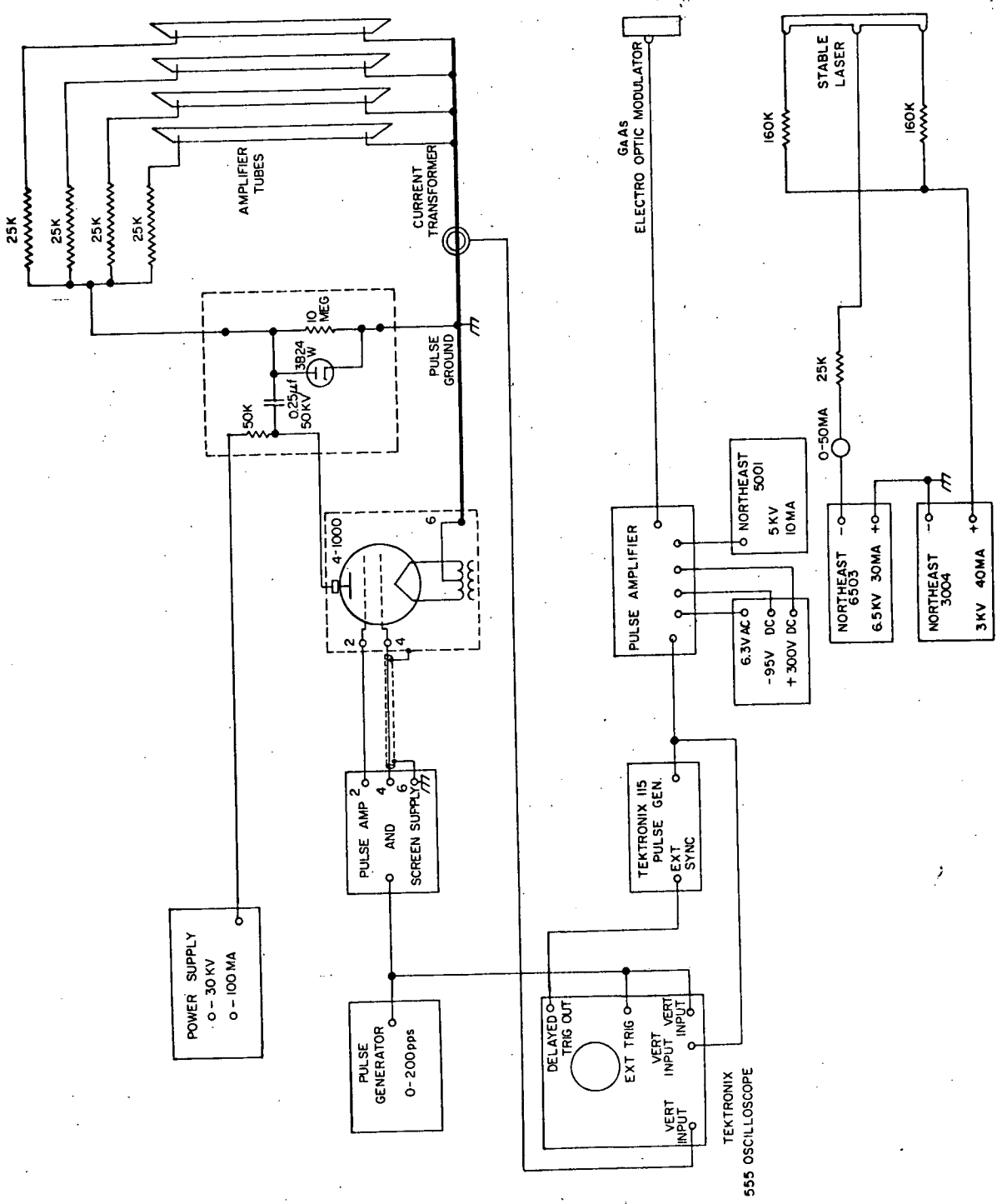

Figure 6-27 Electrical Diagram for CAT Transmitter

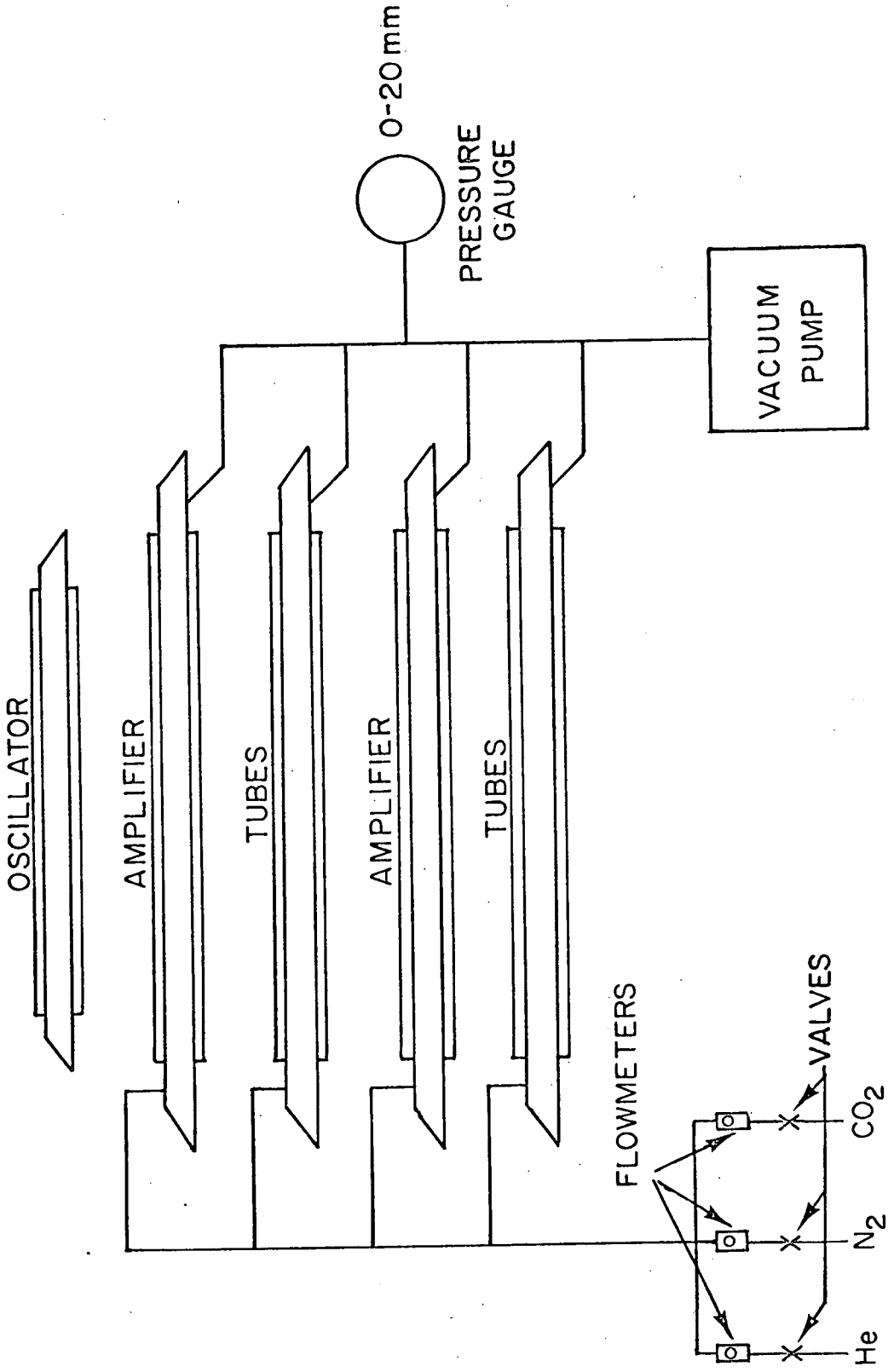

Figure 6-28 Gas Flow System for CAT Transmitter

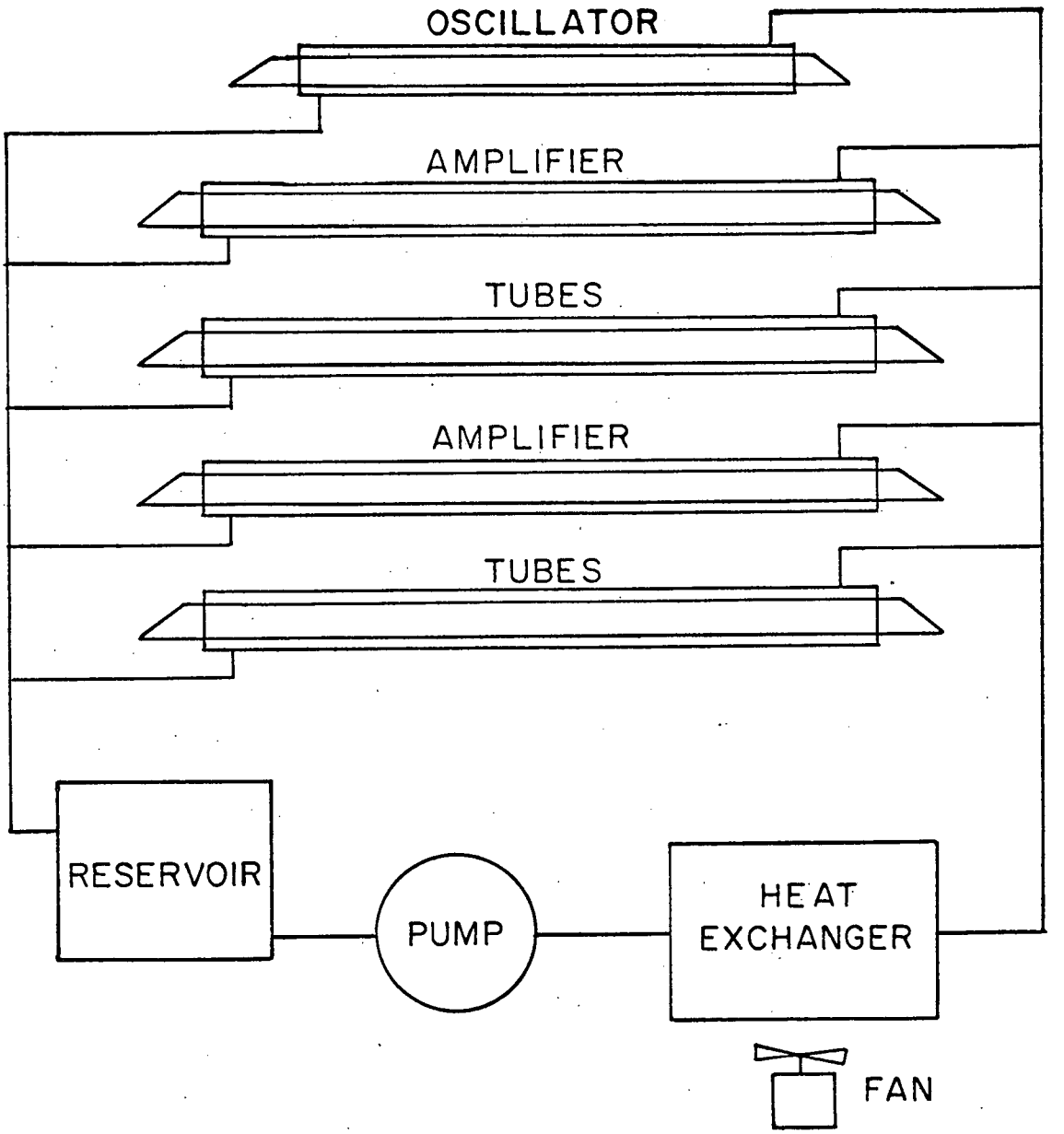

Figure 6-29 Cooling System for Mark II CAT Transmitter

The configurations are shown as linear geometries; i.e., the laser oscillator, modulator, amplifier and telescope are in a straight line. Visualization of the heterodyne configurations is facilitated by this type of layout; however, the transmitter to be developed will have many turn-around mirrors and will be folded many times.

The packaging arrangement is shown schematically in Figure 6-30. Here, the laser oscillator discharge tube and eight laser amplifier discharge tubes are packaged in a side-by-side arrangement with turn-around mirrors at the back end. At the front end of the tubes there is an open volume which will contain the more critical components of the system. These components include (1) the modulator, (2) the transmit-receive separator, (3) the recombining beamsplitter, (4) a quarter wave or a half wave plate, (5) polarizer, (6) the beam-splitter used for obtaining a local oscillator beam from the laser oscillator output beam, and (7) the detector and its lens. For more complex configurations, other components, such as a spinning disc, an electro-optic switch, and a Faraday isolator can be located at the front end of the tubes. Also located here will be several turn-around mirrors, one or two small telescopes, and several high precision mechanical alignment fixtures which will be used to orient the various components and to assure heterodyne recombination.

6.5.1 TRANSMIT-RECEIVE BEAMSPLITTER CONFIGURATION

Several types of interferometers that perform optical heterodyne measurements have been used successfully. The configuration shown in Figure 6-31 which uses a 50-percent beamsplitter as a transmit-receive separator is in reality a modification of a Mach-Zehnder interferometer. The other configurations discussed in the paragraphs that follow are also modifications of a Mach-Zehnder interferometer. There are, however, significant differences, advantages and disadvantages in these diverse variations. The

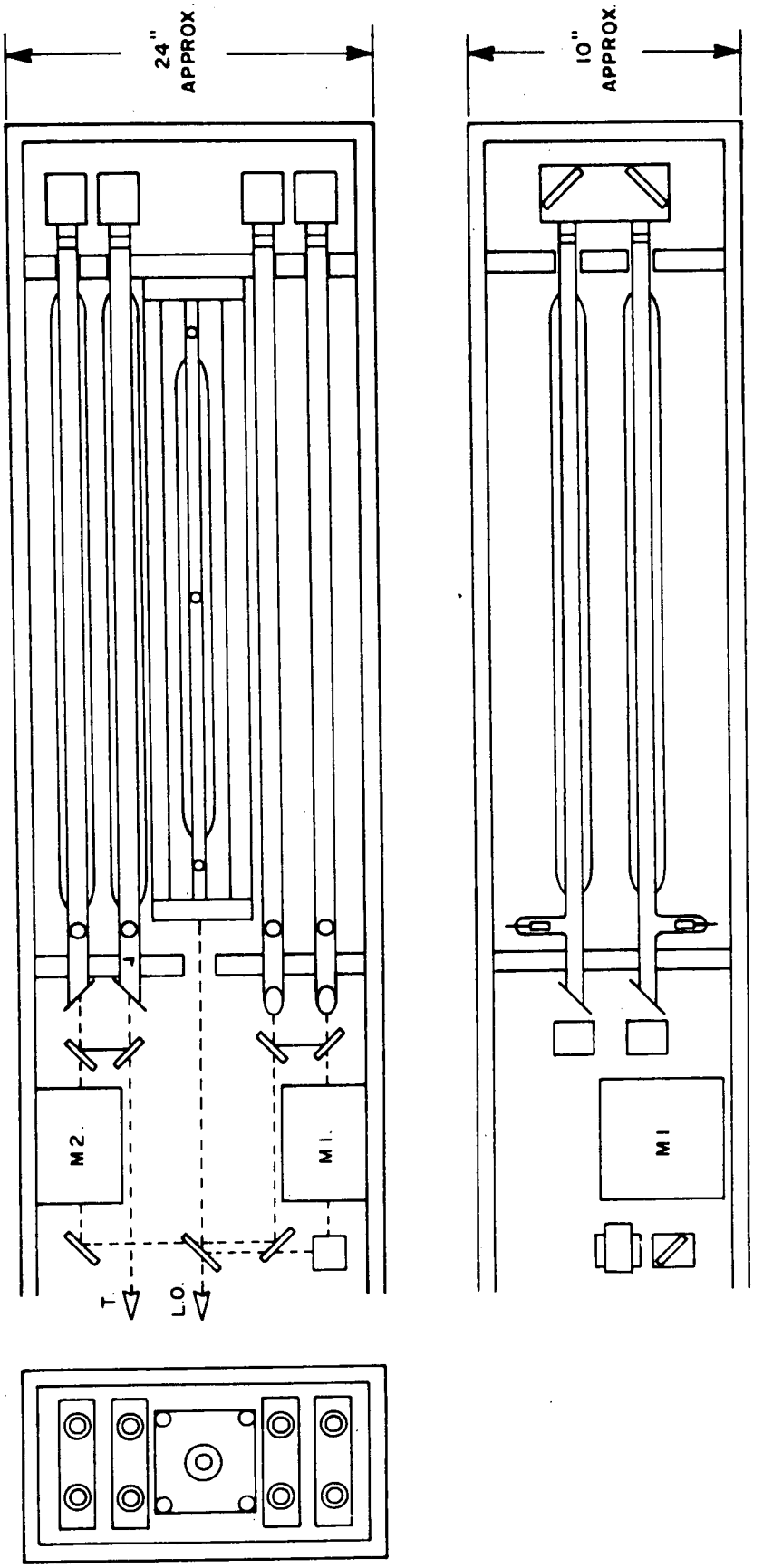

Figure 6-30 Layout for CAT Transmitter

transmit-receive beamsplitter configuration, the least complicated of the lot, serves as an introduction to the more sophisticated versions.

The modified Mach-Zehnder interferometers discussed herein have two features in common: (1) the beam to be transmitted is divided by one beamsplitter at the output of the laser oscillator, and (2) the local oscillator beam and the return signal beam are recombined and divided by a second beamsplitter. In contrast, a Michelson interferometer separates and recombines on the same beamsplitter. Provision is incorporated in the local oscillator and signal beams (when necessary) by means of a fractional wave plate.

The configuration of Figure 6-31 uses a 50-percent beamsplitter for transmit-receive separation; i.e., on transmission through the splitter one-half of the beam is lost. This gives a net loss of 4X for the beamsplitter. Care must be exercised to insure proper beam recombination at the last beamsplitter.

It should be noted that the modulator rotates the polarization of the beam by 90 degrees while the voltage is applied for the transmission (or pulse) mode, and that the polarization of the beam emerging from the telescope is in the plane of the paper. The radiation scattered from the atmosphere will have the same polarization as that of the transmitted beam, provided that the aerosols are small compared to the 10.6 μm wavelength. Therefore, the return beam having its polarization vector in the plane of the paper reenters the optical system and reflects from the 50 percent beamsplitter. The local oscillator beam passes through a half wave plate so that its polarization is also in the plane of the paper; then it is combined with the return beam on the last beamsplitter (bottom right beamsplitter in the Mach-Zehnder configuration of Figure 6-31.

Beam expanders consisting of two NaCl or KCl lenses may be included (but are not shown) in these configurations to match the

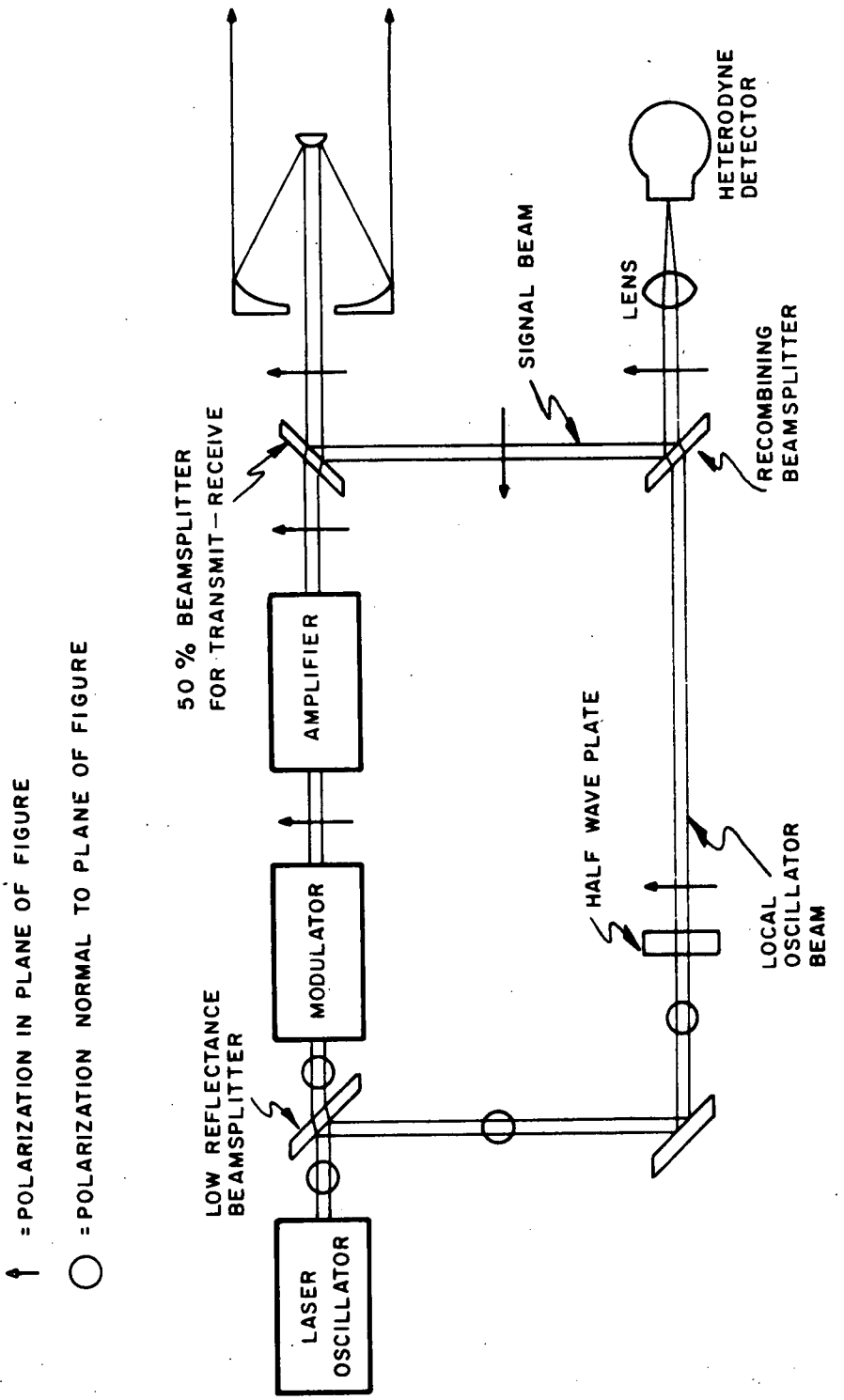

Figure 6-31 Transmit-Receive Beamsplitter Configuration

diameters of the local oscillator beam and the signal beam. These expanders may also be used to match the diameter of the transmitted beam to the apertures along the propagation path, such as the modulator, the amplifier, and telescope apertures.

This configuration has an advantage over some of the other configurations in that the modulator need not be held open in order for a return signal to be detected. It has a disadvantage because of the fact that the isolation between the transmitted and received beams is not maximized. Scattering of the transmitted beam from the beamsplitter has a direct propagation path to the heterodyne detector. Also, the amplifier may have a tendency toward self-oscillation by means of reflections from the front end of the modulator and from the secondary mirror of the telescope.

6.5.2 CIRCULAR POLARIZATION CONFIGURATION

This technique shown in Figure 6-32 is similar to the previously discussed transmit-receive beamsplitter configuration of Figure 6-31. The significant difference between the two configurations is the method used to separate the transmitted and received beams. In the circular polarization method, the linearly-polarized beam emerging from the amplifier is directed through a Bewster angle polarizer and a quarter-wave plate so that the polarization of the transmitted beam is circular. The return beam is also circularly polarized provided the scattering aerosols are small compared to the 10.6 μm wavelength. The return beam reflects from the Brewster angle polarizer with little loss. Therefore, this configuration is approximately four times more sensitive than the transmit-receive beamsplitter configuration.

The circular polarization technique has an additional advantage over the configuration discussed previously: specifically, the amplifier, which is of necessity a high gain device, can be forced to oscillate if the feedback at its ends is sufficiently high. The feedback in this case is the sum of the unwanted

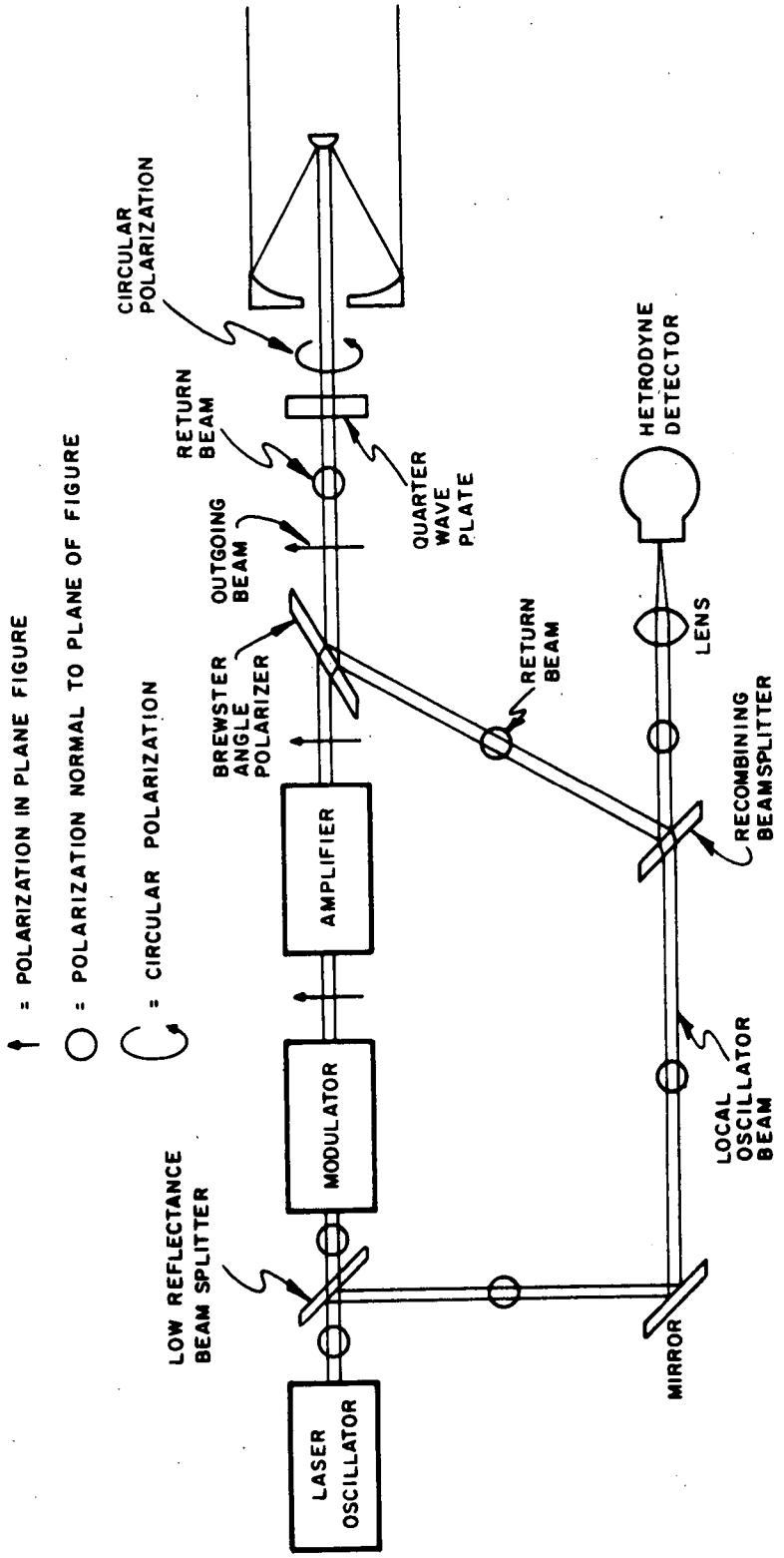

Figure 6-32 Circular Polarization Configuration

scattering of amplifier spontaneous emission from the various components in the optical system at both ends of the amplifier. The circular polarization technique minimizes the scattering from the telescope elements by rejecting a majority of the returning scattered spontaneous radiation in the same manner that the Brewster angle polarizer and quarter-wave plate prevent the wanted return signal beam from entering the amplifier.

In other words, one polarization component of the spontaneous emission is rejected by the Brewster angle polarizer on the way out. The other polarization component transmits through the polarizer once and through the quarter wave plate twice so that its polarization is rotated 90 degrees, and then reflects from, or is rejected by, the polarizer. This has the effect of reducing the feedback so that the self-oscillation threshold is increased; i.e., the amplifier can be pumped to higher gain without self-oscillation.

6.5.3 SPINNING DISC CONFIGURATION

The configuration of Figure 6-33 includes a spinning disc used as a transmit-receive switch located between the amplifier and the reflecting telescope. This configuration will be used only if all previously described isolation techniques prove unsatisfactory.

The disc chops the radiation at the common focus of the two adjacent lenses. On transmission, the focused radiation emerging from the amplifier passes through a hole in the disc. Transmitting by this technique minimizes scattering that causes radiation from the main pulse to fall on the detector and subsequently generate unwanted noise.

The disc rotates so that the hole leaves the focal region, and causes a mirrored portion of the disc to enter in its place. This has two major effects. First, the return signal beam is reflected from the disc and directed toward the recombining mirror. This gives negligible loss in signal, making the sensitivity of this

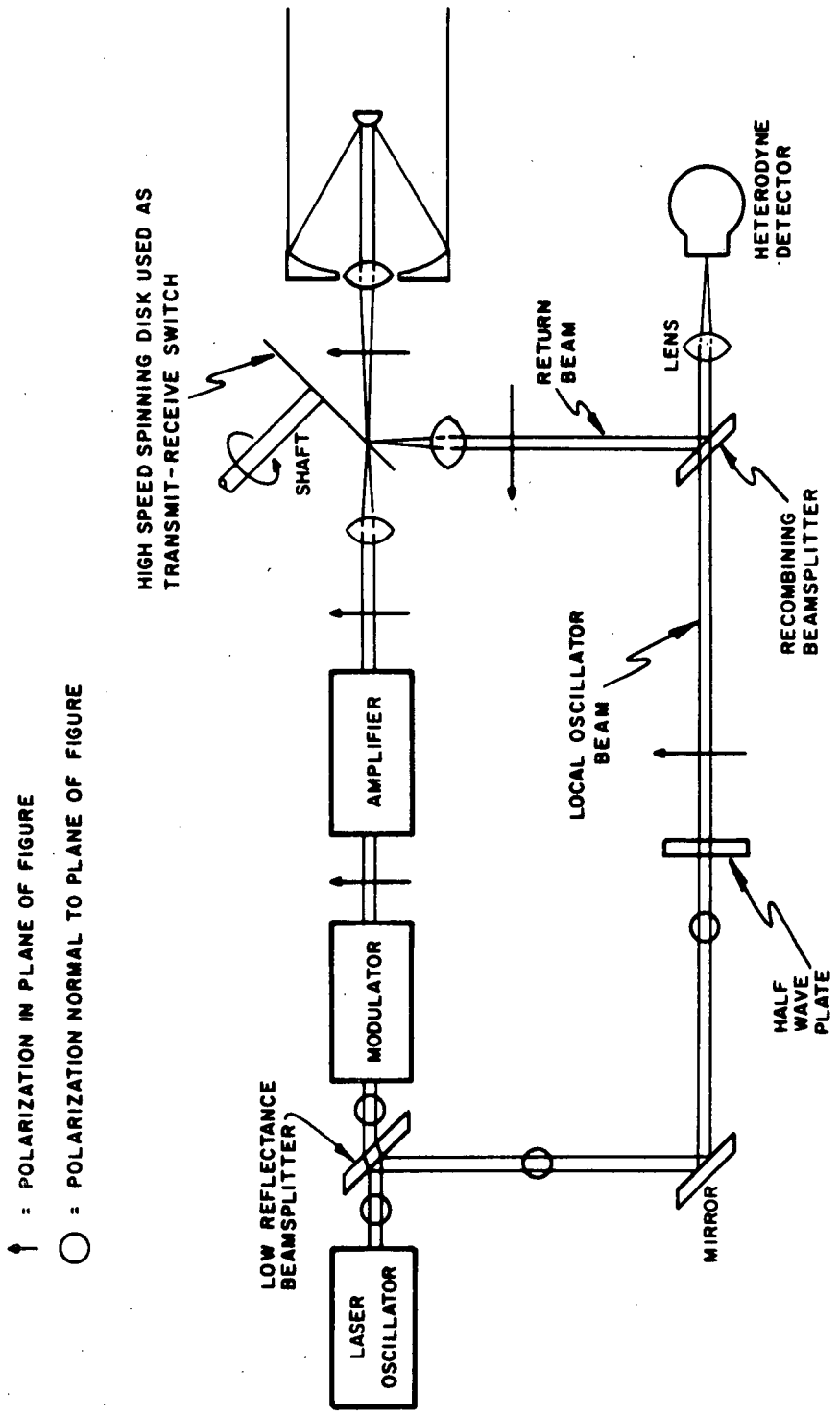

Figure 6-33 Spinning Disc Configuration

configuration comparable to that of the circular polarization technique. Second, the radiation leaking through the amplifier after the primary pulse is transmitted is also reflected from the disc, but is directed away from the detector. This reflection reduces or minimizes another source of unwanted radiation that could possibly generate unwanted noise in the electronics of the detector and receiver and interfere with the detection of a weak signal.

The design, fabrication, mounting, alignment and use of the disc in the system must be performed carefully. The disc, which is one of the optical elements in a diffraction limited Doppler heterodyne system, must itself satisfy the diffraction limit condition while rotating at high angular rates. Translation, or shaft runout, must also be minimized to assure beam overlap.

6.6 SUMMARY

A transmitter has been designed that provides a peak-pulse power of 5 kW, pulse widths (that can be varied) of 2 μsec, and a pulse repetition rate of 200 pps. Problem areas were discussed and recommendations made.

SECTION 6 REFERENCES

1. White, J. U., J. Opt. Soc. Am. 32, 295 (1942).
2. Dezenberg, G. J., and Merritt, J. A., Appl. Opt. 6, 154, (1967).
3. Kogelnik, H. and Bridges, T. J., IEEE J. Quant. Elect. QE-3, 95 (1967).
4. Hieslmair, H., Bickard, C. J., and Fulton, J. M., IEEE J. Quant. Elect. QE-6, 86, (1970).
5. Carbone, R. J., IEEE J. Quant. Elect. QE-5, 48, (1969) and erratum in QE-6, 241, (1970).
6. Kiefer, J. E. and Yariv, Appl. Phys. Letters 15, 26, (1969).

SECTION 7

CONCLUSIONS

This section summarizes the conclusions evolved during the course of the analytical, experimental, and developmental work performed on the CO_2 laser-Doppler instrumentation for detection of CAT. The conclusions which have been stated previously in other sections of this report are repeated here for reasons of clarity. They are as follows:

1. Clear air turbulence is characterized by a spectrum relating energy to spatial frequency.
2. The amount of turbulent energy in the atmosphere is proportional to a parameter, ϵ, the dissipation rate.
3. The width of the Doppler spectrum is proportional to ϵ.
4. Therefore, the width of the Doppler spectrum is a measure of the amount of atmospheric turbulent energy.
5. A CO_2 pulsed amplifier has been designed developed, and successfully tested.
6. The CAT transmitter will provide a peak output pulse power of 5 kW, a 10-mj pulse of 2 μs duration with a variation capability of 0.5 to 10 μs and a pulse repetition rate of 200 pps.
7. Operation of ranges at a considerable distance from the aircraft should be possible with the integration of the returns of approximately 100 pulses.

8. Design drawings of the CAT transmitter have been completed.

9. Due to lack of experimental data, it is not possible to determine the optimal transmitter pulse length.

10. The CAT receiver should be capable of operating efficiently with a variety of pulse lengths.

11. A versatile receiver capable of operating with filter bandwidths of 125 kHz, 250 kHz, and 500 kHz has been designed.

12. An RVI-type display with integration occurring on the face of the oscilloscope should be used.

13. Additionally, tape recording of the turbulence in an individual range cell could be provided.

14. It has been shown that the feasibility transmitter built and tested under this program should be capable of detecting clear air turbulence at a considerable distance in front of an aircraft.

SECTION 8

RECOMMENDATIONS

As a result of this program, Raytheon Company makes the following recommendations:

1. The development of the CO_2 laser transmitter should continue through the fabrication and flight-test phases.

2. The aircraft to be used for flight testing should be carefully selected to ensure that it has sufficient size and electrical power for the system.

3. Due to lack of sufficient atmospheric experimental information, the transmitter should have a variable pulsewidth, and the receiver should have a variable resolution bandwidth.

4. An RVI display should be used with the possibility of adding a tape recorder.

5. A continuing program should be implemented, aimed at updating the CAT detection capability of the laser-optical radar system, commensurate with contemporary meteorological data.

6. A program study should be instituted and directed toward utilizing additionally acquired data for the possible design of a less expensive and less complex receiver system.

APPENDIX A

CLEAR AIR TURBULENCE BIBLIOGRAPHY

1964-1968

The following bibliography has been selected from recent literature (1964-1968) on the basis of its potential utility to the theoretician and experimentalist interested in the creation of an airborne clear air turbulence detector.

Atlas, D., et al, "Optimizing the Radar Detection of Clear Turbulence", AFCRL-ERP-248, AFCRL-66-854, L. G. Hanscom Field, Mass., Apr. 66, Published in Jour. of App. Meteor. v.5, No.4, pp.450-460, Aug. 1966.

Breece, R. C., et al, "Design Study of Laser Radar for Detection of Clear Air Turbulence", Space and Information Systems Div., North American Aviation, Inc., Downey, Calif., Final Report, Apr. 65-15 Apr. 66, June 66, Rept. No.SID-66-450, AFCRL 66-354, AD-634886.

Clear Air Turbulence Meering, 23-24 Feb. 66, Soc. of Auto. Eng., Inc., New York, New York 10017.

Clear Air Turbulence Meeting, 26-27 Apr. 65, Department of the Air Force, Washington, D. C., AD-668080.

Colson, D., "Analysis of Clear Air Turbulence During Selected 5-Day Data Periods, "Weather Bureau, Silver Spring, Md., Techniques Development Lab., Final Rept., Dec. 66, AD-648610.

Endlich, R. M. and Mancuso, R. L., "The Turbulence Climatology of the United States Between 20,000 and 45,000 Feet Estimated from Aircraft Reports and Meteorological Data," Stanford Research Inst., Menlo Park, Calif., AFCRL-68-0337, 1968.

Endlich, R. M., et al, "Forecasting Clear Air Turbulence by Computer Techniques", Stanford Research Inst., Menlo Park, Calif., Final Report, Sept. 67, AD-664721.

Endlich, R. M., et al, "Techniques for Determining a World-Wide Climatology of Turbulence through Use of Meteorological Data," Stanford Research Inst., Menlo Park, Calif., May 1966.

Endlich, R. M., et al, "Studies of the Climatology of Winds, Temperature, and Turbulence in Jet Streams", Stanford Research Inst., Menlo Park, Calif., Final Report, Oct. 64, AFCRL 64834, AD-608773.

Endlich, R. M., et al, "Clear Air Turbulence and its Analysis by Use of Rawinsonde Data", Stanford Research Inst., Menlo Park, Calif., Final Report, Jun. 64, AD-603570.

Franken, P. A., "Airborne Investigations of Clear Air Turbulence with Optical Radar", Michigan Univ., Ann Arbor, Progress Report, Dec. 65, AD-635030.

Glover, K. M., et al, "Radar, Aircraft, and Meteorological Investigation of Clear Air Turbulence", Proc. 13th Radar Meteorology Conf. Amer. Meteor. Soc., Boston, Mass., pp.242-246, 1968.

Hardy, K. R., "Radar Investigation of Clear Air Turbulence", in Proc. of the OAR Research Applications Conference, 21 March 1968, Vol. 1, Mar. 68, AD-666800.

Hardy, K. R., et al, "Multiwavelength Backscatter from the Clear Atmosphere", AFCRL-ERP-191, AFCRL-66-308, L. G. Hanscom Field, Mass., Dec. 65, AD-635317, Published in Jour. of Geophys. Rsch. V.71, No.6, pp.1537-52, March 15, 1966.

Helvey, R. A., "Observations of Stratospheric Clear Air Turbulence and Mountain Waves Over the Sierra Nevada Mounts: An Analysis of the U-2 Flights of 13-14 May 1964," Univ. of California at Los Angeles, Dept. of Meteorology, Final Report, 14 June 64-14 Sept. 67, Dec. 67, AFCRL 68-0001, AD-667222.

Kadlec, P. W., "Flight Observations of Atmospheric Turbulence," Final Report, June 66, FAA-RD 66-72, AD-643554.

Long, R. R., "Vertical Velocities in Clear Air Turbulence", Boeing Scientific Research Laboratories, Seattle, Wash., Boeing Document DI-82-0738, 1968.

Mather, G. K., "Flight Evaluation of an Infrared Spectrometer as a Clear Air Turbulence Detector", May 67, NAE, FAA-RD, LR-477, 66-70, AD-819533.

McLean, G., "An Investigation into the Use of Temperature Gradients as an In-Flight Warning of Impending Clear Air Turbulence", Report No.ERP-85, AFCRL-65-117, L. G. Hanscom Field, Mass. Feb. 65, AD-613691.

Nanevicz, J. E., et al, "Correlation Between Clear Air Turbulence and Aircraft Electrical Activity", Stanford Research Inst., Menlo Park, Calif., Final Report, Oct. 63 - Aug. 65, Oct. 65, AFCRL-65-614, AD-625309.

Panofsky, H. A., et al, "Case Studies of the Distribution of CAT in the Troposphere and Stratosphere", J. Appl. Met. V.7, No.3, pp.384-389, 1968.

Penn, S., et al, "Mesoscale Structure of the Atmosphere in Regions of Clear Air Turbulence, Vol. 1, AFCRL-67-0115, L. G. Hanscom Field, Mass., Apr. 67, AD-654267.

Reiter, E. R., "Recent Advances in the Study of Clear Air Turbulence (CAT)", U.S. Navy Weather Research Facility, Norfolk, Virginia, NWRF15-0468-136, 1968.

Reiter, E. R. and Lester, P. F., "Richardson's Number in the Free Atmosphere", Archiv. Meteor. Geophys, Bioklim. Sec. A, 17(1): 1-7, 1968.

Serebreny, S., et al, "The Distribution of Clear Air Turbulence Reports and Cloud Patterns as Seen in Satellite Photographs", Stanford Research Inst., Menlo Park, Calif., Final Report, Jan. 64.

Shur, G. N., "The Spectral Structure of Turbulence in a Free Atmosphere Based on Data Obtained by Aircraft", Redstone Scientific Information Center, Redstone Arsenal, Ala., Report No. RSIC-543, June 66, AD-637728.

Smirnova, G. A., "Passive-Reflector Experiments in Radar Measurement of the Turbulence of the Clear Sky", Amer. Meteor. Soc., Boston, Mass. Jan. 66, Report No.T-R-517, AD-630553.

Tenbroek, H. W., et al, "Low Frequency Electric Field Characteristics of Clear Air Turbulence", Final Report 15 Mar. 66 - 15 July 67, July 67, Report. No.12037-FRI, Honeywell, Inc., St. Paul, Minn., Research Dept., AFCRL67-0457, AD-658875.

Tenbroek, H. W., et al, "Study of Low Frequency Electrical Characteristics of Clear Air Turbulence and Storm Front Centers", Final Report, 15 Mar. - 15 Sept. 65, Feb. 66, Report No.12011-FR-1, Honeywell, Inc., St. Paul, Minn., Systems and Research Div., AFCRL 66-240, AD-636050.

Wells, E. W., "Project TOPCAT: Summary of Meteorological Observations and Aircraft Measurements During Routine Flights in the Australian Jet Stream", Roy. Air. Est., Farnborough, England,

Tech. Report, Apr. 66, Report No.TR-66922, AD-640375.

Zirkle Jr., R. E., "Study of Techniques for Detection and Measurement of Clear Air Turbulence", Final Report, 15 Nov. 62 - 30 Oct. 65, Jan. 66, Honeywell, Inc., Roseville, Minn., Systems and Research Center, AFCRL-66-115, AD-636325.

APPENDIX B

METEOROLOGICAL CONSIDERATIONS

B.1 INTRODUCTION

Clear Air Turbulence (denoted by the acronym CAT) may be defined as "all turbulence in the free atmosphere of interest in aerospace operations that is not in or adjacent to visible convective activity. This includes turbulence found in cirrus clouds not in, or adjacent to, visible convective activity". CAT thus considers all bumpy flight conditions in regions without convective clouds as they affect airplanes, rockets, v/stols, etc. Certainly, it would be useful to have an airborne CAT detector which would detect and display the presence, location and intensity of turbulence in clear air, regardless of proximity to convective regions, and regardless of altitude.

Although a thorough physical, dynamical and kinematical understanding of CAT is still lacking, enough information is available to provide some firm guide lines for the theoretician and experimentalist interested in the creation of an airborne clear air turbulence detector.

Information will be supplied on the typical spatial dimensions of turbulence; namely, width, height and depth as well as duration where duration represents the time during which a particular airborne platform responds to this atmospheric phenomenon.

The only small-scale atmospheric eddies which will affect jet aircraft of present day design are those characterized by strong kinetic energies with a nearly isotropic distribution and with eddy dimensions of 20 to 200 meters. As the speed of the aircraft increases, so will the eddy size. Thus the eddy range may be increased approximately one order of magnitude for supersonic aircraft.

The actual turbulent regions in the atmosphere, which are composed of these smaller cells or eddies, extend in patches from about 10 to 100 kilometers in the horizontal. The vertical extent of turbulent layers usually is shallow (~ 1 km) although at times they may reach considerable thickness (~ 5 km). These regions are usually elongated in the direction of the prevailing wind; are transitory in nature and their duration may be of the order of 30 minutes. However, turbulent regions associated with mountainous terrain and gravity waves induced by this terrain may be larger and may last longer.(1)

Whether CAT is a form of undulance (wave motion) or turbulence is largely academic. Theoretically, either wave motion or atmospheric turbulence could result in aircraft accelerations called CAT by the pilot. It has been stated that CAT in a stable environment is due to gravity waves which will break up into isotropic turbulence. Turbulence is characterized by large chaotic vorticity, whereas waves usually have small values of vorticity. The energy spectrum is broad with energy being fed from the longer to the shorter wavelengths. Typical wavelengths of gravity waves in the atmosphere are from several thousand feet up to 20,000 feet, with the longer wavelengths associated with mountain waves. However, theory shows that the waves of sufficiently small wavelengths (which can cause aircraft bumpiness) are likely to be unstable and will break up in the presence of wind shear, thus changing into true turbulence.

The operational meteorologist does not have any instrument for the direct measurement of turbulent intensity. He has a good knowledge of the meteorological data from a rawinsonde observational network and the synoptic patterns derived therefrom. The upper air data are smoothed and are only reported at fixed levels. The data may be in the form of temperature lapse rates and wind shears whereas the synoptic patterns may be upper level fronts and jet stream configurations. These furnish valuable information on the

regions in which turbulence is more likely to occur. However, these data are only available, in most cases, every 12 hours and from stations 200 - 300 miles apart. Thus the network has a wide mesh, wider than the scale of the phenomenon we are interested in. These data must be processed and are often several hours old before reaching the aviation forecaster. Thus, this professional is dependent on the accuracies of the subjective intensities reported by the pilots.[2]

The classical pattern of CAT distribution around the jet stream indicates a relatively high frequency of occurrence on the cyclonic side of, above and below, the jet stream core. In these regions the atmosphere is generally thermally stable, but shows strong lateral and vertical wind shears.

More CAT is found over mountain ranges and over continents than over oceans, suggesting that the roughness of the terrain provides a source of perturbation energy or convective activity furnishes thermal energy which acts to play a role in CAT.

The patchiness of CAT is the cause for the difficulties which are experienced in locating and forecasting this phenomenon accurately. The average dimensions of CAT areas suggest that the origin of turbulence lies in the mesoscale structure of the atmosphere which defies analysis and forecasting from the macroscale network of radiosonde observations. At best, correlations between macroscale flow patterns, such as merging jet streams and troughs and CAT may be made.[3,4] Further, it occurs more often and more strongly in winter than in summer.[5]

B.2 DATA REQUIREMENTS FOR A TURBULENCE DETECTOR

The fundamental data required for a remote turbulence detector are time histories of the longitudinal, lateral and vertical true gust velocity components from which their respective power spectra are computed. Experimental data so far indicate the shape of the spectrum remains fairly constant over a wide range of altitude. The magnitudes of the spectra where this similarity exists depend only on the variance.

Figures 1, 2 and 3 show typical turbulence spectra of the u, v, and w (longitudinal, lateral and vertical) components of turbulence measured during Project TOPCAT over Australia in a log-log presentation. Entered on these diagrams are the theoretical slopes indicative of the Kolmogoroff -5/3 power law of turbulence. This law states that the kinetic energy of turbulent motion in the wave number range k to k + dk may be expressed as

$$E(k) = f(k^{-5/3})$$

for the inertial subrange; i.e. for turbulent motion of a scale small enough to be unaffected by buoyant forces, yet large enough so that viscous forces are still negligible. Within this range, kinetic energy is dissipated by larger eddies breaking up into smaller ones. Under such conditions the kinetic energy E(k) has been found proportional to the -5/3 power of the wave number k.

The eddy sizes involved in CAT -20 to 200 m - suggest that the aforementioned law may not be strictly applicable to CAT. From figures 1, 2 and 3, it appears that the inertial subrange of turbulence extends to larger eddy dimensions aloft than near the ground (ca 100 to 200 m, as compared to ca 30 m). Beyond this subrange of turbulence, where the generation, the re-distribution, and the disspation of kinetic energy by various physical processes becomes important, a variety of conditions may occur.

a) The turbulent energy within the isotropic subrange may be supplied by the kinetic energy of the flow over rough terrain in near-neutral stratification.

b) In the free atmosphere, eddy sizes beyond the isotropic inertial subrange may be influenced by positive and negative buoyance forces. The former would occur under free convection and - if they are of appreciable magnitude - would most likely be associated with clouds. Negative buoyance forces due to evaporative cooling may occur at cloud bases.[6] Positive forces would generate kinetic energy whereas negative forces would dissipate them. In

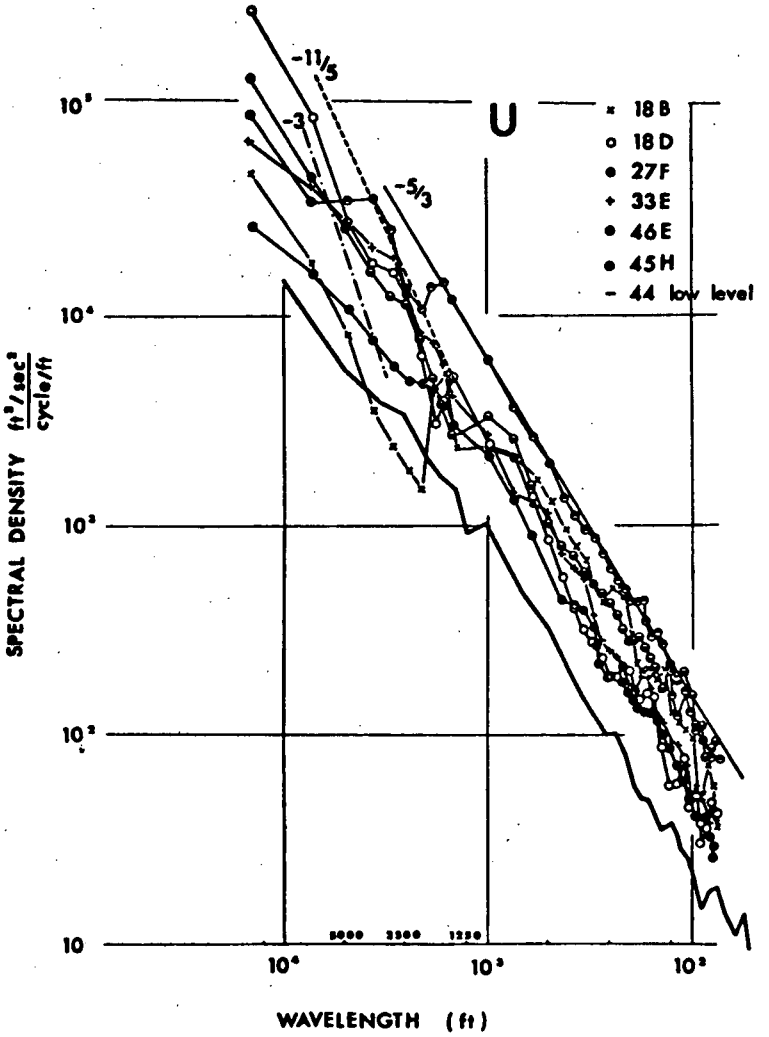

Figure B-1 Spectra of u-(longitudinal) component of turbulence measured by Project TOPCAT over Australia for flights as indicated in the diagram. Ordinate contains log E (k), abscissa is log k. Slopes of -5/3, -3 and -11/5 have been entered for comparison. (12)

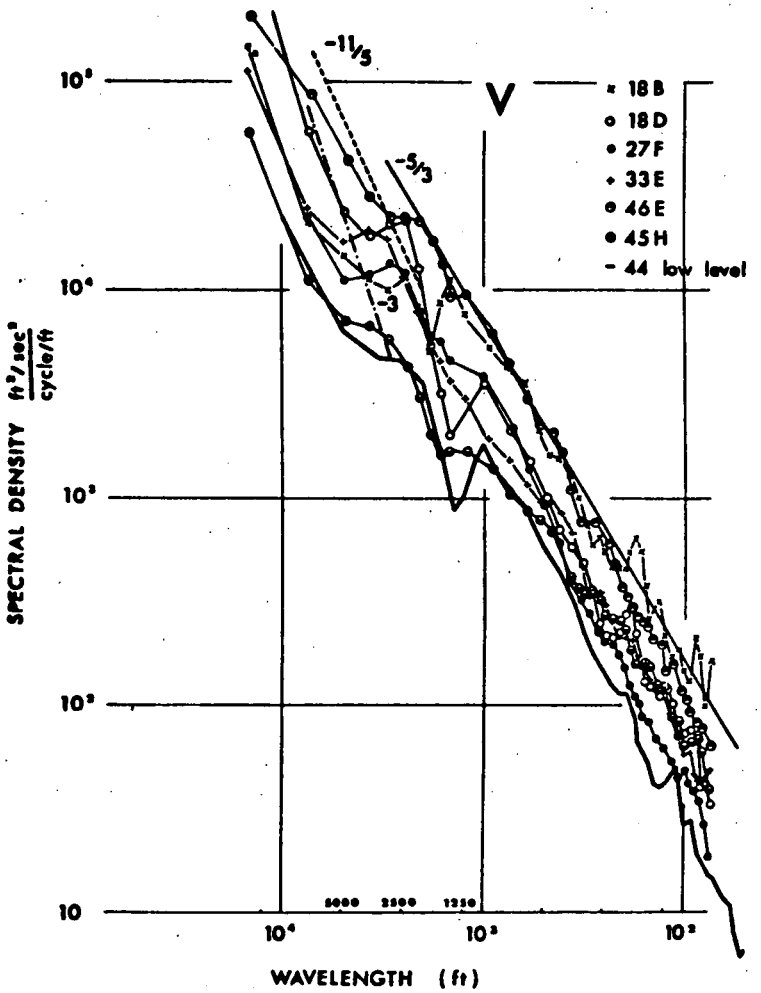

Figure B-2 Same as Figure B-1, except v-(transverse) component.(12)

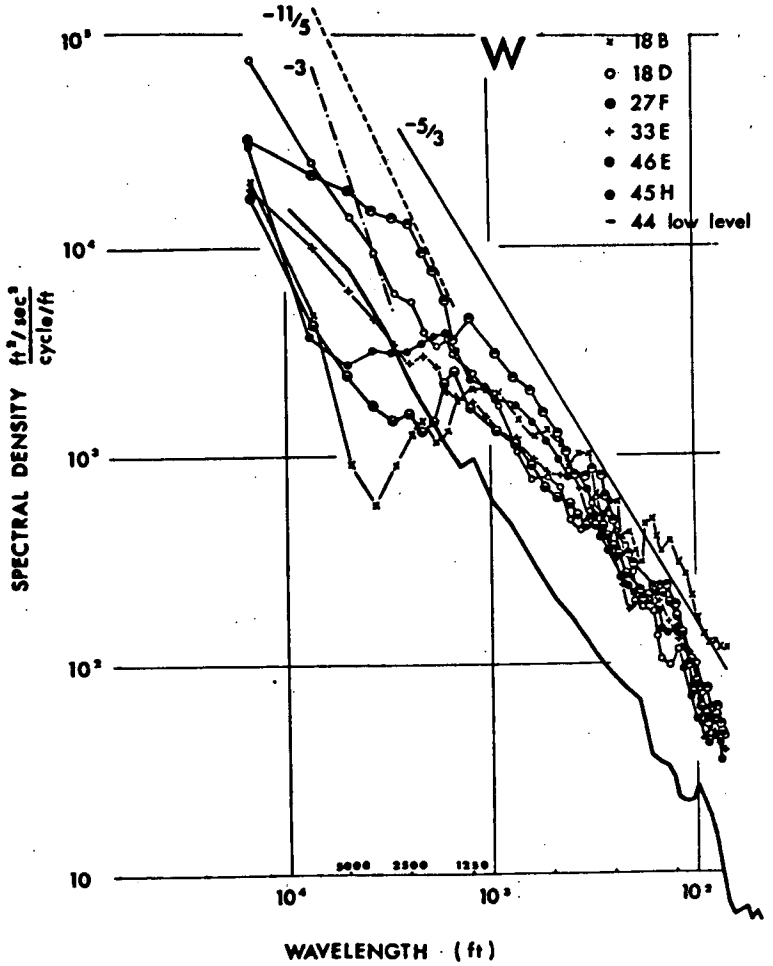

Figure B-3 Same as Figure B-1 _, except w-(vertical) component. (12)

the "buoyant subrange" of turbulence, the exponent of spectral density E (k) is expected to be larger than | -5/3 |.

c) In the presence of vertical wind shears in a thermally stable layer, CAT may be generated by eddies produced in the shearing layer.

Most of the flight data presented above stem from stable regions in the stratosphere above, or in the troposphere underneath, the jet stream. Turbulence at these levels is generated by an excess of shearing stresses over thermal stability and may be due to the formation of unstable waves.

In the free atmosphere, turbulence of small wavelengths has to be generated spontaneously without the aid of a rough surface. Turbulence of the wavelength of CAT, occurring away from the friction layer near the ground, should be considered of spontaneous origin. The local imbalance between shear and thermal stability may, however, be controlled by mesoscale eddies which, in turn, may still be correlated with the roughness of the terrain. This would explain the relative prevalence of CAT over mountains and hills.

Buoyant effects in stable stratification, leading to -3 to -11/5 slopes of the spectrum curves may be of importance near the ground where turbulence is mechanically induced by roughness. In the case of CAT, however, one should not expect the existence of a buoyant subrange of turbulence because the very existence of turbulence in a thermally stable environment already indicates that shearing stresses have over-compensated for buoyant effects of thermal stability. In agreement with this, no buoyant subrange was found from TOPCAT measurements.

To see what generates CAT, we may inspect Figures 1, 2, and 3 as well as Figure 4. From Figure 4 it is evident that the spectra in the CAT wavelength range (ca 100-600 ft.) do not follow the -5/3 slope of energy decay. The u and w spectra of Flight 18B

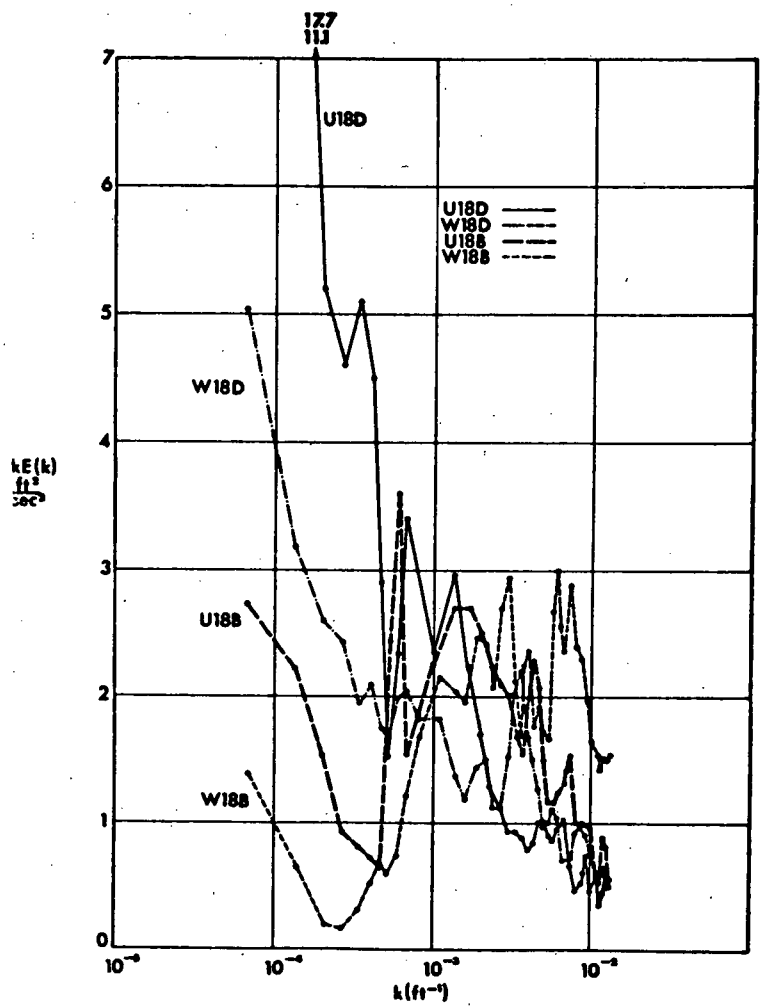

Figure B-4 Power-spectra of u- and w-component of turbulence, measured by Project TOPCAT Flight Nos. 18B and 18D over southern Australia on August 21, 1963. Ordinate contains k . E (k), abscissa is log k.(12)

show a hump, indicating that turbulent energy is added to the atmosphere between wave numbers of approximately 3×10^{-4} ft.$^{-1}$ and 5×10^{-3} ft.$^{-1}$ (i.e., between wavelengths of ca 3000 ft. and 200 ft.)

We may use Flights 18B and 18D as an example. These flights were made near 29,000 ft. pressure altitude, near a range of mountains of ca 3000 ft. elevation. Both sets of spectra were obtained from the same turbulence region within minutes of each other. Nevertheless, the long-wave portions, especially of the w-spectra, differ appreciably in kinetic energy, as may be seen from Figure 5 which contains these spectra in a smoothed form.

The main difference between the two measurements consists in the angle between course and wind direction. During Flight 18B, flown almost perpendicular to the wind, the spectral density at long waves is drastically reduced as compared with E(k) measured during Flight 18D flown parallel to the wind. The conclusion to be drawn is that a wave assemblage was encountered by the aircraft, the wave crests and troughs showing a preferred orientation nearly normal to the wind direction. As the aircraft flies almost parallel to the wavecrests (i.e. normal to the wind) the effect of up- and down-drafts at the given wave lengths is reduced. As the plane turns into the wind (Flight 18B), it experiences the full force of vertical motion associated with the waves.

The waves sensed by the plane are not sharply defined in terms of one wavelength. Instead these waves are irregularly shaped and encompass a band of wavelengths.

These waves apparently break down into isotropic turbulence and eddies of smaller proportions which are ultimately experienced as CAT.[2]

B.3 THE DISSIPATION OF ENERGY

The best way of estimating the dissipation of eddy kinetic energy to molecular energy or heat is indirectly through the

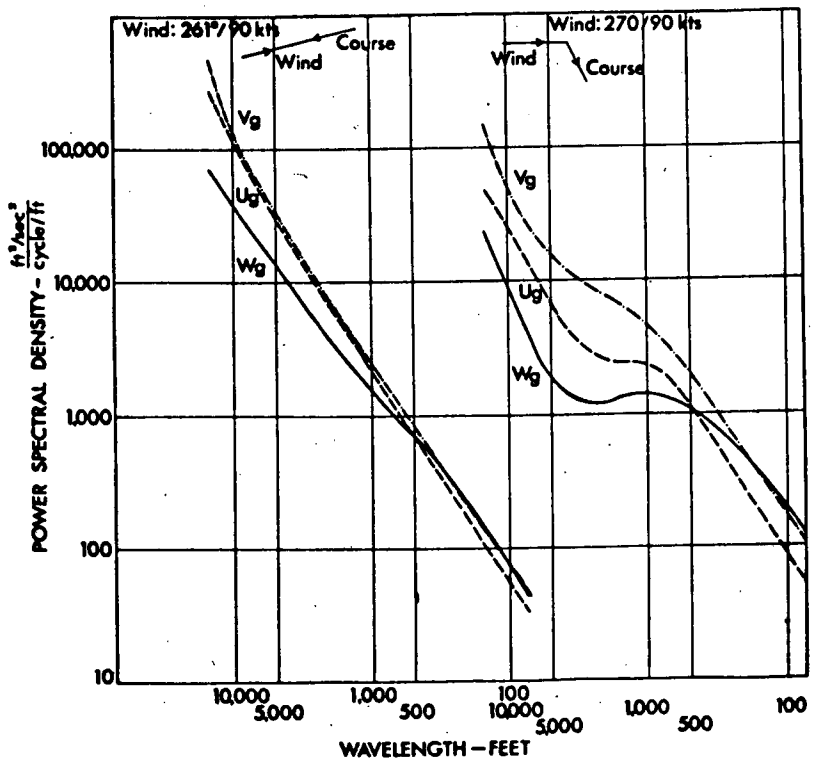

Figure B-5 Smoothed spectra of TOPCAT Flight Nos. 18D (left-hand side) and 18B (right-hand side). Mean wind direction and course are indicated on top of each diagram. (After: (10))

assumptions of "local isotropy" due to Kolmogoroff.[7] This assumes that the small scale but still measurable eddies in the inertial subrange will have their energy ordered thus:

$$S_1(k_1) = \alpha\epsilon^{2/3}(k)^{-5/3}$$

$$S_2(k_1) = 4/3\ \alpha\epsilon^{2/3}(k)^{-5/3}$$

$$S_3(k_1) = 4/3\ \alpha\epsilon^{2/3}(k)^{-5/3}$$

where

ϵ is the rate of dissipation of energy

k is the wave number (reciprocal of length) of eddies in cycles per unit length

α is a universal dimensionless constant determined by experiment

$S_i(k_1)$ is the energy connected with eddies in the i th direction per unit wave number per unit mass along the x_1 axis.

The value of the constant α has been determined to be 0.14 with a precision of perhaps $\pm$5%.

With reference to the Kolmogoroff range, it may be stated that all the energy input to the turbulence is at wave numbers smaller than those in the range and all dissipation at larger wave numbers.

Measurements show that there is a domain of turbulence connected with CAT which is in the inertial sub-range and which may be used to estimate the rate of dissipation ϵ.

From the seven cases indicated in Figures 1, 2, and 3 the following estimates of ϵ have been computed from the three spectrum functions for each run used separately or averaged.

Estimates of ϵ, rate of dissipation of energy (ergs g^{-1} sec^{-1})

Run	from $S_1(k_1)$	from $S_2(k_1)$	from $S_3(k_1)$	Average
18B	133	162	163	153
18D	81	87	52	73
27F	65	67	97	76
33E	102	67	48	72
46E	366	142	116	208
45H	102	24	42	56
44	17	24	8	16

From the mean square gust velocities (truncated at 70 ft. and 15,000 ft. wavelengths), it is possible to get some idea of characteristic dissipation times for the turbulence by dividing the total turbulent energy by the rate of dissipation (average). For the same runs, these times are:

Run	Characteristic dissipation time, seconds
18B	127
18D	490
27F	173
33E	250
46E	160
45H	279
44	273

These times are all on the order of a few minutes. Since CAT patches are known to persist on the order of hours, there must be a continuing input into the CAT systems to keep them active for that length of time. The persistence time may be estimated to be an order of magnitude larger than the "characteristic dissipation time."

C.S.

The impression one receives from the description and measurements quoted above, is of well-developed dissipative turbulence in limited regions of patches, tens to hundreds of kilometers in horizontal extent and hundreds of meters in vertical extent which persist for some hours. In these patches, energy is being degraded at such a rate that an input from larger scale motions must exist, else the turbulence would die away in minutes.

It is not clear that all CAT fits this description. Some may be essentially wave-like motions, either moving or stationary, others may be isolated events which do not persist.

B.4 MOUNTAIN WAVE TURBULENCE

It is well known that a mountain wave consists of a stream of air some thousands of feet deep passing over a mountain range and plunging rapidly down the lee slope, Figure 6.[8] The downward flow is accelerated, and is turbulent due to mechanical interaction with the terrain. Light aircraft cannot penetrate the strong drafts and turbulence of this portion of a well-developed wave. Thus, crashes into mountainsides are all too frequent. At the bottom of the lee slope, a hydraulic jump occurs, and a stream of air rises upward. If the air is sufficiently moist, a roll cloud will form in the rising current. Frequently, dust or snow is carried aloft in the strong updrafts. The low-level air is usually capped by a temperature inversion, smooth (non-turbulent) up-and-down drafts prevail and lenticular clouds form in moist layers.

The base of the inversion layer may harbor extreme turbulence probably due to a combination of shear-gravity waves at this interface and the mechanical turbulence of the boundary layer. Normally, the mid-troposphere above the temperature inversion is smooth. However, a jet stream usually accompanies mountain waves, and those portions of the jet stream that would be turbulent without the wave may become violently turbulent under the added disturbance due to the wave.

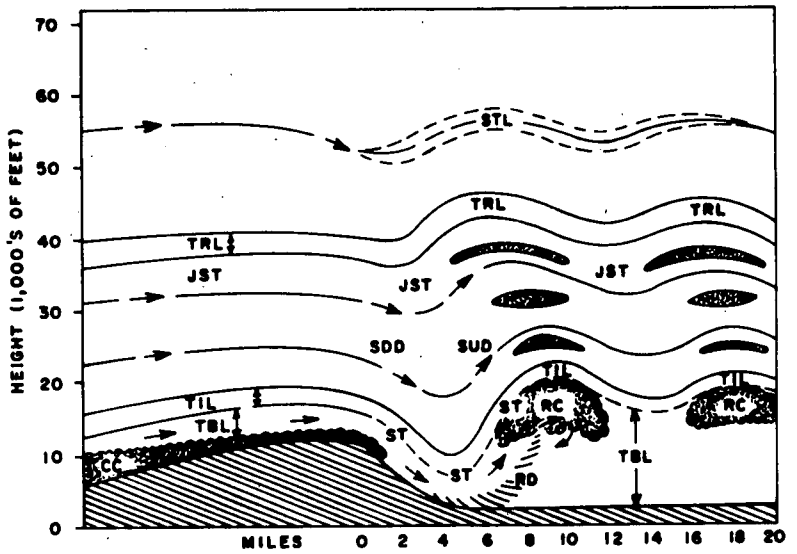

MR – MOUNTAIN RANGE
CC – CAP CLOUD
RC – ROLL CLOUD
LC – LENTICULAR CLOUD
ST – SEVERE TURBULENCE
RD – RISING DUST CLOUD
→ – WIND FLOW

TBL – TURBULENT BOUNDARY LAYER
TIL – TEMPERATURE INVERSION LAYER
SDD – SMOOTH DOWNDRAFT
SUD – SMOOTH UPDRAFT
JST – JET STREAM TURBULENCE
TRL – TROPOPAUSE LAYER
STL – STRATOSPHERIC TURBULENT LAYER

Figure B-6 Mountain Wave Turbulence

The cloud forms of the wave depend on the moisture of the air. The clouds of Figure 6 are typical, but cloudless waves occur in dry air masses. In this case, dust rising rapidly from the surface may be the main visual indicator of wave activity. In other cases, the air may be moist with extensive cloud layers in which rifts are produced in regions with descending motion. To an observer on the ground, wave clouds appear to be stationary and it is not obvious that the winds are blowing through them. Waves may exist in one locality for a number of hours, but tend to migrate with the associated wind patterns. Conditions within them vary with time so that detailed cloud forms may change considerably in appearance within a period of half an hour. The features shown in Figure 6 are generally not as well developed for smaller mountain ranges; however, steep mountains as low as 2,000 feet above surrounding terrain may produce definite wave motions. Mountain waves are common along the Sierra Nevadas, the steep lee slopes of the Rockies and the Sangre de Cristo mountains for northeastern New Mexico.

Mountain waves have been discussed in some detail here because of their low-level hazards and their apparent importance as a major source of turbulence in the stratosphere.

B.5 PROJECT HICAT

The primary objective of Project HICAT (High Altitude CAT) was to obtain a statistically adequate, meteorologically correlated sample of atmospheric turbulence data at 40,000 to 70,000 feet altitude as required to establish adequate gust design criteria for aerospace vehicles. A turbulence instrumented WU-2 high altitude research aircraft was operated from April 1964 to February 1968, from USAF bases within the Continental United States and from worldwide locations such as New Zealand, Australia, Alaska, Hawaii, England, Puerto Rico, Canal Zone, etc.[9]

The fundamental data obtained by the HICAT program are time histories of the vertical, lateral, and longitudinal true gust velocity components from which their respective power spectra are computed.

Data in this form allow the engineer to convert his knowledge of the atmosphere into stress units in a structure, by utilizing Fourier methods. Simply stated, if a designer can calculate the transfer function of a proposed aircraft and the appropriate spectrum of turbulence is known, the spectrum of response can be calculated. Determining the appropriate turbulence spectrum is an essential function of the HICAT program. Experimental data indicate the shape of the spectrum remains fairly constant over a wide range of altitude. The magnitudes of the spectra where the similarity exists depend only on the variance. One of the principal efforts of HICAT is to define the variance as a function of altitude and local meteorological parameters.

HICAT search statistics indicate that during the test period, February '64-February '68, when 1221.6 flight hours were recorded approximately 4.5% of the time, turbulence was encountered. However, this percentage figure is somewhat biased towards conservatism because of the following data editing procedure.[10]

If continuous rapid c.g. acceleration disturbances were observed in excess of ± 0.05 g, turbulence was considered to be present. Data was processed, if frequent c.g. center of gravity acceleration peaks of ± 0.10 g or more were observed. However, those turbulence patches of less than 10 seconds duration, corresponding to about one mile in physical length, were usually ignored.

The determination of the absolute gust velocity components of atmospheric turbulence from an aircraft requires the measurement of (1) the motion of the air disturbances with respect to the aircraft and (2) the motion of the aircraft with respect to the ground.

In the HICAT instrumentation system the air disturbances relative to the aircraft are measured with a gust probe; the aircraft motion relative to the ground is determined by an inertial platform.

Figure 7 compares the envelope of all the HICAT spectra with similar data obtained from the Douglas NB-66B High Altitude Gust Survey and the Australian TOPCAT program. The HICAT spectra overlay the TOPCAT spectra but fall slightly below the upper limit of the B-66 thunderstorm data, as might be expected. To provide a low altitude yardstick for comparison, a spectral envelope of moderate intensity turbulence for HICAT landing approaches is shown. Note the characteristic -5/3 slope.

On the basis of 74 sets of data, cumulative probability curves of power spectral density (psd) were prepared. Psd values were selected at probabilities of 0.01, 0.1, and 0.5. At each of the three probability levels, the psd values thus read were then plotted versus inverse wavelengths to yield Figure 8. An average psd curve was thus obtained at each of three probability levels. The curves corresponding to the lower probability levels are most pertinent for direct practical application, as they reflect the more severe turbulence. The curves corresponding to the higher probability levels, however, are based on much more data and are statistically more reliable.

Comparisons between the psd's for the vertical, lateral and longitudinal components of turbulence, all at the 0.1 probability level, are shown in Figure 9.

B.6 CONCLUSIONS

A few of the conclusions of the HICAT Project relevant to detection are summarized.

(1) The true gust velocity power spectral densities are characterized, on the average, by slopes on log-log plots of -1.44 to -1.71 for the vertical and longitudinal components of turbulence.

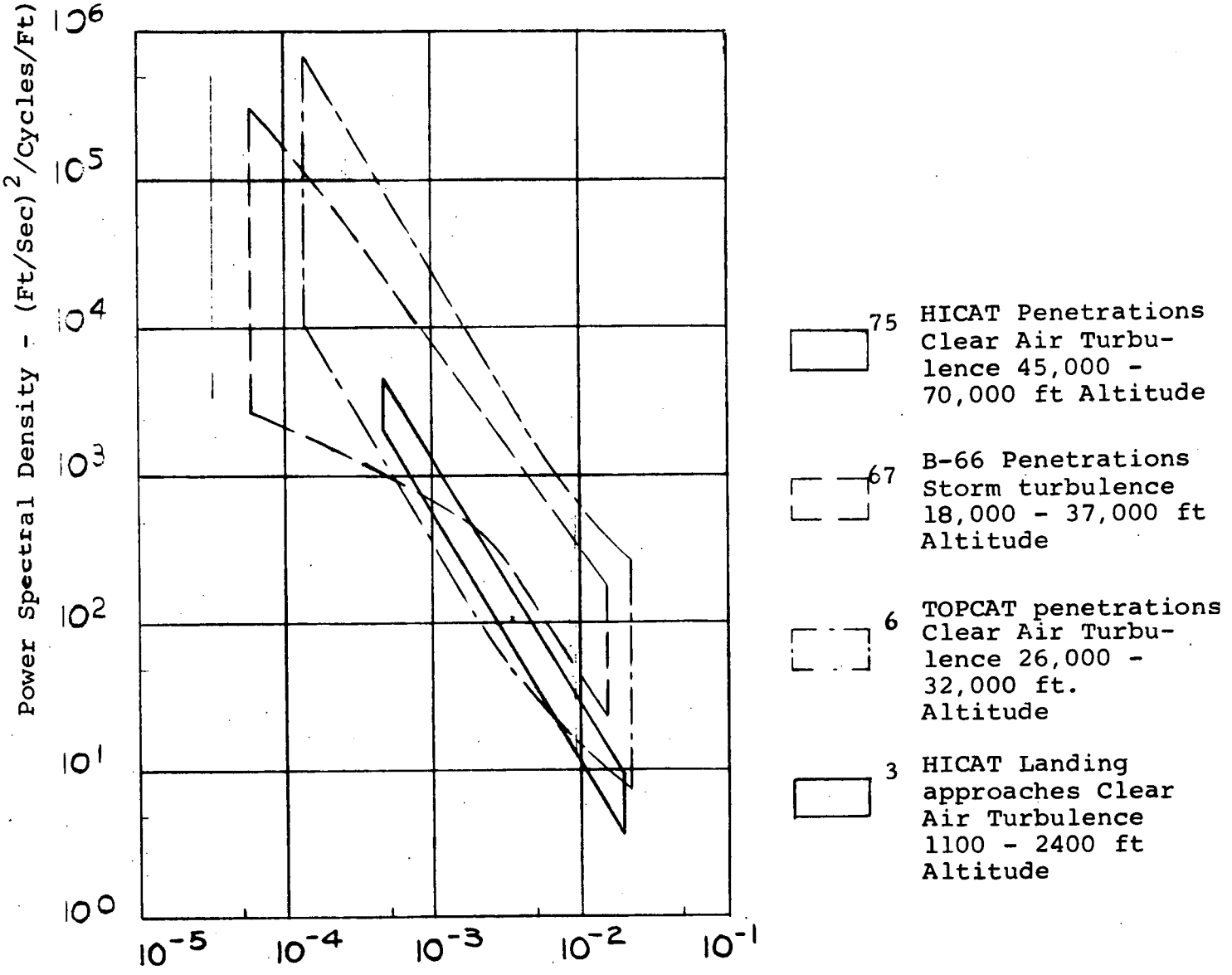

Figure B-7 Comparison of Gust Velocity Power Spectral Envelope

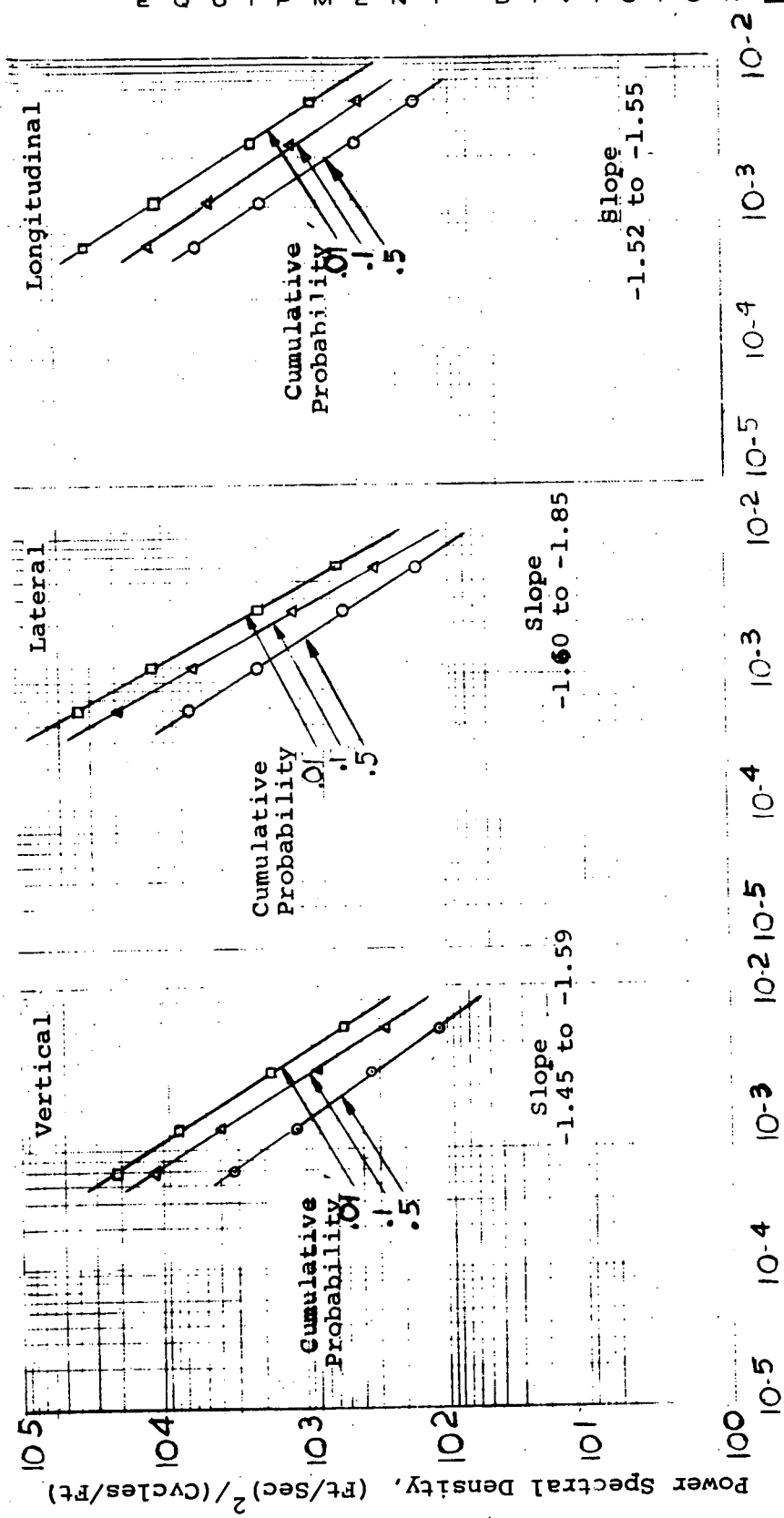

Figure B-8 Average Power Spectral Density Based on Cumulative Probability, Maximum λ = 2,000 ft (10)

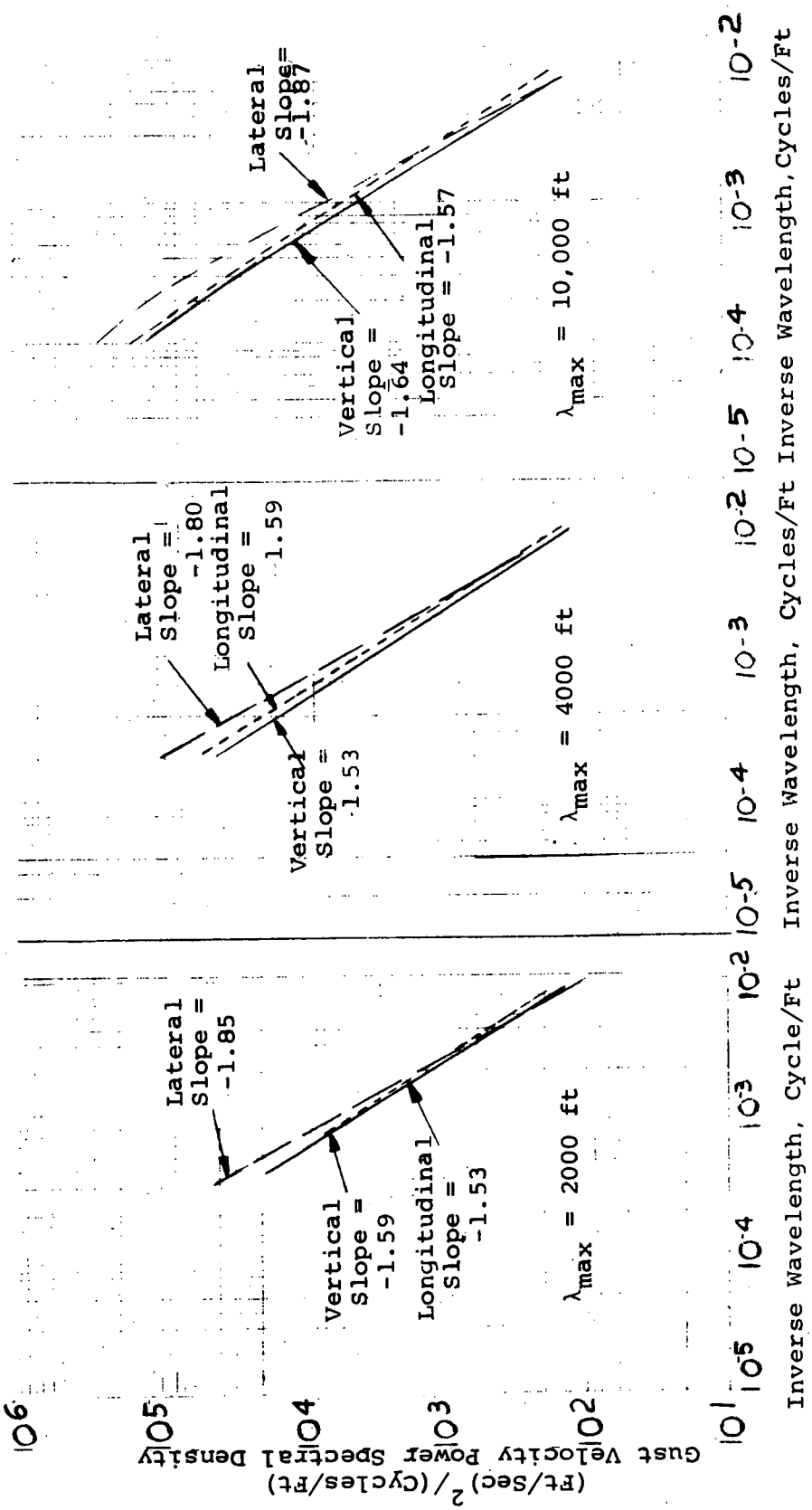

Figure B-9 Comparison of Power Spectral Densities for 3 Components, Cumulative Probability of .1, Maximum λ = 2000, 4000, 10,000 Ft(10)

On the same basis the lateral component was found to have slopes of -1.60 to -1.87. (This higher range of values in this component is attributed to instrument noise.)

(2) The psd curves, on the average, remain straight or nearly straight to wavelengths approaching 10,000 feet. The average scale of turbulence, defined as the constant L in the Von Karman equation or similar equations, is at least 20,000 feet.

(3) The turbulence appeared to be distinctly non-stationary, i.e. the statistical properties of the gust velocity time series data were found to vary significantly within the turbulence samples. Partly because of the lack of stationarity, the ratio of peak-to-rms airplane acceleration was found to range from 1.16 to 2.58 times the ratio predicted by theory (Rice's equation) for a stationary Gaussian time history.

(4) A comparison of the psd's of the components of the gust velocities indicates all three components to be about equal in magnitude at the highest measured frequencies (approximately 0.007 cycles per foot); it shows the lateral components, however, to become more severe at the lower frequencies. RMS gust velocities - obtained by integrating the psd's over the frequency range from 0.0005 to 0.007 cycles per foot (2000 ft. to 100 ft. wavelengths) - indicate that the lateral component is larger than the longitudinal by 10 percent and larger than the vertical by 20 percent. At the longer wavelengths, there is some indication that these percentages increase. However, in view of the lower quality of the lateral gust measurements, the observed percentage differences amongst the three components are not considered large enough to justify a conclusion that high altitude CAT, on the average, is anisotropic.
A possible explanation for the non-Gaussian behaviour of CAT is that the motion is patchy - that is, regions of locally intense turbulent motion are surrounded by spaces in which the turbulence is weak or non-existent. Thus an examination of the statistical nature of the

patchiness of turbulence may be necessary in order to expedite the development of a remote CAT detector.

Energy spectra of atmospheric motions provide a precise representation of some of the essential properties of turbulence. However, for some purposes such spectra are averages over too large a data collection to be pertinent. For example, spectra do not give information on the local distribution of energy in the peak gusts. Such information would be of value in an attempt to introduce turbulence as a forcing function for a remote CAT detector. In addition, the correlation between the spectrum of CAT and the fluctuation spectra of a detector should be investigated and synthesized.

As aircraft speed tends to increase, the plane tends to become more responsive to the high power, low frequencies of turbulence. Thus supersonic aircraft will react to the higher power and lower frequencies of CAT. These lower frequencies will be associated with longer wavelengths. Therefore, a remote, electromagnetic CAT detector should be responsive to a wide range of frequencies.

B.7 BIBLIOGRAPHY

(1) Pao, Y. and Goldburg, A., Edit., "Clear Air Turbulence and Its Detection", Plenum Press, New York, 1969, pp.7-15.

(2) Clear Air Turbulence Meeting, Feb. 23-24, 1966, Soc. of Auto Eng., Inc., New York, New York 10017, Introduction.

(3) Lake, Herman, "A Meteorological Analysis of Clear Air Turbulence", (A Report on the U.S. Synoptic High Altitude Gust Program), Geophys. Res. Papers, No.47, Feb. 1956, GRD, AFCRC, ARDC.

(4) Lake, Herman, "Clear Air Turbulence Associated with Negative Vertical Wind Shear", Journal of Meteor., Vol. 14, April 1957, pp. 188-190.

(5) Panofsky, H. A., "Internal Atmospheric Turbulence", Bull. Amer. Meteor. Soc., Vol.50, No.7, July 1969, Pp.539-543.

(6) Pao, Y. and Goldburg, A., Edit., "Clear Air Turbulence nd Its Detection", Plenum Press, New York, 1969, p.521.

(7) Ibid, pp.113-115.

(8) Endlich, R. M., et al, "Techniques for Determining a World-Wide Climatology of Turbulence Through Use of Meteorological Data", AFCRL-66-355, Standord Research Institute, Menlo Park, California, May 1966, Pp.11-16.

(9) Pao, Y., and Goldburg, A., Edit., "Clear Air Turbulence and Its Detection", Plenum Press, New York, 1969, pp.127-143.

(10) Crooks, W. M., Hoblit, F. M., Mitchell, F. A., et al, "Project HICAT, High Altitude Clear Air Turbulence, Measurements and Meteorological Correlations", Tech. Report AFFDL-TR-68-127, Vol.1, 1968, AF Flight Dynamics Lab., AF Systems Command, Wright-Patterson AFB, Ohio, AD846086.

APPENDIX C

CAT TRANSMITTER

The CAT transmitter is a modulated master oscillator-power amplifier chain system. The major components consist of:

1. Master oscillator
2. Modulator
3. Beam expanders
4. 8-tube amplifier
5. Output telescope
6. Detector

A schematic of the transmitter is shown in Figure C-1. The general layout of the parts are shown in Figure C-2 and Figure C-3. Figure C-4 and Figure C-5 are the artist's concept of the assembly as viewed from the left and right sides.

All major items except the output telescope, the detector and some of the return-beam optics are supported by a closed end H-section box structure. This structure is extremely rigid and will maintain the exact alignment of the system components. This box structure will be constructed of a titanium alloy which was chosen for its low coefficient of thermal expansion. It is one-third that of aluminum and one-half that of steel. Titanium is 45 percent lighter than steel, but 60 percent heavier than aluminum. However, its great strength compared to aluminum allows the use of thinner sections thus giving a total weight nearly as low as an aluminum structure. The sides and end covers will be a honeycomb material to save weight.

This box structure, the output telescope, and the detector with its associated optics are supported by an aluminum I-beam frame. This frame will be attached by means of shock mounts to

the aircraft structure to isolate the transmitter from aircraft vibration.

The master oscillator will be a slightly shortened version of the stable laser that Raytheon has successfully flown in other programs. This laser will be supported by Invar tubes incorporated into the box structure. The output beam will be 3 mm in diameter. A beamsplitter at the output of the laser will direct most of the energy to the modulator with a few percent being used as the local oscillator. The local oscillator beam is directed by adjustable mirrors, attenuated as needed, and expanded to 15 mm before combining with the return signal at the combining beam splitter.

The main 3-mm beam is modulated by the gallium arsenide crystal modulator, which incorporates roof-top polarizers, before going through the 5X beam expander. From the beam expander a modulated 15-mm beam is directed by means of adjustable mirrors into the eight-tube amplifier section. Both the modulator and beam expanders are supported by adjustable mounts to allow precise beam alignment.

The beam is directed back and forth through the eight tubes by retro mirrors supported on precision turnaround blocks. Since stability of these turnarounds is of the utmost importance, the blocks will be made of Invar. The blocks are adjustable to achieve precise beam alignment. Each block has a vee-groove machined centrally along the long axis of the mounting face. Matching grooves are machined in the box structure end plates. Precision dowel pins laid in this groove support the block along a center line, allowing a small amount of rocking of the block. Alignment is accomplished by selective tightening of the four hold-down bolts to give the block the angle required. As each successive turnaround is at 90° to the one before, complete beam direction can be secured by adjusting two successive blocks. Rough beam positioning can be

done by sliding the blocks along the dowel pins before tightening the hold-down bolts.

Because the amplifier is a flowing gas system, gas is fed from control valves on a manifold to each turnaround and window block on the front end of the system (the front end is the beam output end). At the back end, each turnaround is connected to the vacuum system by means of a balanced manifold to assure even gas flow in all the tubes.

The amplifier tubes will be of double-walled Pyrex construction with liquid cooling. There will be one center anode and two end cathodes on each tube. The tubes will have commercial stainless steel flanges and bellows on each end to allow fastening to the turnaround blocks. The bellows permit turnaround adjustment as well as accepting variations in the tubes normal to "glass blowing" assemblies. The tubes will be supported by two adjustable supports as near as possible to the recommended "2/9 of the length from each end" to minimize bending from its own weight. Because of cathodes and water tubulations extending from the tube, some compromise in the position of the supports will be necessary.

The input and output windows of the amplifier will be KCL flats supported on blocks at the Brewster angle of $55^{\circ}36'$. The output beam will be vertically polarized.

From the amplifier, the beam goes through a 14° Brewster angle germanium polarizer, through a 1/4-wave plate which produces circular polarization and to the output telescope, which produces a 12-inch beam. These front elements, other than the telescope, are supported by the I-beam frame and the box frame. The telescope is mounted on the I-beam frame in such a manner as to be compatible to the aircraft being used.

The return signal from the telescope goes through the 1/4-wave plate where it becomes horizontally polarized. It reflects

off the germanium polarizer at 28° onto a diverting mirror. This mirror directs the beam through a 1/2-wave plate that makes the beam become vertically polarized. From here the beam is directed to the combining beamsplitter where it homodynes with the vertically polarized L.O. beam. Finally, the 15-mm diameter combined beams go through a lens that focuses the energy down to the small spot required by the photodetector.

As the path length from the master oscillator to the center of the output telescope is approximately 43-1/2 feet, stability and alignment are very important. Stability has been achieved by using a rigid structure and low thermal expansion materials. Proper alignment is secured by making all mirrors and beamsplitters with precision two-way adjustments. All other parts have the required moving ability built into the mounts while maintaining excellent mechanical stability.

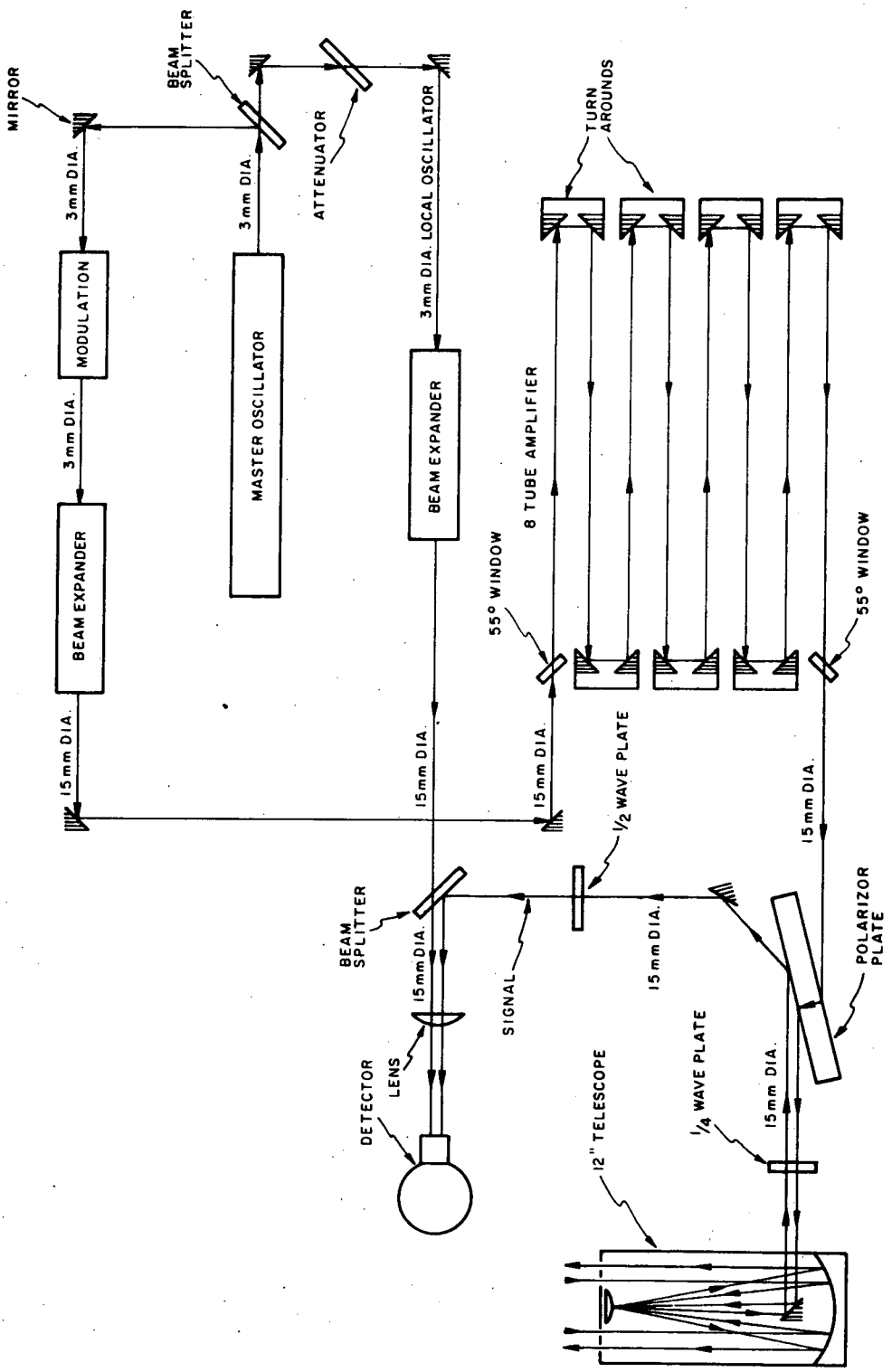

Figure C-1 CAT Transmitter, Schematic Diagram

Page intentionally left blank

Page intentionally left blank

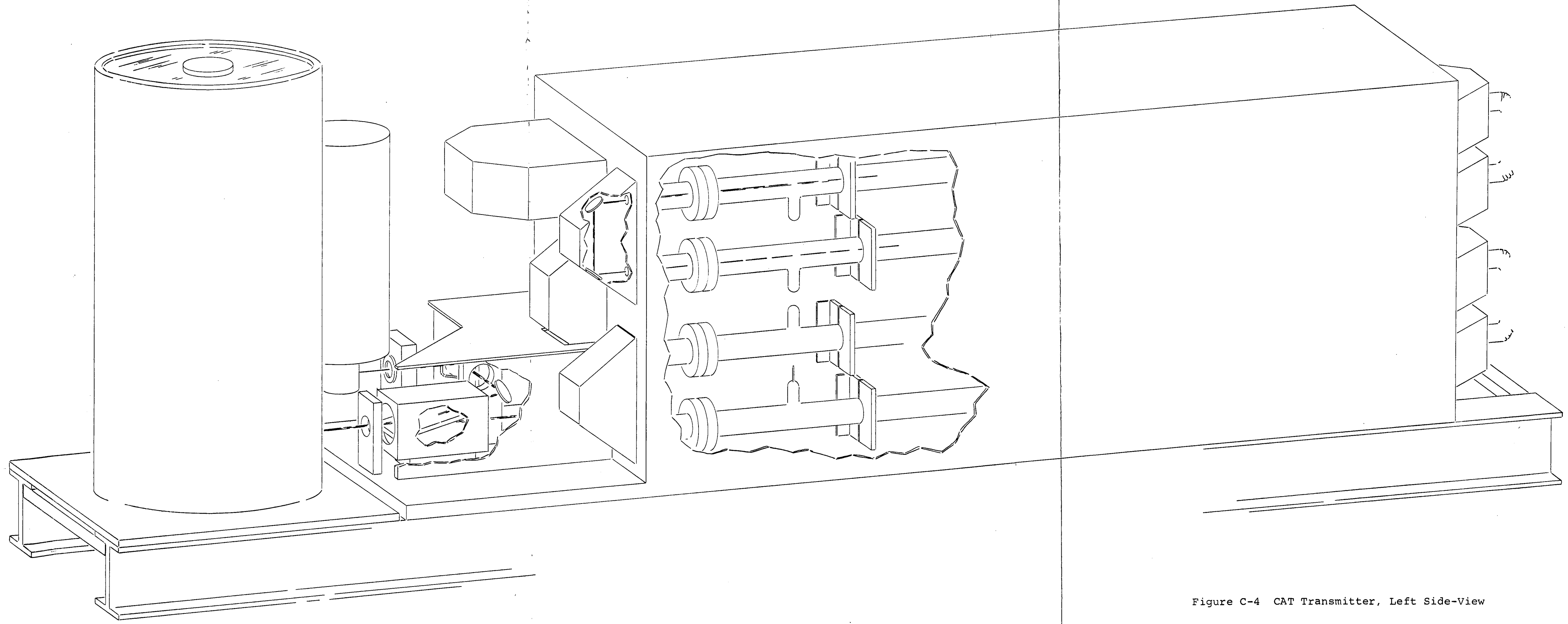

Figure C-4 CAT Transmitter, Left Side-View

FOLDOUT FRAME 1

FOLDOUT FRAME 2

FOLDOUT FRAME 3

RAYTHEON COMPANY
EQUIPMENT DIVISION

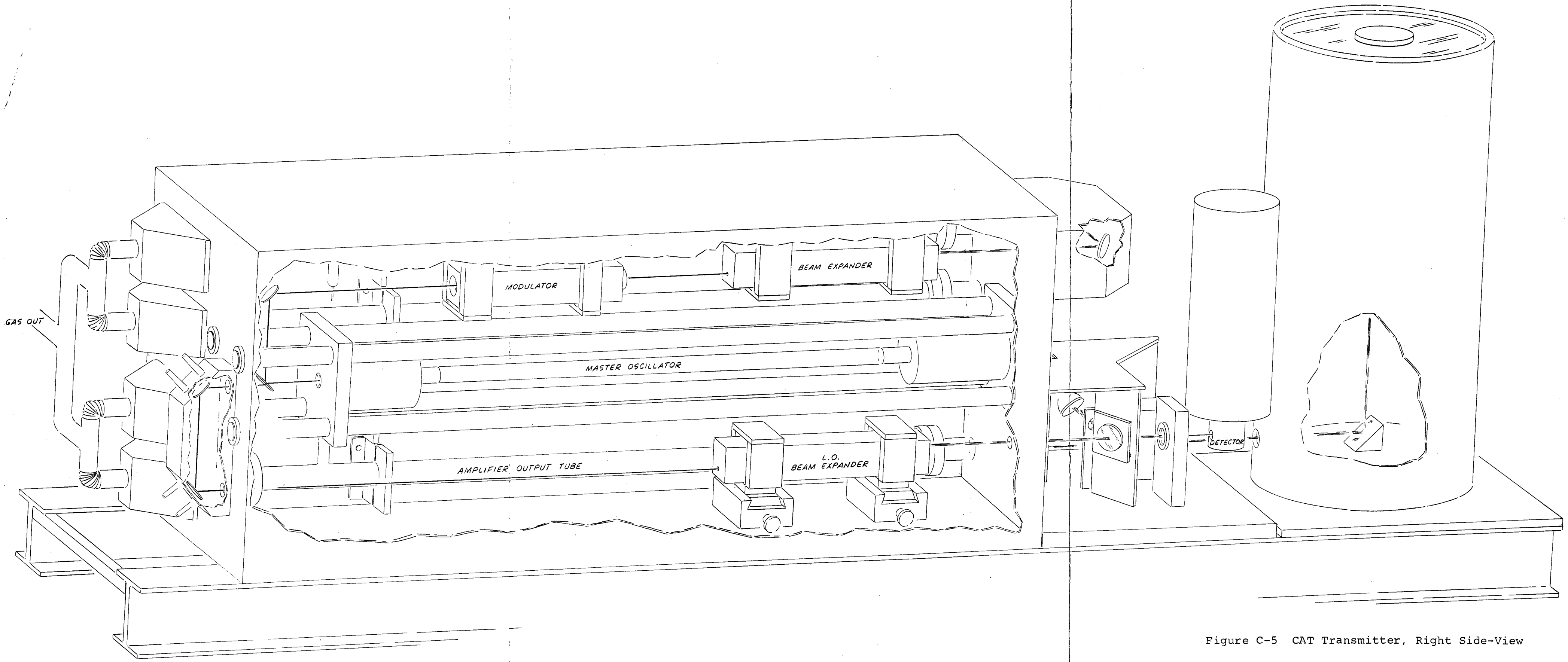

Figure C-5 CAT Transmitter, Right Side-View